Micromechanical modeling of γ-TiAl based alloys

Von der Fakultät für Georessourcen und Materialtechnik

der Rheinisch-Westfälischen Technischen Hochschule Aachen

zur Erlangung des akademischen Grades eines

Doktors der Ingenieurwissenschaften genehmigte

Dissertation

vorgelegt von Dipl.-Ing.

Claudio Renato Zambaldi

aus München

Berichter: Professor Dr.-Ing. Dierk Raabe
Univ.-Prof. Dr. rer. nat. Dr. h. c. Günter Gottstein

Tag der mündlichen Prüfung: 14. Juni 2010

Berichte aus der Materialwissenschaft

Claudio Zambaldi

Micromechanical modeling of γ-TiAl based alloys

Shaker Verlag
Aachen 2010

Bibliografische Information der Deutschen Nationalbibliothek
Die Deutsche Nationalbibliothek verzeichnet diese Publikation in der Deutschen Nationalbibliografie; detaillierte bibliografische Daten sind im Internet über http://dnb.d-nb.de abrufbar.

Zugl.: D 82 (Diss. RWTH Aachen University, 2010)

Printed in Germany.

ISBN 978-3-8322-9717-6
ISSN 1618-5722

Shaker Verlag GmbH • Postfach 101818 • 52018 Aachen
Telefon: 02407 / 95 96 - 0 • Telefax: 02407 / 95 96 - 9
Internet: www.shaker.de • E-Mail: info@shaker.de

Meinen Eltern

Mira, esto de las cosas elásticas es muy raro, yo lo siento en todas partes. Todo es elástico, chico. Las cosas que pacecen duras tienen una elasticidad ...
Piensa, concentrándose.
—... una elasticidad retardada— agrega sorprendentemente.

"Sieh mal, das mit den elastischen Dingen ist sehr seltsam, ich spüre das überall. Alles ist elastisch, Junge. Selbst die Dinge die hart zu sein scheinen, besitzen Elastizität ..."
Er denkt angestrengt nach.
"... eine verlangsamte Elastizität", fügt er überraschend hinzu.

Julio Cortázar
El perseguidor (Der Verfolger), 1958

Acknowledgment

This work was carried out in the department of Microstructure Physics and Metal Forming at the Max-Planck-Institut für Eisenforschung in Düsseldorf. Prof. Dr.-Ing. D. Raabe, head of the department and director of the institute, is thanked for his continuous support during the preparation of this thesis. Valuable and inspiring discussions together with a high amount of scientific freedom have made possible the present results.

Prof. Dr. rer. nat. G. Gottstein is acknowledged for acting as the co-advisor for my examination and for providing valuable comments on a draft of this thesis.

Dr. rer. nat. F. Roters is thanked for decisive discussions about the intricacies of crystal plasticity modeling and simulation. His comments have often set me on the right track towards the solution.

Dr. habil. S. Zaefferer is gratefully acknowledged for his original idea of the fit-rank indexing and the fruitful collaboration that followed from it. Without his support on the arising issues, the microstructural characterization efforts would have hardly worked out in the way they did. Also, Dr. S. Wright (EDAX-TSL) is thanked for the excellent collaboration and discussions on the EBSD optimization and the incorporation of the improved indexing algorithm as part of the EDAX-TSL OIM software package.

I am indebted to Prof. K. Maruyama for hosting me at his laboratory at Tohoku University (Sendai) during a JSPS fellowship from October to December 2007. Further, I would like to thank Prof. K. Yoshimi, Dr. M. Tsunekane, and Dr. H. Ghassemi-Arkmaki for their assistance during that time and for making the visit successful and an enjoyable experience. Prof. K. Kishida is thanked for discussion time and for showing me the laboratories at Kyoto University during the Ti-2007 conference.

Many thanks to my present and former colleagues at the Institute, Prof. S. Nikolov, Prof. C.-S. Han, Dr. D. Ponge, Dr. M. Palm, Dr. F. Stein, Dr. N. Zaafarani, Dr. A. Ma, Dr. P. Romano, Dr. A. Bastos da Silva Fanta, Dr. H. Sato, Dr. H. Fabritius, Dr. P. Eisenlohr, Dr. D. Tjahjanto, S. Voss, D. Steinmetz, H. Knoll, D. Ma, B. Liu, L. Hantcherli, and Dr. K. Balasundaram for valuable discussions and their manifold support. Prof. S. Hild and C. Senöz are thanked for their help with the AFM measurements. Prof. S. Kobayashi deserves special mentioning because of his help and advice during the beginning of the work. Furthermore, I would like to thank Prof. T. R. Bieler for many helpful discussions during his sabbatical year at the institute. All colleagues in the department are thanked for creating a friendly and stimulating atmosphere.

The experimental work was supported by G. Bialkowski, H. Bögershausen, K. Angenendt, M. Nellesen, E. Bartsch, M. Adamek, and H. Faul and I would like

to thank all of them for their assistance. C. Regner and P. Siegmund are acknowledged for the fast and reliable service when it came to ordering books and scientific articles. A. Kuhl and B. Beckschäfer are thanked for their valuable support regarding the used computer infrastructure.

The largest part of the present work was performed within the European Union FP6 IMPRESS integrated project. The financial support and the excellent project management is acknowledged. It was fun to be part of such a successful international project. From the project members I would like to thank U. Hecht, Dr. G. Behr and Dr. W. Löser, C. Gugushev, Dr. D. Hu, Prof. I. Egry, and Prof. J. Lapin for valuable discussions as well as for providing sample material. Prof. H. Fecht and Dr. N. Deyneka are thanked for providing the initial nanoindentation data.

Prof. F. Appel is thanked for a very helpful discussion during a visit at GKSS at the beginning of the project. Dr. V. Kouznetsova and Dr. L. Delannay are acknowledged for valuable hints on the implementation of periodic boundary conditions.

Without free software such as JabRef, Gwyddion, the mtex toolbox and others, generously made accessible by its creators, many tasks that were accomplished during the course of work, would have taken significantly more effort.

Contents

Part I

Introduction, literature review, and state of the art

1

General introduction and research objectives

1.1 Introduction

Since the 1970s, phases in the Ti-Al system have been widely recognized as a possible basis for the development of novel lightweight alloys for high temperature structural applications. The primary driving force behind the considerable research efforts since that time is to partially substitute the much denser superalloys or the less temperature resistant titanium alloys in gas turbines. Indeed, from a current perspective the chances are good, that future aero-engines in civil aircrafts will contain some parts made from titanium aluminide based alloys.

At the moment, the alloys with the best overall mechanical performance are based on the intermetallic, $L1_0$-ordered γ-TiAl phase, strengthened by minor fractions of the hexagonal α_2-Ti_3Al phase. Due to the complex nature of intermetallic alloys some issues that can be approached relatively easy in disordered alloys, remained unresolved despite considerable efforts. Therefore, a better understanding of these alloys presents a formidable challenge to the material scientist. To improve the micromechnical understanding of these alloys was the objective of the work presented in the following.

The work was performed mainly within the European sixth framework program integrated project IMPRESS (Jarvis and Voss, 2005). While the core of the project aimed at the processing in the liquid state and the solidification behavior of Ti-Al based alloys, some amount of work was also directed to the generation of microstructures with well-balanced mechanical properties and to their characterization and understanding.

1.1.1 Present and future applications of titanium aluminides

A recent overview of application fields of titanium aluminide alloys is given in Clemens and Kestler (2000). For automotive applications, several parts have been investigated including valves and turbocharger fans. Applications in automotive parts are a less-critical application compared to a turbine blade in a jet engine, because a failing turbocharger-fan does not lead to catastrophic failure of the car.

In the field of aero-engines the application of titanium aluminides is envisaged for turbine blades. In blade applications not only the direct weight saving from making lighter components can be exploited. Also indirect weight saving effects result from the reduced centrifugal force acting on the disks onto which the turbine blades are mounted. At the moment, engine manufacturers are working on the implementation of γ-TiAl based alloys for new aero-engine products (Weimer and Kelly, 2008) with improved thrust to weight ratios.

1.1.2 Related literature

Since the field of titanium aluminide alloy development is relatively new, no monograph on the topic exists at the moment. Well-presented information has appeared in several key journal articles, conference proceedings and book chapters. Therefore, a short overview on some important sources of information is given in the following.

Pages 2093–2101 of Pope (1996) are dedicated solely to TiAl. The book of Sauthoff (1999) includes a chapter on titanium aluminides. The series of volumes by Westbrook and Fleischer (2000a,b,c,d, 2002) describes many aspects of intermetallic materials in good detail. Several sections on TiAl are included, e. g. Huang and Chestnutt (2000). Appel and Oehring (2003) and Kestler and Clemens (2003) contributed chapters on fundamental and technological aspects of γ-TiAl based alloys in a recently published book edited by Leyens and Peters (2003). Further, the eighth chapter of the recent second edition of *Titanium* by Lütjering and Williams (2007) has a wealth of updated information on titanium aluminides. A section in Polmear (2006) reviews the development of alloys based on Ti_3Al, γ-TiAl and $TiAl_3$.

A large amount of original work has been published in the proceedings of symposia organized with the help of the Materials Research Society (MRS) and The Minerals Metals and Materials Society (TMS). An overview is given in the appendix A.1.

Furthermore, some review articles should be mentioned here. Kim (1989), Kim and Dimiduk (1991), Froes et al. (1992) and (Kim, 1994) gave overviews of relevant aspects of Ti-Al alloy development. The review of George et al. (1994) includes a section (pp. 423-435) on alloying effects, microstructures and mechanical properties of two-phase TiAl. Appel and Wagner (1998) gave an extensive review of 82 pages on the microstructures and mechanics of two-phase titanium aluminides, including 265 references.

1.1.3 Timeline of titanium aluminide alloy development

For information on the early development of titanium aluminides see Fleischer et al. (1989). Dimiduk (1995) marked the mid-1970s as starting point for γ-based Ti-Al alloy development. Kim (1994) classified a first generation of alloys, exemplified by the composition Ti-48Al-1V-(0.1 C) from Blackburn and Smith (1982). The second generation of cast alloys was defined as composition Ti-48Al-2Nb-2Cr and derivatives. All compositions in this thesis are given in terms of atomic percent (at.%) if not stated otherwise.

Kestler and Clemens (2003) defined the 2nd generation as

Ti—(45–48)Al—(1–3)X—(2–5)Y—(<1)Z (at.%),

where X=Cr, Mn, V; Y=Nb, Ta, W, Mo; Z=Si, B, C. Further, Kestler and Clemens (2003) defined the 3rd generation of γ-TiAl based alloys as the high niobium containing alloys with about 5-10 at.% niobium. These alloys were also in the focus of the present work.

1.2 Motivation

Three key problems in the field of γ-TiAl based alloy development were identified at the commencement of the research presented in this thesis. The following pivotal challenges impede progress in the alloy development and in the understanding of the relations between microstructure and macroscopic mechanical properties:

- An efficient method is needed to characterize the precise microstructure of γ-TiAl based alloys. Up to now, only TEM based techniques were capable to resolve the cubic pseudosymmetry of the γ-TiAl order domains. Electron backscatter diffraction (EBSD) orientation mapping in the SEM has developed into an important tool that automatically scans large areas of a microstructure in finite times (Schwartz et al., 2009). Availability of order-domain resolution in such a technique, very likely could improve the understanding of phase transformation as well as the mechanically relevant microstructure property relationships.
- The single-phase constitutive behavior of γ-TiAl is of considerable complexity. Different types of dislocation based deformation mechanisms can operate simultaneously. The relative activities of the competing mechanisms depend strongly on the chemical composition and on the loading conditions. Also in this field, the TEM analysis of deformed microstructures has been the principal method to improve the micromechanical understanding. A method that could decrease the effort for a quantitative characterization of the single crystal plasticity with improved statistics is sought. Such a method could greatly enhance the alloy development through making possible the efficient conduction of comparative studies.
- Pronounced plastic anisotropy is not only found for γ-TiAl single crystals, but also for the fine-scaled microstructures that form in titanium aluminide alloys during different solid state phase transformation routes. Only a constitutive formulation that incorporates the mechanical effect of the spatial arrangement of the two constitutive phases γ and α_2 in a homogenized fashion has a potential to bridge the length-scales of the microstructure and the macroscopic mechanical performance of the material.

1.3 Research objectives

Based on the identified key issues in the process of γ-TiAl based alloy development, three main research objectives were addressed in this thesis:

- First, an EBSD based method should be developed for the identification of γ-TiAl order domains. The progress in the available instrumentation and software for data acquisition and data interpretation brought this delicate task into reach.
- Second, based on preexisting knowledge on single crystal indentation and crystal plasticity constitutive modeling, a method should be developed to characterize the single phase deformation behavior of stoichiometric γ-TiAl in a quantitative fashion.
- Third, a constitutive model should be developed that can take into account the current understanding of the kinematic constraints that are imposed by the crystallographic and phase interfaces in two-phase γ/α_2 microstructures.

For the micromechanical modeling work, emphasis was laid on quantitative validation of the developed modeling approaches against experimental data. Therefore, a restriction to the investigation of the room temperature micromechanics was imposed. In this

way, the corresponding experimental work could be carried out in parallel to the modeling. Furthermore, the room temperature mechanical behavior of titanium aluminides is of interest from the viewpoint of fundamental research as well as through the issue of limited ductility of γ-TiAl based alloys at ambient and intermediate temperatures.

1.4 Outline of this thesis

The presentation of this work is split into two main parts: Part I reviews the state of the art in the understanding of γ-TiAl based alloys. It introduces the Ti-Al binary alloy system, as well as relevant aspects such as compositional effects, phase transformation, crystallographic relations and the formation of different types of microstructures. The current micromechanical understanding is presented and previous crystal plasticity studies of γ-TiAl based alloys are reviewed. Part I closes with a short review of the indentation technique.

Part II contains the contributions of this thesis to the research objectives defined above. An improved microstructure characterization of γ-TiAl based alloys is introduced in chapter 6. The severe limitation of exclusively manual or TEM-based detection of the order variants of γ-TiAl could be overcome. First, an improved method for the automated indexing of backscatter Kikuchi patterns is developed and validated. Then a crystal orientation map of a lamellar microstructure is presented that—for the first time—resolves the order domain structure in the γ-TiAl phase throughout a region of the microstructure.

The crystal plasticity finite element method was chosen as the main tool for the constitutive modeling in this research. This decision is motivated in section 7.1. Correspondingly, the extension of an existing single-phase crystal plasticity model to account for the specific deformation modes of γ-TiAl was the first objective in the course of the modeling work and the results are presented in chapter 7.

Chapter 8 presents a new possibility to characterize the plastic deformation of γ-TiAl at the single-phase level. Based on the developed EBSD technique, the indentation response of stoichiometric γ-TiAl could be analyzed for the first time with respect to the indented crystallographic orientation. A theoretical framework is introduced to represent the deformation of the free surface around the indent in a systematic manner. A combined approach to analyze indentation process by experiments and CPFEM-simulations, with special emphasis on the formed pile-up patterns, is developed and applied to the case of γ-TiAl indentation.

A homogenized constitutive model that incorporates the kinematic constraints for two types of prospective, fine-scaled microstructures of current two-phase titanium aluminide alloys is presented in chapter 9. The model is validated against data on polysynthetically twinned crystals. It is then used simulate quantitatively the effect of different microstructural states on the mechanical performance of polycrystalline material.

Part III presents an overall summary with main conclusions and a short outlook followed by the appendices and the bibliography.

2

Microstructures of γ-TiAl based alloys

2.1 Introduction

Due to the complex phase diagram of the Ti-Al system, a large variety of microstructures can be obtained through different processing routes. Kim (1994) listed four types of two-phase microstructures based on γ-TiAl and α_2-Ti_3Al:

- Duplex, consisting of similar volume fractions of γ-grains and lamellar γ/α_2 grains;
- Fully lamellar (FL), containing only lamellar grains;
- Refined fully lamellar (RFL), same as above, but with a smaller grain size of the α_2-phase prior the lamellar transformation;
- Thermomechanically treated;

An additional type of microstructures, the so-called convoluted microstructure (Wu et al., 2004) that is formed through a massive transformation and annealing treatment, is discussed in section 2.9 of this chapter. An overview of some microstructures together with the appropriate processing, including thermo-mechanical treatment, is given in Kestler and Clemens (2003).

2.2 The Ti-Al phase diagram

After Braun et al. (1995), binary TiAl was first discovered in 1951/52 by two independent groups (Ogden et al., 1951, Bumps et al., 1952). The binary Ti-Al phase diagram is given in figure 2.1. The eutectoid composition of γ-phase and α_2-phase is found at around 38 at.% aluminum. For high-temperature applications, the best balance of mechanical properties is obtained for an aluminum content between 45 and 48 at.%.

For application purposes the high temperature mechanical properties of γ-TiAl based alloys can be improved by addition of heavier elements. Currently, the addition of 5 to 8 at.% niobium seems to be beneficial in this respect. Therefore, the ternary phase diagrams need to be taken into account.

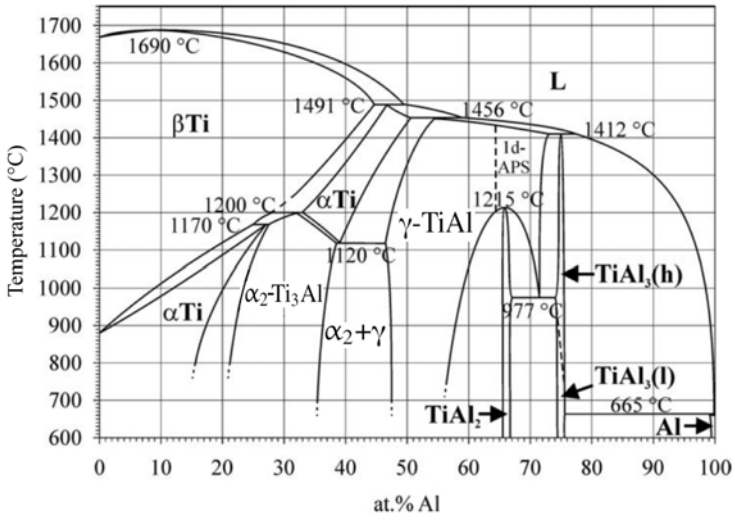

Fig. 2.1: Binary Ti-Al phase diagram (Schuster and Palm, 2006);

Takeyama et al. (1998) gave an isothermal section of Ti-Al-Nb at 1200°C. Appel and Oehring (2003) presented a comparison between the binary phase diagram and the TiAl-8Nb isopleth of the ternary phase diagram taken from Chen et al. (1999). Raghavan (2005) have also studied the system Al-Nb-Ti and gave isothermal sections between 1000°C and 14000°C. Hecht et al. (2009) gave an 8%Nb isopleth of the ternary phase diagram. Cupid et al. (2009) have reviewed the experimental work on constitution and phase stability in the Ti-Al-Nb system.

2.3 Crystallographic phases in γ-TiAl based alloys

The Ti-Al binary phase diagram is of considerable complexity. Phase transformations and ordering reactions therein are a research topic of its own, well beyond the scope of the present work. The two main phases that are involved in many current efforts towards high temperature structural alloys are γ-TiAl and α_2-Ti_3Al. Their crystallographic structures are given in table 2.1 and illustrated in figure 2.2. A detailed table of the observable phases in the Ti-Al system is given in Schuster and Palm (2006).

Gamma-TiAl has a $L1_0$ structure. This structure can be visualized as a tetragonally distorted face centered cubic lattice. Alternate (002) planes are occupied by the two different species. The structure of γ-TiAl is reviewed in detail in Braun et al. (1995). From the discussion therein it is only mentioned here that the strong and anisotropic bonding between Ti atoms on (0 0 1) planes is probably responsible for the $^c/_a$ ratio being larger than unity in TiAl. Furthermore, Braun et al. (1995) points out that TiAl is one of very few examples for AuCu-type structures for which the $^c/_a$ ratio is larger than unity.

The α_2-Ti_3Al-phase is hexagonal with a $D0_{19}$-ordered structure. It is formed through an ordering reaction during cooling of the the high temperature, disordered α-phase.

Tab. 2.1: Some characteristics of the most important phases in γ-TiAl based alloys (from Pearson's Handbook of Crystallographic Data for Intermetallic Phases, Villars and Calvert (1991)).

Phase	γ-TiAl	α_2-Ti_3Al	α-Ti_3Al
System	fct	hcp	hcp
Prototype	AuCu	Ni_3Sn	Mg
Strukturbericht	$L1_0$	$D0_{19}$	A3
Space group	P4/mmm	$P6_3/mmc$	$P6_3/mmc$
No.	123	194	194
Pearson symbol	tP2	hP8	hP2
Lattice parameters			
a	0.400 nm	0.577 nm	–
c	0.407 nm	0.465 nm	–

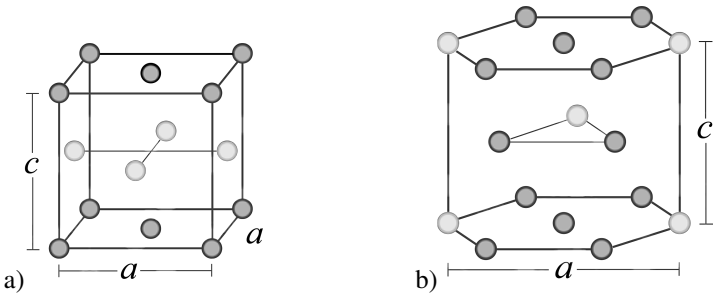

Fig. 2.2: Crystal structures of a) γ-TiAl; b) α_2-Ti_3Al; dark spheres depict Ti atom positions.

2.4 Metallurgy of titanium aluminides

Melting of titanium aluminide alloys is a technologically challenging operation. Similar to other titanium alloys the reactivity of the melt excludes routes that involve oxidic crucibles since oxygen uptake or partial dissolution of the crucible material is often observed. Vacuum arc remelting is widely used to melt titanium aluminide alloys. To ensure good homogeneity of the ingot prealloyed starting materials are used often and up to 3 remelting cycles are performed. More details on the production of high quality ingots are given in Kestler and Clemens (2003, sec. 14.4.1).

Products made from Gamma-TiAl based alloys are produced either by powder metallurgical processing or the parts are cast directly. Both routes are pursued in the current development. No material of powder metallurgical origin was investigated in this work. Casting of TiAl is difficult because of the high melting temperature and the low density and heat capacity of the material. Centrifugal casting seems to be a viable route for the production of high quality components. Details of the solidification of Ti45Al8Nb (at%) were discussed in Hecht et al. (2009). Segregation of heavy alloying elements is a common issue in the processing of TiAl alloys.

The effect of some important alloying elements is shortly described in the following. Interstitials like *boron* and *carbon* have been introduced to obtain grain refinement which is known to improve ductility in the case of lamellar microstructures. *Chromium* has been found to improve the room temperature ductility but it can reduce the long term high-temperature strength. *Niobium* improves the high temperature resistance of TiAl alloys. It distributes evenly into γ and α_2-phase (Yamamoto et al., 2002). In γ-TiAl, niobium has a strong site preference for Ti-sites, see Scheu et al. (2007) and references therein. The diffusivity of niobium is low when compared to other alloying elements in α_2- and γ-phase (Yamaguchi et al., 2007, Mishin and Herzig, 2000, Herzig et al., 2001) but higher than that of tantalum. The slow diffusion leads to a refinement of the microstructure. Since there is a compositional difference between α_2 and γ-phase, no phase transformation can occur without – at least partial – equilibration of the phase chemistry by diffusion. With an atomic weight of 93 g/mol, niobium increases the density of TiAl alloys considerably in comparison to the binary composition. Huang et al. (2007a) measured a density of 4.3 g/cm^3 for the composition Ti-46Al-8Nb, while Appel and Wagner (1998) gave a density of about 3.8 g/cm^3 for the binary alloy. Appel et al. (2004) found significant strengthening for niobium contents higher than 5 at-% and related it to structural refinement as the most significant source of strengthening in this material. Liu et al. (2002) found niobium additions of up to 10 % to increase the stress constant in a Hall-Petch analysis of lamellar spacing, and to decrease the microstructural degradation at 1050°C/30h.

Oxygen embrittles the γ-phase but it partitions mainly into α_2-phase in two-phase alloys. Based on atom probe measurements, Menand et al. (1996) reported the concentrations of oxygen in α_2-phase being 40 to 90 times higher than in the γ-phase in two-phase alloys. The oxygen scavenging effect of α_2-phase, however, was not confirmed by the data of Menand et al. (1996), who measured constant oxygen concentrations of about 250 at.-ppm. in the γ-phase for α_2-phase volume fractions of up to 30 %. Kad and Fraser (1994) have investigated two Ti-52Al alloys with different oxygen levels and found the activation of ordinary dislocations, $\boldsymbol{b} = 1/2[1\,1\,0]$, to be promoted by low oxygen contents. Lefebvre et al. (2002) found oxygen in two-phase material to sup-

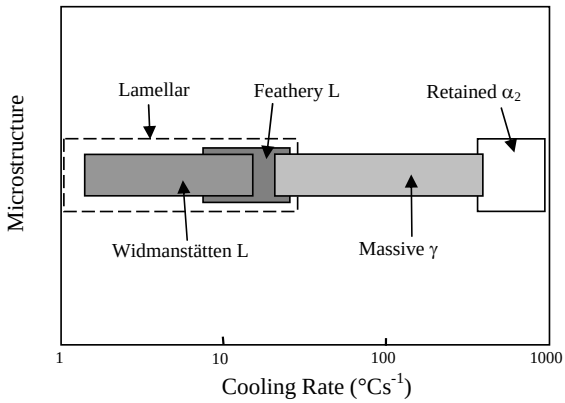

Fig. 2.3: Correlation between microstructures of Ti-46Al-8Nb and cooling rate during continuous cooling (Hu et al., 2005, Fig. 5).

port the ordering reaction from α to α_2-phase. Lamirand (2007) reported oxygen to stabilize the formation of lamellar microstructure instead of duplex type.

Site occupancies of ternary alloying elements in TiAl and Ti_3Al were investigated by Hao et al. (1999) using the atom location channelling enhanced microanalysis (ALCHEMI) method. The site preference of ternary alloying elements and influence on the γ-TiAl $^c/_a$ ratio were investigated through first principle calculations by Erschbaumer et al. (1993), Jiang (2008) and Liu et al. (2009b).

2.5 Phase transformation in titanium aluminides

The phase transformation behavior from the high temperature disordered, hexagonal α-phase field depends strongly on the cooling rate. The formation of γ-TiAl follows two possible paths as proposed by Denquin and Naka (1996):

$$\alpha \rightarrow \alpha_2' \rightarrow \alpha_2 + \gamma$$

$$\alpha \rightarrow \alpha_2 + \gamma$$

During cooling, the α-phase undergoes an ordering reaction to α_2-phase. Jones and Kaufman (1993) presented schematic continuous cooling transformation (CCT) diagrams for binary Ti-Al with 42, 45 and 48 at-% Al. Veeraraghavan et al. (1999) have generated a CCT diagram for Ti-47.5Al, including lamellar, feathery and massive transformation start temperatures. Hu and Botten (2002) have reported a CCT and TTT diagrams for Ti-46Al-Nb-2Cr-1B, Ti-46Al-4Nb-4Hf-0.1Si-1B and Ti-44Al-4Nb-4Zr-0.2Si-0.3B. Further, the Jominy end quench test was successfully applied to the investigation of phase transformation kinetics in TiAl alloys (Hu et al., 2005, Saage et al., 2009). Figure 2.3 summarizes the possible microstructures resulting from different cooling rates after heating to the α-phase field.

A numerical model for the competitive phase transformation to massive γ-phase, γ_m, or lamellar γ/α_2 microstructures was presented by Rostamian and Jacot (2008). They

characterized the phase transformation behavior of Ti-48Al and Ti-47.5Al by the continuous cooling transformation diagrams, and accounted for both mechanisms.

Chladil et al. (2006) studied the phase transformation temperatures in Ti-45Al-5-Nb-(0,0.5)C and Ti-45Al-7.5Nb-(0,0.25,0.5)C. For Ti-45Al-7.5Nb they reported a eutectoid temperature of 1159°C, about 40°C higher than in the binary phase diagram by Schuster and Palm (2006).

Very recently, Dey et al. (2009) have investigated the effect of increasing cooling rate after annealing in the α-phase field for a Ti-46.8Al-1.7Cr-1.8Nb alloy. The resulting microstructures are lamellar, Widmannstätten laths, feathery and massive γ-phase as reported earlier by Hu et al. (2005). figure 2.3.

2.6 Blackburn orientation relationship between γ- and α_2-phase

The orientation relationship at the interface between α_2- and γ-phase in TiAl was reported by Blackburn (1970):

$$(1\,1\,1)_\gamma \parallel (0\,0\,0\,1)_{\alpha_2} \text{ and } \langle 1\bar{1}0]_\gamma \parallel \langle 11\bar{2}0\rangle_{\alpha_2} \tag{2.1}$$

In lamellar two-phase γ/α_2 alloys, the Blackburn orientation relation is precisely followed by the $\langle 1\bar{1}0]$ direction, while the $\langle\bar{1}01]$ directions show deviations of 0.2° to 0.3° to the respective α_2-directions (Inui et al., 1992b).

Due to the tetragonal structure of γ-TiAl, the atomic arrangement is not perfectly coherent. Ledges and misfit dislocations accommodate the lattice mismatch and reduce the elastic stresses in the lamellar plates. Mahon and Howe (1990), Singh and Howe (1992), and Lay et al. (2000) presented HRTEM studies of the interface structure. Maruyama et al. (2004) have studied the transition from extremely fine and perfectly coherent growth of γ-lamellae in α_2-phase, to semicoherent interfaces with misfit dislocations at a lamellar width of about 50 nm. This transition occurs to relax the lattice mismatch between α_2 and γ-phase, that initially is accommodated by purely elastic distortion.

At the interface between α_2- and γ-phase, due to the lattice mismatch, the α_2-phase is under biaxial-compression whereas the γ-phase is under tensile loading (Hazzledine, 1998). The γ-phase domain structure results in additional elastic stresses due to tetragonality misfit along the {1 1 1}-interface planes.

2.7 The domain structure of γ-TiAl

Gamma-TiAl usually forms during cooling in a phase transformation from the α-phase (disordered) or α_2-phase ($D0_{19}$-ordered). Both of these phases show a hexagonal base lattice. A detailed description of the formation of the lamellar structure is given in Denquin and Naka (1996). The phase transformation occurs according to the Blackburn orientation relation (2.1) which leads to six different orientation variants in the γ-phase as indicated in figure 2.4. Anti-phase boundaries (APB) – while observed in other $L1_0$-structures – are not observed in γ-TiAl because of the high ordering energy (Zhang et al., 1996). But misfit from minor misorientations can occur naturally when two identical γ-variants are growing together.

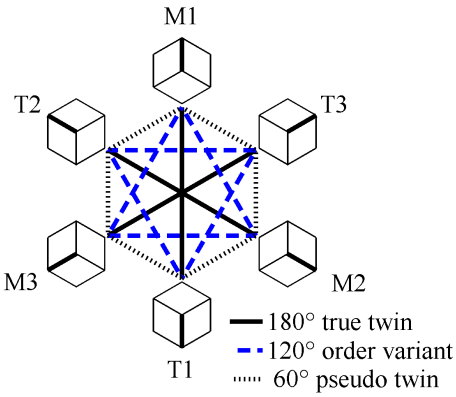

Fig. 2.4: Orientation relationships between the six orientational variants in γ-TiAl. The *c*-axis is emphasized. Opposing variants are in true-twin relationship, e. g. T1 and M1. The assignment of the twin (T) and matrix (M) labels is arbitrary. In presence of α_2-phase the $(0\,0\,0\,1)_{\alpha_2}$ basal plane will be parallel to the plane of illustration.

The six orientational variants of the γ-phase fall into two groups of three. Within these groups the variants have mutually perpendicular *c*-axes. These variant triplets are called order variants. The order variants can alternatively be visualized as generated by a 120° rotation around the (111) plane normal. For the notation of γ/γ disorientations, it is sometimes useful to assume a cubic structure. This practice will be followed throughout the remainder of this work.

The orientational variants result in a domain structure of the γ-phase. In addition to high angle grain boundaries with no specific orientation relation, domains of crystallographic orientations are formed which exhibit specific disorientations. The domain structure in lamellar $TiAl/Ti_3Al$ has been described for example by Inui et al. (1992b) based on a detailed TEM analysis. Generally, the domains are observed to form in the shape of extended plates along a common (111) plane. The domain structure was observed in lamellar two-phase material (Inui et al., 1992c) as well as in γ-single phase material (Bird et al., 2000). Misfit between the domains, resulting from the slight tetragonality, is accommodated by elastic distortion or by misfit dislocations (Appel and Christoph, 1999, Paidar et al., 1999).

The γ-phase forms a domain structure of twin-related lamellae. However, due to the ordered structure the fcc 60°-around-[111] twin type splits into three types: One true or coherent 180°-around-[111] twin-relation, where the intermetallic order is not disturbed, and two ±60°-around-[1 1 1] pseudo-twin relations, for which an order-fault is formed additionally to the change of stacking order. For the first case of a perfect twin relation, the projections of the *c*-axes onto the (1 1 1) interface are parallel to each other, see figure 2.4. The term 'pseudo-twin' boundary derives from the notion that this type of boundary would be a simple 60°-around-⟨1 1 1⟩ twin if the intermetallic order as well as the tetragonal distortion of the lattice would be ignored, i. e. in the fcc case.

The γ/γ-interfaces can be classified into three categories: variant interface, pseudo-

and perfect-twin boundaries (Yamamoto et al., 2002). Details of the domain structure are given in table 2.2. A method to resolve the order domain structure via electron backscatter diffraction in an SEM is presented in chapter 6 of this work.

Tab. 2.2: Nomenclature of γ-TiAl domain boundaries; arrows denote parallel (↗↗) and antiparallel (↗↙) crystallographic directions;

Name	Inui et al. (1992c)	generated by
Order variants	$[1\,\bar{1}\,0]$ ↗↗ $[\bar{1}\,0\,1]$	pseudo-cubic tetragonal symmetry
True-twin	$[1\,\bar{1}\,0]$ ↗↙ $[1\,\bar{1}\,0]$	twinning shear ($\approx 1/\sqrt{2}$)
Pseudo-twin	$[1\,\bar{1}\,0]$ ↗↙ $[\bar{1}\,0\,1]$	combination of both

Under the assumption of perfectly random formation of variants and boundaries, the theoretical boundary area fractions for the different kinds of boundaries can directly be determined from figure 2.4. Under this assumption, the boundary fractions for true twin, order variant and pseudo twin boundaries are expected to exist in the relative fractions: L(180°) : L(120°) : L(60°) = 3 : 6 : 6 = 20 % : 40 % : 40 %. In reality, these fractions are additionally influenced by the nucleation and growth mechanisms during solid state phase transformation. These depend additionally on elastic misfit stresses and boundary energies. Generally, the formation of perfect twin boundaries is favoured due to their lower interface energy, see Dey et al. (2006a) for experimental results on boundary frequencies.

The formation of order domains in γ-TiAl with different Al-contents has been investigated in Bird et al. (2000). At Al-contents over about 56 at.%, ordered superstructures are formed. Nakano et al. (2005) studied their formation and effect on the mechanical properties.

Atomistic and molecular dynamics studies have been performed on the interface structure of different types of γ/γ-interfaces by Vitek et al. (1997), Znam et al. (2003) and others. One result of these simulations are the relative interface energies of the boundaries, table 2.3. They are important to understand the formation and degradation of these interfaces. The misfit from the $^{c}/_{a}$ ratio has often been neglected in the simulations, since its inclusion would require the simulation of large cells that can form misfit dislocations to relax the coherency stresses. Nevertheless, the simulation results compare well against experimental studies on the surface energies that are also given in table 2.3.

2.8 Formation of lamellar microstructures during slow cooling

The phase transformation from α_2 or α-phase to γ-phase involves a change in lattice structure from hexagonal to face centered tetragonal. This is thought to occur by propagation of Shockley partial dislocations. Further, a change in composition has to take place in which the titanium content of the resulting γ-phase is reduced. The change in composition can only be accomplished by diffusional processes.

A typical lamellar microstructure, created by slow cooling, consists of all six γ-variants. The Blackburn orientation relationship is strictly obeyed between α_2-lamellae

Tab. 2.3: Relative magnitudes of interface energies in a γ-TiAl domain structure, TT: true twin, PT: pseudo twin, OD: order domain;

Reference	TT : PT : OD	method
Inui et al. (1992b)	1 : 7 : 6	estimated
Znam et al. (2003)	1 : 4.2 : 4.1	bond order potential
Znam et al. (2003)	1 : 4.2 : 4.5	ab initio (FLAPW)
Lu et al. (1996)	1 : 6.7 : 5.8	surface groves
Pan and Luzzi (2006)	1 : 4.8 : 4.6	surface groves

and the γ-lamellae and therefore in any of the variants one of the {1 1 1} planes is parallel to the basal plane of the hexagonal α_2-phase.

The propagation of Shockley partials and the diffusional composition change involve different time scales and temperature dependencies. Together with the nucleation and growth kinetics, this leads to many possible routes to form a lamellar microstructure. The choice of the routes will depend on the local chemical and micromechanical situation. The resulting chemistry and microstructure of the lamellar phases cannot be predicted in all details from the processing conditions at the moment.

Hazzledine and Kad (1995) attributed the formation of a lamellar microstructure mainly to the elastic stresses that result from the slight misfit between the (111) planes of adjacent γ-domains that are not in true-twin relation.

Denquin and Naka (1996) have studied the lamellar formation in binary TiAl of 46% and 48% aluminum content. According to their results, the formation of a lamellar structure is not mainly governed by the minimization of elastic energy as stated frequently in the literature. Rather the lateral growth of γ-phase from alpha is related to the diffusional processes that have to equilibrate the chemical composition during the reaction from Ti_3Al to TiAl. They can be performed through the 'terrace-ledge-kink'mechanism, leading to faster growth rates perpendicular to the interface plane.

Perdrix et al. (1999) investigated the effect of cooling rates from 1.6 to 280 °C/min on the lamellar spacing, α_2-volume fraction and microhardness of a Ti-48Al alloy.

Maruyama et al. (2002) presented a time temperature precipitation diagram for the growth of lamellar microstructure from a pure α_2-material of near-eutectoid composition Ti-39.4 at.% Al. Zghal et al. (2005) have investigated the competition between high temperature and low temperature growth of lamellae in Ti-47Al-2Cr-2Nb. Depending on the driving force either interfacial growth at high temperature (1250°C) or homogeneous nucleation at lower temperatures was observed. A quantitative study of the kinetics of lamellar phase transformation in Ti-48Al-2Cr-2Nb was presented by Charpentier et al. (2008) together with a CCT diagram. Several authors found a good match of a log-normal distribution for the description of lamellar spacings (Parthasarathy et al., 1998, Charpentier et al., 2008).

Figure 2.5 and figure 2.6 both illustrate the structure of a γ-TiAl based alloy with fully lamellar microstucture. The Backscatter electron picture shows different domain orientations of the γ-phase in different shades of gray, thin α_2-lamellae are also visible. On this length scale all crystallites are connected by the Blackburn Orientation relationship

and could be traced back to the previously existing α- or α_2-grain of similar size. On a larger length scale, figure 2.6, different lamellar colonies are observed and they do not show a specific crystallographic orientation relation with each other. Instead they are separated by high angle grain boundaries, similar to single phase metals.

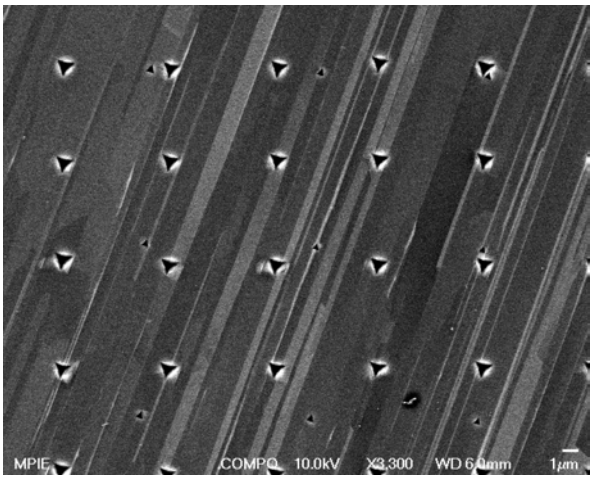

Fig. 2.5: Backscattered electron image of a lamellar structure in Ti-46Al-8Nb (at.%); the white thin structures are α_2-lamellae; shades of gray indicate different orientation of γ-phase; Berkovich nanoindents from 800 μN and 3000 μN maximum loads are also visible;

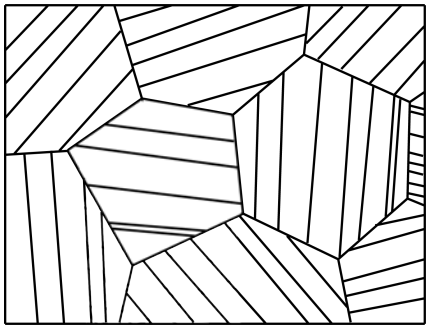

Fig. 2.6: Fully lamellar microstructure; the size of lamellar colonies is usually on the order of 20 to 200 μm; lamellar widths can range from several 10 nm to micrometers.

The formation of lamellar microstructures has been modeled by the phase-field method (Wen et al., 2001, Katzarov et al., 2006). Figure 2.7 shows the result a three-dimensional phase-field simulation for the lamellar transformation that was obtained by the inclusion of the energy contribution from the so-called stress free transformation strains into a phase-field model.

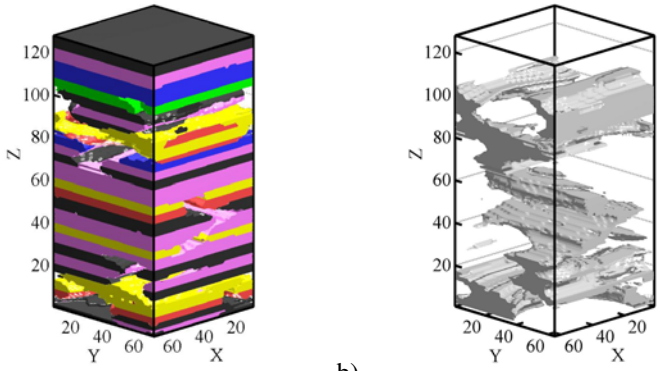

Fig. 2.7: Three-dimensional phase distribution from a phase field simulation (Wen et al., 2001, 3D data from figure 3), dataset courtesy Y. H. Wen; a) γ-phase, order variants are discriminated by color b) α_2-phase.

The mode of phase transformation has been discussed for example by Nie et al. (2000) in their comment to Sun (1998a,b) and in the author's reply (Sun, 2000). The matter of discussion was, whether the necessary diffusion allows for a displacive mechanism of phase transformation and which mechanism completes first or is the rate limiting one. At least one of the authors of Nie et al. (2000) has later agreed with Sun (2000) that "[...] strain preceding complete interdiffusion is possible" (Howe et al., 2009). Howe et al. (2009) introduced the term of a *transformation disconnection* which has a combined dislocation and step character on the interface between two phases. These have also been called ledge dislocations (Maruyama et al., 2004).

2.8.1 Polycrystalline fully lamellar (FL) microstructures

Refined fully lamellar microstructures are obtained via tailored heat treatment or thermomechanical treatment. Liu et al. (1996) have reported a high ductility for Ti-46Al-2Cr-2Nb-0.15B with a refined fully lamellar microstructure obtained via hot extrusion and annealing. The colony size was 22 µm and the reported room temperature ductility was 4.7 %.

Different parameters are used to describe the lamellar microstructure. The size of lamellar grains is usually termed the colony size, D. The average lamellar spacing, $\overline{\lambda}$, influences the mechanical properties strongly. It can be separated into the α_2-spacing, $\overline{\lambda}_{\alpha_2}$, and the average width of γ-domains, $\overline{\lambda}_{\gamma}$. Parallel to the lamellae also the domain length, L_D, can be measured which is in most cases shorter than the colony size. The α_2-spacing is usually determined from backscattered electron images in the SEM since the α_2-phase appears much brighter than the γ-phase. Determination of the detailed parameters of the γ-phase, namely L_D and $\overline{\lambda}_{\gamma}$ has been carried out seldom in the past, since only the TEM technique was able to discriminate the γ-order variants. A technique to perform this discrimination in an EBSD system inside a SEM is presented in chapter 6.

Novoselova et al. (2003) have investigated the influence of different holding times in the α-field and different cooling rates on the formation of FL microstructures in

Ti-46Al-3Nb-1.9Cr. Chraponski (2006) performed image analysis on micrographs of lamellar microstructures and related the lamellar widths to the mechanical performance in terms of hardness (HV10) and peak flow stress under compression at 1000°C.

2.8.2 Polysynthetically-twinned (PST) crystals

A special kind of lamellar microstructure is the *polysynthetically-twinned* (PST) type. The term originates from the field of mineralogy, where polysynthetic twinning, the alignment of densely spaced lamellae in twin relation, is a common phenomenon (Inui et al., 1992b). PST material consists of lamellae of multiple twinned γ-crystals that are all in Blackburn orientation relationship with thin lamellae of α_2-phase. Only one lamellar plane is present. Therefore, PST-samples represent the behavior of a single lamellar colony from polycrystalline material.

PST material can be obtained from floating zone furnace solidification. Withdrawal rates of 2.5 to 20 mm/h have been reported. Takeyama et al. (2002) investigated the possibility of lamellar orientation control through seed crystals in Ti-48Al. Yamamoto et al. (2002) grew PST-crystals from Ti-48Al-8Nb at 20 mm/h.

2.9 Massive transformation during rapid cooling

Porter and Easterling (1992) defined the massive transformation as *diffusionless civilian transformation* that only involves thermally activated jumps across the interface, without change in composition. Massive transformation of γ-TiAl has been observed by e. g. Jones and Kaufman (1993) and others (Wang and Vasudevan, 1992, Denquin and Naka, 1993). Very recently it has also been modeled by the phase-field approach (Singer et al., 2009).

Hono et al. (1996) studied ultrafine γ-lamellae that form in Ti-48Al, quenched into ice-water from the single-phase α-field and showed that even for these high cooling rates diffusion can take place and further that massive transformation probably is nucleation limited at high cooling rates.

Nie and Muddle (2002) have investigated the orientation relation between massively transformed γ-phase and the α_2-phase. While no strict Blackburn relationship was found in their case, they described a one-dimensional coherency along the Moiré plane between α_2- and γ-phase.

Massive transformation was investigated as a processing route that could provide grain refinement without addition of particle forming elements. The usual addition of boron to refine the grain size, might lead to boride particles larger than the critical particle size, thereby decreasing the low and intermediate temperature ductility. Massive transformation provides an alternative approach to microstructural refinement and might allow to avoid boron or carbon additions.

The γ_m-phase is not stable at high temperatures. It will transform to the usual γ-phase and at the same time α_2-phase is precipitated (Wen and Chen, 1995). Massive transformation in combination with a succeeding annealing treatment to form α_2-phase, has been investigated as a method to refine the grain size in cast material and to obtain a balanced profile of mechanical properties (Hu and Botten, 2002, Pouchou et al., 2004, Hu et al., 2006b, Clemens et al., 2006, Hu et al., 2007, Huang et al., 2007a, Imayev et al., 2008, Huang et al., 2009, Saage et al., 2009).

Denquin and Naka (1995) have proposed two possible mechanisms for γ_m formation: The first one is the direct transformation from a hexagonal structure to a $L1_0$-ordered structure, the second introduced a intermediate fcc phase before ordering can occur. The latter mechanism seems more probable today, since later research found the $^c/_a$ ratio of the massive phase to be close to unity. After massive transformation from the high temperature α-phase to γ-phase the microstructure is far from the thermodynamic equilibrium. That can be seen for example from the $^c/_a$ ratio which is found to be approximately unity in comparison to the equilibrium ratio between 1.015 and 1.02. After annealing, the equilibrium $^c/_a$ ratio is retained (Bartels et al., 2005). Further, α_2-phase is precipitated during an annealing treatment at sufficiently high temperatures. Annealing of massive γ-phase will recover the $L1_0$-ordered tetragonal structure. Scheu et al. (2007) reported about the lattice parameter of γ-TiAl formed by massive transformation to have a $^c/_a$ ratio close to unity in a high Nb-containing alloy (9 at-pct). The loss of tetragonality was found to be caused by occupation of Al-sites by Nb-atoms as opposed to almost exclusive occupation of Ti-sites in the equilibrium phase.

Annealing of γ_m-phase in Ti-46Al-9Nb for 1 h at temperatures above 700°C was reported to lead to a decrease in hardness and partial recovery of the lattice parameters into the direction of the equilibrium $^c/_a$ ratio. After 1 h at 1200°C almost full recovery of the $^c/_a$ ratio could be achieved (Bartels et al., 2005).

In binary and low-alloyed TiAl the massive transformation occurs at cooling rates on the order of 100°C/s which necessitate water or salt-bath quenching. For high-Nb and especially high-Ta alloying, also air cooling can lead to massive transformation in parts of about 20 mm diameter (Hu et al., 2007).

Huang et al. (2007b) studied the influence of the difference in atomic volume between γ- and α_2-phase. The α_2-phase has a higher atomic volume leading to smaller α_2 volume fractions, when a pressure of e. g. 150 MPa is applied during hot isostatic pressing in the two-phase field. Lefebvre et al. (2002) investigated the influence of oxygen on massive transformation in Ti-48Al.

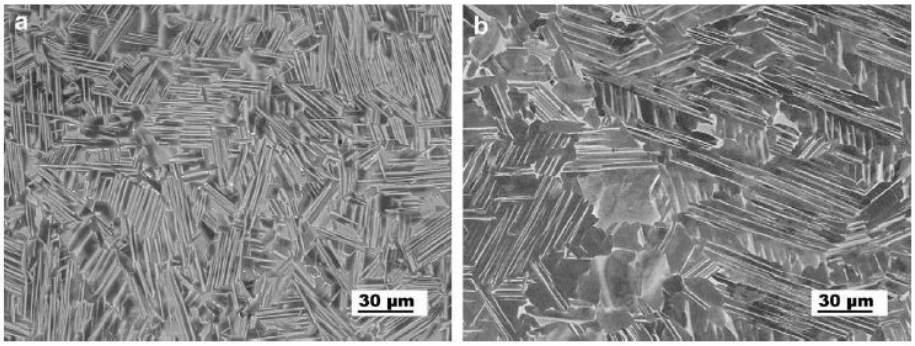

Fig. 2.8: Back-scattered electron image of a) Ti-46Al-8Ta and b) Ti-46Al8Nb after heat treatment at 1360°C/1h and succeeding air cooling (a) or salt bath quenching at 850°C (b); additional hot isostatic pressing (HIP) and annealing was carried out to precipitate α_2-phase (bright) and form the so called convoluted microstructure; micrographs taken from Saage et al. (2009, figure 5).

Massive transformation from α- to γ_m-phase occurs during appropriate heat treatment for alloys with aluminum contents larger than 45 at% (Wu et al., 2004). The result of massive transformation, followed by an annealing treatment, is the so called *convoluted microstructure* (Wu et al., 2004), figure 2.8. Because of the quenching step, there exists a limit for the maximum diameter of parts that can consist completely of this convoluted microstructure.

3

Micromechanics of titanium aluminides

3.1 Introduction

Similar to other intermetallic alloys, the micromechanical behavior of TiAl alloys is of considerable complexity (Yamaguchi and Umakoshi, 1990, Umakoshi, 1993). From the available literature it is clear that optimal alloy compositions and microstructures for many fields of application still have to be developed. Difficulties arise from the sensitivity of the mechanical response against influences such as oxygen content, composition and microstructural variations. In many cases it is not possible to study the effect of these influences separately, because any change in alloying or processing route will have multiple intertwined side effects.

3.2 Linear elasticity

Linear elastic behavior is described by the generalized Hooke´s law

$$\boldsymbol{\sigma}_{ij} = \mathbb{C}_{ijkl}\boldsymbol{\varepsilon}_{kl} \tag{3.1}$$

where $\boldsymbol{\sigma}_{ij}$ is the Cauchy or true stress tensor, $\boldsymbol{\varepsilon}_{kl}$ is the classical small-strain tensor and $\mathbb{C}_{ijkl}$ is the fourth-rank linear elastic operator.

The stiffness tensor is rotated by an orientation matrix, $\boldsymbol{g}$, in the following way:

$$\mathbb{C}^{rot}_{ijkl} = \boldsymbol{g}_{im}\boldsymbol{g}_{jn}\boldsymbol{g}_{ko}\boldsymbol{g}_{lp}\mathbb{C}_{mnop}. \tag{3.2}$$

This rotation can be implemented in a computationally efficient way by the method given by Doghri (2000, App. C.2).

For all crystal symmetries, because of symmetry and energetic considerations, the number of independent components of the fourth-rank stiffness operator can be reduced from $3^4 = 81$ to 21. Because of symmetry of stress and strain the following relations apply

$$c_{ijkl} = c_{ijlk} = c_{jikl} = c_{jilk}$$

which reduce the number of independent components to 36. They are usually represented as a 6×6 matrix.

$$\mathbb{C}_{ijkl} = \begin{pmatrix} c_{1111} & c_{1122} & c_{1133} & c_{1123} & c_{1113} & c_{1112} \\ c_{2211} & c_{2222} & c_{2233} & c_{2223} & c_{2213} & c_{2212} \\ c_{3311} & c_{3322} & c_{3333} & c_{3323} & c_{3313} & c_{3312} \\ c_{2311} & c_{2322} & c_{2333} & c_{2323} & c_{2313} & c_{2312} \\ c_{1311} & c_{1322} & c_{1333} & c_{1323} & c_{1313} & c_{1312} \\ c_{1211} & c_{1222} & c_{1233} & c_{1223} & c_{1213} & c_{1212} \end{pmatrix}$$

The four indices can be contracted as follows:

$$11 \sim 1, \quad 22 \sim 2, \quad 33 \sim 3, \quad 23 \sim 4, \quad 13 \sim 5, \quad 12 \sim 6,$$

resulting in the 6×6 Voigt matrix representation of the stiffness operator. The existence of a strain energy potential further reduces the independent components to a number of 21 that are arranged in a symmetric matrix (Newnham, 2005):

$$\boldsymbol{C}_{ij} = \begin{pmatrix} c_{11} & c_{12} & c_{13} & c_{14} & c_{15} & c_{16} \\ & c_{22} & c_{23} & c_{24} & c_{25} & c_{26} \\ & & c_{33} & c_{34} & c_{35} & c_{36} \\ & & & c_{44} & c_{45} & c_{46} \\ & \textit{sym.} & & & c_{55} & c_{56} \\ & & & & & c_{66} \end{pmatrix}$$

The approximate values for polycrystalline material can be derived from the single-crystal constants by simple relations (Nakamura, 2000, original reference: Anderson (1963)).

3.2.1 Elastic behavior of γ-TiAl

In γ-TiAl the tetragonal symmetry imposes additional simplifications (Nye, 1957) and the stiffness operator takes the form of

$$\boldsymbol{C}_{ij} = \begin{pmatrix} c_{11} & c_{12} & c_{13} & 0 & 0 & 0 \\ c_{21} & c_{22} & c_{23} & 0 & 0 & 0 \\ c_{31} & c_{32} & c_{33} & 0 & 0 & 0 \\ 0 & 0 & 0 & c_{44} & 0 & 0 \\ 0 & 0 & 0 & 0 & c_{55} & 0 \\ 0 & 0 & 0 & 0 & 0 & c_{66} \end{pmatrix}$$

with the additional conditions: $c_{11} = c_{22}$, $c_{13} = c_{23}$ and $c_{44} = c_{55}$. This leaves six independent components. Their numerical values from different sources are given in table 3.1.

The elastic anisotropy can be visualized in the unit orientation triangle , figure 3.1, or by the surface of uniaxial stiffness, as illustrated in figure 3.2. The elastic anisotropy, or Zener anisotropy ratio (e.g. Hirth and Lothe (1992)), is defined as

$$A = \frac{2c_{44}}{c_{11} - c_{12}}$$

and amounts to A=1.92 for TiAl, based on the values from He et al. (1997).

Tab. 3.1: Elastic constants of γ-TiAl, all values in GPa;

Method	c_{11}	c_{33}	c_{12}	c_{23}	c_{44}	c_{66}	T	Reference
First principles	190	185	105	90	120	50	0 K	Fu and Yoo (1990)
Parallelepiped resonance	183	178	74	74	105	78	298 K	Tanaka et al. (1996a)
Parallelepiped resonance	183	177	75	75	104	77	300 K	He et al. (1997)
Ab initio (VASP)	179	177	97	97	125	72	0 K	Woodward and Rao (2004)

The approximated effective values for polycrystals, based on the RT constants from He et al. (1997), are $\bar{K}_{Hill} = 110\,\text{GPa}$, $\bar{G}_{Hill} = 78\,\text{GPa}$, $\bar{E}_{Hill} = 190\,\text{GPa}$ and $\bar{\nu}_{Hill} = 0.21$. Only the Hill approximations are given here, defined as the average between the iso-strain Voigt model and the iso-stress Reuss model. The calculated values compare reasonably well to the experimentally measured ones, e. g. Yoo et al. (1995).

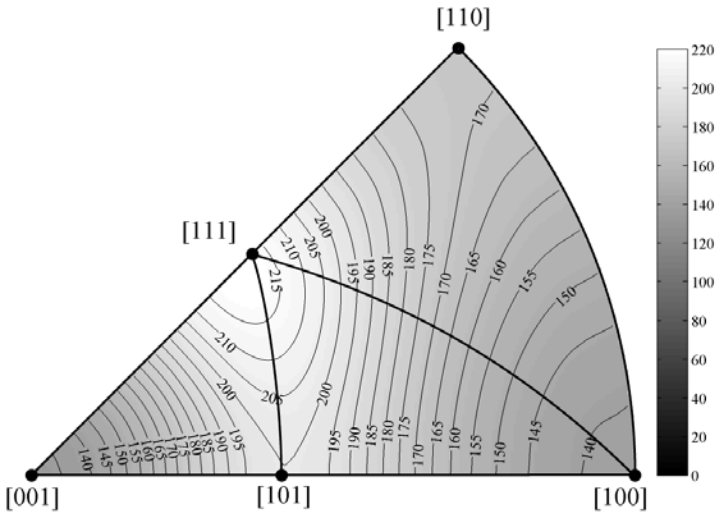

Fig. 3.1: Orientation dependence of the uniaxial elastic modulus for γ-TiAl in GPa. Stereographic projection is used. The projection shows the values for the room temperature (298 K) elastic constants given in He et al. (1997) for Ti-56Al (at.%).

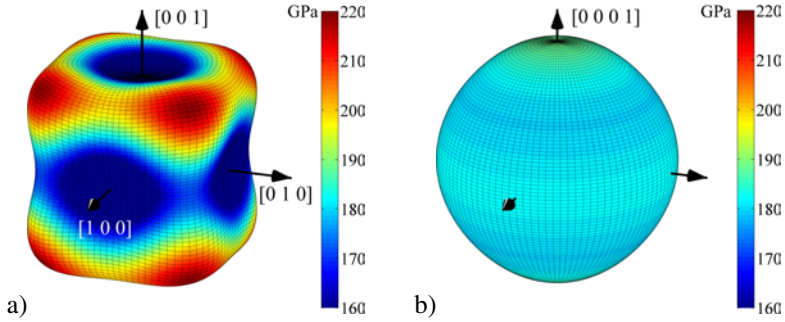

Fig. 3.2: Uniaxial elastic modulus surfaces for the stiffness constants of a) γ-TiAl, as given in He et al. (1997) and b) α_2-Ti_3Al as given in Yoo et al. (1995);

3.2.2 Elastic behavior of α_2-Ti_3Al

The additional simplifications from crystallographic symmetry are almost identical to the ones of γ-TiAl with the additional constraint of (Nye, 1957) $c_{66} = 1/2\,(c_{11} - c_{12})$ which leaves five independent constants. Hexagonal crystals are elastically isotropic in the basal plane (Hirth and Lothe, 1992, 13-5), i. e. they are transversely isotropic. The transversely isotropic behavior becomes evident in figure 3.2-b through the axisymmetry of the modulus-surface with [0 0 0 1] as symmetry axis. Values for the elastic constants of α_2-Ti_3Al are given in table 3.2

Tab. 3.2: Elastic constants of α_2-Ti_3Al, all values in GPa;

Method	c_{11}	c_{33}	c_{12}	c_{13}	c_{44}	T	Reference
First principles	221	238	71	85	69	0 K	Yoo et al. (1995)
Parallelepiped	183	225	89.1	62.6	64.1	0 K[a]	Tanaka et al. (1996b)
resonance	175	220	88.7	62.3	62.2	290 K	

[a] extrapolated

3.3 Inelastic deformation of γ-TiAl

3.3.1 Deformation of γ-TiAl by dislocation glide

Early works on the plastic deformation of γ-TiAl are Shechtman et al. (1974) and Lipsitt et al. (1975). Due to the crystallographic structure, two different types of dislocations are important in γ-TiAl: ordinary or perfect dislocations with a Burgers vector of $\boldsymbol{b}^{O} = 1/2\langle 110]$ and superdislocations with $\boldsymbol{b}^{S} = \langle 101]$. The mixed notation $\langle uvw]$, first introduced by Hug et al. (1988), emphasizes the reduced symmetry of the tetragonal structure in comparison to a face centered cubic lattice. The activation of these two major types of dislocations in γ-TiAl is a complex function of temperature and alloy chemistry.

Superdislocations with Burgers vector $1/2[1\,1\,2]$ were reported to exist in γ-TiAl after room temperature deformation (Inui et al., 1992a, Kishida et al., 1998). They are not

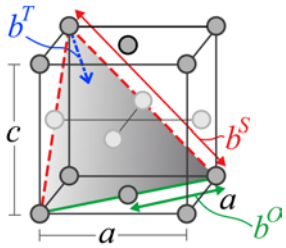

Fig. 3.3: The main deformation modes of γ-TiAl. One of the four {1 1 1} planes is shown together with the slip directions of ordinary (green solid line) and super dislocation glide (red dashed line) as well as one of four twinning Burgers vectors (blue dotted arrow).

Tab. 3.3: Slip systems in γ-TiAl; deformation type is super (s) dislocation glide or ordinary (o) dislocation glide and morphology in lamellar material is longitudinal (l), mixed (m) or transversal (t); for the morphological classification, c. f. section 3.6.1, the (1 1 1) plane was chosen arbitrarily to be parallel to the lamellar interfaces.

No.	slip plane	slip direction	type	morphology
1		[0 1 1]	s	t
2	(1 1 $\bar{1}$)	[1 0 1]	s	t
3		[1 $\bar{1}$ 0]	o	m
4		[0 $\bar{1}$ 1]	s	m
5	($\bar{1}$ 1 1)	[$\bar{1}$ 0 $\bar{1}$]	s	t
6		[$\bar{1}$ $\bar{1}$ 0]	o	t
7		[0 1 1]	s	t
8	(1 $\bar{1}$ 1)	[1 0 $\bar{1}$]	s	m
9		[1 1 0]	o	t
10		[0 1 $\bar{1}$]	s	l
11	(1 1 1)	[1 0 $\bar{1}$]	s	l
12		[1 $\bar{1}$ 0]	o	l

taken into account in the following because dislocations of this type are expected to form sessile configurations at room temperature and presumably will only contribute to plastic deformation at elevated temperatures (Appel and Wagner, 1998, Liu et al., 1999).

Figure 3.3 illustrates the slip directions on the closest packed {1 1 1} planes. Table 3.3 lists the twelve main dislocation glide systems in γ-TiAl.

In the experimental and modeling parts of this work, focus is laid on the characteristics of γ-TiAl dislocation glide during room temperature deformation in near-stoichiometric compositions as found in two-phase γ-TiAl/α_2-Ti_3Al microstructures.

In that kind of γ-phase, the deformation by ordinary dislocations can be activated easier than shear on superdislocation systems (Inui et al., 1992b). An increase in aluminum content changes this behavior and superdislocations are easier to activate in single phase γ-alloys of aluminum rich compositions (Inui et al., 1997).

The transition between the predominant activation of ordinary dislocation glide and superdislocation glide, seems to depend also on the level of interstitial impurities which are present in the γ-phase. Vasudevan et al. (1989b) added erbium to a Ti-50Al-0.4Er polycrystalline alloy and reported that ordinary dislocations contributed mainly to the deformation during room temperature compression. Häussler et al. (1999) found ordinary dislocations to dominate the deformation of a Ti-52Al (750 at.ppm O) polycrystalline, single γ-phase sample for ambient and high temperatures. Court et al. (1990), for a similar composition of Ti-52Al of nominal purity , reported superdislocations to operate during deformation at room temperature. After Aindow et al. (1990), the material of Court et al. contained relatively high levels of interstitial elements and this difference is put forward as the reason for the activation of different types of dislocations. Aindow et al. (1990) further substantiated their argument by investigating a Ti-52Al-0.4Er alloy. Again erbium was added to react with the oxygen and thereby leave high-purity γ-phase. In agreement with Häussler et al. (1999), Aindow et al. found mainly ordinary dislocations in the deformed material. Kad and Fraser (1994) performed similar experiments which confirmed the proposed oxygen dependence further, but the exact mechanism by which the dislocation character is changed, remained unresolved.

Single crystals of Ti-56Al deform mainly by glide of superdislocations at room temperature (Inui et al., 1997, Sun, 1999, Zupan and Hemker, 2003). Ordinary dislocation glide for Al-rich compositions is limited to a very narrow region around the [0 2 1]-axis, for uniaxial testing (Inui et al., 1997). In this orientation the maximum Schmid factor for ordinary dislocation glide is 0.49 but only 0.25 for superdislocation glide.

The plastic deformation of the near-stoichiometric compositions of γ-TiAl is difficult to investigate since the α_2-Ti_3Al phase and order domains are formed under these conditions. No bulk single crystals can be grown for stoichiometric or Al-lean γ-TiAl. After Pope (1996) and Bird et al. (2000), single phase γ-TiAl polycrystalline material can be obtained starting from about 52 at.% Al; single crystals without order domains can only be grown for aluminum contents starting from 54 %.

Mahapatra et al. (1995) characterized the single phase mechanics of near-stoichiometric γ-TiAl through a special approach: a thin layer of near-stoichiometric γ-TiAl was grown at the interface of a diffusion couple between Ti-56Al and polycrystalline Ti-39Al (Ti_3Al). After annealing at 1265°C for 144 hours in vacuum, a layer of near-stoichiometric γ-TiAl of only 150 μm width had developed. This layer was then co-deformed with the surrounding material to characterize the micromechanical behavior. Mahapatra et al. (1995) concluded that near-stoichiometric γ-TiAl deforms primarily by twinning. However, the applied deformation was compression along the tetragonal *c*-axis. In this orientation, the Schmid factors for twinning are the highest and the Schmid factors for ordinary dislocation glide are zero, figure 3.5. Therefore, the relative contributions of ordinary glide and twinning are difficult to assess from this single experiment.

In the alloys currently under development for high temperature applications, alloying elements such as niobium or tantalum slow down solid state diffusion significantly.

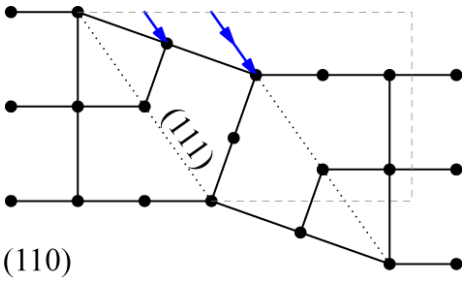

Fig. 3.4: An embryonic twin consisting of two sheared (1 1 1) planes; projection of (1 1 0), the twinning deformation results in horizontal elongation.

Thus, for these alloys a similar experiment would be more demanding in terms of annealing times. As a consequence, at the moment no simple method exists to measure the mechanical properties of the γ-TiAl phase. This impedes the investigation of deformation mechanisms as well as alloy development significantly. To overcome this limitation, the nanoindentation technique was applied to the γ-phase in two-phase microstructures, see chapter 8.

3.3.2 Deformation of γ-TiAl by twinning

Twinning is a fundamental deformation mechanism in many materials, e.g. Christian and Mahajan (1995). Good progress has been made in recent time in the understanding of fundamental aspects of twinning (Tadmor and Bernstein, 2004, Kibey et al., 2007). For example Kibey et al. (2007) showed that the stacking fault energy, which was often correlated to the propensity for twinning in fcc materials, is not the main parameter when trying to assess the tendency for deformation by twinning in an alloy. Rather, the energy of the intermediate states during the necessary atomic rearrangement gives a more meaningful parameter which can answer the question why one material shows twinning deformation and another one does not.

Twinning of γ-TiAl was reported in Shechtman et al. (1974). Farenc et al. (1993) presented in-situ TEM observations of twinning in Ti-54Al γ-phase between 20°C and 600°C. Yoo (1998, 2002) discussed twinning mechanisms in $L1_0$ structures with special emphasis on γ-TiAl. Twinning in γ-TiAl has also been analyzed by Skrotzki (2000). The high resolution electron microscope technique was applied to the investigation of twinning and twin intersection by Appel (2005).

A disordered fcc lattice features twelve $[1\,1\,\bar{2}]\{1\,1\,1\}$ twinning systems. In γ-TiAl the ordering structure permits only one twinning system per octahedral (1 1 1) plane and therefore the number of admissible twinning systems is reduced to four, table 3.4. Figure 3.4 illustrates the formation of a two-layer thick twin embryo. The Schmid factors of dislocation glide and twinning for all possible orientations of a uniaxial loading axis in γ-TiAl are illustrated in figure 3.5.

The four admissible twinning systems are regarded as important for the ductility of TiAl based. With superdislocations being very hard to activate in near-stoichiometric

Tab. 3.4: Four true twinning systems of γ-TiAl; the different morphologies refer to the orientation of the planes and directions with respect to the (1 1 1) lamellar interface for a lamellar microstructure.

Twin plane	twinning direction	morphology
$(1\,1\,\bar{1})$	$[1\,1\,2]$	transversal
$(\bar{1}\,1\,1)$	$[\bar{1}\,1\,\bar{2}]$	transversal
$(1\,\bar{1}\,1)$	$[1\,\bar{1}\,\bar{2}]$	transversal
$(1\,1\,1)$	$[1\,1\,\bar{2}]$	longitudinal

γ-TiAl, the von Mises criterion of five independent slip systems can only be fulfilled if additionally the twinning systems can be activated (Mecking et al., 1996, Goo, 1998).

In γ-TiAl, deformation twins are very narrow. For a Ti-48Al-(Mn,Cr) alloy after high temperature tensile testing at 800°C, Appel and Wagner (1994) measured 884 twins in the TEM and the maximum of their width distribution was found at around 15 nm. Skrotzki (2000) measured an average twin width of 50 nm in a TiAl based alloy after creep testing at 700°C under 225 MPa to a maximum strain of 2%.

Fischer et al. (2003) considered different energy contributions to investigate the nucleation of twins in TiAl. Earlier, Jin and Bieler (1995) have studied the same problem. Twin nucleation in binary and Nb-containing alloys was also discussed in detail by Appel (2005). Hsiung et al. (2002) reported twin nucleation from the interfaces in crept samples and calculated the critical stress to nucleate twins by pile-up of interfacial dislocations in the lamellar interfaces.

In lamellar microstructures the twin nucleation is probably assisted by the stress concentrations close to the interfaces (Appel et al., 1993, Appel, 2005, Hsiung et al., 2002). Furthermore, twinning activity was found to be virtually insensitive against temperature variation up to 800°C (Kishida et al., 1998).

Alloying with niobium reduces the stacking fault energy in γ-TiAl and twins are often found in grains with many stacking faults. Therefore twinning is thought to be promoted by addition of niobium (Appel et al., 2000). Wide dissociation of superdislocations is another indicator for the reduced stacking fault energy by 5-10at.% niobium (Appel and Oehring, 2003, pg. 116).

3.4 Deformation systems of hexagonal ordered α_2-Ti_3Al

Ti_3Al has a $^c/_a$ ratio of $\frac{0.465}{(1/2)\times 0.577} = 1.61$. For $^c/_a$ ratios below the theoretical value for closest packing (1.63), hexagonal structures are known to deform by dislocation glide on basal, pyramidal and prismatic planes, figure 3.6 (Gottstein, 2003, ch. 6). Similar to other hexagonal materials with $^c/_a$ ratios below the ideal value, such as titanium (c/a=1.587) and beryllium (c/a=1.568), glide on prismatic $\{1\,0\,\bar{1}\,0\}$-planes is the easiest mode of deformation. Basal and pyramidal deformation have also been observed, table 3.5.

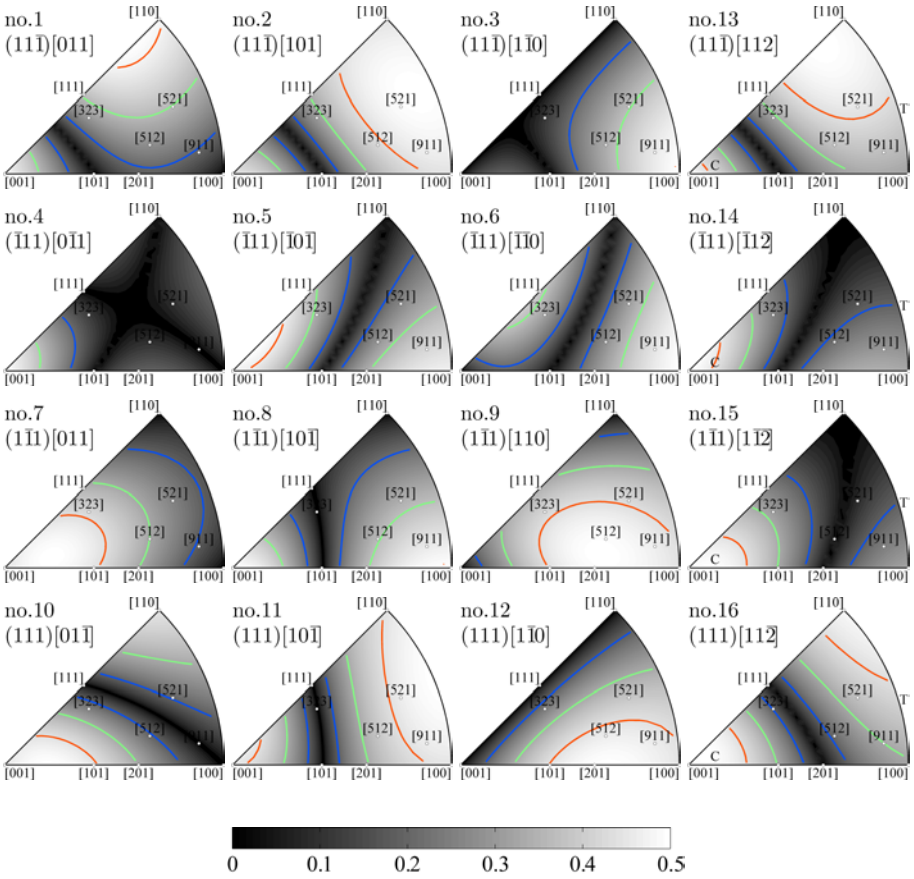

Fig. 3.5: Schmid factors for γ-TiAl under uniaxial loading (stereographic projection). The first two columns show super dislocation glide systems, the third one ordinary dislocation glide and the fourth column shows the four twinning systems. The twinning system Schmid factors are changing sign in the black regions and therefore are activated only during compression (C) or tension (T). Some orientations from Inui et al. (1997) are shown in addition. Contour lines at values 0.1, 0.25, and 0.4.

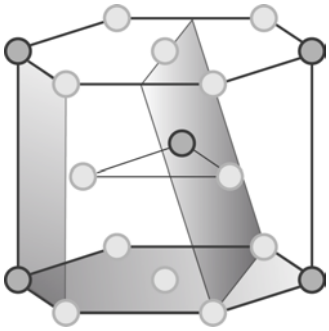

Fig. 3.6: Illustration of the basal (0 0 0 1), prismatic ($\bar{1}$ 0 1 0) and pyramidal (2 $\bar{1}$ $\bar{1}$ 1) deformation systems of α_2-Ti_3Al.

Tab. 3.5: Slip systems in α_2-Ti_3Al;

Number	slip plane	slip direction	type
1		[$\bar{2}$ 1 1 0]	
2	(0 0 0 1)	[1 $\bar{2}$ 1 0]	basal
3		[1 1 $\bar{2}$ 0]	
4	(1 $\bar{1}$ 0 0)	[1 1 $\bar{2}$ 0]	
5	(0 1 $\bar{1}$ 0)	[$\bar{2}$ 1 1 0]	prismatic
6	(1 0 $\bar{1}$ 0)	[1 $\bar{2}$ 1 0]	
7	(1 1 $\bar{2}$ 1)	[$\bar{1}$ $\bar{1}$ 2 6]	
8	(1 $\bar{2}$ 1 1)	[$\bar{1}$ 2 $\bar{1}$ 6]	
9	($\bar{2}$ 1 1 1)	[2 $\bar{1}$ $\bar{1}$ 6]	pyramidal
10	($\bar{1}$ $\bar{1}$ 2 1)	[1 1 $\bar{2}$ 6]	
11	($\bar{1}$ 2 $\bar{1}$ 1)	[1 $\bar{2}$ 1 6]	
12	(2 $\bar{1}$ $\bar{1}$ 1)	[$\bar{2}$ 1 1 6]	

The CRSS values of α_2-Ti_3Al have been measured by Inui et al. (1995) for Ti-36.5Al at room temperature. Later, Kishida et al. (2004) measured the CRSS values in a temperature range of -200 to 1100 °C. The results for room temperature are given in table 3.6. Twinning in α_2-Ti_3Al is only observed at very high temperatures above 1000 °C (Kishida et al., 2004).

Tab. 3.6: CRSS values for Ti-36.5Al off stoichiometric α_2-phase. The room temperature value for prismatic glide is taken from Inui et al. (1995);

	pyramidal	basal	prismatic	reference
Ti-36.5Al, 20°C	900 MPa	320 MPa	100 MPa	Kishida et al. (2004), Inui et al. (1995)

3.5 Non-Schmid effect on dislocation glide

It is known that alloys or pure metals can show a non-Schmid effect during plastic deformation. The motion of dislocations is then not only dependent from the resolved shear stress on the respective glide planes following Schmid's law. Instead, in these materials the activation of dislocation motion depends from more components of the acting stress tensor, which leaves at maximum six independent variables. From the experimental work of Zupan and Hemker (2003) non-Schmid effects seem to be of some importance in Ti-55.5Al.

For stoichiometric γ-TiAl, knowledge about this effect is very limited at the moment and mainly derived from atomistic simulations of dislocation core structures (Woodward and Rao, 2004, Vitek and Paidar, 2008). Possible non-Schmid effects were not accounted for in the present modeling work and therefore are not discussed further.

3.6 Kinematic constraints and Hall-Petch effect

3.6.1 Anisotropic yield strength of PST material

Lamellar microstructures show pronounced anisotropy of their yield stress. The magnitude of the yield stress is mainly governed by the orientation of the lamellar interfaces with the loading axis, figure 3.7[1]. Modeling the flow anisotropy of lamellar TiAl is subject of chapter 9 of the present work.

A morphological classification of slip systems exists for lamellar microstructures with γ-TiAl domains in the shape of extended platelets. In this classification, the deformation systems are not primarily characterized by the types of dislocations that are involved in the deformation. Instead they are classified by the relative orientations of shear direction and shear plane with respect to the lamellar interfaces. Since this classification was used widely in the literature by Lebensohn et al. (1998), Uhlenhut (1999), Dimiduk et al. (2001) and others, it is described in the following.

The $(1\,1\,1)_\gamma$ plane in contact with the basal plane has three slip directions running along its edges and one twinning direction. As the dislocations that operate in these

[1] Appel and Wagner (1998) included a similar figure which also shows data for ternary alloys.

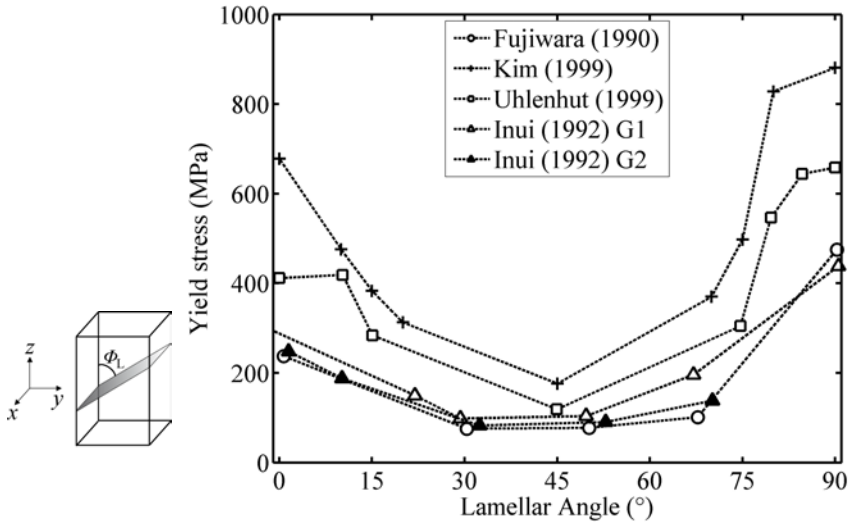

Fig. 3.7: Anisotropic yielding of PST crystals from several sources.

directions, show the smallest amount of interaction with the lamellar interfaces, they are called the *longitudinal* systems. Of the three remaining (1 1 1) planes each has one slip direction in the interfacial plane, and perpendicular to the shear direction there will be some confinement imposed by the lamellar interfaces. These three slip systems are denominated the *mixed* deformation modes.

The highest degree of confinement is expected for the deformation systems, for which the slip direction is inclined to the lamellae and the plane normal is not perpendicular to the phase boundary plane. Theses six dislocation glide systems and three true twinning systems are termed the *transversal* deformation modes and immediate hardening contributions from pile-up effects are expected right after the onset of dislocation motion.

In this terminology, the basal slip systems in the hexagonal phase should be considered as longitudinal deformation modes. The prismatic slip systems as mixed modes and the pyramidal systems correspond to the transversal mode. However, as there is a unique categorization already provided by the character of the deformation systems, this nomenclature is usually not extended to the discussion of deformation in the the hexagonal phase.

Hazzledine and Kad (1995) described many aspects of PST material such as formation of the lamellar structure and implications for the micromechanics. They showed that the yield anisotropy of PST crystals can be reproduced numerically on the basis of few assumptions. Their estimation was based on Schmid factors and the assumption of different critical shear stresses for ordinary dislocations, twinning dislocations and superdislocations, 40, 60 and 80 MPa respectively.

Additionally, Hazzledine and Kad (1995) used a Hall-Petch slope of 0.2 MPa $m^{-0.5}$ and 0.3 MPa $m^{-0.5}$ for soft and hard mode deformation. The former value was based on the experimental work of Nakano et al. (1992), who identified k=0.25 MPa $\sqrt{m}$ for soft

mode deformation ($\Phi_L \approx 45°$). By own calculation they arrived at a Hall-Petch slope k=0.45 MPa$\sqrt{m}$ for deformation in hard mode ($\Phi_L \approx 0°$ or 90°).

The mean free paths were taken to be 40 μm and 1.2 μm for soft and hard deformation respectively. Using theses parameters, Hazzledine and Kad reproduced the experimental yield points for PST deformation from Inui et al. (1992b) with good accuracy.

It should be mentioned in the context of constraint effects from interfaces, that the interfaces have also been reported to contain mobile dislocations. Hsiung et al. (2002, 2004) have observed mobile dislocations in the interfaces of type γ/γ as well as γ/α_2 at room temperature and elevated temperatures. By this mechanism the interface structure would at the same time constrain dislocation motion through the boundaries as well as promote shear deformation along the interfaces.

Recently, Porter et al. (2009) have presented results on micro-pillar compression of PST material. The yield anisotropy was reproduced with good agreement to the experiments on samples with millimeter dimensions. The diameters of the micro-pillars were ranging from 35 μm to 80 μm and no significant size dependence of the material was found in comparison to the results from millimeter-sized samples.

3.6.2 Hall-Petch effect in γ-TiAl based alloys

Umakoshi and Nakano (1993) pointed out that an estimated yield stress resulting from a 'rule of mixture'-approach severely underestimates the yield levels of lamellar microstructures. It follows that the strength of the two-phase alloys is mainly caused by the densely spaced interfaces between the two phases and the order variants. A study of the dislocation mechanics that result in the strengthening of such a kinematical confined microstructure is beyond the scope of this work. Problems of this kind can be approached with methods dedicated to micromechanical processes at smaller length scales than meso-scale crystal-plasticity, like discrete dislocation dynamics (DDD) or molecular dynamics (MD).

The yield strength in lamellar material does not only depend strongly on the loading orientation as described in the previous section. Also the microstructural parameters like lamellar spacing and grain size of the lamellar colonies have an influence on the yield strength. The dependencies are usually described in form of a Hall-Petch type relation (Hall, 1951, Petch, 1953)

$$\sigma_y = \sigma_0 + k\lambda^{-1/2} \tag{3.3}$$

with yield stress, σ_y, intrinsic strength, σ_0, Hall-Petch constant or slope, k, and the microstructural length scale, λ. If different microstructural length scales have to be considered, also composite models with different Hall-Petch constants have been used.

Vasudevan et al. (1989a) analyzed the compressive yield strength of Ti-52Al γ-single-phase polycrystalline material and found the Hall-Petch constant to be k = 1.37 MPa$\sqrt{m}$.

Umakoshi and Nakano (1993), reported values of k for compression of PST-crystals: for a compression axis perpendicular to the lamellar plane k is 0.50 MPa$\sqrt{m}$, for a compression parallel to the lamellae it is reported to be 0.41 MPa$\sqrt{m}$. Sun (1997) presented a dislocation pile-up analysis of lamellar TiAl.

Kad and Asaro (1997) found that reported data on grain sizes from 3000 to 200 μm exhibited an extremely high Hall-Petch slope of 5 MPa$\sqrt{\text{m}}$ test. This unprobably high value was then explained by the relaxing effect of free surface. Compatibility stresses that develop in bulk polycrystalline material will be relieved if the sample gauge cross-section consists only of few grains. Kad and Asaro (1997) performed a numerical analysis based on the dimensionless parameter D/d, with D being the gauge section diameter and d the grain size.

The authors requested at least 200 grains in the sample gauge cross-section, D_{gauge}, for a limited influence of the free surface which releases grain incompatibility stresses. Therefore

$$\pi \frac{D_{gauge}^2}{4} \stackrel{!}{\geq} 200\, \pi \frac{d_{grain}^2}{4} \tag{3.4}$$

and correspondingly, the grain size, d, should be smaller than $\frac{1}{\sqrt{200}} D_{gauge} \approx 0.071\, D_{gauge}$ to maintain the constraint effect of polycrystalline material. A similar argumentation can also be found earlier in Kocks (1970). In the polycrystal simulations performed in the present work, chapter 9, the release of grain incompatibility was avoided by using periodic boundary conditions.

Three relevant length scales were proposed by Appel and Wagner (1998) for lamellar microstructures: the colony size, the gamma domain size in the direction parallel to the lamellar interfaces, and the lamellar spacing.

Maziasz and Liu (1998) collected Hall-Petch plots from several sources. Liu and Maziasz (1998) found that the strengthening contribution from the grain size is negligible in comparison to the lamellar strengthing effect, if fine lamellar microstructures are considered. They presented a room-temperature Hall-Petch constant k_λ of 0.22 MPa $\sqrt{\text{m}}$.

Dimiduk et al. (1998) performed a detailed analysis of several fully lamellar microstructures to separate the influence of the different micrustructural variables like lamellar colony size, γ-width, α_2-spacing, α_2-thickness. They proposed the existence of three Hall-Petch constants of approximate magnitudes of 1 MPa$\sqrt{\text{m}}$ for high-angle non-special γ/γ boundaries, 0.45 MPa$\sqrt{\text{m}}$ for the hard mode deformation of PST material with lamellar interfaces as the dominating dislocation obstacles; and 0.25 MPa $\sqrt{\text{m}}$ in the case of soft mode PST deformation, where the order domain boundaries are ruling the mean free path of the dislocations.

Perdrix et al. (1999) investigated a Ti-48Al alloy with 980 wt.-ppm oxygen content and a fully lamellar microstructure with large grains (1.38 mm ... 1.66 mm). Compression testing on cylindrical specimens of D=6 mm, L=12 mm, led to a Hall-Petch law of the form

$$\sigma_{0.2y_{compr}} = 206.12\,\text{MPa} + 0.078161\,\text{MPa}\sqrt{\text{m}}\;(\lambda)^{-0.5}$$

between 2.6 μm and 1.0 μm α_2-spacing and therefore $k_y = 0.078\,\text{MPa}\sqrt{\text{m}}$.

Yamaguchi et al. (2000) gave a Hall-Petch type law for lamellar material

$$\sigma_y = \sigma_0 + k_d d^{-0.5} + k_\lambda \lambda^{-0.5}$$

with grain size, d, and lamellar spacing, λ, and related to the work of Dimiduk et al. (1998).

Cao et al. (2000) performed an analysis of microstructures with different grain sizes at approximately constant lamellar spacing and of different lamellar spacings at constant grain size of an Ti-45.5Al-2Cr-1.5Nb-1V alloy. Compressive yield strength was studied and the lamellar spacing was defined as edge-to-edge dimension of lamellae (viewed edge-on) counting γ/γ as well as γ/α_2 interfaces. Grain sizes were 260, 390, 690, and 920 μm at a approximately constant lamellar spacing of 160-170 nm. Additionally, for an approximately constant grain size of 360 – 390 μm lamellar spacings of 15, 95, 160, and 500 nm were obtained. The specimen dimensions have been D=4 mm and L=8 mm. The ratio $D/d \approx 11$, for the constant grain size material, is below the value of 20 that Kad and Asaro (1997) proposed as a viable ratio between grain size, d, and gauge section diameter, D, for bulk behavior. Even the smallest of the studied grain sizes (260 μm) yields a D/d ratio of 15.4, below the requested minimum value of 20. Therefore the derived Hall-Petch slope of 2.07 MPa$\sqrt{\text{m}}$ for grain size hardening should be considered as an apparent one, i.e. an over-estimation of the true bulk coefficient, in the sense of Kad and Asaro (1997). For the variation of the lamellar spacing the following Hall-Petch relation was derived $\sigma_y = 334MPa + 0.06MPa\sqrt{\text{m}}\,\frac{1}{\sqrt{\lambda}}$ with λ denoting the lamellar spacing where α_2/γ as well as γ/γ-interfaces counted irrespective of the type.

Maruyama et al. (2001) have studied the Hall-Petch effect in Ti-38Al (at.%). They found a Hall-Petch slope, k, of 0.29 MPa $\sqrt{m}$ at RT and 0.26 MPa $\sqrt{m}$ at 950 K.

The strengthening of lamellar alloys by refinement of the lamellar spacing cannot exceed a certain limit value (Hazzledine, 1998, Maruyama et al., 2002, 2004). Maruyama et al. (2004) have investigated this effect in Ti-39.4Al. For very thin lamellae they found a transition from semi-coherent lamellar boundaries to fully coherent boundaries at about 50 ± 20 nm lamellar spacing. This transition marks the upper limit for Hall-Petch strengthening by lamellar refinement.

Maruyama et al. (2002) used a single pile-up model of edge dislocations to model the Hall-Petch behavior and especially the saturation of the Hall-Petch strengthening for the limit of very thin lamellae. The experimental data was generated by mechanical tests of Ti-39Al, which forms very thin γ-lamellae. The Hall-Petch slope in the model is given by

$$k = M\sqrt{\frac{G\,b\,\tau^\star}{1-\nu}},$$

where M is the Taylor factor ($M \approx 3$), G=61 GPa, b=0.28 nm and ν=0.28M; $\tau^\star$ is the shear strength of the boundary against dislocation motion. The saturation stress level is $\sigma_s = \sigma_0 + \sigma^\star = \sigma_0 + M * \tau^\star$. The lamellar spacing at which the yield stress reaches the saturation level is denominated by

$$\lambda^\star = \frac{Gb}{(1-\nu)\tau^\star}.$$

The fitted values for experimental data on Ti-39.4 mol% are $\sigma^\star = 665MPa$, $\sigma_s = 985MPa$ and $\lambda^\star = 110$ nm. The Hall-Petch constant for the lamellar spacing was found to be $k = 0.218$ MPa$\sqrt{\text{m}}$.

A strength model deviating from the usual Hall-Petch approach, has been developed by Dimiduk et al. (2001), based on the assumtion of a logarhitmic distribution of lamellar spacings and a Taylor-Ashby type formulation of the flow stress.

Caillard and Couret (2009) have performed an in-situ study of slip transmission through γ/γ boundaries. Through pile-up law of Friedel (1964) they arrived at local resolved stres levels of about 100 MPa and at Hall-Petch constants for γ/γ-interfaces of 0.058 MPa$\sqrt{\text{m}}$ and 0.094 MPa$\sqrt{\text{m}}$, respectively. Nakano et al. (2001) performed an extensive study of slip transfer in fatigued PST crystals.

In summary, different kinds of interfaces have to be taken into account to describe the strengthening of lamellar TiAl based microstructures. In the past, during experimental investigations, the relative dimensions of the gauge cross-section and grain sizes have often led to high apparent Hall-Petch slopes which are mainly affected by the release of compatibility stresses at the sample surface. The spacing of lamellar interfaces is the predominant influence on the strength of lamellar microstructures.

3.6.3 Pre-yielding and pre-yield cracking

Another effect that is possibly related to the anisotropic plastic behavior of γ-TiAl based alloys is pre-yielding and pre-yield cracking (Botten et al., 2001, Wu et al., 2006). The flow curves at RT show a well defined yield point for duplex, but not for lamellar microstructures. This can be explained by the occurrence of pre-yielding. Hu et al. (2006a) investigated pre-yielding in lamellar microstructures. They found that the pre-yielding takes place at lower stresses for larger colony sizes. Pre-yielding is discussed in more detail in chapter 9.

The formation of micro-cracks during the first stages of plastic deformation was described in the context of pre-yielding (Wu et al., 2006). the phenomenon of pre-yield cracking presumably is related to the occurrence of pre-yielding. It will not be discussed further here, since fracture initiation was not included in the used constitutive models.

4

Review of crystal plasticity models of γ-TiAl based alloys

4.1 Introduction

The previous modeling work based on crystal plasticity theory is summarized in the following. Various models have been applied since the pioneering work of Lee et al. (1993). Most of the later approaches root in the original crystal plasticity work of Peirce, Asaro and co-workers (Peirce et al., 1983, Asaro and Needleman, 1985) who introduced the visco-plastic formulation of single crystal plasticity. For the solution of the field equations, mainly finite elements have been applied but also self-consistent schemes based on Eshelby's solution for a spherical inclusion have been employed (Lebensohn et al., 1998, Lebensohn, 1999).

4.2 The 2D-CPFEM model of Lee, Ahzi, Kad, Dao, Asaro

This group performed a two-dimensional analysis based on slip systems projected in the plane perpendicular to the lamellar interfaces. Three slip systems were implemented in a two-dimensional model defined in the $\{\bar{1}\,0\,1\,0\}$-projection of the γ/α_2 arrangement after Blackburn. One 'soft' mode with slip direction along $[\bar{1}\,1\,0]$ or $[\bar{1}\,2\,\bar{1}\,0]$ and slip plane $(1\,1\,1)$ or $(0\,0\,0\,1)$. And two hard mode systems derived from the $\langle 1\,1\,\bar{2}\,6\rangle\{1\,1\,\bar{2}\,1\}$ pyramidal slip systems of α_2 (Dao et al., 1996).

The relevant publications are Lee et al. (1993), Kad et al. (1995), Dao et al. (1996), Kad and Asaro (1997). For the soft-mode deformation the critical resolved shear stress, τ_c, values from 50 to 75 MPa were chosen, and for the hard modes, τ_c varied from 300 MPa to 600 MPa.

4.3 The CPFEM model of Parteder, Schlögl, Marketz, Fischer, Clemens

Parteder et al. (1995) implemented a two-dimensional model. Schlögl and Fischer (1997a) extended the model to a full-3D implementation. Four ordinary slip systems were incorporated and split in two groups of longitudinal/mixed mode (2 systems) and transversal mode (2 systems). Additionally, four true twinning systems were included into the model.

Hall-Petch relations after Umakoshi and Nakano (1993) were incorporated for the gamma-domain size and for the lamellar width, equations 4.1 and 4.2.

$$\tau_0 = 70\,\mathrm{MPa} + 0.27\,\mathrm{MPa}\sqrt{\mathrm{m}}\,D^{-0.5} \tag{4.1}$$

$$\tau_0 = 30.1\,\mathrm{MPa} + 0.1161\,\mathrm{MPa}\sqrt{\mathrm{m}}\,\lambda^{-0.5} \tag{4.2}$$

The published works include Parteder et al. (1995), Schlögl and Fischer (1997a,b), Schaden et al. (2005), and Marketz et al. (2003).

For the self hardening behavior the following function was used (Asaro and Needleman, 1985):

$$h_{\alpha\alpha} = h(\gamma) = h_0 \operatorname{sech}^2 \frac{h_0\gamma}{\tau_s^\alpha - \tau_0^\alpha}.$$

Since the hyperbolic secant type hardening law differs from the hardening law used in this work, the parameters are not directly comparable, but are given for completeness, table 4.1. The values for the initial slip resistances, τ_0, were calculated form equations 4.1 and 4.2 with an assumed domain size, D, of 50 µm and an assumed lamellar width, λ, of 2 µm. The cross-hardening coefficient, q, was taken to be 1 and 1.4 for co-planar and non-coplanaer glide systems, respectively.

Tab. 4.1: The crystal plasticity parameters used by Schlögl and Fischer (1997a)

	τ_0 (MPa)	h_0 (MPa)	τ_s (MPa)
γ-ord., longi.	46	500	96
γ-ord., trans.	112	500	162
α_2, pri.	250	800	300
α_2, pyr.	1250	1000	1600

Later, Marketz et al. (2003) introduced the superdislocation glide systems additionally and used different values for the CRSS, table 4.2. No hardening was assumed for the twinning mode of deformation.

Tab. 4.2: The crystal plasticity parameters used by Marketz et al. (2003); hardening parameters were not given in Marketz et al. (2003), but were the same for all slip systems

	τ_0 (MPa)	h_0 (MPa)	τ_s (MPa)
γ, ord.	130	–	–
γ, twin.	130	n/a	n/a
γ, sup.	200, 500	–	–
α_2, pri.	n/a, 260	–	–

For the α_2-phase either elastically isotropic behavior (Schlögl, 1997, Marketz et al., 2003) or a CRSS value of 260 MPa for prismatic slip was used (Marketz et al., 2003).

4.4 The self-consistent crystal plasticity model of Lebensohn et al.

In the work of Lebensohn et al. (1997, 1998), Lebensohn (1999) and Uhlenhut (1999) a self-consistent visco-plastic crystal plasticity formulation was applied to the deformation of PST-material and strongly textured casting material. During that work, the morphological classification of slip systems as described in section 3.6.1 was introduced.

4.5 The CPFEM model of Werwer, Cornec and others

Werwer and Cornec (2000), Cornec et al. (2003), Werwer and Cornec (2006), and Brocks et al. (2009) have presented a modelling approach to lamellar microstructures of TiAl. They have developed representative volume elements (RVEs) consisting of several finite elements from which each was assigned the constitutive behavior of one of the γ-variants or of α_2-phase. Ordinary and super dislocations were included. In Werwer and Cornec (2000) there was no difference in the strength of ordinary and super dislocation slip systems or twinning systems. The deformation system properties were assigned solely on the basis of the orientation of these systems with respect to the lamellar plane. Initial strengths of 55 MPa (longitudinal), 150 MPa (mixed) and 185 MPa (transversal deformation) were assigned.

Later, Werwer and Cornec (2006) improved the flexibility and included the special role of superdislocation deformation in their model. Also grain clusters of lamellar microstructure were simulated.

4.6 The CPFEM model of Grujicic, Zhang, Cao and Batchu

Another set of modeling work is represented by the papers of Grujicic and Zhang (1999), Grujicic and Batchu (2001), Grujicic and Cao (2002) and Grujicic et al. (2003). After the initial two-dimensional treatment (Grujicic and Zhang, 1999), Grujicic and Batchu (2001) implemented a three-dimensional, elasto-viscoplastic crystal-plasticity formulation for the description of single phase γ-TiAl and α_2-Ti_3Al, for use in an explicit finite-element solver.

Crystal plasticity constitutive parameters were identified by running a simplex algorithm against experimental data for single crystal deformation in different orientations. No twinning was considered for the deformation of the γ-phase. The fitting procedure yielded good matches with experimental flow curves of five different orientations of γ-phase and α_2-phase.

From the two sets of single crystal parameters a homogenized model for lamellar PST crystals was implemented, through introducing another two parameters. Optimization of these two parameters lead to a constitutive model for PST material. The agreement to the experimental uniaxial compression data from Fujiwara et al. (1990) for five orientations of PST crystals is excellent.

The excellent match for the PST material is somewhat surprising because the γ-phase behavior was fitted to single crystal γ-TiAl-experiments by Kawabata. While the composition of the single crystals is not given in the original work (according to Woodward and Rao (2004) it was Ti56Al), it must be assumed that the material contained more than 54 at.% of Al, since it is virtually impossible to grow single crystals from material of lower aluminum contents. The deformation behavior of Al-rich single crystals, however, is known to deviate significantly from the one of stoichiometric TiAl present in the PST structure, as discussed in chapter 3.

4.7 The CPFEM model of Brockman et al.

The anisotropic elasticity of PST crystals was studied by Frank et al. (2003) and John et al. (2004). Brockman (2003) used the elastic parameters in a crystal plasticity analysis of PST material. Additionally, Brockman studied the constraint stresses in an aggregate of 512 grains of a duplex microstructure consisting of equal volume fractions of lamellar grains and equiaxed γ-grains.

The model of Brockman (2003) and Frank et al. (2003) used a small-deformation, small rotations formulation. The CRSS values for single phase simulations were 90 MPa for ordinary dislocation glide, 120 MPa for super dislocation glide. In α_2-phase the prismatic slip systems were assigned a CRSS of 100 MPa, the basal 329 MPa and the pyramidal systems 911 MPa.

For the constitutive model of a lamellar microstructure, the slip systems taken into account were ordinary dislocation glide (CRSS 90 MPa), prismatic slip (CRSS 100 MPa) and pyramidal slip (CRSS 911 MPa). Additionally, one 'interlamellar' system was defined, corresponding to shear along the basal slip systems, with a CRSS of 56 MPa.

4.8 The CPFEM model of Heripré, Roos et al.

Heripre (2006) and Héripre et al. (2007) applied the digital image correlation technique to mechanical tests on a near-gamma microstructure of TiAl. The strain fields were then transferred to the boundaries of a finite element crystal plasticity model and the simulated strain fields were compared with the experimentally measured ones.

Roos et al. (2004) employed a multiscale-modeling approach based on the finite element method and single crystal plasticity. They chose the morphological orientation factors, i. e. the relative strengths, in the γ-phase for longitudinal, mixed and transversal slip to be 1.0, 1.3 and 2.2 respectively.

Simulations were carried out for PST material. Additionally, aggregates of 40 randomly oriented grains were simulated, with volume fractions for α_2-phase, γ-phase and lamellar grains that represent an idealization of the near-gamma, duplex, near-lamellar and the fully lamellar microstructure.

4.9 The CPFEM model of Bieler et al.

Bieler et al. (2009) studied the crack initiation and crack propagation in a TiAl microstructure by means of crystal plasticity. Based on the findings of Mahapatra et al. (1995) they assumed twinning to be the easiest mode of deformation in the near-stoichiometric γ-TiAl-phase. Values for the initial slip resistances were 50, 60, and 180 MPa for twinning, ordinary and super dislocation glide, respectively.

4.10 Conclusion

The mechanical behavior of titanium aluminides has been modeled successfully by various approaches. No modeling was carried out up to now for the case of stoichiometric single crystalline γ-TiAl, because no experimental data for validation of the results was available. Different sets of crystal plasticity parameters were identified and the deviations can easily be justified by the strong dependence of the mechanical response

on the precise microstructural arrangement, microstructural dimensions and compositional differences. The finite-element based approaches as well as the self-consistent method have shown a high potential to improve the micromechanical understanding of γ-TiAl based alloys through careful application and interpretation of constitutive modeling.

5

The instrumented indentation technique

5.1 Basics of Indentation

The historical development of hardness as a material property has recently been reviewed by Mukhopadhyay and Paufler (2006). A classical treatment of indentation testing is *The hardness of metals* by Tabor (1951).

Classically, hardness is defined as the resistance of a solid against prenetration with a rigid tool. It can be quantified by dividing the force that is applied to the indenter through the contact area between indenter and sample:

$$H = \frac{P}{A} \tag{5.1}$$

with load, P, and contact area A. Two concepts of hardness have been used, depending of whether the projected contact area, $A_\perp$, (Meyer, 1908) or the actual contact area between the indenter and the sample are used. Using the projected contact area makes the calculated hardenss value interpretable as a mean pressure under the indenter. Although friction is neglected in this interpretation, it is physically more satisfying than using the actual, curved contact area. The measured hardness value depends on the shape of the used indenter. This dependence gives the hardness measure a less fundamental significance when compared to the uniaxial flow stress, which generally is assumed independent of the test design.

Tabor (1948) put forward a simple relation between the yield strength and the hardness of a material

$$H \approx C\,\sigma_y \tag{5.2}$$

where H is the measured hardness, C is a constant and σ_y is the uniaxial yield stress of the material. An approximate value of $C \approx 3$ was found for polycrystalline metals ($E/\sigma_y \gg 1$). As Gerk (1977) pointed out, this relation, sometimes called the Tabor relation, is not applicable to single-crystal indentation. For example in copper, the hardness was found to be about 1% of the shear modulus (Gerk, 1977, Vlassak and Nix, 1994) and therefore about 100 times the yield strength. Gerk (1977) concluded that the ratio between hardness and yield stress increases with increasing work hardening of the tested material.

5.1.1 Hardness testing and intermetallics

It is interesting to note that hardness testing has always been tightly connected to the study of intermetallics. This relation is probably due to the efficiency of the testing

method. No complicated sample geometries have to be machined; a flat polished surface of the sample is sufficient to carry out a hardness test. Indentation testing is therefore particularly suited to application in intermetallic research: there often a large number of measurements is needed to analyze for example the composition dependence of the mechanical properties, as exemplified by figures 3 (figure 5.1) and 7 in the book of Desch (1914).

The close relationship between research on intermetallic compounds and hardness testing can also be observed in the works of Westbrook who edited several volumes on intermetallics and also a book on hardness testing (Westbrook and Conrad, 1973).

5.1.2 Instrumented indentation and nanoindentation

The early developments of the instrumented indentation technique are marked by the works of Bulychev et al. (1975), Fröhlich et al. (1977), Pethica et al. (1983), and Doerner and Nix (1986). They provided the initial developments in hardware and data analysis that would define the technique of instrumented indentation. A good introduction to the general concepts and state of the art of micro- and nanoindentation is given in the monograph *Nanoindentation* by Fischer-Cripps (2004).

Instrumented indentation is commonly applied to analyze the elastic and the plastic properties of the indented material. The hardness is calculated from equation (5.1). However, the determination of the contact area at maximum load is generally non-trivial. The contact area is influenced by the elasto-plastic deformation of the indented material. Piling-up or sinking-in, figure 5.5, can have a large effect on the calculated hardness. Some issues of the technique are discussed in the review of Oliver and Pharr (2004).

The continuous monitoring of displacement, h, and load, P, of the indenter, makes possible the evaluation of the contact stiffness at initial unloading, S, defined by $S = \frac{dP}{dh}$ (Vlassak and Nix, 1993), figure 5.2. The contact stiffness can be used to calculate back the elastic properties of the sample. Pharr and Oliver (1992) have extended Sneddon's solution of a cylindrical punch indenting an elastic half-space (Sneddon, 1965), to indenters of general shape

$$\frac{dP}{dh} = \frac{2}{\sqrt{\pi}} \sqrt{A} E_r$$

with projected contact area A, and reduced modulus E_r. The reduced modulus E_r is defined as

$$\frac{1}{E_r} = \frac{1-\nu^2}{E} + \frac{1-\nu_i^2}{E_i}$$

with ν, ν_i and E, E_i being the Poisson ratio and Young's modulus of the sample and the indenter, respectively. The use of the reduced modulus has been criticized (Chaudhri, 2001).

The elastic recovery of conical indentations has been studied by Stilwell and Tabor (1961). Pronounced elastic recovery is observed for low ratios of E/H or E/σ_y.

The basic principles of instrumented indentation, as described above, have been implemented in international standards (ISO, 2003a,b,c).

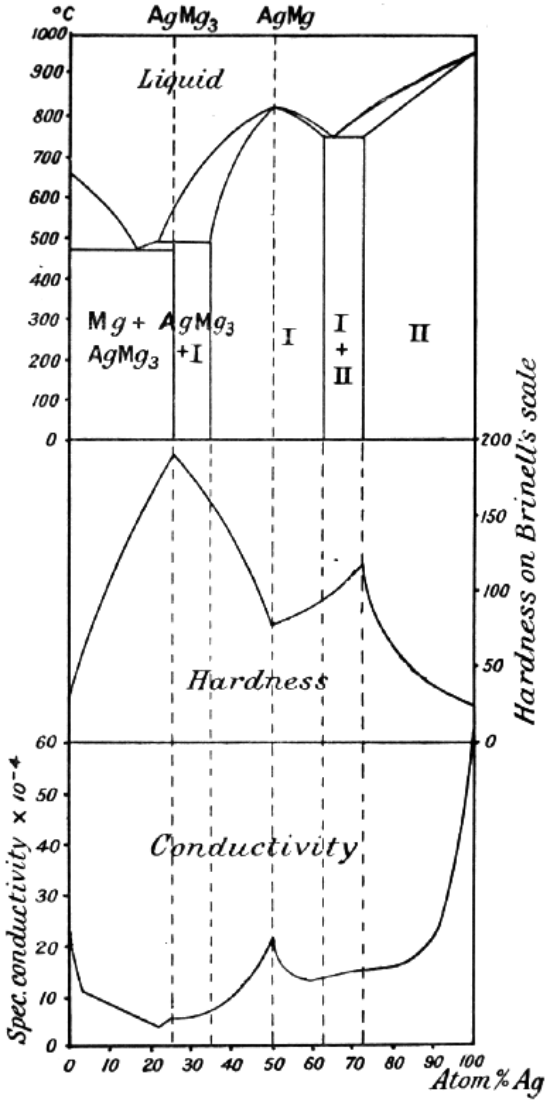

Fig. 5.1: Composition dependence of the Brinell hardness in the Ag-Mg system, figure 3 from Desch (1914);

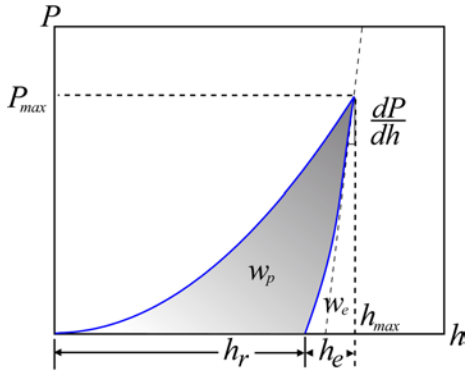

Fig. 5.2: Load-displacement curve during instrumented indentation; load, P, and penetration depth h; The total work of indentation, w, is split in the plastic work, w_p, and the elastically recovered work, w_e, under the unloading curve. The contact stiffness is measured from the initial unloading slope. Characteristic values for the indenter displacement are the maximum penetration depth, $h_{\max}$, at maximum load, $P_{\max}$, and the remaining indent depth, h_r, after elastic rebound of magnitude h_e.

An increase in hardness at small indentation depths, the indentation size effect (ISE), has been observed and interpreted by Pethica et al. (1983), Nix and Gao (1998), Tymiak et al. (2001), Swadener et al. (2002a,b), Nabarro et al. (2006), Rao et al. (2008), Demir et al. (2009). The most widely used quantitative model of the indentation size effect was developed by Nix and Gao (1998).

$$\frac{H}{H_0} = \sqrt{1 + \frac{h^*}{h}}$$

with H_0 denominating the hardness at infinite depth, h^* the characteristic length, h for the indentation depth and H being the hardness at this indentation depth.

Advanced area functions will be needed for further development of the nanoindentation technique. The contact area between indenter and indented material as a function of the indentation depth, is relevant for the calculation of the hardness as well as for the indentation modulus. The study of pile-up patterns in single crystal indentation constitutes an important first step towards this goal.

5.1.3 Identification of constitutive parameters by instrumented indentation

Conventional hardness measurements delivered a single data point, correlating the indentation load with the impression depth or diameter. Instrumented indentation records the load-penetration curve which is an analogue to the flow curve in uniaxial testing. Both of these types of curves are one-dimensional data sets. Mathematical optimization methods have been applied to calculate back the full constitutive behavior from the indentation curve (Huber and Tsakmakis, 1999, Dao et al., 2001). The uniqueness of the identified constitutive law from the 1D indentation curve is in dispute (Liu et al., 2009a).

Tab. 5.1: Indenter geometries for nanoindentation; α is the angle between indenter axis and face normal and $A(h^2)$ is the projected area, dependending from the indentation depth, h;

Indenter	description	α	$A_{proj}(h)$	eff. half cone angle
Sphere	-	n/a	$A \approx \pi 2Rh$	N/A
Cone	-	α	$A = \pi h^2 \tan^2 \alpha$	α
Vickers	4-sided pyramid	68.00°	$A = 4h^2 \tan^2 \alpha$ $\approx 24.504h^2$	70.3°
Berkovich	3-sided pyramid, same projected area as Vickers	65.274°	$A = 3\sqrt{3}h^2 \tan^2 \alpha$ $\approx 24.5033\, h^2$	70.3°
Cube corner	3-sided pyramid	35.26°	$\frac{3\sqrt{3}}{2} h^2 = 2.598\, h^2$	42.28°

5.2 Indenter geometries

Generally, the measured Meyer hardness depends on the geometry of the indenter Sakai (2008). The surfaces of the indenter that will be in contact with the sample during indentation can have angles with the indentation axis between 0° (theoretical case of an infinitely sharp needle) and 90° (flat punch) . Various geometries, ranging from flat-punches to needle-like sharp indenters have been used for indentation experiments (Tammann and Müller, 1926, Carrasco et al., 2008). Standardized methods for four-fold (Vickers), three-fold (Berkovich, cube corner) and two-fold (Knoop) symmetries around the axis of indentation have been developed. Also axisymmetric spherical (Brinell) or conical (Rockwell C) indenters are in use for hardness testing and have specific advantages in single crystal indentation as will be discussed later.

An overview of commonly used indenter geometries is given in table 5.1. More details for the various indenter shapes can be found in Fischer-Cripps (2004).

5.2.1 Berkovich geometry

The Berkovich geometry (Berkovich, 1951) is in wide use for nanoindentation testing. The three-sided pyramid is can be produced with very sharp tips. Tip radii are usually in a range of a few ten nanometers. Figure 5.3 shows the Berkovich indenter geometry in different views. Due to the sharp tips and the constant face angle, indentations with Berkovich pyramids approximate geometrically self-similar deformation even at relatively small indentation depths.

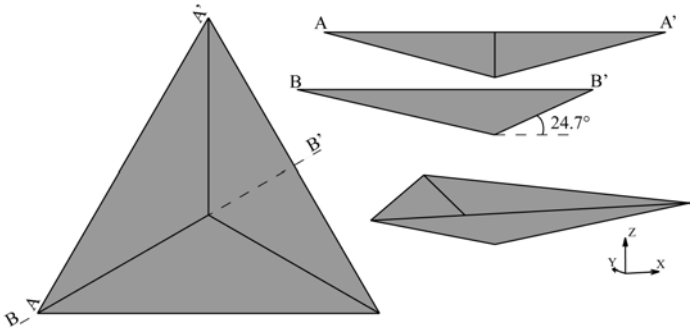

Fig. 5.3: Some views of the Berkovich indenter geometry.

5.2.2 Spherical and sphero-conical indenters

The case of spherical indentation was investigated by Hill et al. (1989) and Chaudhri (2000). In contrast to pyramidal indenters and the ideal cone, a spherical indenter is not geometrically self-similar. The indentation strain raises with indentation depth.

In principle, a perfectly conical indenter would combine the advantageous features from spherical indenters and the three-sided pyramidal geometries: the axisymmetry from spherical indenters and the self-similar deformation from pyramid-shaped tools. However, sharp conical indenters with tip radii smaller than 1 µm are difficult to manufacture with good accuracy. Therefore, for the range of small indentation depths, the rounded part of the indenter tip cannot be neglected. It is important to know the transition point, h_{trans}, at which the conical part of the indenter begins to make contact. If the indentation depth is lower than this value, the indentation is made only by the spherical part of the tip. If the indentation is much deeper than the transition point, the spherical contribution might be negligible. Figure 5.4 illustrates the transition from spherical contact to the conical part of the indenter for various tip radii.The transition from spherical contact to conical contact is at

$$h_{trans} = R(1 - \sin\alpha) \tag{5.3}$$

with tip radius, R, and half cone angle α. This relation assumes a tangential transition from the spherical to the conical shape. For $R = 1\,\mu m$ and half cone angle α=45 °, $h_{trans} = 293\,nm$.

Due to the tip rounding, a sphero-conical indenter at a certain indentation depth, generally has a higher contact area than the corresponding ideal conical geometry. The truncation, Δh, of the indentation depth can be calculated from (Fischer-Cripps, 2004, eq. 4.9i)

$$R_{tip} = \Delta h \left(\frac{1}{1 - \sin\alpha} - 1 \right) \tag{5.4}$$

$$\Delta h = \frac{R_{tip}}{\frac{1}{1-\sin\alpha} - 1}$$

For example, a tip radius of 1 µm for a 45° half cone angle results in a truncation of 414 nm.

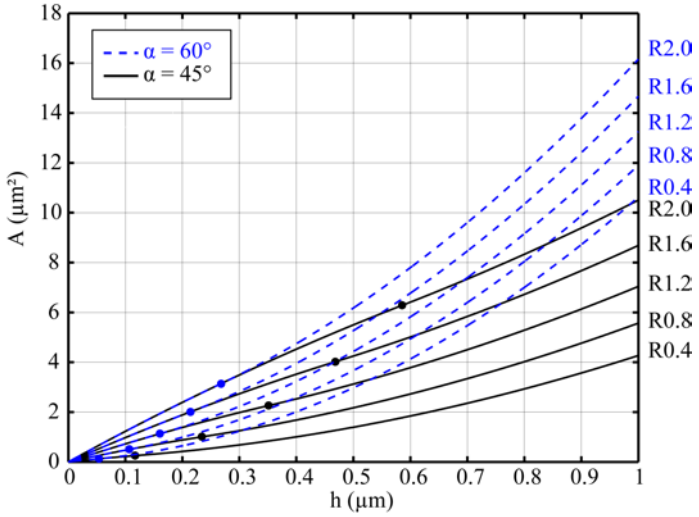

Fig. 5.4: Theoretical area functions, $A(h)$, for various tip radii, R, of sphero-conical indenters with half cone angles, α, of 45° (—) and 60° (- -). The transition points from spherical geometry to sphero-conical geometry are also indicated.

5.2.3 Tip geometry imperfections

Deviations from the theoretical indenter shape are always present. The most widely used materials to produce indenter tips are diamond and to a lesser degree sapphire. Due to their crystalline nature, anisotropic elastic and plastic properties lead to difficulties in the manufacturing process of sharp tips. The most accurate tip geometries are achieved for three-sided pyramidal indenters such as the Berkovich or the cube corner geometry. Due to the geometrical boundary conditions, grinding and polishing of the intersection of three planes will automatically result in a pointed tip with very small radii, down to 20 nm.

Even more difficult is the preparation of conical indenter shapes. The anisotropic grinding properties of the mentioned materials will affect the product shape and will lead to more or less deviation from the axisymmetric ideal. Commonly, sphero-conical tips can be obtained with a defined tip radius of down to about 1 µm.

5.3 Indentation response of single crystals

5.3.1 Studies on ionic crystals, and metals with different crystal structures

Brookes et al. (1971) presented the anisotropic hardness response of a number of single crystals. Indentations where performed with Knoop tools which themselves exhibit a strong geometrical anisotropy by an approximate length to width ratio of 7:1. Therefore, the results reflected the interaction between the plastic anisotropy of the crystal and the shape anisotropy of the indenter.

Chaudhri (2004) have reviewed the response of single crystals during indentations. They focused on the analysis of dislocation patterns in ionic single crystals by the etch pit technique. Also interferograms of the pile-up were shown.

The single crystal indentation of fcc metals has been investigated for copper (Dyer, 1965, Coulet et al., 1969, 1970, Minari et al., 1970, Flom and Komanduri, 2002, Peralta et al., 2004, Wang et al., 2004, Zaafarani et al., 2006, 2008), aluminium (O'Neill, 1923, Flom and Komanduri, 2002), nickel (Rickerby and Macmillan, 1979, Nibur and Bahr, 2003, Nibur et al., 2007, Zong et al., 2006), γ-iron (Osmond and Cartaud, 1906), silver (Chen and Hendrickson, 1971, Ma and Clarke, 1995), and gold (Gane and Cox, 1970, Kiely and Houston, 1998, de la Fuente et al., 2002, Carrasco et al., 2003, 2008).

Single crystal indentation of bcc metals has been investigated for α-iron (Osmond and Cartaud, 1906, Pfeil, 1927, Smith et al., 2003, Pfetzing et al., 2009), tantalum (Biener et al., 2007), and tungsten (Stelmashenko et al., 1993, Lee et al., 2008).

The selection of references on fcc and bcc indentation focuses mainly on those works which also include some data and discussion on the formation of pile-up which is the topic of the following section. For the case of micro- and nanoindentation, the Vickers and Berkovich indenter geometries dominate in the literature and only few studies used axisymmetric indenters.

5.3.2 Indentation pile-up as the finger print of single crystal plasticity

Several terminologies have been used to describe the topographic changes around indentations. They included *Druckfigur* (German, in Tammann and Müller (1926)), *silhouettes* (German, in Osmond and Cartaud (1906), English in Pfeil (1927)); *pressure figure*, *raised lobes* (O'Neill, 1923, crystal C, approx. cube face); *percussion figure* (Moses, 1899, Schmid and Boas, 1950); *plastic convexity* (Fröhlich et al., 1977, fig. 6), *upheaval*, *hillocks*, *lifting of material* (Hirsch et al., 1985), The variability in the used vocabulary is an indicator that the phenomenon is far from being well-understood. Nowadays, the term *pile-up* or *piling-up* seems to get established despite the unfortunate interference with the piling-up of dislocations against an obstacle.

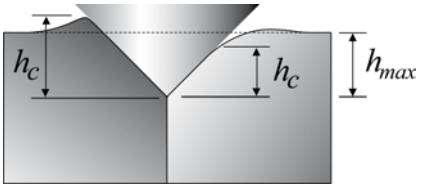

Fig. 5.5: Variation of contact depth, h_c, for piling-up (upheaval) and sinking-in during indentation to the maximum penetration depth, $h_{\max}$.

Figure 5.5 illustrates how piling-up or sinking-in of material around the indenter can change the actual contact area between tool and sample. Indeed the pile-up effect on measures like the indentation modulus or hardness is two-fold. For upheaval of material against the indenter the actual contact area will be increased. At the same time, for a constant load the indentation depth will be reduced through better distribution of the load over a larger area. The combined effect of such shape and contact area changes is that the application of standard evaluation methods like the Oliver-Pharr area calibration (Oliver and Pharr, 1992), will lead to a significant underestimation of the elastic stiffness and of the hardness. Analogous effects are present in the case

of sink-in behavior and the mechanical characteristics will be overestimated. Correspondingly, Fischer-Cripps (2006) stated: "*Piling-up is perhaps the most important unresolved issue in nanoindentation testing*".

After Fischer-Cripps (2004, pg. 80), piling-up is most pronounced for materials in which have high stiffness combined with a low yield stress, i. e. E/σ_y is high and are non-strain-hardening at the same time. Sinking-in is observed for strain-hardening and non-strain-hardening materials with a low E/σ_y. Howell et al. (2008) have observed pile-up even in the widely used reference glass 'fused silica' (SiO_2).

For the indentation of crystals, the topography of the free surface around the indent, the pile-up profile, can be used as a finger print of the underlying crystal deformation processes. In the 1920s, Tammann and Müller (1926) have reviewed the characteristic patterns evolving around indents made with gramophone, sewing needles and quartz or steel tips. They focused on indentation into high-symmetry planes of copper, α-iron, and γ-iron, as well as the basal plane of zinc. The experimental findings on iron were taken from the pioneering work of Osmond and Cartaud (1905, 1906). Already Osmond and Cartaud observed that the deformation patterns around a conical indent in single crystals is characteristic of the structure of the indented crystal, as well as for the orientation of the indented plane.

The formation of pile-up patterns in single-crystals does not depend heavily on the scale of the indentation. Pile-up patterns have been observed in macroscopic indentations as well as on the level of nanoindentation. Carrasco et al. (2003) reported on four-fold hillock patterns around Au (001) indents of only around 30 nm in diameter, surface steps from individual dislocation half-loops are visible in the same figure. The characteristic features of the pile-up are maintained throughout the scales. However, the formation of slip lines might interfere with and affect the formation of pile-up on the small length scales.

While the Tabor relation (5.2), mentioned above, did not prove expandable to the single-crystal regime (Tabor, 1970, Gerk, 1977), another principle that Tabor described in his monograph, did. After Tabor (1951), *piling-up* occurs during indentation of highly-worked materials and *sinking-in* for indentation of annealed materials. Both effects are illustrated in figure 5.5. Tabor's idea was defined under tacit assumption of indentation into polycrystalline material. But later it was confirmed, for example, by Alcalá et al. (2000) for indentations into work-hardened (pile-up) and annealed (sink-in) copper polycrystals with grain-sizes not much smaller than the size of the indents. It was further confirmed for single-crystalline copper by McElhaney et al. (1998), who reported piling-up after Berkovich indentation into coarse grained, work-hardened copper with grain size much larger than the indentation. And for indentation into annealed, (1 1 1)-oriented copper they have observed sinking-in behavior.

The early results on impression shapes in single crystals are more of phenomenological nature since the surface topographical measurement techniques, in the precision needed for the characterization of the remaining indents, were either not developed or not available to the researchers. The pile-up patterns were mainly observed by light microscopy through the pronounced generation of glide steps. The glide steps roughly follow the direction of topological contour lines on the hillocks. More recently, the atomic force microscopy (AFM) technique enabled precise characterization of pile-up topographies and facilitated the study of deformation mechanisms during indentation Smith et al. (2003), Biener et al. (2007).

The anisotropic pile-up profiles in single crystals are caused by the plastic – not the elastic – anisotropy and Stelmashenko et al. (1993) have proved this by indenting tungsten crystals. Tungsten exhibits a virtually isotropic elastic behavior. The upheaval around the Vickers indents was observed to be anisotropic and clearly related to the crystallographic directions of slip. Further, Stelmashenko et al. (1993) showed that similar pile-up develops for [0 0 1] indentation even for a rotation of the used Vickers indenter by an angle of 45°.

Hollatz et al. (1996) indented NiAl coated with a thin Al_2O_3 film. While their interest mainly was on the film properties, the observed crack patterns of the thin film could also be interpreted as phenomenological strain gauges for the near-surface plasticity of the substrate. Cracks indicate tensile deformation of the substrate in perpendicular direction to the crack extension.

Nibur and Bahr (2003) and Nibur et al. (2007) analyzed the slip steps around indentations in nickel, based on AFM and EBSD measurements.

Pronounced pile-up formation can change the projected contact area between indenter and sample significantly. McElhaney et al. (1998) corrected for the pile-up by assuming constant compliance and additionally by imaging remaining indents in the SEM. Lee et al. (2008) showed how the real contact area can be measured by AFM topographical analysis. The contact boundary is taken as the border between the flat and the rough areas of the remaining impression. This border is found by differentiating the height profile in radial direction from the indent center. They investigated the case of Berkovich indentation in a tungsten (0 0 1) surface. The projected contact area was changed significantly by pile-up formation and leading to a 40 % over-estimation of the hardness when a standard Oliver-Pharr tip calibration was applied.

It is interesting to note that the hardness calculation from the remaining indent topography takes the method back to the common procedure of most standardized hardness testing methods where the hardness is calculated from the unloaded state. However, for metals the differences should be small and the main reason for the large deviation in the hardness values as reported by Lee et al. (2008) is the neglection of the influence of pile-up through usage of the Oliver-Pharr fit for the area function.

The shape and amount of anisotropic indentation pile-up in crystalline materials is depending on the indented orientation. The pile-up profile for indentations in high-symmetry orientation of copper single crystals was simulated by Wang et al. (2004), figure 5.6. The identical problem has been investigated by Liu et al. (2008). Other problems such as lattice rotations (Zaafarani et al., 2008) or the amount of stored plastic deformation energy after indentation (Zambaldi et al., 2007) have been successfully investigated by application of the crystal plasticity finite element method.

5.3.3 Incipient plasticity during single crystal indentation

Recent detailed studies of nanoindentation were mainly focused on incipient stages of plasticity. An example of this branch of literature is the work by (Carrasco et al., 2003, 2008), who showed, how the movement of individual dislocation half-loops can be observed around very small indentations made with a tungsten scanning tunneling microscope (STM) tip on a gold (0 0 1) surface.

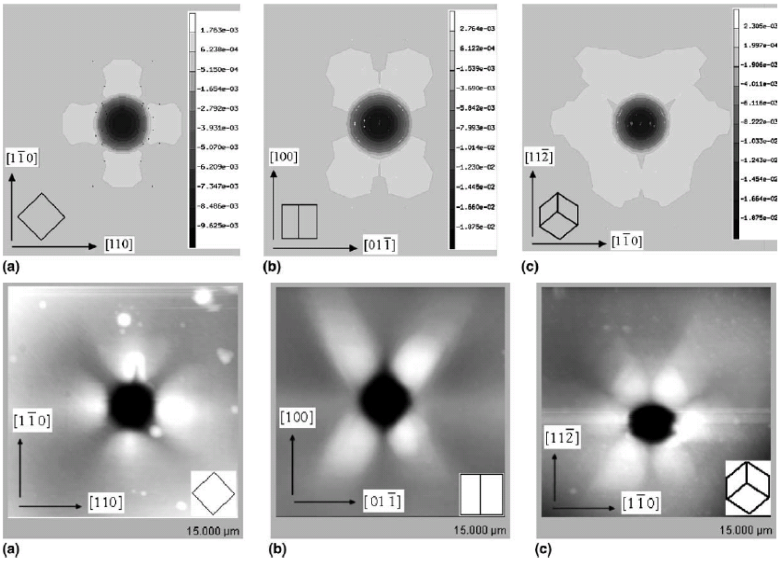

Fig. 5.6: Simulated (top) and measured (bottom) pile-up topographies reported by Wang et al. (2004) on copper single crystals;

Mason et al. (2006) performed a statistical evaluation of the discontinuous strain burst events, the 'pop-in', observed in nanoindentation of pristine metal surfaces, to provide information on the thermal activation of dislocation nucleation. A nanoindenter equipped with a heating stage was used in this study on platinum.

In the context of dislocation nucleation, mechanical modeling is often carried out using molecular statics or molecular dynamics simulation (Van Vliet et al., 2003, Eidel and Stukowski, 2009). The orientation dependence of dislocation nucleation in copper was investigated in Liu et al. (2008). The work directed at the very early stages of plastic deformation is of high importance from the viewpoint of fundamental research. It should be mentioned, however, that the applied simulation methods still suffer from limitations in computational resources, as they require extremely small time steps and are therefore mostly carried out at very high strain rates.

5.4 Continuum simulation of indentation

Finite element modeling of the indentation process has played an important role from the early years of development of the indentation technique (Bhattacharya and Nix, 1988, Hill et al., 1989, Laursen and Simo, 1992, Giannakopoulos et al., 1994, Biwa and Storåkers, 1995, Larsson et al., 1996, Bolshakov and Pharr, 1998, Knapp et al., 1999, Mesarovic and Fleck, 1999, Dao et al., 2001, Durst et al., 2002, Nowak et al., 2003, Cheng and Cheng, 2004, Deng et al., 2004, Shim et al., 2005, Larsson, 2006, Antunes et al., 2007, Chudoba and Jennett, 2008). However, the modeling strategies have evolved significantly over time. In the earlier works often two-dimensional models under tacit assumption of a plain strain wedge indentation or axisymmetric element formulations were used. Both are computationally efficient but limited to isotropic material laws.

As the used constitutive laws evolved from isotropic, elastic-perfectly plastic behavior to the most recent implementations of large-strain three-dimensional formulations in crystal plasticity, also the finite element models had to change to fully 3D models. These crystal plasticity finite element models are able to take into account the elastic and plastic anisotropy in metals and have been applied successfully for various crystal structures and indenter shapes (Wang et al., 2004, Liu et al., 2005, Bouvier and Needleman, 2006, Kearney et al., 2006, Zaafarani et al., 2006, Zambaldi et al., 2007, Casals et al., 2007, Alcala et al., 2008, Zaafarani et al., 2008, Liu et al., 2008, Casals and Forest, 2009, Gerday et al., 2009, Beom and Zikry, 2009, Britton et al., 2010).

5.5 Nanoindentation studies on Ti-Al

The nanoindentation response of γ-TiAl has been investigated by Göken and coworkers (Göken et al., 2001, Kempf et al., 2002, Gebhard et al., 2009). Maximum loads of 1, 2 and 3 mN were used and, depending on the orientation, different pile-up characteristics were observed. Two, three or four hillocks formed around the indents and also the shape of the remaining impression (square or elliptical) depends on the crystallographic direction that was indented and on the load applied. The pile-up behavior was found to be characteristic of the indented orientation: Indents in identically oriented crystals exhibited similar pile-up behavior even at different maximum loads.

Göken et al. (2001) investigated γ- and α_2-phase in lamellar PST-crystals (pg. 34) with a maximum indentation force of 1 mN. The same tip was used for topographic characterization and indentation. Kempf et al. (2002) observed the pile-up to be more pronounced in indentation by cube-corner and conical indentaters, than in Berkovich-indentations. Some hardness values for titanium aluminides from the literature are given in table 5.2.

Tab. 5.2: Hardness testing results for titanium aluminides; indenter geometries are Berkovich (B), cube-corner (CC), sphero-conical (SC), Vickers (V). In Gebhard et al. (2009) two different alloys were investigated.

Phase	Indenter geometry	P_{max}	Hardness (GPa)	Reference
γ-TiAl	B	1 mN	5.2	Göken et al. (2001)
γ-TiAl	CC	1 mN	6.8	Göken et al. (2001)
γ-TiAl	SC/CC/B	0.8–1 mN	5.2–6.8	Kempf et al. (2002)
γ-TiAl	V	4.9 N	3.4	Zhao et al. (2003)
α_2-Ti_3Al	V	4.9 N	3.8	Zhao et al. (2003)
γ-TiAl	B	1.5 mN	4.4–6.0[a], 4.4–5.5[b]	Gebhard et al. (2009)
α_2-Ti_3Al	B	1.5 mN	7.6–9.5[a], 6.8–8.0[b]	Gebhard et al. (2009)

[a] Ti-45Al-4.6Nb-0.2B-0.2C (at.%), various microstructures
[b] Ti-45Al-1Cr (at.%), lamellar microstructures

Zhao et al. (2003) performed indentations in PST material with a diamond cube corner tip. The indentation size effect in γ-TiAl was found to be the lowest when compared to the following materials: Ag > Ni > Al > Cu > α_2-Ti_3Al > γ-TiAl. The internal length after Nix and Gao (1998) is therefore much smaller in the two TiAl phases than in the pure metals with fcc structure. However, the use of two different indenter geometries, a cube corner tip for γ-TiAl and α_2-Ti_3Al and a Berkovich tip for the other materials, makes the direct comparison of the measured data problematic. The results from above are plotted together with the indentation results from this work in figure 8.3.

Part II

Microstructural and mechanical characterization, and crystal plasticity modeling of γ-TiAl and γ-TiAl based alloys

Introduction to the results of this thesis

For convenience of the reader a concise overview of the results that will be laid out in the following chapters is given here:

- Chapter 6 presents an improved EBSD technique for crystal orientation mapping of the γ-TiAl-phase in the scanning electron microscope. The method makes possible the reliable automatic indexing of γ-TiAl order domains which, due to their cubic pseudo-symmetry, previously had to be identified manually in the SEM or even in the TEM.
- Chapter 7 describes the elasto-viscoplastic crystal plasticity formulation that will be used in the following chapters to model the micromechanical response of γ-TiAl based alloys. The necessary modifications of the model for the implementation of the γ-TiAl specific deformation behavior are explained and the modified model is validated through CPFEM simulations of simple loading cases.
- In chapter 8, the new EBSD method is employed to study the orientation dependent response of γ-TiAl during nanoindentation experimentally. A theoretical framework is introduced for a detailed study of orientation dependent piling-up during single crystal indentation. The framework is used to compare experimental and computational results on the orientation dependent indentation pile-up of γ-TiAl. Thereby the easy activation of $^1/_2$[1 1 0]{1 1 1} dislocation glide could be verified independently form the study of dislocations in the TEM. The most important advantage of the developed combination of nanoindentation experiments with CPFEM simulation is that it is based only on data that can be quantified with high accuracy in the experiments.
- In chapter 9, a CPFEM model is developed that realistically describes the plastic deformation of two-phase γ/α_2 microstructures through the choice of a subset of relevant deformation systems. This model is validated on the length-scale of single lamellar grains, i. e. a PST-crystal. It is then used to simulate two types of two-phase microstructures with different geometrical arrangement of the phases. Thereby, important mechanical properties such as initial yielding and ductility of the two types of microstructures are explained quantitatively through the model.

6

EBSD characterization of γ-TiAl order domains

6.1 Introduction and motivation

In this chapter a novel technique in electron backscatter diffraction (EBSD) based orientation microscopy is described. It makes possible the discrimination of γ-TiAl order domains with good accuracy. The development of this method was a cruical step towards the combined work on nanoindentation characterization and simulation presented in chapter 8.

The domain structure was described in section 2.7. Although the lattice parameters of γ-TiAl almost correspond to a cubic lattice, the orientation of the tetragonal axis of the lattice has important consequences, particularly for the deformation behavior because the *c*-component deformation systems can be very different in properties from the deformation systems containing no *c*-component, chapter 3. In order to better understand not only the mechanical behavior, but also the various solid state phase transformation routes of the material, characterization techniques are required which are able to reliably reveal the type and spatial arrangement of the orientational variants. Improved knowledge on the domain structure will promote the understanding for the microstructure properties relation of titanium aluminides. The densities of different types of interfaces are the dominant variables in the application of multi-scale mechanical analysis of Hall-Petch type such as Dimiduk et al. (1998) and Maruyama et al. (2002), see section 3.6.2.

Additionally, as turbine manufacturers are starting to use TiAl based alloys for high-temperature structural components, a need emerges for precise and efficient characterization of the microstructure. Coarsening and degradation processes can change the domain microstructure during service of turbine parts. This phenomenon is investigated for example in Yamamoto and Takeyama (2005).

6.2 Discrimination of γ-TiAl order variants by superlattice reflections

The ordering variants of γ-TiAl (section 2.7) exhibit very similar diffraction patterns. Their discrimination by x-ray or electron diffraction techniques can be based on either the detection of the slight tetragonal distortion of the lattice cell. Or the atomic stacking

order is analyzed by the detection of superlattice reflections. The detection of the tetragonal distortion will be discussed in the main part of this chapter. The origin of superlattice reflections is shortly described in the following.

Superlattice reflections are those reflections in a diffraction pattern that are kinematically extinct in a disordered (or monoatomic) base lattice but arise when this lattice adopts an ordered structure. In the present case the disordered base lattice is an fcc lattice in which the {1 1 0} reflections, for example, are extinct due to the kinematical extinction rules. In the tetragonal $L1_0$ structure, in contrast, the {1 1 0} reflections appear as superlattice reflections, while the{1 0 1} reflections continue to be extinct (note, that in the tetragonal structure{1 1 0} and{1 0 1} are not equivalent).

In general, for a fcc crystal of disordered structure or consisting only of a single atomic species the condition for systematic absence of diffraction intensity is that h, k, l are not all odd or not all even. For the $L1_0$ structure the systematic extinction is not complete in some of these cases because of the ordered arrangement of Ti and Al which possess different scattering amplitude. Under the condition that the sum of h and k is even and h, k, l are not all even or not all odd, superlattice diffractions can be observed (Dey et al., 2006b). From the reflectors that fulfill this condition {0 0 1} and {1 1 0} have the largest intensities in electron diffraction patterns.

The determination of the domain microstructure in TiAl for long time has been carried out by transmission electron microscopy (TEM). Here the superlattice reflections are easily recognized and can be used to determine the orientation of the c-axis of a given area in the microstructure. TEM selected area diffraction patterns have been used by Inui et al. (1992b) to investigate the domain microstructure in lamellar Ti-49.3Al (at.%). Zaefferer (2000, 2002), for example, and Dey et al. (2006a) used transmission Kikuchi diffraction patterns (TKP) to determine the crystal orientation of order domains. Unfortunately, the TEM techniques suffer from the known limitations like small observable sample volume, complicated sample preparation and difficult practice of measurement.

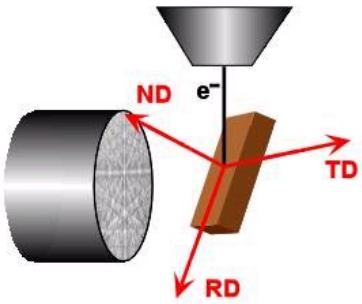

Fig. 6.1: The tilted sample setup inside the scanning electron microscope for an EBSD measurement; Also shown is the used convention for the reference sample axes (courtesy EDAX/TSL OIM);

An electron diffraction based technique which overcomes these limitations is electron backscatter diffraction (EBSD) applied in the scanning electron microscope (SEM), see figure figure 6.1. Instead of working in transmission on a thin foil, the technique is

used to investigate the surface of bulk samples. The electron diffraction information is created in a thin layer on the surface of the material. EBSD patterns can be evaluated in the same way as TKP. However, while TKP show only a solid angle of reciprocal space of about 20°, EBSD patterns span under usual conditions about 70° to 100° which allows a very wide overview of the crystal symmetry of the investigated area.

The combination of automated acquisition and analysis of EBSD patterns with scanning of the electron beam across the sample surface, results in the orientation microscopy technique: from the orientation measured at every point of the scan grid the microstructure can be reconstructed and displayed in great detail. This very powerful microscopy tool allows the quantitative crystallographic description of large sample areas with a resolution down to approximately 50 nm.

6.3 Limitations of conventional EBSD analysis of γ-TiAl

When analyzing EBSD patterns of γ-TiAl, two difficulties arise: first, the large solid angle of the patterns usually precludes the observation of fine details within the patterns, for example the occurrence of superlattice reflections. As part of the automated orientation determination process, the bands within the EBSD pattern need to be detected. This is typically done using an image processing technique termed a Hough transform (this technique is detailed in section 6.4.2). The Hough transform is very efficient for determining the location of bands in the patterns; however, fine line details are veiled by the Hough transform and therefore the superlattice reflections cannot be easily detected automatically. Second, the $^c/_a$ ratio of γ-TiAl is so close to unity that the EBSD patterns of γ-TiAl exhibit a pseudo-cubic symmetry and the position of the *c*-axis cannot be unambiguously determined with standard algorithms. For these reasons EBSD-based orientation microscopy has, up to now, not been applied successfully to distinguish all six orientation variants of γ-TiAl microstructures.

Cubic pseudo-symmetry is also observed for other materials than γ-TiAl. EBSD optimization has been performed for materials such as chalcopyrite type semiconductors with $c/2a \approx 1$ (Baba-Kishi, 2002, Abou-Ras et al., 2008) and ceramic superconductors with $c/3a \approx 1$ (Grossin et al., 2006).

Previous studies that applied the EBSD technique to γ-TiAl, often used a cubic crystal symmetry for indexing, which can only discriminate between the twin and matrix family of variants, but not between the order variants. To resolve the tetragonal orientation, these authors additionally employed either selected area channelling pattern (SACP) to identify the order variants Simkin et al. (2003) or combined the EBSD results with a semi-automated TEM identification of the ordering domains Dey et al. (2006a). Pouchou et al. (2004) increased the distance between the sample and the EBSD-detector to make visible the superlattice diffractions.

Recently, Huang et al. (2007a), reported to be able to distinguish the *c* and *a*-axis directions, but the focus of their work laid on massively transformed γ-phase. Massive γ-phase is known to have a $^c/_a$ ratio much closer to unity than the equilibrium phase (Bartels et al., 2005).Therefore the large scatter in some of their orientation maps is not surprising. Additionally, Nave and Inoue (2007) presented results which suggest

Tab. 6.1: Reflectors with a relative reflection intensity of greater than 5 % of the intensity of {1 1 1}; Intensities as calculated with TOCA (Zaefferer, 2000) for Ti-50Al (at.%); Tetragonal lattice distortion as expressed by the angular deviation of pseudo-symmetric diffraction vectors; The short notation (c_x, c_y, c_z) means the c-axis of the tetragonal structure is either aligned with the x, y or z-axis. The values for $^c/_a$ ratios of 1.015 and 1.02 are shown in the columns with labels 1.5 % and 2.0 % respectively. Superlattice reflectors are marked with an asterisk. The sensitivity of angular deviation against $^c/_a$ ratio is shown in the two right-most columns; the absolute values in the four columns in the center can be calculated as: sensitivity×[($^c/_a$) − 1], where $^c/_a$ is 1.015 or 1.020 respectively.

hkl	Intensity	(c_z, c_x)[°]		(c_z, c_y) [°]		$^c/_a$ sensitivity [°]	
		1.5%	2.0%	1.5%	2.0%	(c_z,c_x)	(c_z,c_y)
111	1.000	0.69	0.92	0.69	0.92	45.71	45.71
002	0.748	0.0	0.0	0.0	0.0	0.0	0.0
200	0.715	0.0	0.0	0.0	0.0	0.0	0.0
202	0.322	0.85	1.13	0.43	0.57	56.30	28.15
220	0.315	0.43	0.57	0.43	0.57	28.15	28.15
113	0.219	0.53	0.70	0.53	0.70	34.74	34.74
311	0.211	0.53	0.70	0.36	0.48	34.74	23.67
222	0.191	0.69	0.92	0.69	0.92	45.71	45.71
004	0.134	0.0	0.0	0.0	0.0	0.0	0.0
400	0.127	0.0	0.0	0.0	0.0	0.0	0.0
313	0.102	0.83	1.10	0.50	0.67	54.75	33.13
001*	0.102	0.0	0.0	0.0	0.0	0.0	0.0
331	0.100	0.50	0.67	0.50	0.67	33.13	33.13
204	0.097	0.68	0.91	0.34	0.46	45.05	22.76
402	0.093	0.68	0.91	0.34	0.45	45.05	22.29
420	0.092	0.34	0.46	0.34	0.45	22.76	22.29
224	0.073	0.65	0.87	0.65	0.87	42.93	42.93
422	0.071	0.65	0.87	0.49	0.65	42.93	32.13
110*	0.063	0.43	0.57	0.43	0.57	28.15	28.15
115	0.062	0.36	0.47	0.36	0.47	23.47	23.47
333	0.060	0.69	0.92	0.69	0.92	45.71	45.71
511	0.059	0.36	0.47	0.23	0.31	23.47	15.08

Tab. 6.2: The first five solutions for indexing a γ-TiAl backscattered Kikuchi pattern in the vote rank algorithm as implemented in OIM-DC. By applying the fit-ranking to the first three solutions, the (correct) solution number three will be assigned the first rank. The correct solution is marked with an asterisk;

No.	Orientation solution $(\varphi_1, \Phi, \varphi_2)$	Votes	Fit
1	(221.6°, 108.0°, 270.7°)	632	0.69°
2	(38.6°, 162.4°, 177.3°)	622	0.70°
3*	(131.1°, 90.3°, 72.2°)	582	0.60°
4	(80.3°, 33.5°, 280.7°)	77	1.91°
5	(273.0°, 57.6°, 352.8°)	70	1.98°

Tab. 6.3: The first five indexing solutions for the two patterns shown in figure 6.4, each pattern was calibrated for individually, 12 Hough peaks were taken into account, interplanar angle tolerance 3°;

	Pattern from figure 6.4-b		Pattern, figure 6.4-c	
Solution	Votes	Fit [°]	Votes	Fit [°]
1.	220	0.26	220	0.25
2.	210	0.54	200	0.65
3.	182	0.51	189	0.65
4.	14	1.92	12	1.90
5.	14	2.02	12	2.01

that the tetragonal lattice can actually be resolved by EBSD. However, they did not systematically validate their results.

These previous efforts illustrate the considerable demand for a fully automatic acquisition of crystal orientation maps with fully identified order domains. In the following a new algorithm, based on ideas of Zaefferer (2009), is introduced which allows a reliable and automated determination of the correct tetragonal orientation of γ-TiAl crystals using EBSD-based orientation mapping. A careful procedure for validation of the algorithm is described. An order domain-resolved crystal orientation map, acquired in a fully automatic manner, is presented.

6.4 Enhanced accuracy EBSD pattern analysis

The basic principle of the new approach for discrimination of γ-TiAl order variants is the determination of the tetragonal distortion of the diffraction pattern. Three points had to be considered: first, the projection center of the pattern (often simply called the 'pattern center') needed to be known precisely, second the positions of the Kikuchi bands needed to be accurately determined and finally, an algorithm needed to be employed which determined the correct indexing for these bands.

6.4.1 Pattern center calibration

The projection center of the pattern is that point on the sample surface where the electron beam impinges, measured in detector coordinates. It is most easily calibrated using a crystal of known structure and lattice constants. In this work a silicon single crystal was used. The pattern center could then be determined by the standard procedure available in the software OIM Data Collection (OIM-DC). The pattern center x, y and z coordinates were varied and the position for which the lowest fit value was achieved, were used as the calibration setting. The fit is defined as the average angular deviation between the bands as detected by the computer and the location of the bands simulated from the measured orientation (see Nowell and Wright (2004)).

Alternatively, the pattern center was determined using a simple optimization procedure newly implemented in the software TOCA (Zaefferer, 2002): First a sharp diffraction pattern was acquired in OIM-DC. The positions of the Kikuchi band were detected manually, which eliminates inaccuracies related to the Hough transform. The bands were then indexed using an initial guess for the pattern center. Afterwards the x, y and z coordinates of the pattern center were systematically varied and each time the pattern was indexed and a fit value determined. The latter was calculated as the average angular deviation between the input diffraction vectors (determined from the position of the Kikuchi bands in the pattern) and the corresponding recalculated diffraction vectors after indexing and orientation determination (Zaefferer, 2002). The pattern center coordinates which result in the smallest fit value were selected and the procedure was carried out again with smaller variations, until no further decrease in fit value occurred. This procedure did not require any assumptions about the orientation of the crystal nor did the first guess of the pattern center have to be good enough to obtain a correct indexing in the first step.

Both calibration methods lead to very similar results for the pattern center, usually within an error of less than 0.2 % of the pattern dimensions. Figure 6.2 illustrates how

critical the correct pattern centre calibration is for the determination of the correct indexing of γ-TiAl variants: for this illustration the distance of the pattern centre from the detector (z coordinate) was fixed to the previously determined optimum value. The figures display the dependence of the fit value from the (x, y) position of the pattern centre. Each figure shows one of the three possible orientations of the c-axis. Solution number one corresponds to the correct orientation. It is visible that this solution exhibits the lowest minimum value throughout a systematic variation of the pattern centre. The other two pseudo-symmetric orientations show similar behavior, with a distinct minimum at certain (x, y) positions of the pattern centre. However the observed minimum fit values are always larger than those for the correct solution. The figure illustrates the necessity of careful pattern centre calibration, as the minima of the correct solution (0.33°) and the pseudo-symmetric ones (0.53° and 0.66°) are very close to each other.

For the measurement of large orientation maps it is important to account for the variation of pattern center due to the scanning movement of the electron beam. This change of pattern center needs to be calibrated and corrected during the scan. For the present investigations the pattern center shift correction algorithm built into OIM-DC was used.

6.4.2 Accurate Kikuchi band detection

The algorithm presented here, solely relies on the accurate detection of the angles between the diffraction vectors. Therefore, in order to obtain an impression on how accurate the detection has to be, it was useful to analyze the angular relations between the reflectors used for indexing. The angles between reflectors *hkl* are listed in table 6.1. Values are given for the angular deviation between the tetragonal and the two pseudo-symmetric tetragonal structures for c/a ratios of 1.015 and 1.02.

It turns out that in order to find the correct solution from the three possible order variants, the diffraction vectors have to be determined with an accuracy of less than one degree. Within the reflectors included in table 6.1, the {2 0 2} reflectors exhibit the maximum sensitivity measured as angles between the diffraction vectors. They deviate by 1.13° (0.85°) for a c/a ratio of 1.02 (1.015). The minimum non-zero sensitivity is observed for the {5 1 1} and {1 1 5} bands which have an angular distance of 0.47° (for c/a=1.02) and 0.36° (for c/a=1.015).

The Hough transform is the standard method for identifying the Kikuchi bands in an EBSD pattern, first applied by Krieger-Lassen et al. (1992). It identifies every straight line by two parameters: the polar coordinates, ρ and θ, where ρ is the distance of the line from the center of the screen and θ is the angle of the normal vector to the band measured with respect to the horizontal axis of the screen. By summation of the intensities of all pixels along straight lines in a Kikuchi diffraction pattern and displaying this value in the parameter space (ρ, θ) (the 'Hough space') one obtains an image where each bright Kikuchi band is represented as a spot of high intensity, figure 6.3. Since these so-called Hough peaks are created from discrete pixels in a digital image they are not sharp and well-confined spots but blurred maxima of a typical shape. The detection of the position of these features occurs by convolution of the Hough image with a particular convolution mask whose size and intensity distribution

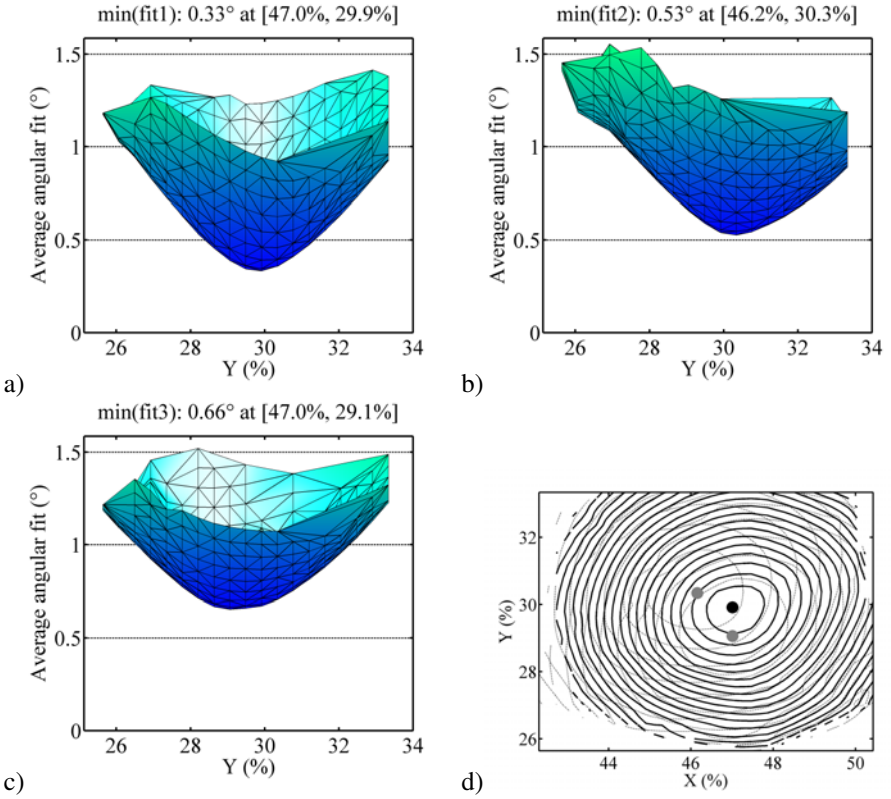

Fig. 6.2: Sensitivity of the fit measure against variation of the pattern center coordinates in the projection plane (*x*- and *y*-coordinates). The surface of fit values is shown for the correct indexing solution (a), and the two pseudo-symmetric solutions (b,c); d) contour levels for the possible solutions in steps of 0.1° for the pseudo-symmetric solutions (gray) and 0.05° for the correct solution (black). During the variation of x and y the z-coordinate of the pattern center was kept constant at its previously determined optimum position.

fits well to the shape of typical Hough peaks. Whenever the mask fits to the intensity distribution a maximum is created in the convoluted Hough space.

The accuracy of band detection via Hough transform is determined mainly by three parameters, the resolutions of ρ and θ, given by $\Delta\rho$ and $\Delta\theta$, and the size of the convolution mask, m, where m is equal to the number of rows and columns of the mask. In OIM-DC the resolution of ρ is determined through the number of pixels across the detector, ρ_{max}. From this the angular pixel resolution is calculated as $\Delta\rho \approx 2\ \mathrm{atan}(r_{detector}/z_{detector})/\rho_{max}$, where $r_{detector}$ and $z_{detector}$ are the radius of the detector and the distance between the pattern center on the sample and the detector. Note, that the pixel resolution changes across the screen, and is getting better with increasing distance of a pixel from the center. The equation gives the optimal resolution value found on the rim of the detector.

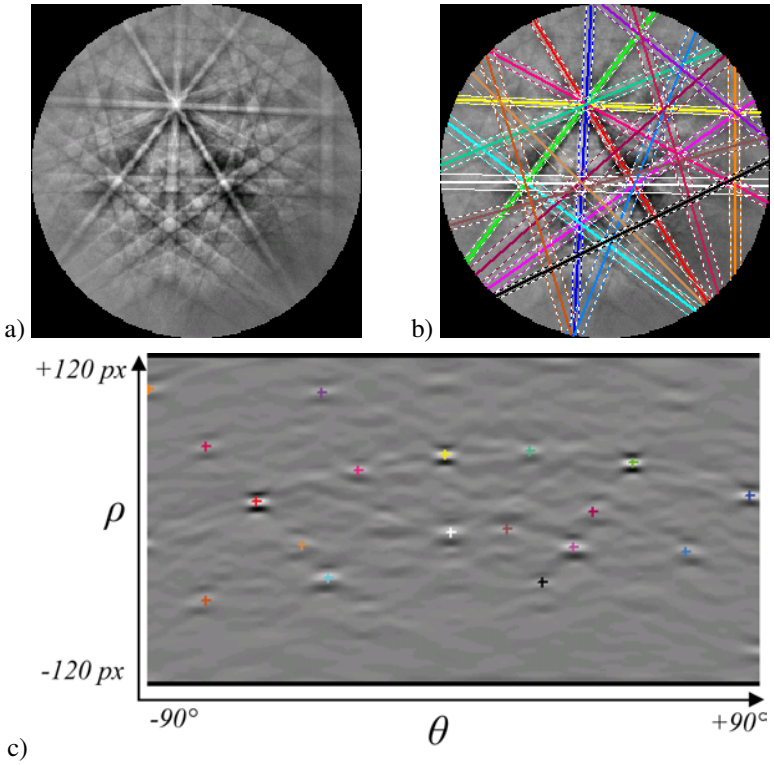

Fig. 6.3: a) EBSD pattern of binary TiAl; b) bands as detected by the hough transform; c) the hough space with some peaks identifying the position of the bands; pattern binned down to ρ_{max}=240 px; θ-resolution: 0.5°; 13×13 convolution mask

The following values were used: ρ_{max}= 240 pixel, resulting in an angular pixel resolution of $\Delta\rho$= 0.375°, $\Delta\theta$= 0.5° and m = 13 pixels. The value of m was selected in order to allow accurate convolution for an average Kikuchi band width at the selected detector width. A comparison of the resolution values with the required accuracy values shows that the resolution obtained with the applied Hough transform parameters is just enough to detect the tetragonal crystal orientation.

Note here, that in TiAl the $^{c}/_{a}$ ratio depends on the local chemical composition (Kobayashi et al., 1995, Kawabata et al., 1998) and the degree of ordering (Bartels et al., 2005). Additionally, common alloying elements such as niobium show strong segregation behavior (Hecht et al., 2009). These dependences can modify the required angular accuracy.

6.4.3 Accurate and robust indexing and the fit-rank indexing method

From the determined Hough peaks the positions of the respective diffraction vectors are calculated. Next, indexing of these diffraction vectors is performed. In OIM-DC this is accomplished by selection of triplets of non-coplanar diffraction vectors. These are assigned Miller indices until their inter-vectorial angles match those precalculated for the crystal structure under consideration. From the indexed diffraction vector triplets the crystal orientation is easily calculated. The procedure for indexing and orientation calculation from triplets of diffraction vectors results in a number of different orientations which are subsequently sorted and counted. The orientation with the highest number of occurrences, the 'votes', is selected to be the correct one (Wright and Adams, 1992). This algorithm has been proven to be efficient and reliable for indexing EBSD patterns.

In materials with pseudo-symmetry, however, this scheme results in very similar vote numbers for the pseudo-symmetric orientation variants, see table 6.2. Depending on the chosen set of reflectors, the indexing tolerances and the Kikuchi pattern under consideration, the standard procedure can result in an incorrect ranking of the solutions. In order to improve this behavior, a novel fit-rank method has been implemented in the OIM-DC software. It is characterized by a post-processing step on the vote-rank indexing result.

First the standard vote rank indexing as described above is applied. It identifies the three pseudo-symmetric candidate orientations as those three solutions that received the highest number of votes. For each of the candidates the angular deviation of the measured diffraction vector positions from those simulated for the determined orientation is calculated. The fit-rank method then simply consists in choosing from the three candidate solutions the one with the smallest fit value. The candidate orientation, for which the experimentally measured band positions match the recalculated ones with highest accuracy, will be selected.

6.5 Experimental details

From a sample of Ti-45.9Al-8Nb (at.%), grown in an optical floating zone furnace, a cylinder with a diameter of 5 mm and a height of 4 mm was cut by electric discharge machining. The crystal growth and cooling conditions (growth velocity 10 mm/h, 1 bar argon atmosphere, for further details see Souptel et al. (2007)) lead to the formation of a columnar microstructure with lamellar grains of about 500 µm grain size. After grinding to 1000 grit and a successive polishing with 3 µm diamond paste, electrolytic polishing was carried out to remove any remaining surface deformation. A solution of 6 % perchloric acid in ethanol was used as electrolyte. Polishing was carried out with a voltage of 35 V at a temperature of -30 °C.

A Schottky-type field-emission gun scanning electron microscope JEOL JSM 6500F was used for acquisition of electron backscatter diffraction (EBSD) data. The SEM

was operated at an acceleration voltage of 30 kV and the sample was tilted to 70° out of the horizontal position. The working distance was 15 mm. An EDAX/TSL EBSD acquisition system with a DigiView II camera was used for pattern recording. The recording phosphor screen had a diameter of 40 mm and was positioned at a distance of 19.1 mm from the pattern source. Diffraction patterns were recorded at a resolution of 936×936 pixels and an exposure time of 0.5 seconds. For acquisition and processing of the patterns the commercial software system OIM-DC was employed. For accurate line detection a high resolution Hough transform of 240 px×0.5 ° (resolution in ρ and θ) and a large convolution mask (13×13 px^2) were applied. Sixteen bands were used for the subsequent indexing. The interplanar angle tolerance of the vote indexing was set to a value of 3°. The following reflectors were included for indexing the patterns: {0 0 1}, {1 1 1}, {2 0 0}, {2 0 2}, {2 2 0}, {1 1 3}, {3 1 1}, {3 1 3}, {3 3 1}, {0 2 4}, {4 0 2}, {2 4 0}.

6.6 Results and discussion

6.6.1 Validation of the proposed fit-rank method

Before applying the fit-rank method the pattern center was accurately determined as described in section 6.4.1. Having determined the correct pattern center, the three possible solutions can be differentiated by their fit value. Table 6.2 shows the number of votes as well as the average angular fit value for the first five solutions obtained by a representative indexing run in OIM-DC. Clearly, the first three orientations have a significantly higher number of votes when compared to the following ones and are therefore the three candidate orientations. The proposed fit-rank procedure correctly promotes solution number three, which has the lowest number of votes, to the first position.

In order to validate the approach it is necessary to have an independent check for the correct orientation. This is given by the observation of the superlattice reflections. Exposure times on the order of one second were used to collect the EBSD patters. At these exposure times {1 1 0} superlattice reflections start to become visible inside {2 2 0} bands. The superlattice bands, being half as wide as the {2 2 0} bands, appear as faint internal structure of higher intensity. An example is given in figure 6.4: Here two EBSD patterns from two neighboring lamellae with different order variants are shown. In both patterns the positions of the {2 2 0} and {2 0 2} base reflections are marked by arrows. The {2 2 0} reflection which contains the {1 1 0} superlattice reflection is marked by a magenta arrow. The superlattice band could be recognized although the calculated kinematical intensity (table 6.11) of the superlattice band is only about 20 % of the intensity of the {2 2 0} bands in stoichiometric TiAl. In the present case, where 8 at.-% Nb are replacing Ti-sites the intensity of the superlattice reflections are actually higher: With increasing Nb content, the intensity of the superlattice reflection increases approximately proportional to the Nb content. If all Ti would be replaced by Nb, the theoretical intensity of the {1 1 0} bands would be 60 % of the intensity of the {2 2 0} bands.

Since the existence of the superlattice reflection may not be easily visible to the reader, figure 6.5 displays the integrated intensity profile of the {2 2 0}/{1 1 0} reflection and the

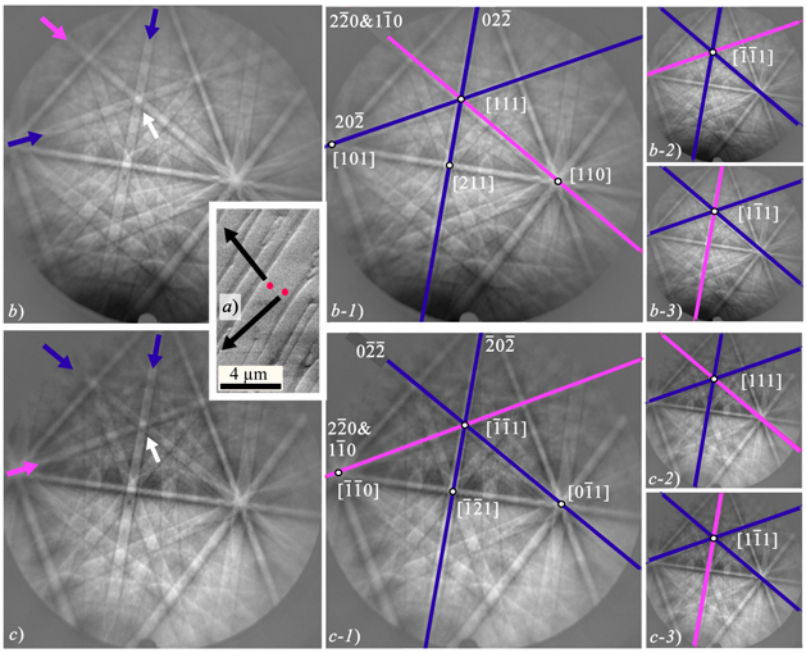

Fig. 6.4: Determination of the correct orientation of the tetragonal unit cell by means of superlattice reflections. a) The lamellar microstructure of the alloy. Two positions have been measured. b,c) Patterns of the two positions. The (1 1 1) pole, where the different {2 2 0} and {0 2 2} bands intersect, is marked. The {2 2 0} band which contains the superlattice reflections is marked in both patterns in magenta. The three possible indexing solutions for each of the two patterns are shown on the right hand side of the figure. The correct indexing solutions for each pattern (b-1, c-1) are shown in large. The existence of superlattice reflections is used to proof the correct orientation determination on the basis of the geometrical distortions.

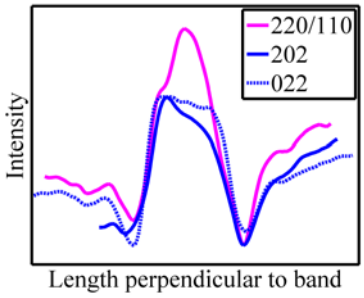

Fig. 6.5: Intensity profiles of the 220/110 reflections and the 202 and 022 reflections in the pattern shown in figure 6.4.

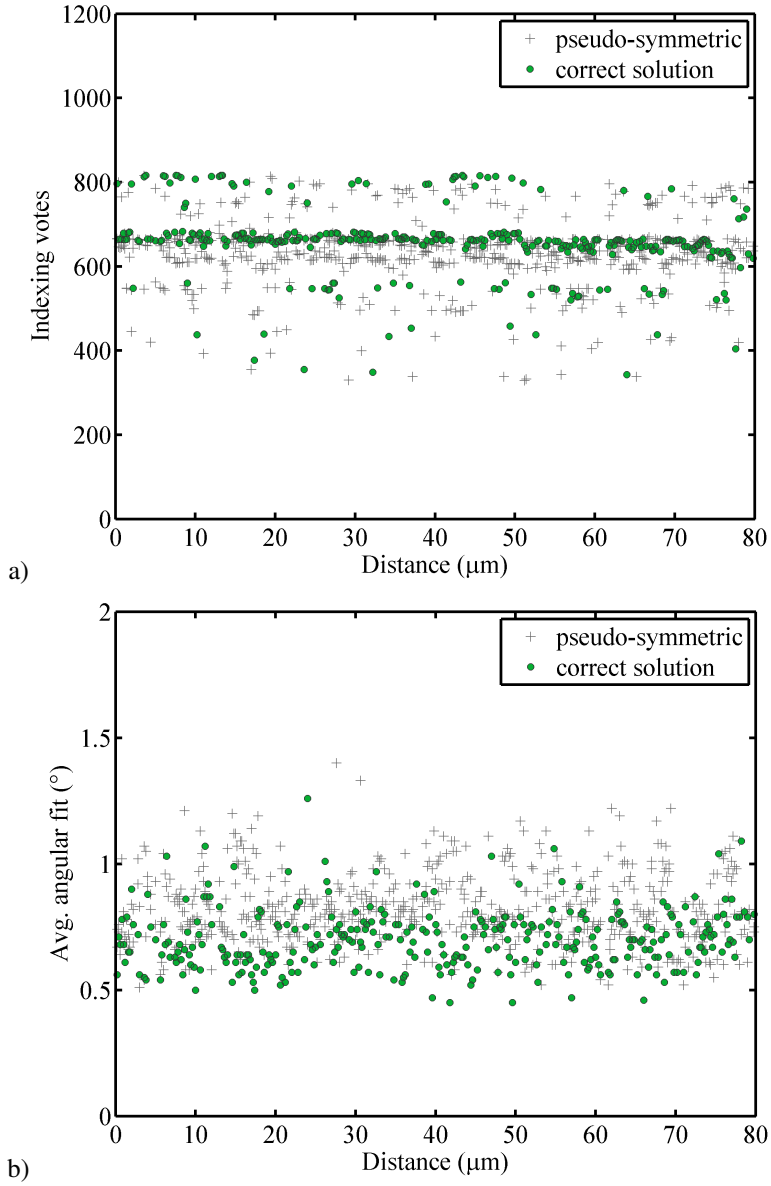

Fig. 6.6: a) Indexing votes and b) angular fit values for the recorded line data; the filled circles (green) mark the correct solution. Gray plus signs display the indexing quality measures for the pseudo-symmetric orientations.

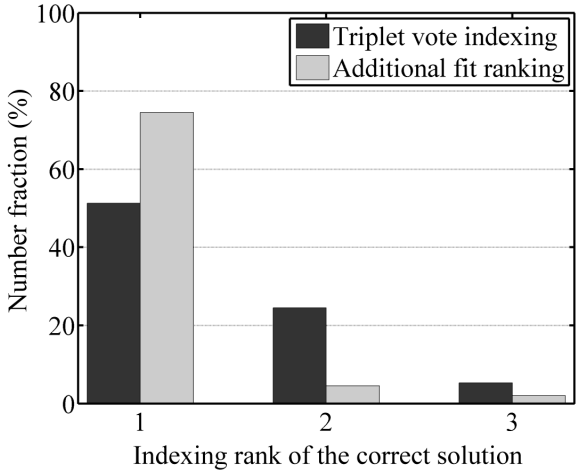

Fig. 6.7: The overall performance of the fit-rank method versus the pure vote indexing, applied to the validation data set.

{2 0 2} and {0 2 2} reflections along a part of their extension in figure 6.4-b. Although the structure of the superlattice reflection is not fully resolved, a distinct additional intensity contribution from {1 1 0} is obvious for the position inside the {2 2 0} reflection.

On the right hand side of figure 6.4 the three respective indexing solutions are shown overlaid on the diffraction pattern. The determined numbers of votes as well as the angular fit values are given in table 6.3. The first-ranked solutions with the highest number of votes and simultaneously the lowest fit value are the solutions with the correct position of the superlattice reflection. In this case the vote-rank indexing and the fit-rank indexing yield identical results.

For a more systematic validation, a line scan was carried out. It consisted of 400 patterns taken with a step size of 0.2 µm along a horizontal line through the center of the microstructure shown in figure 6.8. The patterns were collected with an exposure time of 1.2 seconds to be able to visually identify the {1 1 0} superlattice reflections. Figure 6.6 shows the results of the validation procedure. From 80 % of the recorded patterns the position of the {1 1 0} superlattice bands could be identified with confidence by visual inspection. The remaining 20 % were obtained from areas close to γ/γ or α_2/γ boundaries. These patterns showed overlapped patterns or poor contrast and the {1 1 0} band position could not be determined by the eye.

Figure 6.6-a illustrates the number of votes that were given to the correct solution as identified manually. Also the vote numbers given to the pseudo-symmetric solutions are shown. Ideally the correct solution would get the highest number of votes for each measurement. However, during automatic indexing, the conventional vote rank indexing identified only 50 % of the 400 patterns correctly. The distribution of fit values between the correct and the pseudo-symmetric solutions is displayed in figure 6.6-b. When the newly developed fit-based solution ranking was applied, the ratio of successfully identified orientations increased to about 75 %. Keeping in mind that only 80 % of all patterns could be identified correctly by the manual procedure this is an excellent

rate of correct indexing. Figure 6.7 compares the fraction of correctly indexed points and the fractions of misindexed patterns for the two methods.

Taking as a reference only those 80 % of the 400 patterns that could be unambiguously indexed in the manual procedure, the fraction of correctly indexed patterns rises to 94 % percent. This high ratio of correct indexing represents the upper limit in the case of excellent pattern quality. In conclusion, for an automatic mapping with applied fit-rank procedure, the fraction of correctly indexed patterns is expected to be in the range of 75 % to 94 % in comparison to an upper bound of 63 % for pure vote indexing.

6.6.2 Orientation mapping of the order domain structure

The developed fit-rank method was applied to a lamellar microstructure of Ti-45.9Al-8Nb (at.%). Figure 6.8 displays the results, measured at a step size of 0.2 µm on a hexagonal grid. The phase distribution map shown in figure 6.8-a illustrates the prevalence of γ phase in contrast to the thin lamellae consisting of α_2-Ti_3Al. Two percent of the measured points are assigned to the α_2-phase. This α_2-phase volume fraction is underestimated because of the limited resolution of the EBSD technique at high acceleration voltage: On the thin α_2 lamellae, patterns from the surrounding γ-phase frequently overlap with the α_2-pattern, thus leading to identification of γ phase. The minor curvature of the lamellar structure is an artefact due to specimen drift during the relatively long measurement time of about nine hours. The backscattered electron (BSE) image in figure 6.9 shows some thin α_2-lamellae not visible in figure 6.8-a as well as perfectly flat lamellar interfaces. Figure 6.8-b shows an orientation map for indexing with a generic fcc structure. Only the two twin-related variant families can be distinguished. One family of order domains comprises 62 % of the mapped points. The twin-related family, shown in blue, has an area fraction of 36 %. No obvious difference was found in the size distribution of the twin and matrix domain-triples.

Figure 6.8-c and 6.8-d show the orientation maps as obtained with a tetragonal structure (c/a = 1.02) by using the vote rank and the fit-rank indexing algorithm, respectively. The order domains are clearly resolved in both cases. However, map 6.8-c shows a higher amount of isolated points of differing orientation. These are due to the selection of the wrong order variant by the vote rank method. Map 6.8-d, which is calculated using the fit-rank method, gives a clear picture of the order domain structure. No post-processing step to clean up the data was applied. Very few isolated points - where the wrong order variant has been selected by the indexing software - remain in this map obtained with the fit-rank method.

A good indication of the correct detection of the order domain structure is given by the distribution of pattern quality. The position of order domain boundaries is indicated by a reduced sharpness of the Kikuchi bands which results from misfit stresses and defects along the boundaries and therefore lower values in the pattern quality maps. In figure 6.8-d the identified domain boundaries follow the lines of lower band contrast. They appear darker because the band contrast is overlaid in form of gray levels. In addition the order domain structure was compared to the backscattered electron image in figure 6.9. It shows the same region as the EBSD results. The α_2-phase appears bright. Different orientations of γ-TiAl can be discriminated by their gray-level contrast. The comparison showed very good agreement with the EBSD orientation maps.

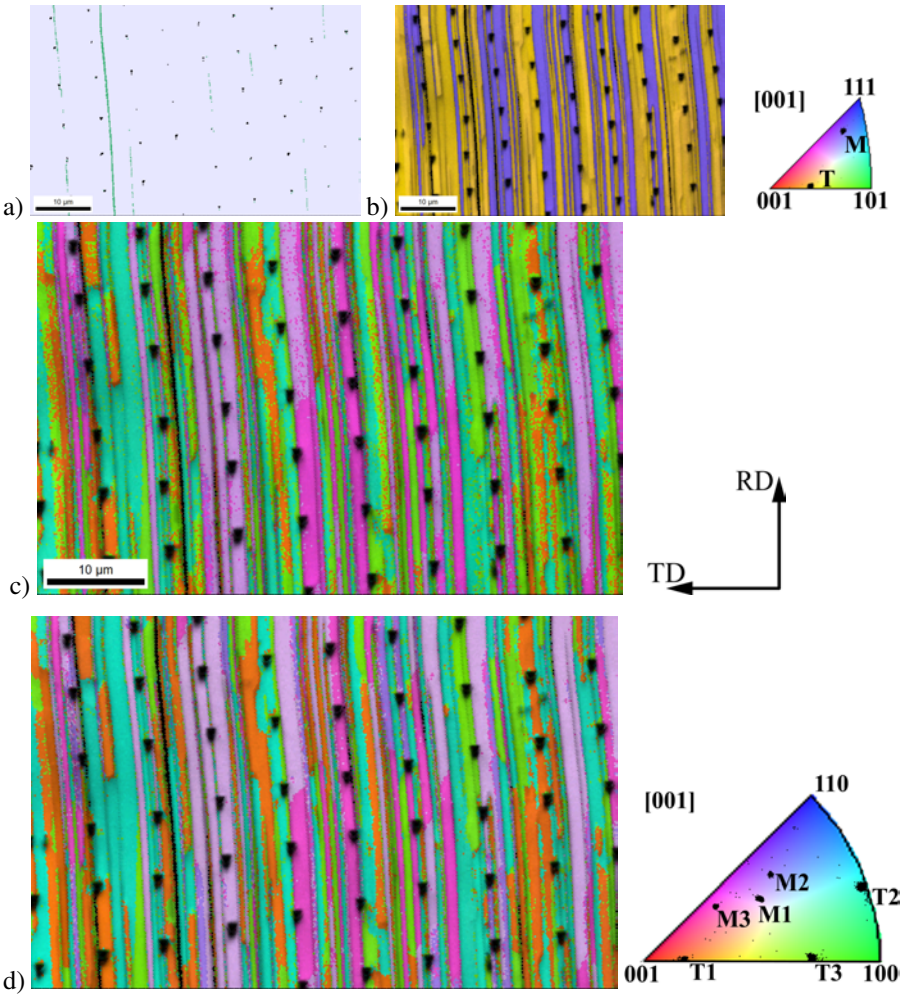

Fig. 6.8: EBSD maps of lamellar Ti-45.9Al-8Nb (at.%), measured with step size 0.2 µm (hexagonal grid); a) Phase map, light gray is γ-TiAl, green is hexagonal α_2-Ti_3Al b) Indexing with fcc structure, inverse pole figure (IPF) coloring scheme (see legend) combined with a greyscale image of the band contrast (BC) c) Vote Rank indexing result, IPF&BC colors; d) Fit Rank indexing result, IPF&BC colors; The black markings, indicating very low band contrast, are nanoindentations which made it possible to precisely locate positions in the microstructure during interactive SEM observation.

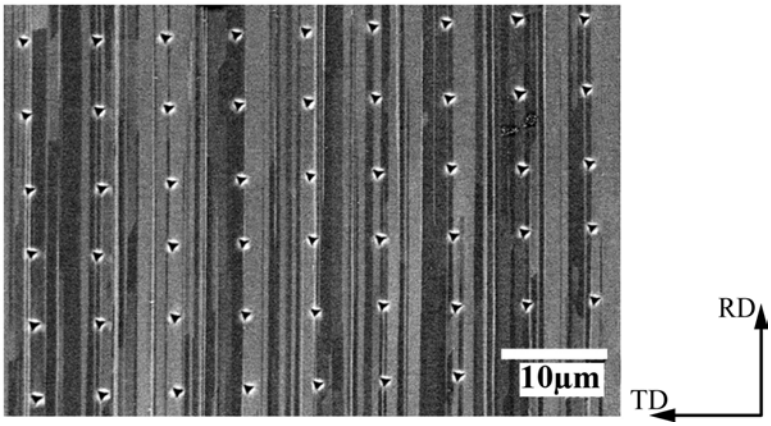

Fig. 6.9: Backscattered electron image of the microstructure shown in the orientation maps in figure 6.8. α_2-Ti_3Al appears bright while γ-TiAl shows different shades of gray.

Twin boundaries were observed to be almost exclusively aligned with the lamellae, while order domains may change along the lamellae. The width of the order domains was about 1 µm to 2 µm. The lamellae were inclined to the surface at an angle of 68°. In figure 6.8-d the length of order domain boundaries (120°±1° rotation for a {1 1 1} plane normal) was analyzed to be 3.52 mm. Converted to boundary length per area (60 µm × 38 µm), this value corresponds to 1.55 µm $^{-1}$.

Figure 6.10 shows a fit-rank orientation map of a lamellar microstructure in Ti-50Al, grown at IFW Dresden under the same conditions as the Ti-46Al-8Nb material. Discrimination of order domains is not as good as in the previous measurements, since patterns were taken at a higher rate of 4 s^{-1}. Additionally, the binary composition leads to a decrease in pattern intensity in comparison to the Nb-alloyed material. The Blackburn orientation relation is strictly followed as demonstrated by the common positions of one type of the (1 1 1) and all (0 0 0 1) poles and three of the ⟨1 1 0⟩ directions being parallel to the ⟨1 1 $\bar{2}$ 0⟩ directions. The refining effect of the Nb-alloying on the γ-phase order domains becomes obvious when the microstructures in figures 6.8 and 6.10 are compared.

It is emphasized here again that an accurate pattern center calibration is essential for obtaining correct data: For an incorrect calibration the fit rank indexing may produce a proper looking microstructure, which might nevertheless contain significant amounts of wrongly indexed points. Therefore, the conditions of the setup have to be checked before each scan by manual evaluation of individual back-scattered Kikuchi patterns. This on-site validation should be performed with patterns taken at longer exposure times, that exhibit the mentioned {1 1 0} superlattice reflection.

6.6.3 Further improvement of the algorithm

It is possible that the usage of appropriate, particularly sensitive reflectors (see table 6.1) could enhance the proposed indexing scheme. This could, for example, be

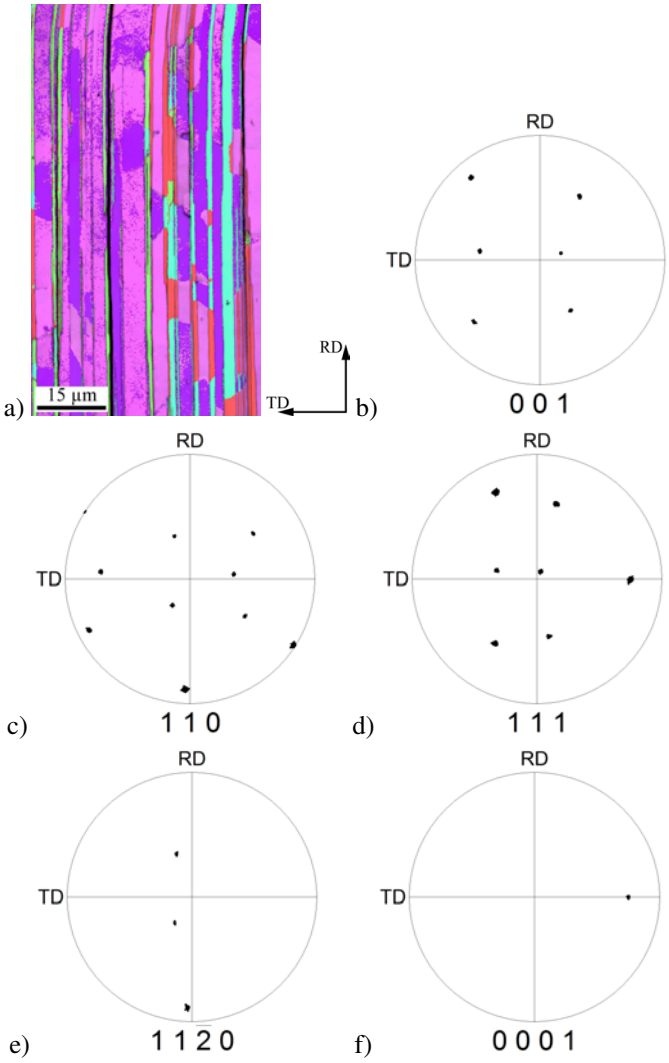

Fig. 6.10: EBSD orientation map of a lamellar structure in Ti-50Al; IPF coloring (α_2-phase data is not shown and appears in black) overlayed with pattern quality grayscale, uncleaned data; (b) (001) pole figure showing six orientations, corresponding to the six orientational variants; c–f show pole figures for γ- and α_2-phase that confirm the Blackburn orientation relationship between α_2 and γ-phase;

achieved by assigning a higher weight to these sensitive reflectors during the calculation of the average angular fit measure.

Certainly, the selection of a higher resolution for the Hough transform is another possibility for further development. A fundamental problem with the current Hough transform approach is caused by the use of a static convolution mask: first, due to its constant size an accurate band position detection is only possible for a limited range of Kikuchi band widths. Furthermore, the use of a convolution mask veils the contrasts of superlattice reflections which could otherwise be used to check the correctness of the solution. A possible way around these problems is the use of the Hough backmapping transform as it was introduced by Krieger-Lassen (1998). The Hough backmapping transform results in a very sparsely filled Hough space so that the band or line maxima can be detected without further filtering of the image.

It might be possible to adjust the internal tolerances of the vote-rank procedure to identify the order domains. For example a decrease of the interplanar angle tolerance parameter, as defined in the software OIM-DC, was observed to reduce the number of misindexed points. However, in the current setting, when the calibration of the EBSD system is carried out with high accuracy, the average angular fit measure was found to be more sensitive to the correct solution than the number of votes.

In general, the proposed two-step procedure seems to be computationally most efficient for situations in which crystal orientations related to very similar Kikuchi patterns need to be discriminated: First the robust and fast vote-rank method is applied to find a finite number of candidate solutions. Afterwards, a tailored criterion such as the fit-rank or possibly a computationally more demanding evaluation of the candidates can be applied.

6.7 Conclusions

A new approach to resolve the slight tetragonality of $L1_0$ ordered γ-TiAl by electron backscatter diffraction (EBSD) was presented. The new algorithm enables the reliable identification of order domains in γ-TiAl based alloys. The approach is based on the detection of the tetragonal distortion of the diffraction patterns. An accurate pattern center calibration together with high accuracy parameters for pattern acquisition and indexing were employed. The applied Hough transform parameters were just sufficient to resolve the slight tetragonal distortion of the material but a higher resolved Hough transform would be beneficial for still more reliable data analysis.

The average angular fit between the measured and simulated band positions was shown to be a more sensitive parameter for the identification of TiAl order domains, than the triplet vote measure. The approach was successfully validated and indexing of a crystal orientation map was performed with a newly developed fit-rank algorithm. It was shown that with the developed method, the rate of successful indexing in γ-TiAl can reach values of up to around 90 % in fully automatic orientation mapping.

7

Crystal plasticity modeling of γ-TiAl

7.1 Motivation

As discussed in chapter 3, γ-TiAl exhibits plastic anisotropy due to different modes of inelastic deformation. The complex deformation behavior with involved interactions between the individual types of dislocations, renders its systematic computational treatment an attractive tool to improve the micromechanical understanding. The use of computational plasticity makes possible the quantitative study of highly nonlinear material behavior that originates in simple underlying relations such as different shear strengths and the hardening interaction of the deformation systems. These relations are the core interest during such efforts and they cannot easily be studied by experiments only.

The crystal plasticity finite element method (CPFEM) can approach the micromechanics of crystalline matter on the meso-scale, just above the resolution of individual dislocations, but still taking into account the discrete slip systems as the most prominent feature of crystal plasticity. The treatment of sophisticated boundary conditions through the finite element method makes possible a quantitative comparison to experimental data. This will be demonstrated later for the cases of nanoindentation and polycrystal deformation of different microstructures.

7.2 The finite strain elasto-viscoplastic crystal plasticity formulation

A general treatment of continuum mechanics and plasticity can be found in Khan and Huang (1995) or in Simo and Hughes (1998). Wriggers (2001) gives details about the non-linear finite element method involved in the solution of the boundary value problems.

For recent reviews of viscoplastic crystal plasticity see McDowell (2008) and Roters et al. (2010). Books which contain smaller or larger sections on crystal plasticity formulations are Khan and Huang (1995), Jirásek and Bažant (2001), Raabe et al. (2004a), Bertram (2005); and de Neto et al. (2008, ch. 16).

Apart from the examples given in the review of titanium aluminide modeling, chapter 4, elasto-viscoplastic crystal plasticity simulation has been applied successfully to a variety of problems (Roters, 2005, Roters et al., 2010). Application fields of CPFEM modeling include

- Single crystal deformation (Wang et al., 2004, Zaafarani et al., 2006, 2008, Zambaldi et al., 2007, Raabe et al., 2007)
- Grain-resolved mechanics of polycrystalline aggregates (Raabe et al., 2001, Delannay et al., 2006, Musienko et al., 2007, Zhao et al., 2008, Bieler et al., 2009)
- Prediction of texture evolution during plastic deformation of polycrystals through homogenization schemes (Kalidindi et al., 1992, Raabe et al., 2004b)

The given examples are by far not complete but will suffice to illustrate the current state in crystal plasticity simulation and its role as a widely used and highly successful technique in the mechanics of crystalline solids.

The model that was used in the present approach is based on the work of Kalidindi et al. (1992). A short summary is given in the following sections before addressing the specifics of implementing the constitutive behavior of γ-TiAl.

7.2.1 Continuum mechanics

To define a deformation, the coordinates $d\boldsymbol{X}$ of an infinitesimal line element in the reference configuration are projected by the mapping $\boldsymbol{F}$ into the current configuration (coordinates $d\boldsymbol{x}$):

$$d\boldsymbol{x} = \boldsymbol{F} d\boldsymbol{X}$$

Therefore the deformation gradient is defined by

$$\boldsymbol{F} = \frac{\partial \boldsymbol{x}}{\partial \boldsymbol{X}}$$

The deformation gradient gives a complete description of the deformation of a material point. It does not contain the translation of the material point that might occur in a physical deformation process. The deformation gradient is symmetric if it does not contain rigid body rotations. $\boldsymbol{F}$ can be decomposed into a rotational and a deviatoric part in two ways, yielding a rigid body rotation and a stretch:

$$\boldsymbol{F} = \boldsymbol{R}\boldsymbol{U} = \boldsymbol{V}\boldsymbol{R}$$

where $\boldsymbol{R}$ is the rotation tensor and $\boldsymbol{U}$ and $\boldsymbol{V}$ are the right and left Cauchy-Green stretch tensors.

The mathematical description of large-strain elasto-plasticity is based on the multiplicative decomposition of $\boldsymbol{F}$. The multiplicative decomposition of the deformation gradient is performed as (Kröner, 1960, Lee, 1969)

$$\boldsymbol{F} = \boldsymbol{F}^* \boldsymbol{F}^p \tag{7.1}$$

where $\boldsymbol{F}^p$ maps the initial configuration into the isoclinic, intermediate configuration, figure 7.1. The intermediate configuration is also sometimes called the 'relaxed' configuration, since only plastic deformation is assumed and no elastic distortion is present.

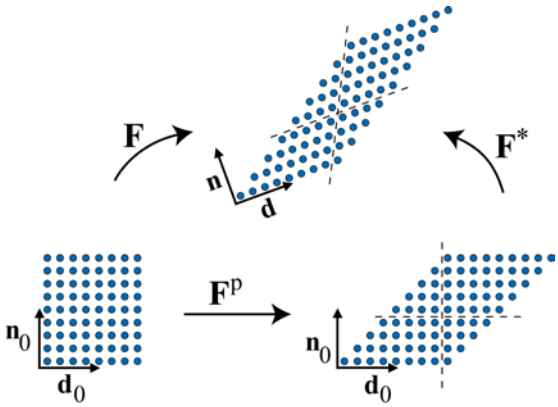

Fig. 7.1: Initial, intermediate (through $\boldsymbol{F}^p$) and current configuration (through $\boldsymbol{F} = \boldsymbol{F}^*\boldsymbol{F}^p$) of the crystal lattice in the elasto-plastic formulation;

Since the plastic deformation is taken to be volume preserving, also the incompressibility condition, $\det(\boldsymbol{F}^p) = 1$, holds. Elastic distortion as well as rigid-body rotations are both contained in $\boldsymbol{F}^*$ which maps the intermediate configuration to the current configuration.

From the elastic part of the deformation gradient, the elastic Green-Lagrange strain, $\boldsymbol{E}^e$, is calculated as

$$\boldsymbol{E}^e = \frac{1}{2}(\boldsymbol{F}^{eT}\boldsymbol{F}^* - \boldsymbol{I}) \tag{7.2}$$

The second Piola-Kirchhoff stress, $\boldsymbol{T}$, resulting from the elastic distortion, can be calculated as

$$\boldsymbol{T} = \mathbb{C}\boldsymbol{E}^e. \tag{7.3}$$

with elastic operator $\mathbb{C}$. It is the work-conjugate stress measure to the Green-Lagrange strain.

The Cauchy stress, $\boldsymbol{\sigma}$, in the current configuration is related to the second Piola-Kirchhoff stress in the reference configuration, through

$$\boldsymbol{\sigma} = \frac{1}{J}[\boldsymbol{F}\boldsymbol{T}\boldsymbol{F}^T]\,, \text{ with } J = \det(\boldsymbol{F}) \tag{7.4}$$

The plastic velocity gradient, $\boldsymbol{L}^p$, will be used in the formulation of the constitutive model and can be calculated from

$$\boldsymbol{L}^p = \dot{\boldsymbol{F}}^p\boldsymbol{F}^{p-1}$$

7.2.2 The constitutive model

Deformation of crystals by dislocation glide can be described by the Orowan equation (Orowan, 1934)

$$\dot{\gamma} = b\,\rho_{mobile}\,v, \tag{7.5}$$

with $\dot{\gamma}$ being the crystallographic shear rate, b the Burgers vector length, ρ_{mobile} the mobile dislocation density and v the dislocation glide velocity. However, the dislocation

densities and velocities in γ-TiAl are not known. To be able to simulate the constitutive response, it is useful to retreat to the quantitative description of the shear rates resulting from the different types of dislocations.

Since only shear on individual deformation systems is allowed to contribute to plastic deformation, $\boldsymbol{L}^p$ is calculated from the sum of the shear rates $\dot{\gamma}^\alpha$ on all deformation systems

$$\boldsymbol{L}^p = \dot{\boldsymbol{F}}^p \boldsymbol{F}^{p-1} = \sum_\alpha \dot{\gamma}^\alpha \, \boldsymbol{d}_0^\alpha \otimes \boldsymbol{n}_0^\alpha \tag{7.6}$$

The unit vectors $\boldsymbol{d}_0^\alpha$ and $\boldsymbol{n}_0^\alpha$ are denominating the shear direction and the normal on the glide plane of the slip system α. The index zero is given since in this total lagrangian formulation the slip plane normals and slip directions are assumed to stay constant throughout the calculation as shown in the intermediate configuration in figure 7.1. The Schmid matrix, $\boldsymbol{S}_0^\alpha$, is calculated by

$$\boldsymbol{S}_0^\alpha = \boldsymbol{d}^\alpha \otimes \boldsymbol{n}^\alpha = \begin{pmatrix} d_1 \\ d_2 \\ d_3 \end{pmatrix} \cdot \begin{pmatrix} n_1 & n_2 & n_3 \end{pmatrix} = \begin{pmatrix} d_1 n_1 & d_1 n_2 & d_1 n_3 \\ d_2 n_1 & d_2 n_2 & d_2 n_3 \\ d_3 n_1 & d_3 n_2 & d_3 n_3 \end{pmatrix}$$

$\boldsymbol{S}_0^\alpha$ transforms an arbitray stress state in the material point into the resolved shear stress in the coordinates defined by $\boldsymbol{d}_0^\alpha$ und $\boldsymbol{n}_0^\alpha$.

$$\tau^\alpha = \boldsymbol{\sigma} : \boldsymbol{S}_0^\alpha$$

To make a unique choice of active slip systems has been a non-trivial problem in the modeling of crystal plasticity. It was elegantly solved (Peirce et al., 1983, Asaro and Needleman, 1985) by avoiding the reduction to a set of slip systems. Instead, all shear rates, $\dot{\gamma}^\alpha$, are taken as a visco-plastic function of the resolved shear stresses, τ^α, on the deformation systems.[1]

$$\dot{\gamma}^\alpha = \dot{\gamma}_0 \left| \frac{\tau^\alpha}{\tau_c^\alpha} \right|^{1/m} \operatorname{sign}(\tau^\alpha) \tag{7.7}$$

where $\dot{\gamma}_0$ and m are material parameters. The influence of the strain rate sensitivity parameter, m, on the shear rate is illustrated in figure 7.2.

The slip resistance, τ_c^α, evolves with the shear rate, $\dot{\gamma}^\beta$, of all systems as:

$$\dot{\tau}_c^\alpha = \sum_\beta h^{\alpha\beta} \left| \dot{\gamma}^\beta \right| \tag{7.8}$$

with the 'instantaneous moduli' (Hill, 1966) $h^{\alpha\beta}$, also called the hardening matrix. It is calculated as

$$h^{\alpha\beta} = q^{\alpha\beta} h^{(\beta)} \tag{7.9}$$

where $q^{\alpha\beta}$ are the components of the cross-hardening matrix with its diagonal elements equal to unity. Typically, in fcc crystals, the values of $q^{\alpha\beta}$ are chosen to be 1.4 for non-coplanar systems and 1 for coplanar slip (Peirce et al., 1982). Parameter $h^{(\beta)}$ is the

[1] This function is analogous to the Norton creep law $\dot{\varepsilon} = B \left(\frac{\sigma}{\sigma_{ref}} \right)^n$, e. g. Rösler et al. (2006, pg. 385)

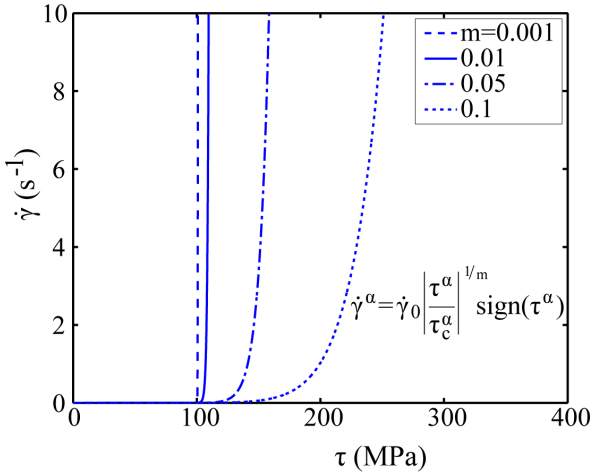

Fig. 7.2: Dependency of the shear rate on a single slip system from the resolved shear stress on that system. The influence of the strain rate sensitivity, m, is shown; $\gamma_0 = 0.001$, $\tau_c = 100$.

hardening contribution for single slip ('self hardening') and is given by:

$$h^{(\beta)} = h_0^{\beta}\left(1 - \frac{\tau^{\beta}}{\tau_s^{\beta}}\right)^{a^{\beta}}. \tag{7.10}$$

Note the change in comparison to the original formulation of the model from constant values, h_0, τ_s, a, for all slip systems, to h_0^{β}, τ_s^{β}, a^{β}, dependent of the respective slip system β. Alternative types of hardening relations are possible and some are given in Kalidindi and Schoenfeld (2000).

This leaves only few parameters for the description of the flow behavior: the initial slip resistance, τ_0 and the saturation slip resistance, τ_s; the parameter h_0 determines the initial hardening slope, and the hardening exponent, a, influences the shape of the self-hardening curve.

Since the primary meaning of the reference shear rate, $\dot{\gamma}_0$, and the strain rate sensitivity parameter, m, in the scope of the present work is rather of numerical nature than related to the micromechanical properties, they are assumed constant throughout the simulations presented in this work. Parameter m is suitable to include strain rate sensitivity of the flow stress into the model. To approach time-independent behavior its value is kept small, figure 7.2. However, too small values make robust convergence of the time-integration procedure difficult.

7.2.3 Time-integration of the phenomenological crystal plasticity law

For the calculation of finite-strain problems by the finite-element method, the deformation is split up into a number of incremental deformation steps. This is done in an updated-Lagrange framework, where the current configuration of the increment

at time t_0 is used as the reference configuration for the current configuration at time $t_{n+1} = t_n + \Delta t$. The time-integration at the local material point is carried out in a total Lagrangian fashion (Kalidindi et al., 1992, Kalidindi, 2004) as shown in figure 7.1, meaning that the undeformed reference configuration of the material point is not changed at any time.

The finite element framework provides an estimate for the deformation gradient at the end of the time step. In the crystal-plasticity subroutine the corresponding stress response as well as the tangent stiffness, $\mathbb{D}$, of the material points have to be calculated and returned to the finite element solver.

Kalidindi et al. (1992) proposed a fully-implicit time-integration scheme which was followed in the implementation of the constitutive law used in the present work. Integration of the flow rule (7.6) is carried out as follows.

Weber and Anand (1990) presented an exact solution for the calculation of $\boldsymbol{F}^p$:

$$\boldsymbol{F}^p(t_{n+1}) = \exp\{\Delta t \boldsymbol{L}^p(t_{n+1})\}\, \boldsymbol{F}^p(t_n). \tag{7.11}$$

Following Kalidindi et al. (1992), the exponential is then substituted by the approximation

$$\exp\{\Delta t \boldsymbol{L}^p(t_{n+1})\} \approx \boldsymbol{I} + \Delta t \boldsymbol{L}^p(t_{n+1}) \tag{7.12}$$

which does not guarantee incompressibility. Incompressible inelasticity is ensured by a renormalization of $\boldsymbol{F}^p$ at the end of the time step:

$$\boldsymbol{F^p} = \boldsymbol{F}^p(t_{n+1}) \left\{\det[\boldsymbol{F}^p(t_{n+1})]\right\}^{-1/3}. \tag{7.13}$$

Omitting some steps in the derivation, the stress at the end of the current time step is formulated as (Kalidindi et al., 1992)

$$\boldsymbol{T}(t_{n+1}) = \boldsymbol{T}^{trial} - \sum_{\alpha} \Delta\gamma^{\alpha}(\boldsymbol{T}(t_{n+1}, \tau_c(t_{n+1}))\, \boldsymbol{C}^{\alpha} \tag{7.14}$$

with

$$\boldsymbol{T}^{trial} = \mathbb{C}\left[\frac{1}{2}\{\boldsymbol{A} - \boldsymbol{I}\}\right]$$

and

$$\boldsymbol{C}^{\alpha} \equiv \mathbb{C}\left[\frac{1}{2}(\boldsymbol{A}\boldsymbol{S}_0^{\alpha} + \boldsymbol{A}\boldsymbol{S}_0^{\alpha T})\right]$$

$$\boldsymbol{A} \equiv \boldsymbol{F}^{p^{-T}}(t_n)\boldsymbol{F}^T(t_{n+1})\boldsymbol{F}(t_{n+1})\boldsymbol{F}^{p^{-1}}(t_n)$$

The evolution of the critical shear stresses of the slip systems is given by

$$\tau_c^{\alpha}(t_{n+1}) = \tau_c^{\alpha}(t_n) + \sum_{\beta} h^{\alpha\beta}(\tau_c^{\beta}(t_{n+1}))\left|\Delta\gamma^{\beta}\left(\boldsymbol{T}(t_{n+1}), \tau_c^{\beta}(t_{n+1})\right)\right|. \tag{7.15}$$

Numerical simultaneous solution of the system of equations (7.14) and (7.15) is implemented through a two-level iterative scheme (Kalidindi et al., 1992), also called

a predictor-corrector scheme. Initially, the stresses are computed with the previous values for τ_c. After convergence in the stress, the resulting hardening is calculated from (7.15). If the maximum change in any of the calculated slip resistances is larger than a given tolerance, convergence is not reached. In this case the stresses are computed again, using the updated values of the slip resistances. If the residuals for the stresses and the slip resistances are below the respective tolerances, the two-level iterative scheme has completed. The remaining task then is the computation of the consistent tangent stiffness described in the next section.

If convergence cannot be reached for the given deformation increment, the internal time step of the material point time integration can be reduced independently from the finite-element time step. When moving from time step t_n to the time t_{n+1}, the state variables (F^p, τ_c) have to be updated. For further details see Kalidindi et al. (1992).

7.2.4 Numerical approximation of the material point tangent stiffness

A guess for the global deformation gradient at the end of the finite element time step, $\boldsymbol{F}(t_{n+1})$, is handed to the material subroutine. After the stress integration in the subroutine the resulting stresses will be used in the finite element procedure. If the global equilibrium conditions cannot be satisfied by the stresses, $\boldsymbol{F}(t_{n+1})$ is revised by the finite element code. For this revision the material point's tangent stiffness is used. It is defined as $\mathbb{D} = \frac{\mathrm{d}\boldsymbol{\sigma}_{n+1}}{\mathrm{d}\boldsymbol{\varepsilon}_{n+1}}$. The consistent tangent, sometimes also called the Jacobian (matrix) or algorithmic tangent of the material point (Wriggers, 2008), is computed numerically by successively perturbing the components of the deformation gradient and carrying out the material point time-integration each time to find the stresses for each of these perturbations.

The tangent stiffness is computationally expensive to calculate. At the same time its accuracy only affects the *number of iterations* needed to satisfy the FE equilibrium conditions, but not the accuracy of the final result. Therefore it is usually not recalculated in every single time step. Instead the same tangent stiffness is reused a number of times. Its recalculation can be enforced if the number of iterations in the FE loop is becoming larger than e.g. four (Kalidindi et al., 1992).

After calculation of the consistent tangent stiffness, the stresses and the material tangent are returned to the finite element solver and the evaluation of the constitutive routine is performed for the next integration point. When the constitutive behavior in all integration points was calculated, the nonlinear finite element procedure determines the nodal displacements, that satisfy the global equilibrium conditions.

7.3 Implementation of ordinary and super dislocation glide systems of γ-TiAl

An existing crystal-plasticity subroutine was changed to take variable hardening parameters τ_0, τ_s, h_0 and a for the octahedral slip systems of γ-TiAl. The convergence tolerance values of the two-level iterative procedure are defined dependent from the single constant value for τ_0 in the original work of Kalidindi et al. (1992). Since different values of τ_0 are possible here, the choice was made to use the minimum value of all values τ_0^α for the convergence testing. The tolerance for the inner stress integration

loop is chosen to be $10^{-4} \times \min(\tau_0^\alpha)$. The outer loop reaches convergence when the maximum change in the components of the calculated shear strengths becomes smaller than the minimum initial shear strength of all systems

$$\max(\Delta\tau_c^\alpha) < 10^{-3} \times \min(\tau_0^\alpha).$$

7.4 Implementation of twinning on four true twinning systems of γ-TiAl

Kalidindi (1998) discussed the incorporation of twinning systems into crystal plasticity formulations comprehensively and proposed an incorporation of twinning based on volume fractions. A simpler approach to the implementation of twinning systems was chosen here.

Four $\{1\,1\,1\}[1\,1\,\bar{2}]$ true twinning systems were implemented. True twinning refers to the four twinning directions in γ-TiAl, which do not generate an order fault at the twin interface. The twinning systems are implemented as uni-directional slip systems: if the resolved shear stress on the twinning plane is positive, the stress integration is carried out in the same manner as for the dislocation glide systems. If the resolved shear stress is negative, the shear on this glide system will be set to zero for the current increment.

In reality twinning leads to reorientation of the twinned material volume. This reorientation is neglegted in the present model. Also twinning in reality cannot produce shear values higher than $1/\sqrt{2} \approx 0.71$ corresponding to a shear angle of $\text{atan}(1/\sqrt{2}) \approx 35.3°$. This limitation is not incorporated in the model since this shear value is relatively high and therefore appropriate hardening behavior makes it virtually impossible to reach this value.

7.5 Incorporation of the single crystal constitutive law into the finite element method

The finite element method is a robust and highly developed method for structural calculations (Zienkiewicz and Taylor, 2005, Bathe, 1996, Wriggers, 2008). The finite element framework solves the field equations and ensures the satisfaction of global equilibrium, i. e. the balance of masses and momentums and the satisfaction of energy conservation.

In each time step of the nonlinear finite element calculation the material subroutine is called for every integration point. The global deformation gradient of the material point is handed to the subroutine and the material law is expected to return the local stresses as well as the tangent stiffness matrix.

Internal variables of the subroutine are used to store the orientation evolution, the critical shear strengths and the shear values on the individual slip systems. More result values are derived from those primary variables. For example the accumulated slip is a characteristic measure during the crystal-plasticity finite-element simulations and is defined as the sum of (absolute) shear values over all systems: $\gamma^\Sigma = \sum_\alpha |\gamma^\alpha|$. Furthermore, the crystallographic misorientation from the initial undeformed state is tracked during the simulations.

All models were generated in the finite element system MSC.MARC.MENTAT. The product name MENTAT refers to the pre- and post-processing tool and MARC is the

finite element solver. The crystal plasticity formulation was included into the model by using the material subroutine `hypela2.f` (MSC Software, 2007c).

A set of python (Python, version 2.6) classes was programmed to enable efficient model generation for standard models and indentation calculations. The python classes generated so-called procedure files which were used to automatically build the finite element model in MENTAT.

One advantage of the programmed model generation is the small file size of the generated procedure files which is often well below 1% of the model size. Therefore, the files can be stored easily for later reference. Nevertheless, all details of the simulations can be read from the procedure files, which makes the modeling work more transparent. Finally, while there is a considerable overhead in designing the programs, once the framework is built it can be used in a much more flexible way and further developments become more easy to implement.

7.6 Validation of the CPFEM implementation of the deformation modes

Figure 7.3 shows a simple model of eight isoparametric hexahedral elements. It was used to validate the implemented deformation modes. In all simulations carried out with MSC.MARC2007r1, the `Large Strain` procedure was invoked in an updated Lagrangian framework. This results in the stress and strain values to be output as Cauchy stress and logarithmic strain (MSC Software, 2007a,b).

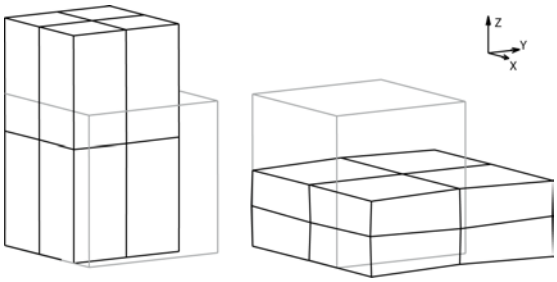

Fig. 7.3: An eight element model in two deformed states after tensile and compressive deformation to 50 % engineering strain.

The strength and hardening parameters of the slip systems of γ-TiAl are not known for the high-Nb alloyed compositions that are of primary interest in this work. In chapter 8, a nanoindentation approach is presented to analyze the intrinsic behavior. In the modeling work presented here, only rough guesses were made for the strength and hardening parameters.

The chosen parameters for the single-slip hardening are listed in table 7.1. The effect on the evolution of the shear resistance of the respective deformation systems during single-slip is shown in figure 7.4.

Tab. 7.1: Parameters of the crystal plasticity model for ordinary dislocation glide ($\boldsymbol{b}^{\mathrm{O}}$), superdislocation glide ($\boldsymbol{b}^{\mathrm{S}}$) and twinning ($\boldsymbol{b}^{\mathrm{T}}$) systems, m=20, $\dot{\gamma}_0 = 0.001\,\mathrm{s}^{-1}$; τ_0 is the initial slip resistance, τ_s the saturation slip resistance, h_0 influences the initial hardening slope and a is the hardening exponent, equation (7.10);

	τ_0, MPa	τ_s, MPa	h_0, MPa	a
$\boldsymbol{b}^{\mathrm{O}}$	150	1200	150	2.5
$\boldsymbol{b}^{\mathrm{S}}$	300	2400	150	2.5
$\boldsymbol{b}^{\mathrm{T}}$	150	1200	150	2.5

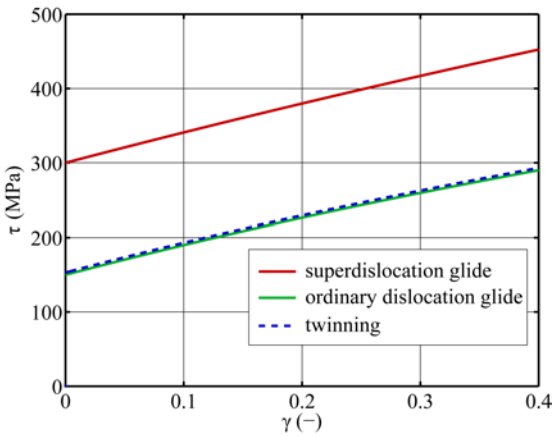

Fig. 7.4: Assumed self-hardening behavior of the deformation systems in the γ-TiAl model; shear resistance, τ_c, versus plastic shear, γ.

Validation of the implementation was carried out on the eight element model which was assigned a cube orientation with the *c*-axis parallel to the loading axis. In this orientation the ordinary slip systems all have Schmid factor 0.0, the super-dislocation slip systems have a Schmid factor of 0.408 and the twinning systems have a Schmid factor of 0.471. Twinning is expected to operate solely during compressive deformation.

Indeed, after technical compressive strain of 50 % the twinning systems show shear values of about 0.35, figure 7.5. The amount of shear on super and ordinary systems is below 10^{-7} and therefore the deformation is exclusively taking place in the twinning mode. Figure 7.6 shows the relative shear contributions from the individual slip systems together with the evolution of the accumulated shear. Only twinning deformation, equally distributed on the four systems, is observed.

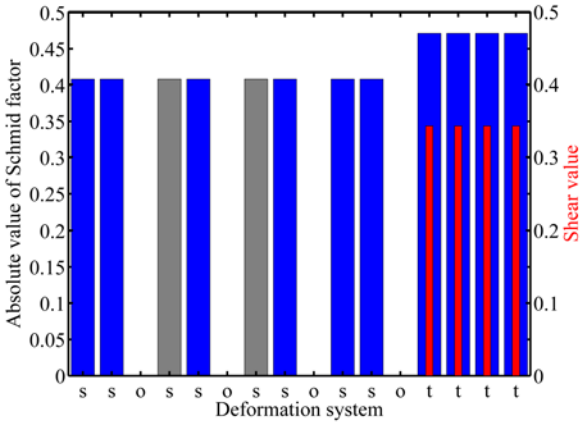

Fig. 7.5: Simulated compression of γ-TiAl along the *c*-axis. Deformation systems are ordinary dislocation glide ('o'), superdislocation glide ('s') and twinning ('t'). Blue color indicates positive Schmid factor values, gray negative values. Twinning systems can only operate with positive values. The shear values on the individual slip systems are given by the narrow red bars.

After tensile deformation, the resulting deformation is only distributed between the eight super dislocation deformation modes which show a shear value of about 0.12, figure 7.7. The twinning systems and four ordinary slip systems do not deform.

In figure 7.8 the tension-compression asymmetry resulting from the different activated deformation modes is shown. The much harder super dislocation systems, activated in tensile deformation mode, result in higher stresses than observed for the compressive deformation along the *c*-axis. By the authors knowledge, this kind of simulated tensile test on stoichiometric TiAl was not performed experimentally until now. The results can only be compared to the experimental data in Zupan and Hemker (2003). However, there binary Ti-55.5Al was tested and since superdislocation glide is easy for these Al-concentrations, the yield stress in tension was lower than in compression.

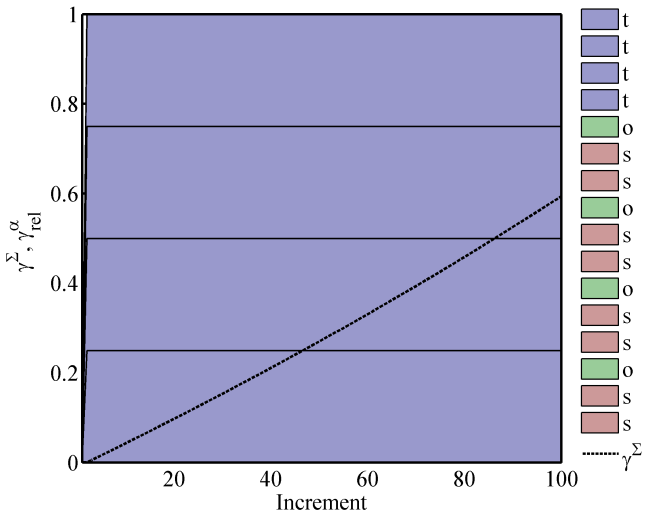

Fig. 7.6: Relative shear contributions, $\gamma^{\alpha}_{rel} = \gamma^{\alpha}/\gamma^{\Sigma}$, from different types of slip systems to the total accumulated shear, γ^{Σ}. The evolution of the accumulated shear is also shown. The amount of strain is proportional to the finite element increments and 50 % nominal compression is reached at 100 increments; deformation systems are ordinary dislocation glide ('o'), superdislocation glide ('s') and twinning ('t').

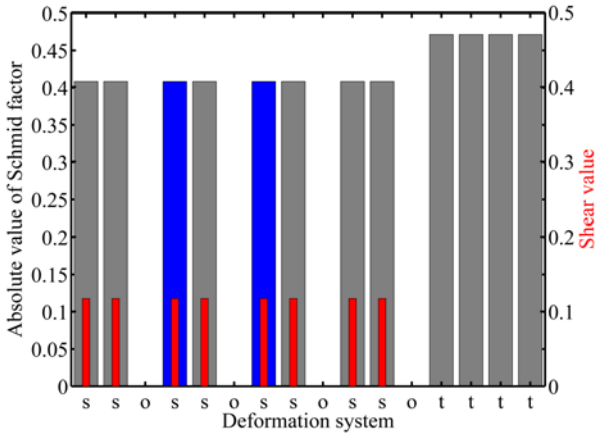

Fig. 7.7: Schmid factors for tensile deformation of γ-TiAl along the crystallographic *c*-axis. Resulting shear deformations after 50 % nominal strain, as calculated by the crystal-plasticity model are shown in red; deformation systems are ordinary dislocation glide ('o'), superdislocation glide ('s') and twinning ('t').

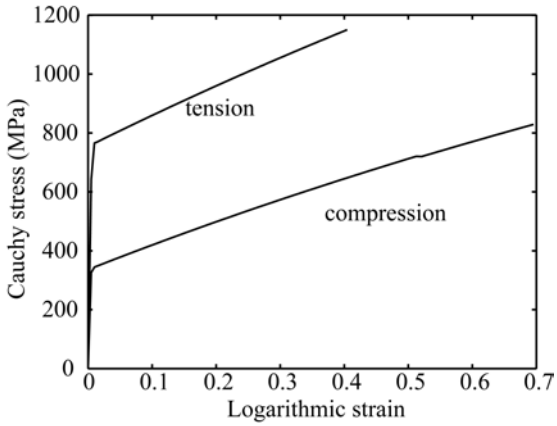

Fig. 7.8: Volume averaged stress-strain curves for the eight element model in cube orientation.

Additionally, in contrast to stoichiometric γ-TiAl, no twinning is expected to operate in Ti-55.5Al. For compression of Al-rich γ-TiAl in *c*-direction the 0.2% yield stress was measured at 270 MPa. While Zupan and Hemker (2003) did not give the tensile yield stresses at room temperature, an approximate value was extrapolated from their high temperature curves (the minimum temperature was 450 °C) and might lie around 170 MPa. It follows that in Al-rich γ-TiAl the tensile yield stress for loading along the *c*-axis is significantly lower than the compressive yield strength. The opposite behavior is expected for experiments on near-stoichiometric γ-TiAl, which have not been carried out up to date. The aim of the modeling work here was to simulate the mechanics of Nb-alloyed, near-stoichiometric γ-TiAl. For these alloys the uniaxial flow stresses are expected to be, at least qualitatively, similar to the curves shown.

In contrast to the simple picture of deformation along the [0 0 1] axis, most other orientations are much more complex in their deformation behavior even for uniaxial deformation. Figure 7.9 illustrates the relative plastic shear contributions during simulated compression of a [1 1 1] oriented crystal. Initially the deformation is mainly taking place on six deformation systems: two ordinary dislocation glide systems shown in green, two superdislocation glide sytems (red) and two twinning systems (blue). At the later stages of deformation, two additional superdislocation systems are activated and the relative amount of shear on the twinning systems decreases. The orientation of the deformation systems makes necessary a higher amount of total accumulated crystallographic shear in comparison to compression along [0 0 1]. This becomes evident through the higher slope of the γ^{Σ}-curve in comparison to figure 7.6.

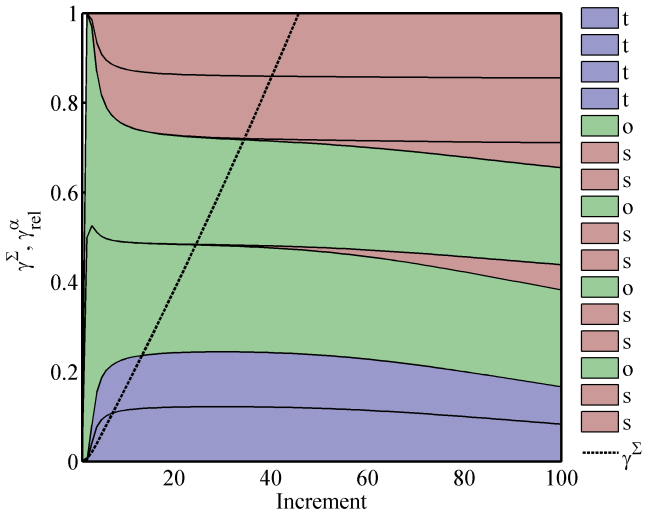

Fig. 7.9: Simulated compression for the γ-TiAl material model along the [1 1 1]-axis. Relative shear contributions, $\gamma^{\alpha}_{rel} = {}^{\gamma^{\alpha}}/_{\gamma^{\Sigma}}$, from different types of slip systems to the total accumulated shear, γ^{Σ}. The evolution of the accumulated shear is also shown. The amount of strain is proportional to the finite element increments and 50 % nominal compression is reached at 100 increments; deformation systems are ordinary dislocation glide ('o'), superdislocation glide ('s') and twinning ('t').

7.7 Discussion of appropriate hardening parameters of single phase γ-TiAl

The phenomenology of latent hardening in fcc crystals is discussed in detail in Peirce et al. (1982, sec. 3.2). Kocks and Mecking (2003) have reviewed the hardening behavior of fcc alloys. The work of Franciosi and Zaoui (1982) illustrates how difficult the analysis of latent hardening parameters is from conventional uniaxial mechanical testing. Carefully designed experiments need to be carried out to investigate the interaction coefficients between dislocation activity on different co-planar or non-coplanar glide systems. Small deviations from the nominal crystal orientation can result in large deviation from the expected behavior (Cuitino and Ortiz, 1992, Raabe et al., 2007).

Therefore, the influence of dislocation activity on one plane, on the slip resistance on another system is only known for extensively characterized materials such as copper (Franciosi and Zaoui, 1982). In γ-TiAl it is not known and only rough assumptions can be made at this point. It is not possible to simply neglect the cross-hardening effect as its contribution to the flow stress can be higher than the strengthening from the self-hardening that would occur under single slip conditions. The reason for the observed strong cross-hardening is that dislocations on one plane act more efficiently as obstacles for dislocations moving on a different plane. The picture of a *dislocation forest* is sometimes used to illustrate the situation.

Cross-hardening between the 16 deformation systems of γ-TiAl includes interaction of four ordinary dislocation glide systems ($\boldsymbol{b}^{\mathrm{O}}$), eight super dislocation glide systems ($\boldsymbol{b}^{\mathrm{S}}$) and four twinning ($\boldsymbol{b}^{\mathrm{T}}$) systems. Additional variability is imposed by the possibilities of the co-planar (cp) or non-co-planar (ncp) cross hardening mode. For pure γ-TiAl the $q^{\alpha\beta}$-matrix needs to be populated with 16^2=256 values. Sixteen different types of cross-hardening relations can be found, see table 7.2. Taking into account the precise dislocation interaction would increase the number of coefficients further as exemplified by Bassani and Wu (1991) for the case of fcc alloys.

If one assumes that cross-hardening between co-planar systems of dislocation glide and twinning does not take place, i. e. $q^{cp}_{o,s\,t} = q^{cp}_{t\,o,s} = 0$, the number of variables can be reduced to 16-8=8. Furthermore, co-planar cross-hardening between the super and ordinary dislocation systems is assumed to act only at the level of self-hardening:

Tab. 7.2: Sixteen types of cross-hardening coefficients, q, in γ-TiAl; the types of deformation systems are ordinary dislocation glide, $\boldsymbol{b}^{\mathrm{O}}$, super dislocation glide, $\boldsymbol{b}^{\mathrm{S}}$ and twinning, $\boldsymbol{b}^{\mathrm{T}}$. The superscript denotes co-planar (cp) or non co-planar (ncp) arrangement of the respective glide planes; the subscript indicates the interacting deformation systems.

	$\boldsymbol{b}^{\mathrm{S}}$	$\boldsymbol{b}^{\mathrm{O}}$	$\boldsymbol{b}^{\mathrm{T}}$
$\boldsymbol{b}^{\mathrm{S}}$	$q^{cp}_{ss}, q^{ncp}_{ss}$	$q^{cp}_{so}, q^{ncp}_{so}$	$q^{cp}_{st}, q^{ncp}_{st}$
$\boldsymbol{b}^{\mathrm{O}}$	$q^{cp}_{os}, q^{ncp}_{os}$	q^{ncp}_{oo}	$q^{cp}_{ot}, q^{ncp}_{ot}$
$\boldsymbol{b}^{\mathrm{T}}$	$q^{cp}_{ts}, q^{ncp}_{ts}$	$q^{cp}_{to}, q^{ncp}_{to}$	q^{ncp}_{tt}

Tab. 7.3: Estimated values for the cross-hardening coefficients; cp=co-planar, ncp=non-co-planar;

	$\boldsymbol{b}^{\mathrm{S}}$	$\boldsymbol{b}^{\mathrm{O}}$	$\boldsymbol{b}^{\mathrm{T}}$
$\boldsymbol{b}^{\mathrm{S}}$	$q_{ss}^{cp} = 1.0, q_{ss}^{ncp}$	$q_{so}^{cp} = 1.0, q_{so}^{ncp}$	$q_{st}^{cp} = 0.0, q_{st}^{ncp}$
$\boldsymbol{b}^{\mathrm{O}}$	$q_{os}^{cp} = 1.0, q_{os}^{ncp}$	q_{oo}^{ncp}	$q_{ot}^{cp} = 0.0, q_{ot}^{ncp}$
$\boldsymbol{b}^{\mathrm{T}}$	$q_{ts}^{cp} = 0.0, q_{ts}^{ncp}$	$q_{to}^{cp} = 0.0, q_{to}^{ncp}$	q_{tt}^{ncp}

$q_{os}^{cp} = q_{so}^{cp} = q_{ss}^{cp} = 1$. Additionally, the following further restrictions are assumed: $q_{ts}^{ncp} = q_{to}^{ncp} > q_{so}^{ncp} > q_{os}^{ncp}$. The updated version of table 7.2 is given in table 7.3.

With these assumptions the remaining parameters mainly affect the influence of dislocation activity on twinning activity on a different plane, namely $q_{s,o\,t}^{ncp}$ and vice versa $q_{t\,s,o}^{ncp}$. Because twinning activity is introducing new interfaces in the crystal it is assumed to harden the non-coplanar dislocation glide significantly. Dislocation activity is expected to strengthen non-co-planar twinning to a lesser degree: $q_{t\,s,o}^{ncp} > q_{s,o\,t}^{ncp}$. The same argument holds for intersection of twinning systems and q_{tt}^{ncp} is assumed to be relatively high, thereby preventing cross-twinning. Finally, the non-co-planar latent hardening contribution from identical dislocation systems has to be assigned, where $q_{ss}^{ncp} > q_{oo}^{ncp}$ is assumed.

7.8 Conclusion

The presented CPFEM technique was extended to incorporate the deformation behavior of γ-TiAl. Despite the different strength and hardening characteristic of the individual types of deformation systems, convergence can be reached in the constitutive law. The uni-directional shearing of twinning deformation was implemented into the model through additional glide systems with suppression of the negative twinning shear mode. The model provides robust convergence behavior in a wide parameter range and up to high plastic strains and therefore is suited to approach almost arbitrary and complex three-dimensional forming problems.

8

Single crystal indentation of γ-TiAl – experiments and CPFEM modeling

8.1 Introduction

The characterization of mechanical properties in individual microstructural constituents is an active and challenging field of research. Experimental methods like micro-pillar compression, micro-tensile tests or micro-bending are working towards the goal to clarify the micromechanical mechanisms of crystal plasticity (Hemker and Sharpe, 2007, Weber et al., 2008, Uchic et al., 2009, Kiener et al., 2009, Dehm, 2009). The indentation method is superior to these methods with respect to efficiency and robustness of sample preparation, since a microscopically planar and undeformed surface is sufficient to perform indentation experiments. The stress and strain fields that develop during indentation are, however, much more complicated than those for the aforementioned methods. In the following it will be shown how the application of three-dimensional crystal plasticity finite element calculations can assist the evaluation of the deformation processes during indentation in an efficient way.

8.2 Indentation experiments

8.2.1 Experimental methods

Cylindrical samples (∅ 6 mm) of Ti-45.9Al-8Nb (at.%), grown in an optical floating zone furnace (Souptel et al., 2007) at a withdrawal rate of 10 mm/h, were provided by IFW-Dresden. Discs of 4 mm thickness were cut by wire electrical discharge machining, ground to 1000 grit, polished with 3 µm diamond suspension, and finally electrolytically polished at -30°C/35 V in a solution of 6 % perchloric acid in ethanol. This surface preparation technique is identical to the one applied for EBSD indexing. The microstructure, was observed by backscatter electron (BSE) imaging which gives good phase contrast between γ- and α_2-phase. The crystallographic orientation of the γ-phase was characterized by the improved electron backscatter diffraction (EBSD) technique described in chapterch:ebsd.

A Hysitron TriboScope 900 was used for indentation. The maximum applied load was 10 mN. The maximum load was applied within 5 seconds. The load was held for 1 second and the unloading was performed during another 5 seconds. A more

sophisticated loading scheme has been used, e. g. by Vlassak and Nix (1994), but since the primary interest in this study was in the characterization of the plastic behavior, the accuracy of the measurements with the simplified loading scheme was taken to be sufficient. Instrumented indentation was performed with indenters of Berkovich and sphero-conical tip geometries. Two sphero-conical diamond tips were used with a nominal opening angle of 90° and nominal tip radii of 'smaller than 1 μm' and 1 μm. They will be referred to as SC_1 and SC_2, respectively. Generally, the lamellar structure was too fine to perform sphero-conical indentation inside the lamellae. Indentations were mainly made in a region of coarser γ-grains of about 20 μm grain size. Some indents were also placed in coarse γ-phase lamellae.

The remaining indent topographies were characterized by a NI/Veeco dimension 3100 AFM in intermittent contact mode (tapping mode). A standard silicon cantilever was used. The lateral resolution of the measurements was either 512 or 256 points along distances from about 3 to 30 microns. Further processing of the data was performed by using the software Gwyddion and own programs.

8.2.2 Results of indentation experiments

Figure 8.1 shows the microstructure into which the indentations were performed. The crystallographic orientation of the grains is indicated by the coloring scheme. The microstructure was almost fully lamellar, with a lamellar colony size of several hundred micrometers and γ-grains along part of the grain boundaries. The γ-grains varied in size and shape with diameters of about 10 to 30 μm.

Figure 8.2 contains some typical load-displacement curves for indents made with different indenter geometries, namely the Berkovich geometry, the cube-corner geometry and a sphero-conical indenter with nominal radius 'smaller than 1 μm' and a cone opening angle of 90° (SC_1). Indents were made into γ-TiAl based microstructures with the Berkovich and cube-corner tools and into single phase γ-TiAl with the sphero-conical indenter. It is obvious that the cube-corner geometry represents the sharpest indenter tip, since its reaches the highest indentation depths for a given load.

The hardness data from Berkovich and cube-corner indentation in two different microstructures is plotted in figure 8.3 together with the available literature data. The hardness level of the microstructures was found to be lower than the literature data for single phase indentation of γ-TiAl and α_2-Ti_3Al. The qualitative trend of an increase in hardness at small indentation loads is in good agreement with the literature data.

One example of a Berkovich indent in γ-TiAl is given in figure 8.4. The image is taken in the 70° tilted position, usually used for EBSD measurements. The perspective was chosen to enhance the 3D perception of the indent shape. Large pile-up and slip traces are visible along one side of the impression. The fine surface structure is a result of the electro-polishing. The main orientation of the indented material is [4 5 7].

Based on the previously applied grid of Berkovich indentations, it was possible to find back any location inside the grid with high accuracy during interactive operation of the nanoindenter. The surface imaging capability of the machine was used to locate the

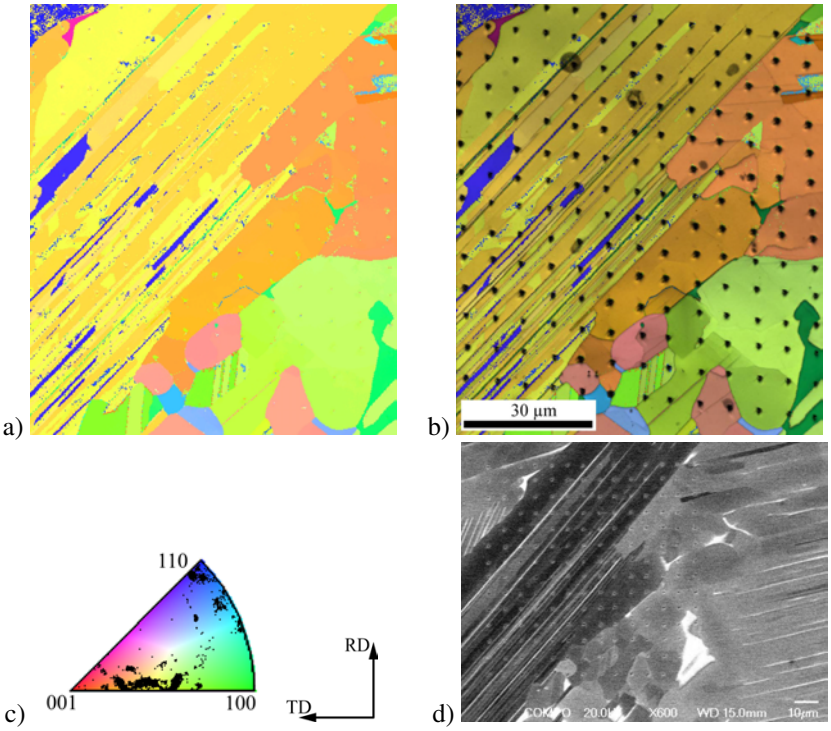

Fig. 8.1: EBSD orientation map of a region with lamellar microstructure and some large gamma grains. a) Only IPF color coding; b) additional indication of the EBSD pattern quality, marks from Berkovich indentations are visible. c) The color IPF legend includes the available indentation axes directions for the γ-phase. d) BSE image of the same region, α_2-phase is bright.

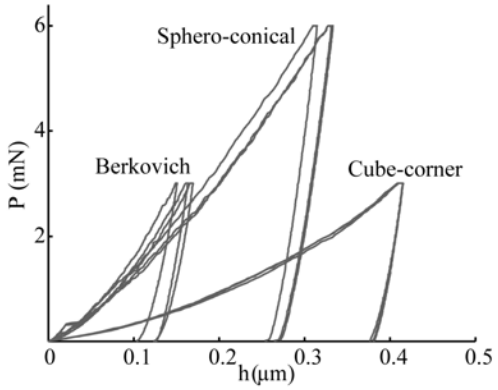

Fig. 8.2: Load-depth curves for indentations with different indenter geometries in TiAl microstructures. Maximum indentation loads P_{max} are 6 mN for the sphero-conical geometry (tip radius ≈ 0.8 µm, 45° half-cone angle) and 3 mN for the Berkovich and cube-corner geometries.

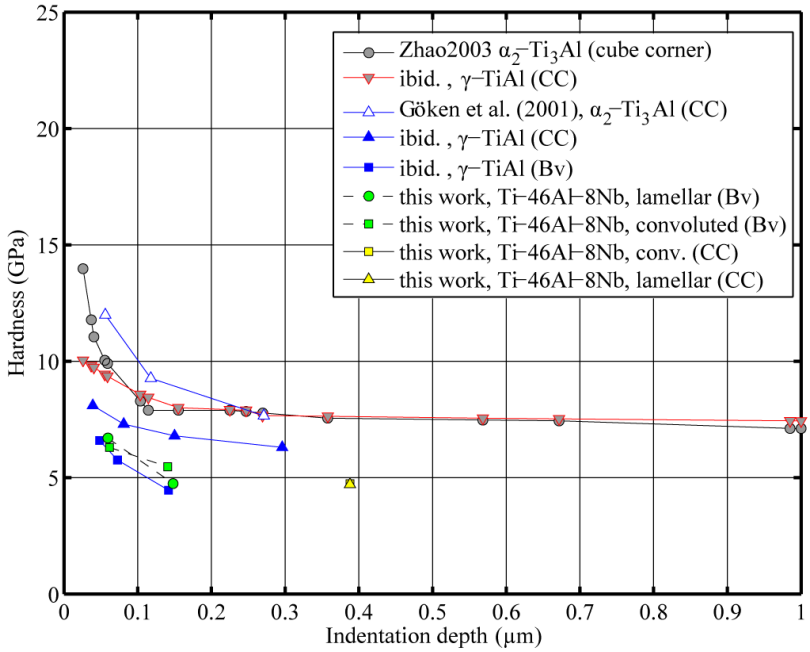

Fig. 8.3: Indentation size effect for γ-TiAl, and α_2-Ti_3Al in two-phase microstructures from the literature, plotted together with the experimental results from Berkovich (Bv) indentation into two-phase microstructures.

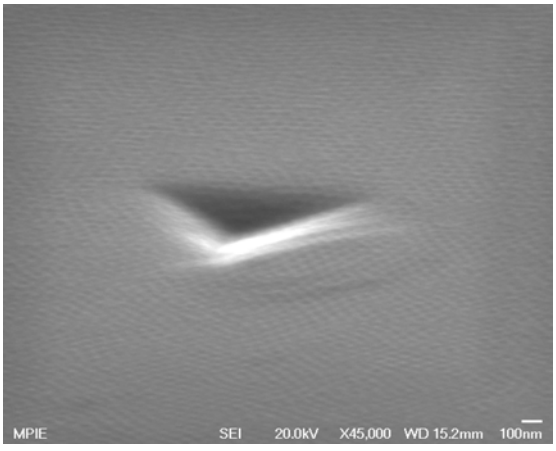

Fig. 8.4: Secondary electron image of a Berkovich nanoindent (3 mN) in γ-TiAl, viewed in 70° tilted position.

Berkovich indents. In this way further indentations with an axisymmetric tool were made inside some of the γ-grains between the Berkovich grid of indents, figure 8.5. Figure 8.6 illustrates the respective crystallographic directions of the indentation axis for the sphero-conical indents.

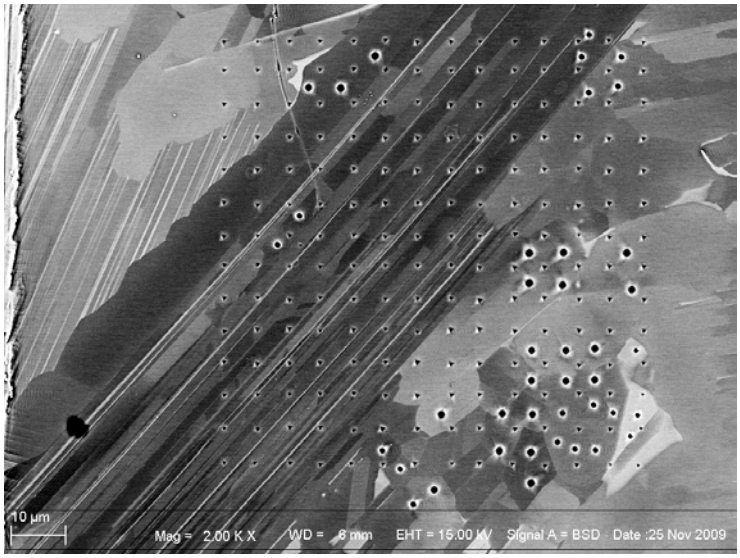

Fig. 8.5: The two-phase γ/α_2 microstructure with a square grid of 14×14=196 Berkovich indents (load 3 mN) and 41 indents made with two different sphero-conical indenter tips (loads 6 mN and 10 mN). The image is taken in backscatter electron mode and α_2-phase and the edges of the larger indents appear bright. Strong orientation contrast between different γ-TiAl domains is also visible.

Maximum indentation depths for different orientations are shown in table 8.2. The reproducibility of the measured maximum penetration depth was good. Several indents were placed not far away from visible grain boundaries and their indentation depths are reduce due to the grain boundary acting as an obstacle for the dislocations emitted from the indent (Yang and Vehoff, 2007).

8.2.3 Experimentally measured pile-up topographies of γ-TiAl

Figure 8.7 shows several Berkovich indents that were made into a lamellar microstructure. The crystal orientation was measured through EBSD and the resulting surface profile of four indents was measrued by AFM. The pile-up topography for one of these indentations (marked) is also given in Figure 8.8. It is the same indent that was already shown in figure 8.4. Indentation was made into a fine lamella of [4 5 7]-oriented γ-phase, 13° away from a [1 1 1] indentation axis. The Berkovich tip was oriented such that one ordinary slip direction operated towards the free surface along one face of the tip, figure 8.8-b. Correspondingly, a pronounced pile-up hillock was formed next to this face.

Tab. 8.1: Experimentally measured orientations for several indents; the indentation axis is given as $[u\,v\,w]$, the indenters had either Berkovich (B) or sphero-conical (SC_1, SC_2) geometries.

Ind. axis $[u\,v\,w]$	Indenter	$(\varphi_1, \Phi, \varphi_2)$, EBSD	$(\varphi_1, \Phi, \varphi_2)$, unit triangle
[4 5 7]	B	(122.5°, 42.2°, 128.0°)	(122.50°, 42.20°, 38.00°)
[14 13 2]	SC_1	(196.8°, 95.5°, 313.3°)	(16.80°, 84.50°, 46.70°)
[1 10 6]	SC_1	(169.9°,59.4°,275.9°)	(169.9°, 59.4°, 5.9°)
[3 1 4]	SC_1	(183.1°, 38.1°, 250.2°)	(183.1°, 38.1°, 70.2°)
[7 13 1]	SC_1	(206.80°, 87.00°, 298.60°)	(206.80°, 87.00°, 28.60°)
[1 11 13]	SC_1	(354.90°, 40.00°, 4.10°)	(354.90°, 40.00°, 4.10°)
[7 1 12]	SC_1	(3.30°, 29.50°, 352.00°)	(3.30°, 29.50°, 82.00°)
[13 1 11]	SC_2	(181.10°, 48.70°, 265.50°)	(181.10°, 48.70°, 85.50°)
[11 1 17]	SC_2	(178.10°, 147.60°, 93.60°)	(358.10°, 32.40°, 86.40°)
[3 1 4]	SC_2	(181.90°, 38.60°, 251.70°)	(181.90°, 38.60°, 71.70°)
[9 2 15]	SC_2	(185.00°, 149.70°, 101.30°)	(5.00°, 30.30°, 78.70°)

Tab. 8.2: Experimentally measured maximum indentation depths.

Ind. axis $[u\,v\,w]$	h_{max}(nm)	indenter
[14 13 2]	329, 335	SC_1, P_{max}=6 mN
[1 10 6]	311, 321, 317, 320	SC_1, P_{max}=6 mN
[13 1 11]	345, 347, 316[a]	SC_2, P_{max}=10 mN
[11 1 17]	369, 348, 345, 368	SC_2, P_{max}=10 mN
[3 1 4]	334, 338	SC_2, P_{max}=10 mN
[9 2 15]	369, 338[a]	SC_2, P_{max}=10 mN

[a] Value measured close to a grain boundary;

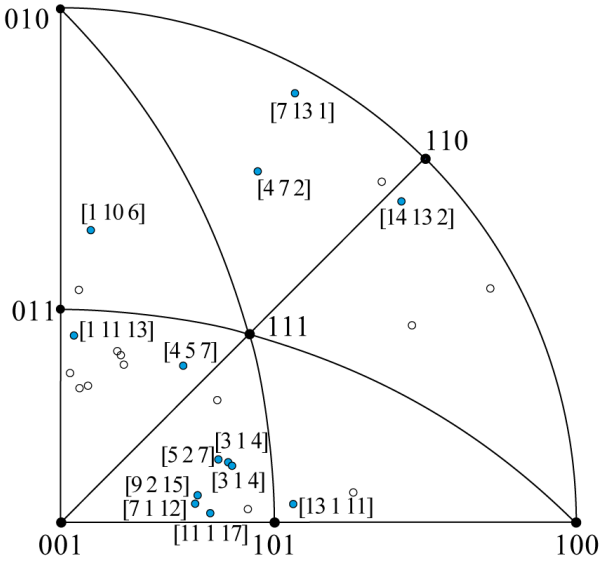

Fig. 8.6: Inverse pole figure of the experimental indentation axes (stereographic projection); filled circles show the actually indented orientations, open circles indicate the respective equivalent indentation axes; [*u v w*] indices were calculated with a tolerance of 1°.

Several γ-grains were indented with a sphero-conical indenter. Figure 8.9 shows the pile-up formation for a [1 10 6] indentation axis, table 8.1. Four hillocks of different sized were formed around the indent.

Figure 8.10 combines the results from an AFM topographic measurement and an EBSD orientation map. The two axisymmetric indentations into the α_2-phase exhibit a markedly different pile-up topography, with only two pile-up hillocks, in comparison to the γ-phase indents.

Figure 8.11 shows the pile-up behavior observed for indentation along the [14 13 2] direction, i. e. close to a [1 1 0] indentation axis. A sphero-conical indenter tip with a nominal tip radius smaller than 1 µm was used to place the indents inside the coarse γ-phase lamella. Also a reduced indentation load of 6 mN was used to limit the size of the impressions. Two pile-up hillocks were formed on opposite sides of the impression.

Since the pile-up pattern are not a uniaxial property of the crystal, their appearance will be mirrored when an improper rotation is applied, figure 8.12. Therefore a the standard triangle should be used, that contains only proper rotations based on orthogonal matrices with determinant 1. It is twice as large as the one that also allows for improper rotations based on orthogonal matrices with determinant -1, see Morawiec (2004). This result is a general one and also holds for pile-up patterns in materials with

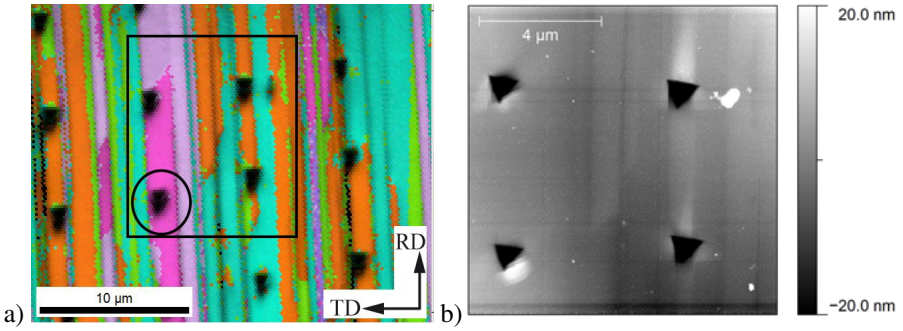

Fig. 8.7: Berkovich indents (3 mN) in a lamellar micostructure of γ-TiAl; a) The local microstructure around the indents as identified by EBSD; black markings are Berkovich indents, some thin α_2-lamellae are also shown in black. b) AFM topographic map of the marked area in (a); additional to the indentation pile-up, minimal height differences between different orientations of the crystallites are visible from electro-polishing.

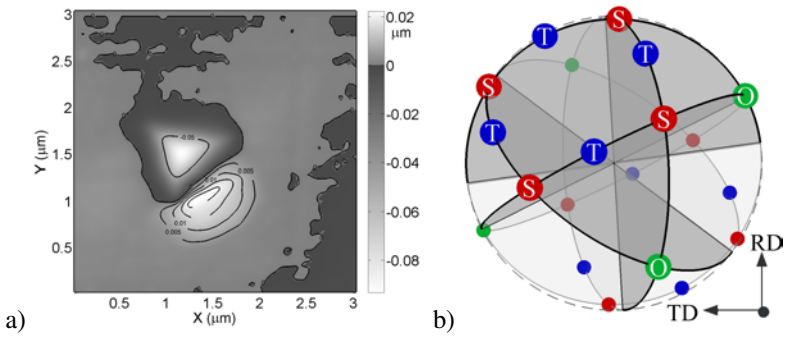

Fig. 8.8: The marked Berkovich indent from figure 8.7 close to a grain boundary; a) Indent topography (smoothed data); b) The indented crystal orientation, illustrated by {1 1 1}-planes and the possible shear directions, perspective projection.

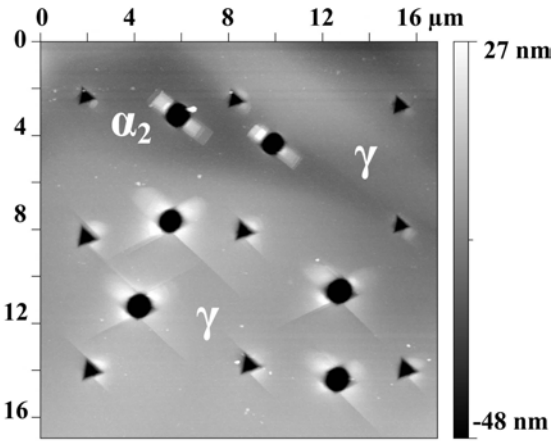

Fig. 8.9: AFM topographic map of nine Berkovich and six conospherical indentations with a maximum load of 3 and 6 mN, respectively. The Berkovich indents were automatically placed in a regular grid, the indents with sphero-conical tips were placed in-between the Berkovich indents after EBSD orientation mapping. The two phases γ-TiAl and α_2-Ti_3Al were indented.

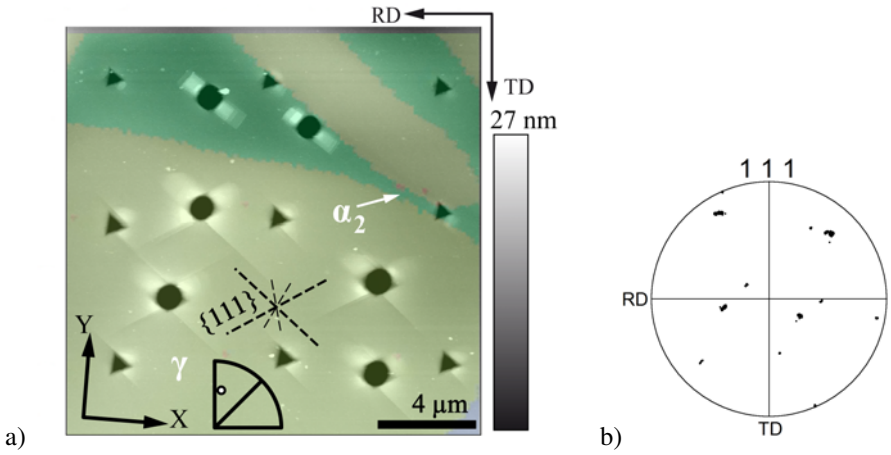

Fig. 8.10: Indentations made with a Berkovich indenter and a conospherical indenter in γ-phase and α_2-phase in a titanium aluminide microstructure. a) The AFM topographic map (grayscale) is overlaid with the inverse pole figure of surface normals expressed as crystal directions, IPF color legend see figure 8.1; b) The $(1\,1\,1)_\gamma$ pole figure of the region.

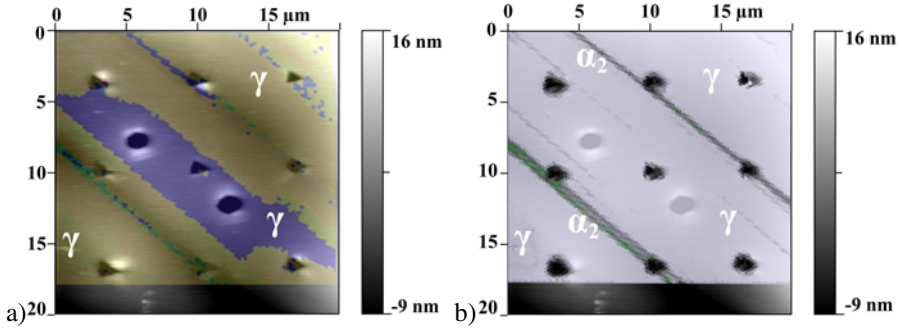

Fig. 8.11: Two sphero-conical indents in a γ-phase crystallite in a lamellar region of the microstructure; the orientation is close to a ⟨1 1 0⟩ indentation axis; two pile-up hillocks were formed on opposite sides of the indents; a) topographic AFM grayscale map overlaid with the EBSD orientation scan; b) occurrence of thin α_2-lamellae is shown in green in the EBSD phase map.

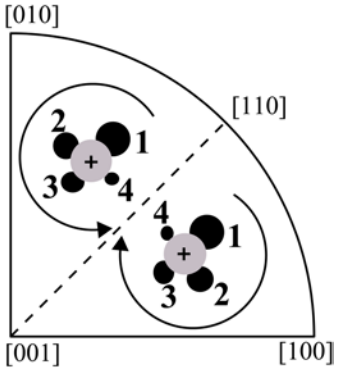

Fig. 8.12: Two pile-up patterns for two indentation axes that can be converted into each other by an improper rotation. The stereographic projection of the indentation axes orientations is marked by the crosses (+). The mark from the indenter is shown in gray and the black circles denote four generated pile-up hillocks of varying size.

other crystal structures.

8.2.4 Discussion of the nanoindentation results

In the presented experiments, almost identical indentation curves were found for both phases with a sphero-conical indenter. Göken et al. (2001) reported the α_2-phase to be significantly harder than the γ-phase. However, in Göken et al. (2001) the α_2-indents were made in narrow lamellae and a hardening effect from the boundaries cannot be excluded, see Yang and Vehoff (2007) for the boundary effect in nickel. Therefore, the intrinsic hardness of α_2-phase is assumed to be not significantly higher than the hardness of γ-TiAl. However, the oxygen content could have a significant effect on the hardness values. It follows that assessing the hardness of α_2-phase in two-phase microstructures is a difficult task, since oxygen is known to segregate stronly into this minor phase, c. f. section 2.4.

Glide steps were observed to be in agreement with slip on closest packed {1 1 1}-planes. In principle, the surface steps could also result from thin twins. Additional EBSD measurements were performed at low accceleration voltages and high magnification, in order to identify EBSD patterns from twinned material around the indent. At 10 kV acceleration voltage, no contribution from twin orientations could be observed in the recorded Kikuchi patterns. The ultimate proof for the absence of fine twins could only be provided through TEM measurements.

Through the use of different indenter geometries, an observation was made, which has important implications for the usage of non-axisymmetric indenters on crystalline samples. As visible in figure 8.9, the Berkovich indentations show pile-up characteristics different from the indents made with a sphero-conical tool. The approximate rule that can be derived is that pile-up formation for three-sided pyramidal indenters will only take place, when the faces are oriented favourably for the formation of this pile-up. If sharp edges are pointing close to the positions where pile-up is formed during axisymmetric indentation, then the formation of this hillock will be reduced or inhibited completely.

8.3 CPFEM simulation of nanoindentation in γ-TiAl

8.3.1 A finite element model of single crystal indentation

It has been shown earlier, that crystal plasticity simulation of the indentation process can give valuable insight into the complex three-dimensional deformation mechanics (Wang et al., 2004, Zaafarani et al., 2006, Zambaldi et al., 2007, Zaafarani et al., 2008).

The intention behind the simulation of indentation in γ-TiAl included the following main points:

- To establish the relation between crystallographic orientation and the mechanical response during instrumented indentation. This included the development of characteristic pile-up patterns. Further the orientation dependence of the intrinsic hardness due to activation and interaction of different sets of deformation mechanisms should be clarified.
- Special orientations should be identified which are especially suited to clarify the relative strength of the different types of deformation mechanisms. Since

the single phase intrinsic strengths of dislocation glide and twinning cannot be tested in single crystals, nanoindentation is an especially attractive technique to characterize these properties.

For the 3D FE-model, figure 8.13, a cylindrical cut-out of the material was chosen. The initial point of contact between indnter and sample was positioned in the center of the upper circular area with coordinateds (0, 0, 0). The indentation direction was the negative z direction.

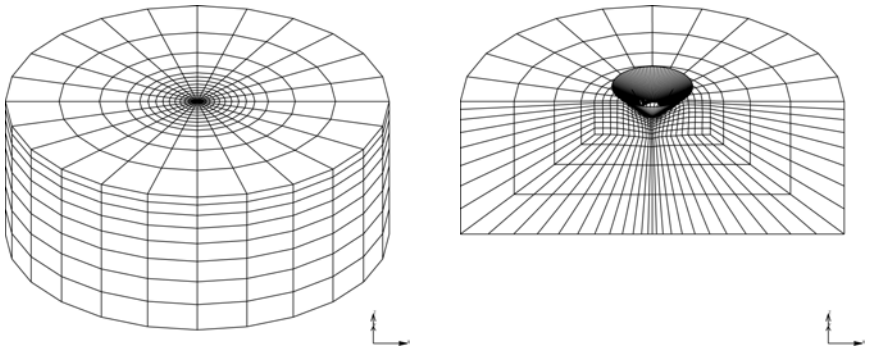

Fig. 8.13: Undeformed and deformed mesh of an indentation simulation with 4224 hexahedral elements. The right side shows one half of the model and the rigid surface of the indenter.

The indenter geometries were modeled by a rigid body. A simple mesh was chosen for the discretization of the problem to be able to parameterize the mesh generation efficiently, figure 8.13. The sample diameter and height were chosen to depend on the indenter geometry and the targeted final indentation depth. The model height was chosen to be at least 10 times the indentation depth.

Different scenarios were used for the boundary conditions in earlier modeling work, to approximate the desired result of an infinite half-space. Here, the boundary conditions were chosen as follows: the outer shell nodes of the virtual indentation sample were fixed against lateral displacements and free in vertical direction. The bottom surface nodes of the sample were fixed against vertical displacements but allowed to move in lateral directions. The indenter was moved along the vertical axis in the center of the cylindrical sample and was fixed against movement or rotation in other directions. The indentation depth was imposed through a constant velocity to the desired indentation depth. After the maximum indentation depth was reached, unloading was started without holding segment and with the same constant velocity as the indentation. Velocities were chosen to complete the loading to the maximum penetration within 1 second.

For the single crystal constitutive behavior the crystal plasticity model as described in section 7.2 was used. The absence of grain boundaries justifies the application of such a non-local model to the problem of single crystal indentation.

8.3.2 Influence of friction on simulated pile-up profiles

Friction is known to have a negligible effect on the load-displacement response in indentation simulation, e. g. (Bhattacharya and Nix, 1988). However, a small coefficient

of friction was found to limit the mesh distortion at larger indentation depths. Therefore, a coefficient of friction of 0.3 was assumed in the simulations.

For the study of the influence of friction on the simulated pile-up profiles, the parameters in table 8.3 were used. Coefficients of friction were varied from 0.1 to 1.

Tab. 8.3: Parameters of the crystal plasticity model, m=20, $\dot{\gamma}_0 = 0.001\ s^{-1}$.

	τ_0, MPa	τ_s, MPa	h_0, MPa	a
$\boldsymbol{b}^{\mathrm{O}}$, $\boldsymbol{b}^{\mathrm{T}}$	150	1200	1000	2.5
$\boldsymbol{b}^{\mathrm{S}}$	300	2400	1000	2.5

Table 8.4 gives the results for the different friction parameters. The simulated indentation was into [0 0 1]-oriented γ-TiAl, with ordinary slip, super slip and the twinning systems activated. The indenter had a tip radius of 0.8 µm and a 90° cone angle. Maximum indentation depth was 300 nm.

Tab. 8.4: Influence of choice of the coefficient of friction (COF) on simulated indentation pile-up height and maximum load;

COF	$z_{\max}$ (µm)	$P_{\max}$ (mN)
0.1	0.044	5.45
0.2	0.040	5.554
0.3	0.035	5.546
0.4	0.031	5.54
0.6	0.031	5.529
0.8	0.031	5.53
1.0	0.031	5.53

8.3.3 Establishing the model and the constitutive parameters

Simulations of nanoindentation were performed. For the three-sided Berkovich indenter geometry a high distortion of the finite element discretization was observed near the edges of the indenter. Too large distortion is not tolerated by the finite element solver and will stop the calculation. This problem could be overcome by using the effective cone indenter geometry. The effective cone is defined by its semi-apex angle, α_{eff}, that results in the same dependence of the projected contact area from the square of the indentation depth, A(h^2), as the related three-sided or four-sided pyramid.

Simulations with a sphero-conical indenter revealed that the pile-up profile around the indent is not mainly influenced by the indenter geometry. The main features of the resulting surface profile were also found in the experimentally measured topographies that were produced by indentation with a three-sided pyramid. Therefore, the deformation of the free surface around the indent can be interpreted as the fingerprint of the deformation processes within the plastic zone, as will be discussed in more detail later.

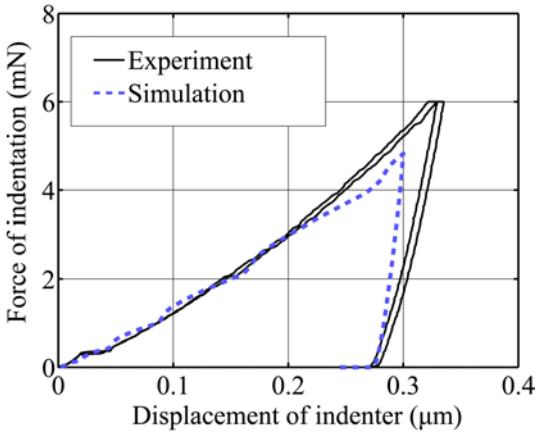

Fig. 8.14: Load displacement curves from simulation and experiment

The simulated load-displacement curves showed reasonable agreement with the measured curves, figure 8.14.

The approach to calibrate the crystal plasticity parameters with nanoindentation experiments is especially appropriate, because the size effect in γ-TiAl and α_2-Ti_3Al is found to be smaller than for other material. This was reported by Zhao et al. (2003) for the case of cube corner indentation, figure 8.3. Already at indentation depths as small as 200 nm the hardness deviates only by a few percent from the macroscopic value. Therefore, the activated deformation and hardening processes are expected to be approximately the same as in the bulk single crystalline phases. Correspondingly, any additional strengthening of fine microstructures should mainly be related to the phase interfaces that act as a dislocation barriers.

The initial values for the critical resolved shear stress, as well as for the self-hardening and latent hardening directly influence the simulated pile-up profile. High hardening rates will lead to the formation of sink-in around the impression, whereas moderate and low hardening rates result in piling-up.

The influence of the self and latent hardening on the load-displacement response is illustrated in figure 8.15. The same model was simulated three times and only the hardening behavior was changed. Three cases were considered, namely the case of constant critical shear stresses on all deformation systems, only self-hardening of the systems or self-hardening with additional cross-hardening. The lowest indentation loads are observed in the case of constant shear strengths. A moderate cross-hardening coefficient of 1.4 increases the simulated loads significantly.

The exact tip geometry is not known a priori. To obtain a reasonable approximation of the true tip geometry, an initial series of simulations was performed, to adjust the tip radius and the cone opening angle. Iteratively, the tip radius of the simulations was changed until the difference between the simulated and the measured remaining indent topographies became minimal, figure 8.16.

After the identification of a suitable tip geometry, the hardening parameters were adjusted to achieve the best possible match between the measured pile-up profiles and

Fig. 8.15: Load-displacement curves from CPFEM simulations; The influence of the latent hardening ratio was investigated through the three simulated cases of no hardening, i. e. constant shear strengths, only self-hardening and additional cross hardening with a coefficient of $q = 1.4$. Results are shown for a near-[1 1 0] indentation axis; only ordinary and super dislocation systems were activated during the simulation (sphero-conical tip with radius 0.6 µm and a cone apex angle of 90°).

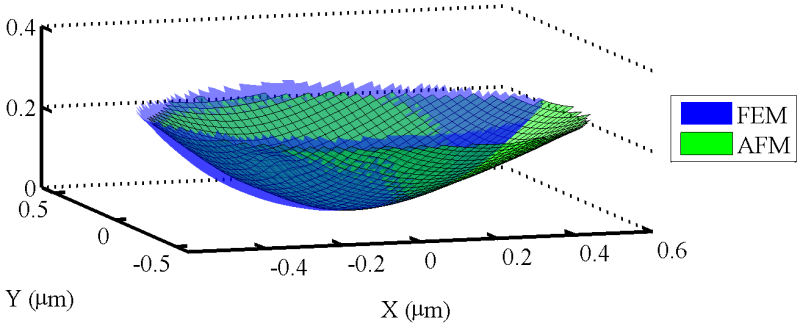

Fig. 8.16: Comparison between AFM and FEM residual impressions. Only the part of the remaining indent is taken into account which is below 10% of the indent depth. Since remaining indentation depths vary slightly, the minimum height value was set to zero for the comparison.

the simulated ones. At the same time, a match between the experimental and simulated load-penetration curves was aimed at.

8.3.4 Computational costs of three-dimensional indentation simulation

Due to the anisotropic character of crystal plasticity and the complex stress and strain fields involved in the indentation, a simplified treatment by planar or quasi-axisymmetric 2D models is not possible. The need for a full 3D simulation, imposes some restrictions in terms of the finite computational resources. Therefore, the computational costs should be shortly considered here.

Using a single core of a dual-core AMD Opteron 880 processor, running at 2.4 GHz, the simulation of an indentation model consisting of 15060 hexahedral 8-node elements in MSC.Marc completed in 40 hours. A significant part of the computational effort is consumed by the material law formulated as a subroutine within the finite element system, the precise fraction depends on the model size. The simulation was performed with a sphero-conical indenter of 0.6 μm tip radius and a 90° opening angle. Maximum indentation depth was 0.3 μm. The deformed mesh is shown in figure 8.17. Another system with improved performance completed similar simulations with a reduced mesh size in about three hours.

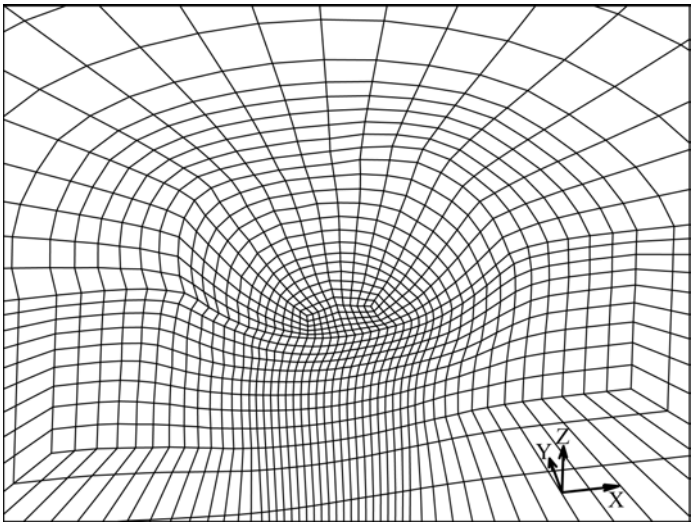

Fig. 8.17: The plastically deformed region of the finite element model. One half of the model is not shown to make visible the details of the mesh structure.

8.4 A method for a combined experimental and simulation study of single crystal indentation

For a combined experimental study of the orientation dependent pile-up behavior during axisymmetric indentation, the following steps were identified:

i. A convention has to be established, which uniquely defines a full crystallographic orientation for a given indentation axis orientation. In the case of an axisymmetric indenter, choosing an indentation axis leaves a rotational degree of freedom around the indentation axis. The convention removes this rotational degree of freedom by defining a unique crystallographic orientation of the laboratory X- and Y-axis for indentation in Z-direction.

ii. On the experimental side, single crystals or polycrystalline microstructures are indented. If only polycrystalline material is available, large grains should be indented far away from the boundary. Indentations are performed into various orientations. Enough data for a specific indentation load or maximum depth of indentation is collected, when the experimental coverage of orientation space approaches the resolution of the theoretical orientations.

iii. The orientation unit triangle needs to be discretized at an appropriate resolution and the discrete orientations are used for simulation of indentations. If the resolution of the discretization is high enough, interpolation between the results becomes feasible. Preferably, the misorientation between the discrete orientations should be constant to obtain a constant resolution throughout the orientation space.

iv. The experimentally collected topographies are deviating from the convention defined under (i) in a random rotation angle around the indentation axis. Therefore this rotation angle around the indentation axis needs to be calculated and the topographic information can then be back-rotated into the orientation following the convention defined under (i).

v. Finally, the back-rotated experimental topographies are compared to the simulation results. Location and shape of the experimental pile-up hillocks will match the simulation results well if an appropriate constitutive law was used in the simulations. The exact ratio between pile-up peak heights and the remaining indentation depth can provide additional information about the hardening and cross-hardening properties.

Remark to (ii): If possible, in the indentation of polycrystalline samples it is not superfluous but beneficial to indent more than one grain with nearly identical indentation axis. This will make visible influences from non-axisymmetric indenter shapes, residual stresses or local dislocation configurations present in specific grains. In the case of scatter of the measured pile-up topographies an averaging procedure could be applied to the measured topographies with identical indentation axes.

8.4.1 An in-plane orientation convention for the unique representation of pile-up profiles

The orientation convention was chosen based on a simple thought experiment in which a spherical single crystal is placed under the indenter. Initially, the crystallographic axes of the spherical crystal are aligned with the laboratory coordinate system, figure 8.18-a. The choice of an initial orientation is straightforward for the tetragonal structure of γ-TiAl, by defining c-axis $\parallel Z$ (Z is the indentation direction), a-axis $\parallel X$,

b-axis ∥ *Y*. For non-orthogonal crystal systems the orthonormal basis has to be defined, see appendix B.3 for the case of hcp structures.

The orientation convention then describes the most simple rotation to reach any point on the sphere inside the unit triangle. In crystal coordinates the indenter axes is rotated into the [0 0 1]–[1 0 0]–[1 1 0] triangle by a rotation by the angle η around a rotation axis. The rotation axis is generated by rotation of the crystallographic *y*-axes around the crystallographic *z*-axes by the angle ζ.

Two angles are defining the position of the indentation axis in the unit triangle. An orthonormal basis of the crystal is given by $[x_c, y_c, z_c]$. The two angles are then defined as the angle between the crystallographic z_c-axis, [0 0 1] in case of γ-TiAl, and the indentation axis, η, and the angle between the indentation axis projected into the x_c-y_c-plane, (0 0 1) for γ-TiAl, and the x_c-axis, here denominated by ζ. In the present work the convention for a unique full orientation was defined in terms of Bunge Euler angles, $(\varphi_1, \Phi, \varphi_2)$, see appendix B.1. These can be calculated from the spherical coordinates, η and ζ, as

$$(\varphi_1, \Phi, \varphi_2) = (270^\circ + \zeta,\ \eta,\ 90^\circ - \zeta).$$

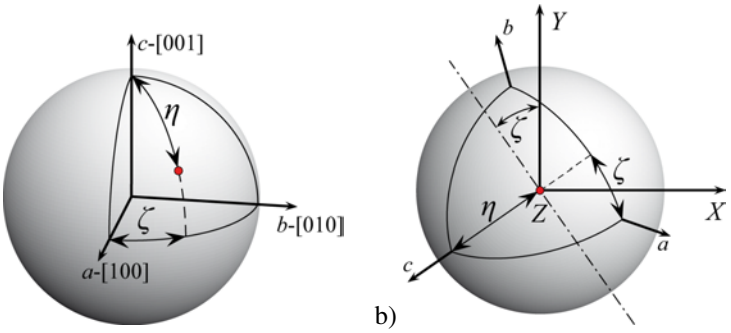

Fig. 8.18: Illustration of the orientation convention for displaying pile-up topographies; a) The crystal coordinate system $[x_c, y_c, z_c]$ where $x_c \parallel a$, $y_c \parallel b$, $z_c \parallel c$; a desired indentation direction, defined by the spherical coordinates $(\zeta,\eta) = (35^\circ, 60^\circ)$, is marked by the red dot. b) The indenter coordinate system [*X*, *Y*, *Z*] with the crystal rotated after the convention as defined in the text; *Z* is anti-parallel to the indentation direction; the rotation axis is shown by the dot-dash line.

The involved calculations are presented for the example of an indentation along the (1 1 1) plane normal of the γ-TiAl phase. The unit vector of the indentation axis, $\boldsymbol{Z} = (0,0,1)$ in laboratory coordinates, in the initial crystal coordinate system, denominated by $\boldsymbol{z}$, is then given by $\boldsymbol{z} \approx (0.581, 0.581, 0.570)$ for a c/a ratio of 1.02. The rotation angle, ζ, around the crystallographic *c*-axis is $\zeta = \mathrm{atan}(\frac{z_y}{z_x}) = 45^\circ$. The rotation angle, η, away from the *c*-axis is $\eta = \mathrm{atan}(\frac{\sqrt{z_x^2+z_y^2}}{z_z}) \approx 55.27^\circ$, slightly larger than in the case of a fcc structure (54.74°). The corresponding Bunge Euler angles can then be calculated as

$$(\varphi_1, \Phi, \varphi_2) = (270^\circ + \zeta,\ \eta,\ 90^\circ - \zeta) \approx (315^\circ,\ 55.27^\circ,\ 45^\circ).$$

If an orientation representation by rotation matrices is preferred, the orientation matrix, $\boldsymbol{g}$, can be calculated from two rotation matrices, $\boldsymbol{R}_y(\eta)$ and $\boldsymbol{R}_z(\zeta)$, given by

$$\boldsymbol{R}_y = \begin{pmatrix} \cos\eta & 0 & -\sin\eta \\ 0 & 1 & 0 \\ \sin\eta & 0 & \cos\eta \end{pmatrix}, \quad \boldsymbol{R}_z = \begin{pmatrix} \cos\zeta & \sin\zeta & 0 \\ -\sin\zeta & \cos\zeta & 0 \\ 0 & 0 & 1 \end{pmatrix}$$

$$\boldsymbol{g} = \boldsymbol{R}_z(\zeta)\boldsymbol{R}_y(\eta)\boldsymbol{R}_z^T(\zeta).$$

8.4.2 Simulation results for 51 orientations in the unit triangle

Helming et al. (1998) suggested a near-equidistant discretization of orientation space. The first stage of their method was used to generate a number of 21 directions in the standard orientation triangle of the fcc structure at an approximate resolution of 9°[1]. By appropriate symmetry operations, these directions were expanded to fill the [0 0 1]–[1 0 0]–[1 1 0] unit triangle of the tetragonal structure figure 8.19. Using the convention defined above, the directions were converted to full crystallographic orientations. Details of the involved calculations and a list of the resulting Bunge Euler angles are given in appendix B.2.

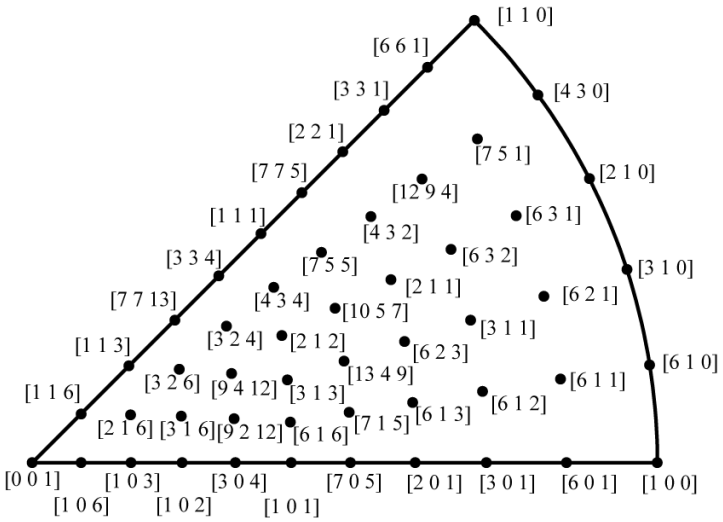

Fig. 8.19: Stereographic projection of equidistant directions at 9° resolution;

Indentation was simulated for 51 orientations in the unit triangle of γ-TiAl. Figure 8.20 presents the resulting pile-up topographies in a graph that will be referred to as the *pile-up inverse pole figure (pile-up IPF)*. The individual topographies are placed at the inverse pole figure representation of their respective indentation axes. The topographies are in-plane oriented after the convention defined in section 8.4.1, with $X \parallel [1\,0\,0]$

[1] Because such near-equidistant discretizations are of interest in the scope of numerical integration on the unit sphere, starting points for other suitable discretizations might be found in Ehret et al. (2009) and references therein, e. g. Bažant and Oh (1986).

and $Y \parallel [0\,1\,0]$. Topographies in the [0 0 1]–[1 1 0]–[0 1 0] triangle can be obtained by a mirror operation of the given topographies through the $(\bar{1}\,1\,0)$ plane, as described above, figure 8.12.

Different regimes are visible for the shape of the pile-up profiles. Between 1 and 4 dominant hillocks are formed for different orientations: close to the [0 0 1] indentation axis a four-fold symmetric pattern emerges with four hillocks of identical height. Close to [1 1 1] there is only one dominant hillock located in the $[1\,1\,\bar{2}]$ direction.

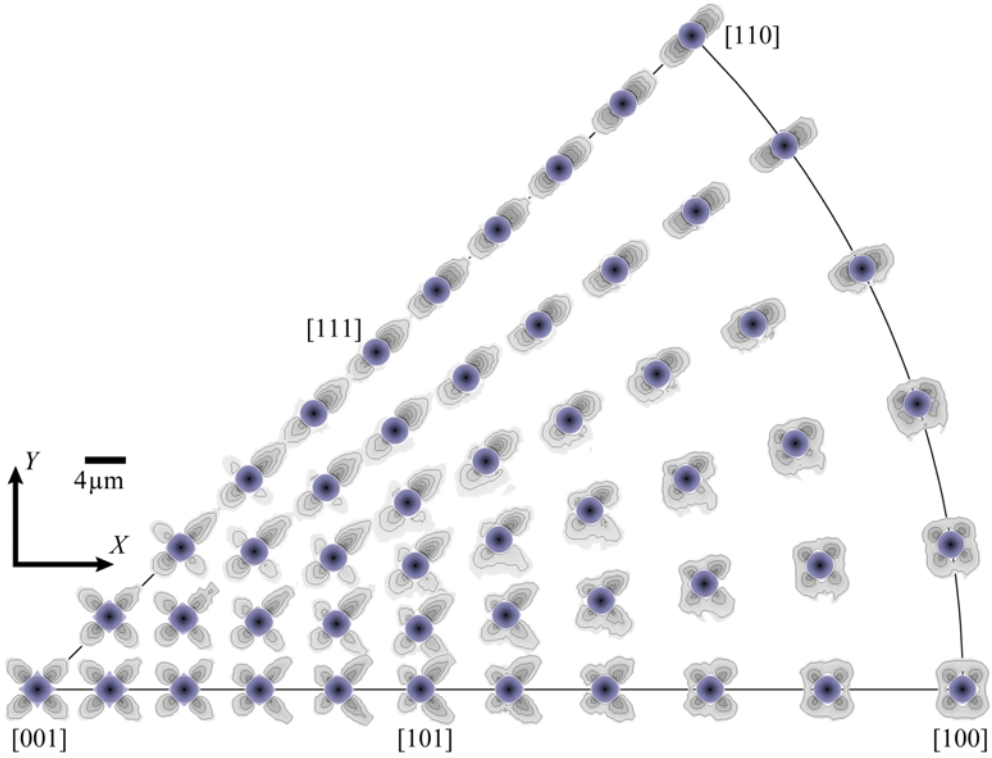

Fig. 8.20: Predicted pile-up patterns evolving in γ-TiAl. The topographic data was obtained from 51 CPFEM simulations. The individual patterns are placed in an inverse pole-figure projection of the respective indentation axes. The impressions are shown in bluish color, the upheaval in grayscale.

The crystal plasticity parameters used in the simulations are given in table 8.5. From the performed indentation simulations it was found that a resolution of 9° provides high enough detail throughout the orientation space to enable smooth interpolation between the supporting points. Generally, the transition from one region to another is smooth and no abrupt changes in the pile-up shapes are observed.

8.4.3 Detailed results for high symmetry orientations

For the five high-symmetry indentation axes [0 0 1], [1 0 1], [1 0 0], [1 1 0], and [1 1 1] between one and four dominant hillocks were observed: for a [0 0 1] orientation axis a

Tab. 8.5: Parameters of the crystal plasticity model for ordinary dislocation glide ($\boldsymbol{b}^{\mathrm{O}}$), superdislocation glide ($\boldsymbol{b}^{\mathrm{S}}$) and twinning ($\boldsymbol{b}^{\mathrm{T}}$) systems, m=20, $\dot{\gamma}_0 = 0.001\,\mathrm{s}^{-1}$; τ_0 is the initial slip resistance, τ_s the saturation slip resistance, h_0 influences the initial hardening slope and a is the hardening exponent, equation (7.10);

	τ_0, MPa	τ_s, MPa	h_0, MPa	a
$\boldsymbol{b}^{\mathrm{O}}$	55	400	300	2.5
$\boldsymbol{b}^{\mathrm{S}}$	165	1200	300	2.5
$\boldsymbol{b}^{\mathrm{T}}$	110	800	300	2.5

Tab. 8.6: Experimentally measured orientations need to be converted to the theoretical convention defined in 8.4.1, the orientation can then be expressed as Bunge Euler angles, $(\varphi_1, \Phi, \varphi_2)$, or as polar coordinates, (ζ, η). Additionally, the angular deviation from the nearest orientation of the near-equidistant discretization is given; also the in-plane rotation angle is specified to transform the experimental pile-up topographies according to the convention.

Ind. axis $[u\,v\,w]$	$(\varphi_1, \Phi, \varphi_2)$	(ζ, η)	dev. angle	in-plane rot. ang.
[14 13 2]	(133.3°, 84.5°, 46.7°)	(43.3°, 84.5°)	2° to #38	243.5°
[1 10 6]	(354.1°, 59.4°, 5.9°)	(84.1°, 59.4°)	5° to #113	4.2°
[3 1 4]	(289.8°, 38.1°, 70.2°)	(19.8°, 38.1°)	3° to #13	106.7°
[7 13 1]	(331.4°, 87.0°, 28.6°)	(61.4°, 87.0°)	4° to #91	124.6°
[1 11 13]	(355.9°, 40.0°, 4.1°)	(85.9°, 40.0°)	5° to #74	274.7°
[7 1 12]	(278.0°, 29.5°, 82.0°)	(8.0°, 29.5°)	5° to #7	265.3°
[13 1 11]	(274.5°, 48.7°, 85.5°)	(4.5°, 48.7°)	5° to #17	93.4°
[11 1 17]	(273.6°, 32.4°, 86.4°)	(3.6°, 32.4°)	4° to #11	264.5°
[3 1 4]	(288.3°, 38.6°, 71.7°)	(18.3°, 38.6°)	4° to #13	106.4°
[9 2 15]	(281.3°, 30.3°, 78.7°)	(11.3°, 30.3°)	4° to #8	263.7°

four-fold pile-up pattern, with four dominant hillocks in the ⟨1 1 0⟩ directions, resulted from the simulation, similar to the pattern in fcc crystals. The [1 0 1] orientation exhibits two dominant hillocks in neighboring positions. A [1 0 0] indentation axis shows a pattern similar to the [0 0 1] axis, but the four-fold symmetry is broken and only two-fold symmetry remains. The [1 1 0] indentation axis results in two major hillocks on opposite sides of the impression. For the case of [1 1 1]-indentation only one dominant protuberance is formed.

8.4.4 Comparison of experimental and simulated pile-up topographies

Generally, experimental and simulated pile-up patterns showed good agreement. Due to the continuum character of the CPFEM simulations, the experimentally observed slip lines will not occur in the finite-element results.

Table 8.6 lists the indented orientations from table 8.1, after application of an in-

plane rotation, to make them compliant with the in-plane orientation convention defined above, section 8.4.1. After the experimentally measured pile-up topographies are rotated according to the convention, they can directly be compared to the simulated pile-up IPF, figure 8.20. If the indented orientation is outside the orientations covered by the simulated pile-up IPF, the experimentally observed pile-up shape can be correlated to their respective counterpart in the predicted pile-up IPF, through a mirroring operation as described above, figure 8.12. This is the case for example for the [1 10 6]-indents shown in figure 8.10.

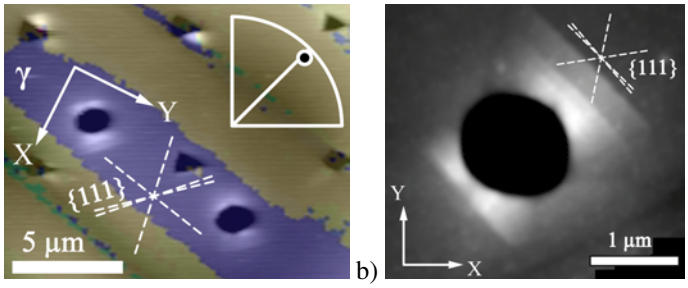

Fig. 8.21: a) Topography (grayscale) of two sphero-conical indents in a coarse γ-phase lamella of orientation [14 13 2], c. f. the inverse pole figure projection of the indentation axis; color indicates grain orientations. The grayscale coloring ranges to about 18 nm surface elevation. The maximum indentation load was 6 mN. The inscribed *X*-*Y* coordinate system is in-plane rotated after the defined convention. Four Berkovich indentations (maximum load 3 mN) are also visible. b) Higher resolution topography of one of these indents, in-plane rotated after the convention defined in section 8.4.1.

The further analysis will focus on indents made into orientations close to high-symmetry indentation axes. Similar pile-up shapes to the ones observed in figure 8.21 are observed in the CPFEM simulations of orientations near the [1 1 0] indentation axis in figure 8.20, with two pile-up hillocks on opposite sides of the impression.

Figure 8.22 compares an experimentally measured pile-up topography to the simulation result for a [1 0 1] indentation axis. The pile-up topographies are displayed following the convention defined above. Agreement between the measured and simulated topographies is discussed below in terms of the activated deformation mechanisms.

8.5 Discussion of the developed nanoindentation method

8.5.1 Relation between surface deformation and plastic anisotropy

The measurement of intrinsic single phase properties in complex alloys and compounds is of high importance. The mechanical response of real microstructures, such as two-phase γ-TiAl/α_2-Ti_3Al-microstructures, results from the combination of intrinsic properties with the influence of the phase boundaries (Parthasarathy et al., 1998, Maruyama et al., 2004). Better understanding of these interface effects can only be gained through their separation from the single phase properties.

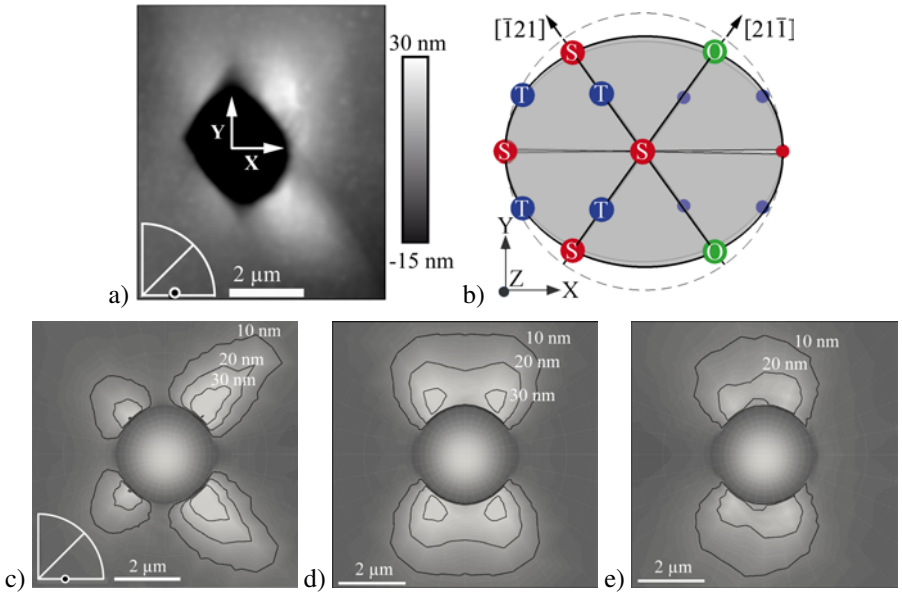

Fig. 8.22: Pile-up topographies for: a) indentation along [13 1 11], about 5° from [1 0 1], AFM topography; b) Perspective projection of the {1 1 1}-planes and shear directions for exact [1 0 1] indentation; green depicts ordinary dislocation glide. c) Simulated indentation along [1 0 1], $\tau_c^O/\tau_c^S < 1$ (stoichiometric γ-TiAl); sphero-conical tip, radius 2.7 µm, cone-angle 146 °; d) A generic fcc-equivalent with $\tau_c^O/\tau_c^S = 1$; e) Simulated pile-up topography for $\tau_c^O/\tau_c^S > 1$, expected for Al-rich TiAl. The topographies are displayed after the convention defined in figure 8.18.

In the previous sections, a combined approach was presented to characterize and understand the plastic anisotropy of γ-TiAl during indentation. Orientation mapping of the indented crystallites was combined with the surface topographies from AFM measurements. CPFEM simulations, based on the experimentally measured orientations and on the preexisting knowledge about possible deformation modes in γ-TiAl, then revealed the potential of the presented approach to link the orientation dependent pile-up patterns to the operating deformation systems. With the identified constitutive parameters, the orientation dependent pile-up behavior was predicted for all possible indentation axes to construct the pile-up IPF.

Height, shape and distribution of the emerging hillocks clearly reflect the distinct shear directions in the material on the individual deformation systems. These processes are observed at single phase level, thereby isolating the mechanical behavior from the influence of grain boundaries as well as lamellar and domain boundaries. The topography of the pile-up shape was a characteristic feature of the indented crystallographic direction as has been previously reported for indentation into high-symmetry orientations of copper (Wang et al., 2004).

In comparison to the known fcc pile-up patterns, the effect of the strong plastic anisotropy of γ-TiAl becomes evident. For [1 1 1]-indentation one dominant pile-up hillock was simulated while in fcc crystals the [1 1 1] pile-up shape exhibits three-fold symmetry (Osmond and Cartaud, 1906, Wang et al., 2004). In fcc crystals the [1 0 1] and [1 1 0] indentation axes result in equivalent topographies, while in γ-TiAl the axes result in different pile-up shapes, figure 8.20.

In γ-TiAl, the [1 0 1] indentation axis is particularly suited to investigate the relative strengths of ordinary dislocation glide, τ_c^O, and superdislocation glide, τ_c^S. Figure 8.22 compares the resulting pile-up topographies for the cases $\tau_c^O/\tau_c^S < 1$, $\tau_c^O/\tau_c^S \approx 1$ and $\tau_c^O/\tau_c^S > 1$. In the first case, which was also observed experimentally, pronounced pile-up is formed in the $[2\,1\,\bar{1}]$ and the $[1\,\bar{2}\,\bar{1}]$ directions, i. e. on the right hand side of the indent. For slip of identical dislocations as in fcc metals, four hillocks of equal height are formed (Wang et al., 2004). Easy activation of superdislocation glide systems, as expected for Al-rich γ-TiAl, leads to pile-up formation similar to the one observed in fcc crystals. Depending on the chosen hardening parameters, the dominant hillocks have also been simulated to appear on the opposite sides compared to stoichiometric γ-TiAl, in the directions $[\bar{2}\,\bar{1}\,1]$ and $[\bar{1}\,2\,1]$, i. e. on the left hand side of the indent when displayed according to the in-plane orientation convention. Taking into account these additional simulations, it can be concluded that in γ-TiAl the [1 0 1] indentation direction could be employed as a sensitive indicator of the relative amounts of dislocation glide activities on ordinary and superdislocation systems: depending on which glide mechanism is easier to operate, pile-up can potentially form on either side of the indent.

The formation of the simulated and experimentally observed pile-up shape in [1 0 1] indentation can be explained by analysing the CPFEM results. Figure 8.23 relates the crystallographic shear on the individual deformation systems to the upheaval of material as shown by the contour lines. The study of slip activities below the indent confirmed the intuition from the crystallographic relations, figure 8.22-b, namely, that easy slip on two ordinary dislocation systems is responsible for the two dominating pile-up

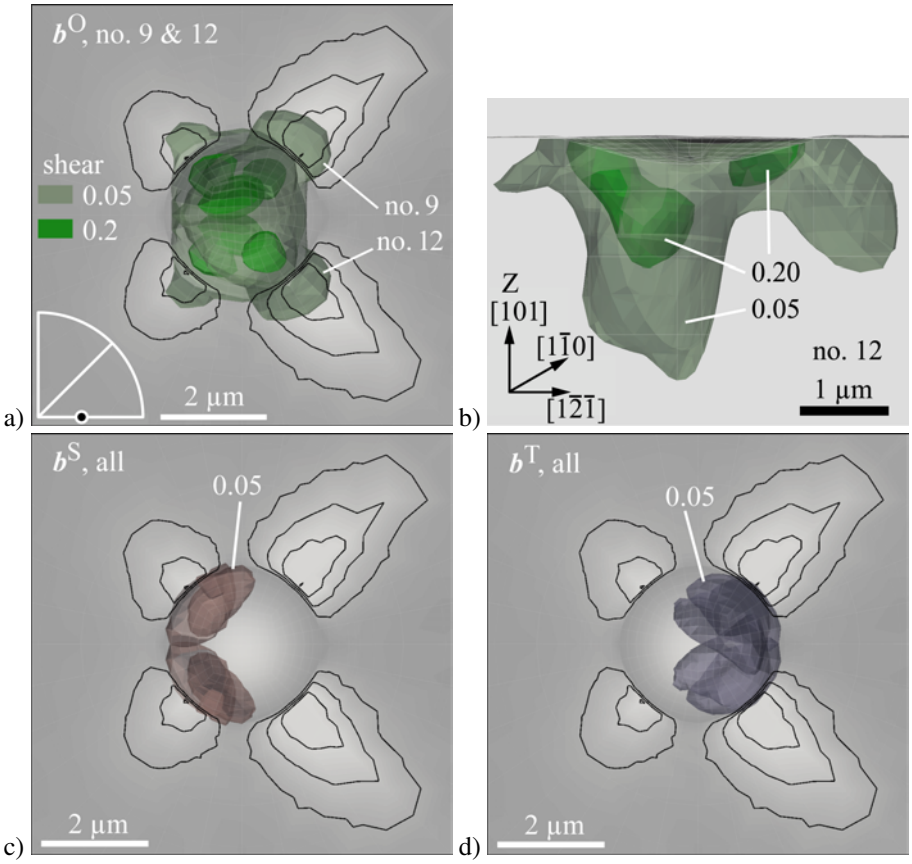

Fig. 8.23: Simulated surface topography from figure 8.22-c, overlaid with the plastic shear distribution: a) highly activated ordinary slip systems no. 9 & no. 12, cf. table 3.3, shown by semi-transparent isolevel-surfaces at levels 0.05 and 0.2, differentiated by saturation; b) shear on system no. 12, viewing axis perpendicular to the shear direction [1 $\bar{1}$ 0]; c) all superdislocation systems; red iso-surfaces: shear level 0.05; d) all twinning systems; blue iso-surfaces: shear level 0.05.

hillocks. The formation of the pile-up hillocks could be related to the existence of distinct zones of slip activity below the surface, revealed by the simulation. Quantification of the relative magnitude of the slip resistances for ordinary and superdislocations is not straightforward due to the nonlinear influence from cross-hardening; however, the performed simulations suggest that superdislocations can resist shear stresses which are higher by a factor of two to three in comparison to the stresses that will initiate ordinary dislocation glide.

Generally, the orientation dependent pile-up formation corresponds to a projection of the 3D anisotropic plasticity of the material into a 2D height distribution around the indent. In analogy to the measurement of crystallographic texture, i. e. the orientation distribution function (ODF), the resulting picture is not complete by measuring just one pile-up topography or pole figure, respectively. Instead, measurements of more than one indentation axis have to be performed in order to compile a 3D understanding of plastic anisotropy. However, for the case of indentation pile-up, the mathematical tools for what is called the pole figure inversion in the realm of texture, still have to be developed. The applicability of non-linear optimization to a similar, computationally less demanding inverse problem has been performed recently for Hill's anisotropic elasto-plastic material formulation (Bocciarelli et al., 2005).

8.5.2 Possible applications of the developed method

Characterization of the orientation dependent pile-up behavior by the presented experimental and computational methods introduces a number of analysis tools: first, the pile-up IPF, figure 8.20, can be used as a lookup-table for a coarse identification of the crystallographic orientation of the indented material. For example, if an fcc structure was used for fast orientation mapping of the γ-phase by EBSD, in many cases the order variant can be uniquely identified based on the pile-up shape. The determination of crystallographic orientation might be done more exactly by including in the analysis the position of the slip traces (Chang and Chen, 1995). Second, the relative contributions of different deformation systems to the plastic deformation can be characterized by the presented method. The uniqueness of this feature should be stressed. While detailed TEM studies are indispensable for the analysis of the types and interaction of dislocations, statistically significant data is difficult to obtain by TEM alone. This limitation can be overcome by the presented method because a large number of dislocations is active to form the pile-up hillocks.

In case that the orientation of indented grains was measured by EBSD, the height of the pile-up hillocks in different microstructural conditions might be compared to asses the microstructural state before indentation. Precise relations between microstructural states such as work-hardened or pre-stressed conditions should be studied experimentally in the future.

8.5.3 Discussion of the influence of indenter shape

Axisymmetric indenters are clearly suited best for the approach developed in this thesis. The interaction of non-axisymmetric geometries will always narrow down the generality of the observed pile-up. Alternatively the edges of non-axisymmetric indenters would have to be oriented with respect to the crystallographic orientation that is indented. Since sensitivity of the pile-up formation against even minor misalignments of around 1° is high, this alternative method is not recommended.

It should be noted here that on the basis of St. Venant's principle (Fischer-Cripps, 2000, pg. 25, sec. 1.2.12) the geometry of the indenter will have decreasing influence on the material flow with increasing distance of the material point under consideration from the indenter surface. Indeed shear contributions for simulated Berkovich indentations showed circular shapes when viewed in direction of the indentation axis.

One major influence that is left for axisymmetric indenters is the usage of blunt or sharp indenters. Sharp tools with small cone angles are believed to lead to inaccuracies in the evaluation. At small indentation depths, the glide steps will interact geometrically with the indenter surface and lead to scatter in the contact area. For larger indentation depths, the work dissipated by friction will be of significant magnitude in comparison to the work of plastic deformation. Gradients in the stress and strain-fields will be higher.

The use of sphero-conical indenters with minimum possible radii and full opening angles of 90° or 120° is recommended. These are also well suited for the CPFEM simulation of indentation. A trade off has to be made for the tip radius, since current manufacturing methods seem to not allow for sharp tips in 120° conical indenters. Further, the axisymmetry of the used indenter should be checked by topographic analysis of remaining indent shapes in plastically isotropic material or direct measurement of the indenter surface by AFM.

Although the shape of the sphero-conical indenter might vary from case to case, the hillock patterns could always be calibrated on a reference state or reference material. However, if reproducibility of the measured pile-up patterns is desired two possibilities exist: either sharp tips and large indentation depths are used for which geometrical self-similarity is approximated, or well-defined tip geometries are used, which are not geometrically self-similar for a variation of the indentation depth and can be manufactured with good accuracy only for relatively large tip radii of about 5 μm and above. In the former case only the opening angle of the indenter enters the pile-up analysis, while for the latter option the tip radius represents an additional variable.

8.5.4 Analysis of deformation mechanisms

From the combined investigation by EBSD, AFM and crystal plasticity simulation, an assessment of the deformation mechanism could be performed. The main deformation mechanism for the γ-phase in the Ti-46Al-8Nb (at.%) alloy was ordinary dislocation glide. This appears to be in contrast to earlier findings by Mahapatra et al. (1995), who reported twinning as the primary deformation mode. However, in those previous experiments the orientation of the near-stoichiometric layer was such that the Schmid factors for ordinary dislocation glide became minimal. Assuming a high Peierls barrier for superdislocation glide, as also supported by the present work, twinning was left as the only deformation mode providing deformation along the [0 0 1] compression axis. Therefore, it is probable that twinning is the predominant deformation mechanism during uniaxial compression of stoichiometric γ-TiAl along [0 0 1]. However, for more general deformation, mainly ordinary dislocation glide is expected to be responsible for the plastic shape change. This finding is in agreement with conclusions from TEM studies (Appel et al., 2000).

Whether the many observed ordinary dislocations in deformed lamellar microstructures are related to the intrinsic properties of the stoichiometric γ-phase or are a result

from the interfaces acting as dislocation source is still under discussion in the current literature (Katzarov et al., 2007, Katzarov and Paxton, 2009). By the combination of nanoindentation experiments with CPFEM simulation, it could be shown that ordinary dislocation glide is activated in the γ-phase in absence of the lamellar interfaces.

Regarding the activity of twinning in the analyzed TiAl-Nb alloy it should be mentioned that the nucleation of twins in γ/α_2-microstructures is thought to mainly take place at stress concentrations at the interfaces Appel et al. (1993), Chen and Zhang (2002), Appel (2005), Hsiung et al. (2002). Since the aim of the present study was to identify the single phase behavior of γ-TiAl, unaffected by interfaces, only indentations away from the interfaces have been analyzed. Therefore, a discrepancy between the relative contributions of dislocation glide and twinning is possible for single phase indentation as opposed to macroscopic deformation of two-phase microstructures. At the same time, absence of pronounced twinning in indentation experiments, combined with experimental evidence for high twin activity in microstructures with densely spaced interfaces, can provide an indirect validation of interface nucleation of twins.

8.5.5 The advantage of relying only on high precision measures

The presented method has an advantage that distinguishes it from conventional nanoindentation experiments. It relies only on data that can be measured with good accuracy. These are the indenter load, the residual indent depth and the surface profile. Current resolutions in load transducers are on the order of 1 nN and the displacement resolution is about 0.04 nm (Hysitron Inc., 2003). The surface profiles can be measured by AFM with vertical resolutions much better than 1 nm. In contrast to the measurement of hardness or indentation modulus, which rely on estimated contact areas, the measurement of remaining indent topographies is a robust characterization method that can be carried out with high precision.

Inaccuracies in the presented method could result from inadequate surface preparation. Another source of inaccuracy are possible deviations of the indenter geometry from the ideal shape. Especially deviations from axisymmetry might introduce changes in the pile-up patterns, as can be observed in the extreme case of the Berkovich geometry.

8.5.6 Other advantages of the presented method

Compared to other indentation analysis methods that are based on cross-sectional analysis such as TEM lamella extraction by FIB, or cross-sectioning by FIB or serial sectioning by surface removal, the AFM characterization is much easier to perform. Therefore, the characterization by indentation, EBSD and AFM is, in principle, well-suited for high-throughput analysis.

The reduction of the 3D plastic anisotropy to a 2D-data set has several advantages in terms of efficient data-handling. Also, more detail is contained in the 2D surface profiles in comparison to the 1D indentation curve. The pile-up profile provides a well-suited interface between experiment and simulation because it is easy to extract in both approaches.

8.5.7 Preliminary estimate on the anisotropic hardness of γ-TiAl

Hardness measurement on single crystals is related to two effects: First the pile-up or sink in behavior will lead to orientation dependent change of the contact area; Second

the discrete slip systems will lead to intrinsic orientation dependence of the resistance against an intruding indenter through the change in Schmid factors or cross-hardening relations. If pile-up effects are not taken into account in the evaluation of the measured data, the resulting hardness values will be affected by both effects simultaneously and the true hardness anisotropy will not be obtained.

Nevertheless, the experimental values for the indentation depths of different orientations, with identical loads and identical tools, can be used for a preliminary analysis of the hardness anisotropy of γ-TiAl, not taking into account the orientation dependent changes in contact area through piling-up. The numbers are indicative for an intermediate hardness level of stoichiometric γ-TiAl for [1 0 1] indentation. Lower hardness is expected for orientations closer to [0 0 1] and higher hardness for orientations closer to [1 0 0]-indentation. These preliminary results are also supported by the CPFEM simulations which additionally predict a global hardness maximum of γ-TiAl between the [1 1 1] axis and the [1 1 0] indentation axis. However, the present amount of experimental data is not sufficient to draw an inverse pole figure projection of the anisotropic hardness of γ-TiAl. The orientation dependence of hardness is much lower compared to the pile-up topographies. The simultaneous action of multiple stress states during indentation makes the hardness also a less anisotropic property than, for example, the uniaxial flow stress. Further, simulations with deactivated cross-hardening revealed that the contribution to the indentation load from the cross-hardening are on the same order of magnitude as the indentation resistance from the self-hardening, figure 8.15. Correspondingly, the cross-hardening parameters will have a significant influence on the simulated hardness anisotropy and have to be investigated further. Figure 8.24 illustrates the subtle differences in maximum indentation loads for the simulated high symmetry indentation axes. Apart from the [0 0 1]-indentation axis which shows a clear minimum load, the load penetration curves are observed at similar load levels.

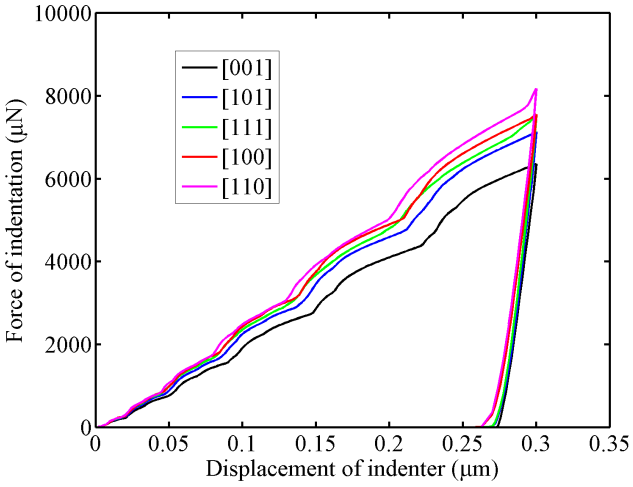

Fig. 8.24: Simulated load displacement curves for five high-symmetry orientations. Maximum loads are predicted close to a [110] indentation axis, minimum loads for the [001] axis;

8.6 Conclusions

Nanoindentation can give valuable information on the single phase behavior of intermetallic phases with complex deformation behavior such as γ-TiAl. Mechanical characterization becomes feasible for materials that cannot be obtained in bulk single crystalline form. Especially the advanced characterization by orientation microscopy and scanning force microscopic techniques provides valuable insight. The extended characterization makes possible the simulation of the indentation process by the crystal plasticity finite element method. In contrast to the measurement of hardness or indentation modulus, which rely on estimated contact areas, the measurement of remaining indent topographies is a robust characterization method that can be carried out with high accuracies.

The indentation pile-up response is a characteristic feature of the deformation processes during indentation. This implies that the out-of-plane material flow is mainly governed by the arrangement of indenter and the possibilities of crystallographic slip provided by the crystal structure. The crystal plasticity finite element method is well suited to predict and analyze the formation of the characteristic surface topography during indentation.

The deformation during single crystal indentation is orientation dependent. The hardness and elasticity, in comparison to uniaxial plastic or elastic deformation, show a smaller sensitivity to the indented crystallographic orientation, due to activation of multiple slip systems and the non-uniaxiality of the elastic deformation. The pile-up pattern formation, however, is orientation dependent and characteristic of the plastic flow in the indented material. For materials such as γ-TiAl which exhibit anisotropic plasticity, a wide variety of pile-up patterns can be observed.

The analysis of pile-up patterns gives information on the contributing deformation systems. In contrast to TEM analysis, statistical significance is not an issue in the evaluation of pile-up patterns since the integrated effect of dislocation motion is represented in the piled-up volume. Neither slip lengths nor dislocation densities or dislocation configurations need to be known to carry out the analysis. Only the total shear contribution of the possible deformation systems are characterized.

The newly introduced pile-up inverse pole figure enables the compact presentation of the indentation pile-up behavior of crystals throughout their fundamental orientation space. Once prepared from experiment or simulation, it can serve as an efficient reference for comparative studies of single-crystal phases with different compositions and identical or different crystal structures. In this way, changes in the activated deformation systems or the hardening behavior can be detected.

The predominant usage of three-sided pyramidal indenters for crystalline matter is mainly based on historical reasons and related to the easy manufacturing of sharp three-sided indenters. Sharp axisymmetric tips are better suited for nanoindentation of crystallites because they do not introduce additional geometrical unknowns into the experiment. Additionally, if the indenter is sharp and the indentation depth much larger than the tip radius, the indentation process becomes geometrically self-similar. Geometrical self-similarity has additional advantages such as better comparability of measured topographies or the possibility of direct re-scaling to compare experimental and simulation results.

9

A homogenized constitutive law for two-phase γ/α_2 microstructures

9.1 Introduction

The nanoindentation work explained in chapter 8 is mainly aimed at the intrinsic single phase behavior without interfaces. This micro-scale analysis is important for influences on the micromechanics from alloy chemistry, such as Al-content, ternary alloying elements, and impurities. However, for the two-phase alloys it is known that the interfaces between the γ-variants and between γ- and α_2-phase dominate the mechanics on the grain level.

The dislocation barrier effect of interfaces is not included in the CPFEM formulation used in this work. Due to the continuum approach of the finite element method the treatment of grain boundaries is difficult and possible implementations of these effects are investigated for disordered model materials at the moment (Ma et al., 2006a,b). At the same time, it is well known that γ-TiAl based alloys obtain their beneficial properties like toughness and good creep resistance mainly through the interface of the γ-domain structure and from γ/α_2 interfaces (Dimiduk et al., 2001).

Therefore, the micromechanical modeling was extended to a homogenized material model which incorporates the anisotropic flow behavior of two-phase microstructures on the length scale of lamellar grains. Good agreement was found between experimental data and the simulated micromechanics in terms of PST yield anisotropy, field fluctuations and the pre-yielding of lamellar microstructures.

9.2 Rationalization of the selection of incorporated slip systems

In previous modeling work crystal-plasticity simulation has been applied to two-phase microstructures of TiAl/Ti_3Al in different ways. In the phase-resolved approaches the γ- and α_2-phase were arranged according to their spatial distribution in the microstructures. Examples are the works of Fischer, Parteder, Schlögl, Marketz et al. (Schlögl and Fischer, 1997a,b), or of Werwer and Cornec (2000, 2006). Both groups incorporated the effect of kinematic constraints additionally into the γ-phase or into both phases.

While those previous approaches might be interesting from the viewpoint of fundamental research, they could possibly also be regarded as a case of over-modeling: the

effect of the two-phase microstructure is used to tune the mechanical properties of both phases, while at the same time the two-phase resolution is maintained in the modeling, i. e. different finite elements are assigned different phases. The two-phase resolution of the model imposes a major restriction on the applicability of those models. They cannot be used to directly model microstructures, since the number of elements necessary to resolve the fine-scaled phase distribution exceeds the computational resources quickly.

In the works of Kad et al. (1995), and later of Brockman (2003) or of Grujicic and Batchu (2001), a different modeling strategy was followed. Only the deformation modes relevant to the kinematically constrained microstructures were incorporated into a single phase crystal plasticity model. Since the restriction to resolve the spatial distribution of the different phases does not apply to this approach, grain aggregates can be modeled with moderate requirements on computational costs. Following these ideas, a similar approach was developed for a micromechanical description of two-phase γ/α_2 microstructures.

Theoretically, the full number of deformation systems for each of the two phases and the six orientational γ-variants, could be implemented into a CPFEM constitutive law. A total number of $6 \times 16 = 96$ systems for the γ-TiAl variants, and additionally 12 systems from the hexagonal phase would have to be considered. The resulting 108 deformation systems would extend the calculation times for the CPFEM method by an unknown high factor. Indeed it is not sure that convergence could be reached in feasible times, as no implementation of such a model was tested.

The special crystallographic relations of the involved phases and deformation systems makes possible a description with a smaller number of deformation systems. As it is assumed that the γ-phase order variants are present in comparable volume fractions in the lamellar microstructure, their cubic pseudo-symmetry can justify the contraction of their super and ordinary dislocation systems to a single set of deformation modes which incorporate the effective behavior of both dislocation types. Following this approach also for the other deformation modes, the theoretical number of 108 deformation systems was systematically reduced to 18 systems of the following types:

- 3 effective systems for super/ordinary dislocation glide on the $(1\,1\,1)_\gamma$ lamellar plane;
- 3 effective (bi-directional) systems for twinning in the $(1\,1\,1)_\gamma$ lamellar plane;
- 6 effective systems along the pyramidal slip systems of α_2-phase, providing the translamellar deformation modes;
- 6 effective systems for mixed mode dislocation glide.

This simplified single phase treatment requires the assumptions of equal volume fractions of orientational γ-variants and a strict Blackburn orientation relationship between α_2 and γ-phase.

The resulting 18 deformation systems were implemented in the elasto-viscoplastic crystal plasticity formulation that was already applied to the case of single-phase mechanics of γ-TiAl. Again different characteristics could be prescribed for different modes of deformation. The deformation systems are listed in table 9.1.

The selected deformation modes have been found to govern the anisotropic flow behavior in lamellar microstructures, c. f. section 3.6.1. For a lamellar angle, Φ_L, close to zero (i. e. the lamellar interfaces are parallel to the loading direction), the *mixed mode* deformation systems have the highest Schmid factor and are activated. The mixed mode deformation is taking place with Burgers vectors parallel to the lamellar interfaces. The slip planes are inclined to the interfaces at an angle of about 70° and therefore some more resistance against dislocation motion is expected since the dislocations are expected to interact with the interface and dislocation half-loops protruding from the interfaces.

In the intermediate range of lamellar angles from 15°-75° the yield stresses fall to a minimum value associated with easy glide on (1 1 1) planes parallel to the lamellar interfaces and with the Burgers vectors also in the (1 1 1) planes. This deformation mode is termed the *longitudinal* or *easy glide mode*.

For lamellar angles close to 90°, i. e. deformation perpendicular to the lamellar interfaces, the interfaces between α_2-phase and γ-phase act as a strong dislocation barrier and the yield stress rises to its maximum value – the *transversal mode* of deformation governs the micromechanics. The *transversal mode* of deformation takes place with the slip planes and the Burgers vectors both being oriented in an angle with the interface plane. For incorporation into the crystal plasticity model, the decision had to be made whether to include the transversal slip systems only from the γ-phase, only from the α_2-phase, or from both phases. The relative barrier strengths of the boundaries are not known and the mechanical properties of the very thin α_2-lamellae can only be guessed. Because quantitative information on the relative strength contributions not available and to increase computational efficiency, only the six pyramidal slip systems from the α_2-phase were taken into account. They are well-suited to represent the translamellar deformation mode. The transversal slip systems of the γ-phase twin and matrix variants would have made necessary the consideration of at least 12 ordinary and super dislocation systems and 6 twin systems and therefore would have resulted in longer computation times with negligible additional value for the simulation capabilities.

Tab. 9.1: Slip systems of the homogenized material law; 'M/T' denotes systems that are present in the matrix family $M = \{M1, M2, M3\}$ as well as the twin family T={T1, T2, T3} of γ-TiAl-domains. 'o/s' is used for systems that will mainly deform by ordinary dislocations in specific domains but superdislocations could be activated in adjacent order domains to relief stress concentrations. 't' denominates the effective twinning deformation modes in the γ-variants, implemented as three additional bi-directional shear-systems, see text.

Number	slip plane	slip direction	type	morphology
1		$[0\,1\,\bar{1}]$	o/s	longitudinal
2	$(1\,1\,1)^{M/T}$	$[1\,0\,\bar{1}]$	o/s	longitudinal
3		$[1\,\bar{1}\,0]$	o/s	longitudinal
4		$[1\,1\,\bar{2}]$	t	longitudinal
5	$(1\,1\,1)^{M/T}$	$[1\,\bar{2}\,1]$	t	longitudinal
6		$[\bar{2}\,1\,1]$	t	longitudinal
7	$(1\,1\,\bar{2}\,1)$	$[\bar{1}\,\bar{1}\,2\,6]$		
8	$(1\,\bar{2}\,1\,1)$	$[\bar{1}\,2\,\bar{1}\,6]$		
9	$(\bar{2}\,1\,1\,1)$	$[2\,\bar{1}\,\bar{1}\,6]$	pyramidal /	transversal
10	$(\bar{1}\,\bar{1}\,2\,1)$	$[1\,1\,\bar{2}\,6]$		
11	$(\bar{1}\,2\,\bar{1}\,1)$	$[1\,\bar{2}\,1\,6]$		
12	$(2\,\bar{1}\,\bar{1}\,1)$	$[\bar{2}\,1\,1\,6]$		
13	$(\bar{1}\,1\,1)^{M}$	$[0\,\bar{1}\,1]$	o/s	mixed
14	$(1\,\bar{1}\,1)^{M}$	$[1\,0\,\bar{1}]$	o/s	mixed
15	$(1\,1\,\bar{1})^{M}$	$[1\,\bar{1}\,0]$	o/s	mixed
16	$(\bar{1}\,1\,1)^{T}$	$[\bar{1}\,0\,1]$	o/s	mixed
17	$(1\,1\,\bar{1})^{T}$	$[0\,1\,\bar{1}]$	o/s	mixed
18	$(1\,1\,\bar{1})^{T}$	$[\bar{1}\,1\,0]$	o/s	mixed

9.3 Application of the homogenized material law to the anisotropic plasticity of PST-crystals

Numerical experiments were carried out with different sets of parameters and the model matched the findings from experiments on PST-crystals well. The well-known anisotropic yielding behavior, see section 3.6.1, was accurately predicted, figure 9.1. In the experiments as well as for the simulation, a pronounced yield stress minimum exists for inclinations of the lamellar interface of approximately 45° away from the loading axis.

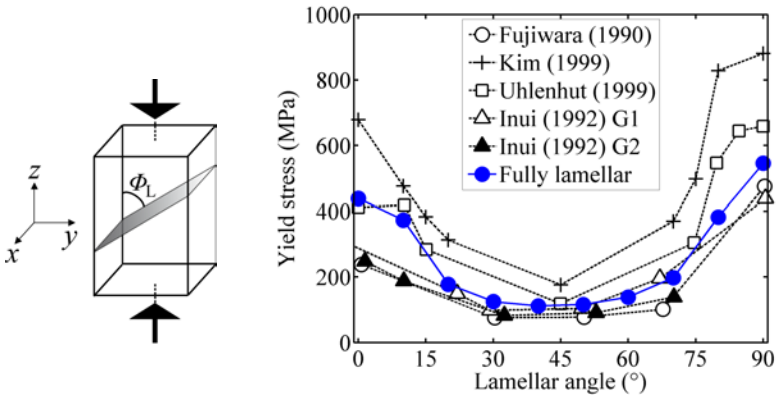

Fig. 9.1: The simulated yield stresses show good agreement to the experimental data for the dependence from the inclination of the lamellar interfaces, Φ_L.

Furthermore, the evolution of relative transverse strains, figure 9.2, was also reproduced with good agreement for the same set of parameters. When the lamellar plane is parallel to the loading axis ($\Phi_L \approx 0°$) no effective length change takes place perpendicular to the lamellar interfaces. All lateral strain is accommodated in the direction along the lamellar interface and perpendicular to the loading axis. If the loading direction is normal to the lamellar planes ($\Phi_L \approx 90°$), the lateral strains are equal and amount to about minus one half of the strain in loading direction. More details about this *channeling of deformation* are given in Kishida et al. (1998), Kim et al. (1999a), and Paidar and Yamaguchi (2007).

Additionally, the model has proven its flexibility to reflect different sets of experimental results obtained for PST-crystals of different microstructures under uniaxial tension and compression.

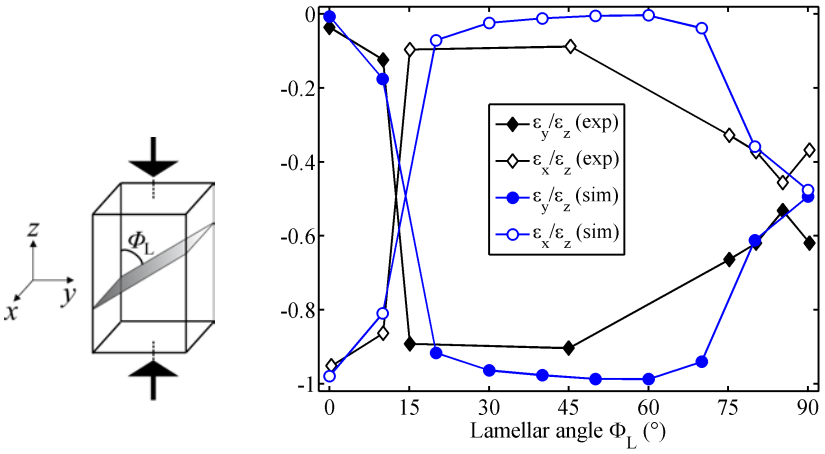

Fig. 9.2: The experimentally observed behavior of the relative transverse strains is captured by the model; experimental data from Uhlenhut (1999). In the used coordinate system the lamellar plane rotates around the x-direction ($[1\,1\,\bar{2}]$ of γ-M1) and uniaxial compression is applied along the z-direction.

9.4 Application of the homogenized law to two different microstructures

The availability of a model which accurately describes the plastic deformation of the lamellar microstructure, in conjunction with the flexibility of the finite element method to solve complex boundary value problems, enabled the simulation of realistic microstructures. To investigate the effect of the microstructural arrangement of the constituent phases on the mesoscopic and macroscopic deformation characteristics, two types of microstructures were targeted for the simulations. On the one hand, the fully lamellar (FL) microstructure was chosen, figure 9.3-a. Neglecting the hardening from the high-angle grain boundaries, it was simulated with the previously identified parameters for the PST-crystals.

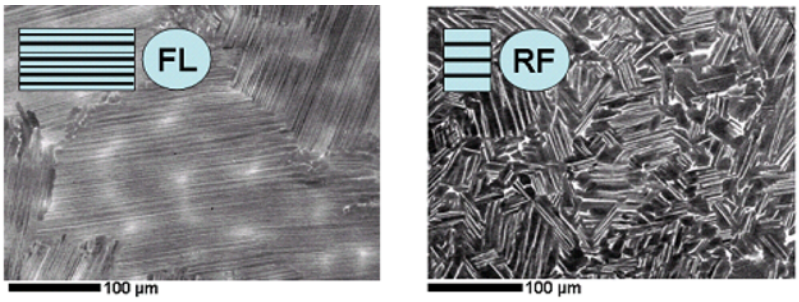

Fig. 9.3: Fully lamellar (FL, left) and refined (RF, right) microstructures of Ti-46Al-8Nb; BSE imaging mode, the refined microstructure is taken from Wu and Hu (2005, fig. 1).

Tab. 9.2: Parameters of the homogenized crystal plasticity model, m=20, $\dot{\gamma}_0$ = 0.001 s^{-1}. The numbering of deformation systems refers to table 9.1. Two sets of parameters were defined for the fully lamellar (FL) and the refined (RF) or convoluted microstructure.

No.	type	τ_0, MPa	τ_s, MPa	h_0, MPa	a
1-6	FL, easy glide	50	500	1000	2.5
1-6	RF, easy glide	117	1167	1000	2.5
7-18	FL, mixed and transversal	250	2500	1000	2.5
7-18	RF, mixed and transversal	225	2250	1000	2.5

For the second type of material, the 'convoluted' microstructure was chosen, figure 9.3-b. It is an example for the general case of a refined (RF) microstructure. It has previously been investigated as a way to refine the microstructure through solid state phase transformation by a quenching and annealing heat treatment (Wu and Hu, 2005). Cast material with a convoluted microstructure was reported to exhibit an improved room temperature ductility when compared to the fully lamellar microstructures (Saage et al., 2009). With a Hall-Petch type argument, the crystal plasticity model was extended to the refined (RF) microstructure. It is not possible to test experimentally the small lamellar-like bundles in the convoluted structure for their micromechanics, as in the the case of PST-crystals. For the simulations, they were expected to show less plastic anisotropy because of shorter and wider 'lamellar-like' plates.

In the employed Hall-Petch type argumentation shorter meant stronger and wider meant weaker, because of a shortening or extension of the mean free path that dislocations can glide before reaching an obstacle. Especially the minimum yield stresses that originate from easy glide along the lamellar planes were expected to be significantly stronger in the refined microstructure because of the fragmented arrangement of the stacked plates of γ- and α_2-phase. The chosen hardening parameters are given in table 9.2 for both types of microstructures. In order to keep the number of constitutive parameters as small as possible, deformation systems 1-6 from table 9.1 were treated equivalent. Also the mixed and transversal modes of deformation were given only one set of crystal plasticity parameters.

The corresponding self-hardening is shown in figure 9.4 and the resulting simulated yield stress anisotropy is given in figure 9.5. While the lamellar interface in the FL microstructure is identical to a {1 1 1}-plane which is also parallel to the {0 0 0 1}-basal plane of the α_2-phase, in the convoluted (RF) microstructure, the definition of a lamellar interface is not as straightforward. Nevertheless, α_2-phase precipitates on the {1 1 1}-planes of the massively transformed γ-phase and therefore the crystallogaphic relations are expected to be similar to the lamellar case. Consequently, in the following, the poly-twinned order domain structure found in lamellar material will also be assumed for the refined microstructure.

With the developed homogenized model a cluster of 64 periodically arranged grains was simulated under tensile deformation, figure 9.6. Periodic boundary conditions

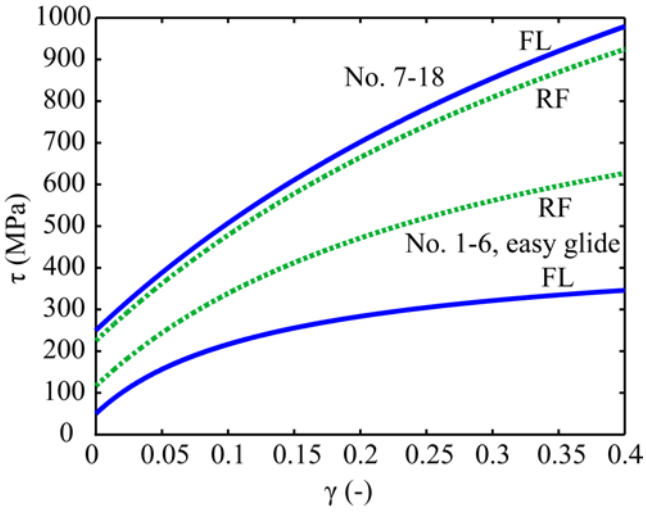

Fig. 9.4: The chosen self-hardening behaviors (table 9.2) of the deformation systems inside the lamellar (FL) and the convoluted (RF) microstructure; shear strength, τ, versus plastic shear, γ. The numbering of deformation systems refers to table 9.1.

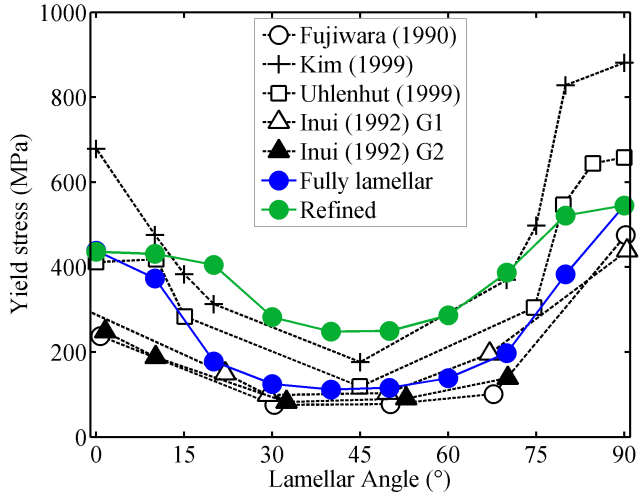

Fig. 9.5: Yield stress dependence from the lamellar angle, for the lamellar (FL) microstructure and for the refined (RF) microstructure.

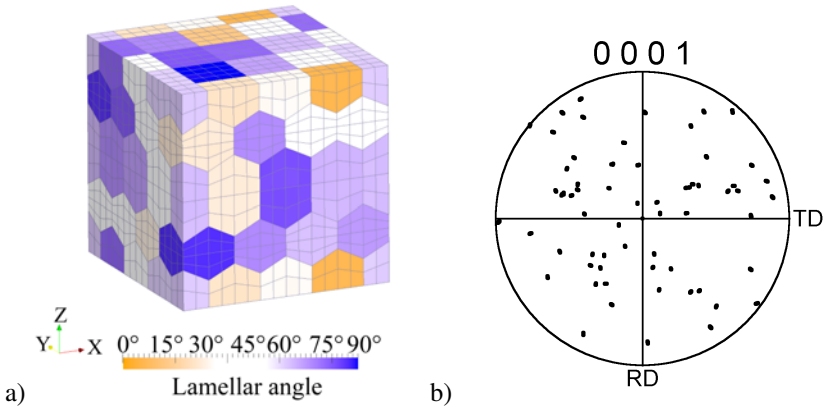

Fig. 9.6: a) Finite element mesh of the periodic 64-grain model; the lamellar angle, Φ_L, between the lamellar interfaces and the tensile axis, Z, is indicated. Soft grains are white, hard grains with angles of the lamellar planes near 0° and near 90° are shown in two different colors. b) (0 0 0 1) pole figure of the 64 random grain aggregate.

were applied to the aggregate in order to minimize surface effects. The application of periodic boundary conditions is detailed further in appendix C. The constitutive parameters were chosen either to represent the fully lamellar (FL) microstructure or the refined (RF or convoluted) microstructure. The crystal plasticity formulation does not contain a fixed length scale. Therefore, for both microstructures the same finite element model was used. It follows that the corresponding physical volume of material was much smaller for the model with convoluted microstructure in comparison to the fully lamellar model.

Figure 9.7 shows the distribution of the axial tensile stresses throughout the microstructure, for both sets of parameters. Strong fluctuations between differently oriented grains are present. Stress levels of few hundred MPa can be observed in some locations, while other regions are loaded with stresses that are exceeding 1000 MPa significantly. While the stress distribution is qualitatively identical for both sets of crystal plasticity parameters, the FL microstructure in subfigure 9.7 shows higher stress contrast. However, the analysis up to now was limited to the surface of the model.

In order to take into account the full 3D results of the simulations, the averaged axial stress per grain plotted against the average axial strain is given in figure 9.8 for the two cases. For the material law representing the convoluted (RF) microstructure, again a narrower stress distribution is observed. Especially the maximum stress levels at the initial stages of plasticity are reduced by about 100 MPa.

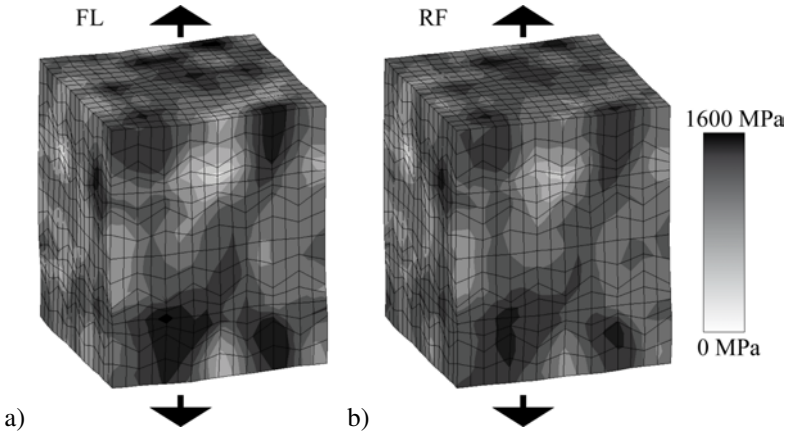

Fig. 9.7: Distribution of the axial stress component in the 64-grain model at 10 % elongation. The simulation result based on parameters for the FL microstructure shows higher stress contrast throughout the microstructure.

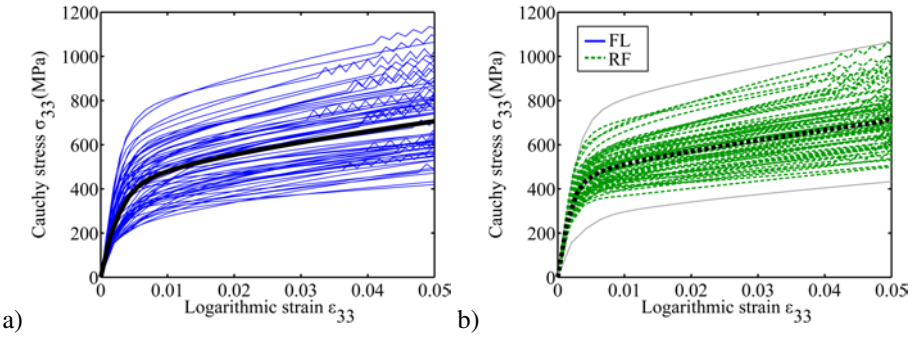

Fig. 9.8: The individual flow curves from the 64 grains (averaged over the 64 elements per grain) are shown for the parameter sets reflecting the a) fully lamellar (FL) microstructure and b) the refined (RF) microstructure; in (b) also the two curves on the highest and lowest stress level from the FL microstructure are shown for better comparison. Higher maximum and lower minimum values are apparent for the FL simulation. Average stress-strain curves for the two materials are drawn in bold. The same set of 64 random grain orientations was used in both simulations. Zig-zag shaped stress fluctuations in some of the curves are assumed to originate from instabilities during the evaluation of the periodic boundary conditions.

9.5 Discussion

The simulation results could help to explain the improved ductility of the convoluted microstructure that was observed in experiments (Saage et al., 2009). The present model does not make any predictions on the nucleation of cracks[1]. However, under the influence of the high peak stresses in the lamellar microstructure, a once formed microcrack is assumed to reach a critical size much faster than in the refined microstructure. It is noteworthy that the reduction in peak stresses was mainly achieved by strengthening the 'easy glide' deformation along the plates in the convoluted (RF) structure in comparison to the lamellar structure.

The findings on stress and strain fluctuations inside the microstructure cannot be easily confirmed experimentally[2]. However, another result was found from the simulated flow curves which could be directly compared to the existing experimental data: the previously investigated pre-yielding behavior of fully-lamellar microstructures (Wu et al., 2003, Hu et al., 2006a, Saage et al., 2009). Figure 9.9 compares the simulated stress-strain curves to experimental flow curves of fully lamellar material and two types of refined microstructures. Generally, the refined microstructures exhibit a defined transition from elastic to plastic deformation, whereas the lamellar microstructures show significant micro-plasticity at relatively low stresses.

The pre-yielding in lamellar microstructures is not discussed explicitly in the work of Couret et al. (2008) on extruded TiAl alloys. The shown flow curves, however, exhibit pronounced pre-yielding in the lamellar microstructures. Also given are the flow curves of a duplex microstructure that showed no pre-yielding but a well-defined yield point. Pre-yielding is assumed to be identical to what Dimiduk et al. (1998) termed a *gradual yield transient* for their results from compression testing on fully lamellar polycrystals. Also Kim (1998) discussed the *low microyielding stresses* of lamellar microstructures in contrast to the defined yield point of duplex material and found the pre-yielding to be less pronounced for small lamellar grain sizes in the observed range from 2500 μm to 230 μm.

The deviation from linearity in the simulated flow curves is to some extent an inherent feature of the underlying elasto-viscoplastic formulation of the material law. Nevertheless, the simulation of the refined microstructure clearly showed a sharper yielding behavior than the fully-lamellar model. Through a linear scaling of the simulated flow curves, an almost perfect match to the experimental data of Saage et al. (2009) could be achieved. The justification for the scaling operation is the different composition of the material of Saage et al.. Addition of large atoms such as Nb or Ta leads to a reduction of the lamellar spacing and also refines the dimensions of the convoluted microstructure. The crystal plasticity parameters were identified based on data of binary PST-crystals. For the alloyed material, however, an increased stress level is expected because of this structural refinement.

The simulation results suggest that the strength of the easy-glide mode dominates the micromechanical behavior in γ-TiAl based two-phase alloys. If the easy-glide mode is strengthened by a refinement of the microstructure, the plastic anisotropy inside the

[1] See Bieler et al. (2009) for an in-depth study of crack nucleation in γ-TiAl microstructures.

[2] For an optical strain mapping approach to Ti-Al microplasticity see Chang et al. (2006) and Jiang et al. (2009).

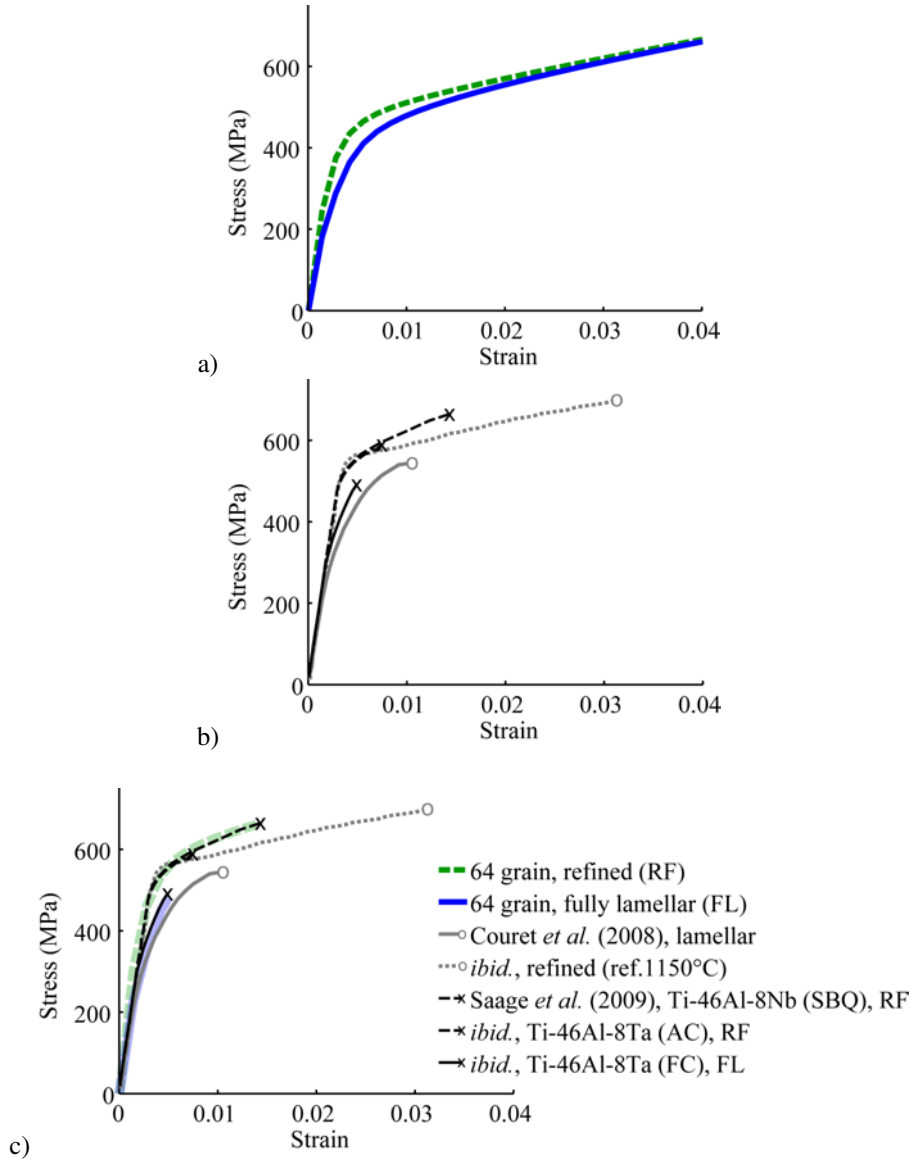

Fig. 9.9: Flow curves of simulated 64-grain clusters with FL (—) and refined (- -) microstructures, subfigure (a), compared to literature data measured at room temperature (Couret et al., 2008, Saage et al., 2009), subfigure (b). The bold, semi-transparent curves in subfigure (c) are the scaled results from the respective simulations and match the experimental curves from Saage et al. (2009) almost perfectly; In Saage et al. (2009) the furnace cooled (FC) microstructure was lamellar, whereas the air cooled (AC) and salt bath quenched (SBQ) microstructures exhibited a refined ('convoluted') microstructure, see figure 2.8. The refined material with the larger failure strain contained 8 at.% tantalum.

microstructure is reduced. As a consequence, a significant increase in the stresses required to initiate plastic flow and a reduction of the stress concentration in hard-oriented grains can be achieved at the same time. Thereby, the issues of pre-yielding as well as the low ductility of the two-phase alloys could be overcome.

9.6 Conclusions

A crystal plasticity model was introduced which describes the micromechanical response of kinematically constrained, γ-TiAl based microstructures by incorporating the relevant deformation modes. It was demonstrated that the model quantitatively captures the plastic anisotropy of two-phase γ/α_2-microstructures. It was validated against experimental data on PST-crystals and the uniaxial flow strengths as well as the relative transversal strains were matched with good agreement.

Through modeling of polycrystalline aggregates it was shown that the pre-yielding phenomenon in fully-lamellar alloys is probably mainly related to the plastic anisotropy of the lamellar colonies. The weakest grains with lamellar angles against the global loading axis of around 45° will start yielding early on during uniaxial loading of a lamellar microstructure. The early yielding of grains with soft orientations at the same time leads to higher stresses in the hard oriented grains. This stress contrast between hard and soft grains could well be the most important reason for the very low ductility of polycrystalline lamellar material at low and intermediate temperatures.

The excellent agreement between the simulations and experiments for the incipient plastic deformation demonstrates the strong potential of the applied CPFEM technique to quantitatively describe the complex micromechanics of γ-TiAl based alloys. It further indicates that the relevant micromechanical features of the microstructures were incorporated in the model.

On the methodological side of CPFEM constitutive modeling it could be concluded that periodic boundary conditions enable a realistic correlation between CPFEM simulation results and experimental data, even at relatively low resolutions of the microstructure. The number of 200 grains in a sample cross section that was requested for experimental studies by Kad and Asaro (1997) is therefore overcome in CPFEM modeling through the use of periodic boudnary conditions.

Part III

Summary, outlook, and backmatter

10

Summary and main conclusions

In the present work, improvements in the understanding of γ-TiAl based alloys could be achieved in three main fields. The first subject of an improved EBSD characterization of γ-TiAl was a prerequisite for the second field of orientation dependent nanoindentation. The third topic was the quantitative treatment of the mechanical microstructure-property relationships in γ-TiAl based alloys.

An improved indexing algorithm for EBSD orientation mapping was presented which makes possible the discrimination of γ-TiAl ordering variants. The technique is based on the identification of the small tetragonal distortion by high accuracy measurement parameters.

The crystal plasticity finite element method was applied to two unresolved issues in the micromechanics of γ-TiAl based alloys: First, the single crystal intrinsic plastic deformation of near-stoichiometric γ-TiAl was analyzed through experiments and corresponding CPFEM modeling of the indentation. In the course of work the pile-up behavior was identified as an important indicator for the activated deformation processes. These novel findings were possible only through the developed EBSD method by which the indentation experiments could be related to the indented crystallographic orientation.

Second, the micromechanics of two-phase lamellar microstructures was cast into a homogenized CPFEM model. Deformation of these microstructures is kinematically constrained through a high density of interfaces. The homogenized model was validated through comparison against published experimental data on the deformation of PST crystals. Good agreement was found for the anisotropic yielding behavior and the relative lateral strains. The model could be extended to a less constrained microstructure ('convoluted' microstructure) and successfully predicted the change in macroscopic yield characteristics, when applied to the simulation of polycrystal aggregates.

To summarize the modeling work, the constitutive behavior of TiAl based alloys was modeled on two length scales: On the single crystal scale, where the interfaces do not influence the deformation; and on the polycrystal scale, where the interface structure is the dominant influence on the micro- and macro-mechanics.

Some important conclusions that could be drawn from the present work are listed in the following, more detailed conclusions are given at the end of each chapter:

- The EBSD technique was shown to be capable of resolving the slight tetragonality of γ-TiAl. This made possible the identification of ordering domains and thus the reliable orientation mapping of the γ-TiAl-phase.

- The CPFEM method was extended to reflect the complex mechanics of the intermetallic γ-TiAl phase. Deformation systems of different strengths and types could be taken into account while the robust convergence of the constitutive law was retained.
- CPFEM simulation was shown to be an ideal tool to clarify the deformation during nanoindentation of individual crystallites. The necessary orientation data can be conveniently collected by EBSD.
- The orientation dependent piling-up behavior of single-crystal γ-TiAl during axisymmetric indentation is highly characteristic of the activated crystallographic deformation systems. For the case of a Ti-46Al-8Nb alloy, predominant deformation through ordinary dislocation glide was observed in the γ-TiAl phase.
- Pile-up topographies of known crystallographic orientations can be efficiently displayed in the unit orientation triangle, based on an in-plane orientation convention. The proposed systematic representation is the inverse pole figure of pile-up topographies, or shortly the *pile-up IPF*.
- CPFEM modeling was also successfully applied to kinematically constrained microstructures, namely the lamellar and the convoluted microstructures. Well-defined crystallographic relationships such as in lamellar Ti-Al alloys make possible the derivation of homogenized models which then represent the effective micromechanics of the two-phase microstructure.
- Using the homogenized model on the grain length scale, multi-grain aggregates could be simulated to relate the micro-mechanical characteristics to the macroscopic material response. In the present case of Ti-Al alloys, the experimentally observed pre-yielding behavior was explained through and quantitatively related to the anisotropic yielding of lamellar grains.

11

Outlook

The EBSD resolution of γ-TiAl order variants, available for the first time, has a wide range of possible applications in the microstructural characterization of γ-TiAl based alloys. It will hopefully help to further clarify the phase transformation processes as well as degradation and coarsening phenomena during thermo-mechanical loading.

The link between the intrinsic single phase properties and the effective mechanics of two-phase microstructures remains unresolved. It constitutes the central problem of mechanically oriented materials science to establish a quantitative connection from the spatial arrangement of defects to the overall performance of the material. Promising developments in this direction can be observed in the field of discrete dislocation dynamics, molecular dynamics and atomistic simulations.

Answers to some questions that are within closer reach might be found through the extension of the presented nanoindentation method: Devices for high temperature nanoindentation are currently under development. Quantification of the temperature dependent activation of deformation mechanisms could be gained from the application of the presented indentation approach to the case of high temperature indentation. Possibly also creep properties could be measured through indentation, as exemplified by Dorner et al. (2003). Further rich possibilities of the indentation technique are expected in the investigation of the composition dependence of plastic deformation.

It will be interesting to follow the evolution of miniaturized mechanical tests (Hemker and Sharpe, 2007, Dehm, 2009). The experimental data that could be generated with these methods would be ideal for comparison to the characteristics that were found through the single crystal indentation method. Possibly, these methods could be automatized to a level where they match the high-throughput capability of the indentation method.

The developed homogenized model has shown its capability to quantitatively analyze the room temperature deformation behavior of γ-TiAl based, two-phase microstructures. An important extension would be the application of similar models to the low-load, high-temperature regime. Such models could be used to investigate and predict quantitatively the creep properties of titanium aluminides.

Appendix A

Literature on titanium aluminides

A.1 Proceedings

Symposia during MRS fall meetings included:
1984 High-temperature ordered intermetallic alloys I
1986 High-temperature ordered intermetallic alloys II
1988 High-temperature ordered intermetallic alloys III
1990 High-temperature ordered intermetallic alloys IV
1992 High-temperature ordered intermetallic alloys V
1994 High-temperature ordered intermetallic alloys VI
1996 High-temperature ordered intermetallic alloys VII
1998 High-temperature ordered intermetallic alloys VIII, George et al. (1999)
2000 High-temperature ordered intermetallic alloys IX, Schneibel et al. (2001)
2004 Integrative and Interdisciplinary Aspects of Intermetallics (Symp. S), Mills et al. (2005)
2006 Advanced Intermetallic-Based Alloys (Symp. II), Wiezorek et al. (2007)
2008 Advanced Intermetallic-Based Alloys for Extreme Environment and Energy Applications (Symp. U), Palm et al. (2009)

TMS meetings included:
1991 Microstructure/Property Relationships in Titanium Aluminides and Alloys, Kim and Boyer (1991)
1995 Gamma Titanium Aluminides I, Kim et al. (1995)
1999 Gamma Titanium Aluminides II, Kim et al. (1999b)
2003 Gamma Titanium Aluminides III, Kim et al. (2003)
2008 Structural Aluminides for Elevated Temperature Applications: Gamma titanium and other aluminides; Kim et al. (2008)

A.2 Journal issues

Metallurgical and Materials Transactions A 29(1), 1997 Symposium on Fundamentals of Gamma Titanium Aluminides – Part I (held as part of 1997 TMS Annual Meeting in Orlando, Florida).

Intermetallics 7(3–4), 1999: Deformation and fracture of ordered solid solutions (DFG program), final colloquium.

Mater. Sci. Engr. A 329-331, 2002, 5th International Conference on Structural and Functional Intermetallics.

Intermetallics 13(9), 2005, 2nd IRC Birmingham International TiAl Workshop, held in the IRC in Materials, the University of Birmingham, UK in July 5–7, 2004.

Appendix B

Crystallographic orientations

B.1 Bunge Euler angles

Euler angles (φ_1, Φ, φ_2) —in Bunge convention— rotate the sample coordinate system (X, Y, Z or RD, TD, ND) into the crystal coordinate system (x_c, y_c, z_c). Three successive rotations are carried out in the following way (Bunge, 1982, pg. 4):

1. Rotate by angle φ_1 around Z, to bring X into the x_c–y_c-plane. The new intermediate axes are X', Y' and Z (Z is unchanged).
2. Now rotate Φ degrees around X', to make Z parallel with z_c. The intermediate axes are X', Y'', Z'.
3. A rotation by angle φ_2 around Z' makes the rotated axes then identical to the crystal axes.

The rotation matrix can be calculated as

$$\boldsymbol{g} = \begin{pmatrix} \cos\varphi_1 \cos\varphi_2 - \sin\varphi_1 \sin\varphi_2 \cos\Phi & \sin\varphi_1 \cos\varphi_2 + \cos\varphi_1 \sin\varphi_2 \cos\Phi & \sin\varphi_2 \sin\Phi \\ -\cos\varphi_1 \sin\varphi_2 - \sin\varphi_1 \cos\varphi_2 \cos\Phi & -\sin\varphi_1 \cos\varphi_2 + \cos\varphi_1 \cos\varphi_2 \cos\Phi & \cos\varphi_2 \sin\Phi \\ \sin\varphi_1 \sin\Phi & -\cos\varphi_1 \sin\Phi & \cos\Phi \end{pmatrix}$$

Other representations of orientations and further detail can be found in Altmann (2005), Morawiec (2004), and Heinz and Neumann (1991).

B.2 Generation of near-equidistant orientations

The near-equidistant orientations used for the simulation of nanoindentations in chapter 8 were generated after the method presented in the first part of the work by Helming et al. (1998).

From the resolution constant, Δ, the near-equidistant directions r_{ij} are calculated by

$$r_{ij} = \begin{pmatrix} x \\ y \\ z \end{pmatrix} = \frac{1}{N_{ij}} \begin{pmatrix} 1 \\ \tan(i\Delta) \\ \tan(j\Delta) \end{pmatrix} \quad \text{, with } N_{ij} = \sqrt{1 + \tan^2(i\Delta) + \tan^2(j\Delta)},\ -\tau < i,j \leq \tau$$

Tab. B.1: The first 21 near-equidistant orientations for $\Delta = 9°$; the orientations cover the fcc unit orientation triangle;

No.	Bunge Euler angles	$[u\,v\,w]$	ζ	η
1	(0.0000°, 0.0000°, 0.0000°)	0 0 1	0.00°	0.00°
2	(270.0000°, 9.0000°, 90.0000°)	7 0 45	0.00°	9.00°
3	(315.0000°, 12.6253°, 45.0000°)	7 7 45	45.00°	12.63°
4	(270.0000°, 18.0000°, 90.0000°)	7 0 22	0.00°	18.00°
5	(295.9873°, 19.8733°, 64.0127°)	43 21 135	25.99°	19.87°
6	(315.0000°, 24.6791°, 45.0000°)	7 7 22	45.00°	24.68°
7	(270.0000°, 27.0000°, 90.0000°)	1 0 2	0.00°	27.00°
8	(287.2677°, 28.0832°, 72.7323°)	3 1 6	17.27°	28.08°
9	(302.5253°, 31.1449°, 57.4747°)	3 2 6	32.53°	31.14°
10	(315.0000°, 35.7757°, 45.0000°)	1 1 2	45.00°	35.78°
11	(270.0000°, 36.0000°, 90.0000°)	5 0 7	0.00°	36.00°
12	(282.2979°, 36.6347°, 77.7021°)	32 7 45	12.30°	36.63°
13	(294.0948°, 38.5158°, 65.9052°)	47 21 66	24.09°	38.52°
14	(305.0420°, 41.5859°, 54.9580°)	10 7 14	35.04°	41.59°
15	(315.0000°, 45.7767°, 45.0000°)	5 5 7	45.00°	45.78°
16	(270.0000°, 45.0000°, 90.0000°)	1 0 1	0.00°	45.00°
17	(279.0000°, 45.3549°, 81.0000°)	50 8 51	9.00°	45.35°
18	(288.0000°, 46.4370°, 72.0000°)	3 1 3	18.00°	46.44°
19	(297.0000°, 48.2988°, 63.0000°)	2 1 2	27.00°	48.30°
20	(306.0000°, 51.0266°, 54.0000°)	51 37 52	36.00°	51.03°
21	(315.0000°, 54.7356°, 45.0000°)	1 1 1	45.00°	54.74°

and integer number $\tau = 90°/\Delta$, and integer indices i, j.

For a resolution constant of $\Delta = 9°$, the method results in 21 orientations inside the cubic standard triangle [0 0 1]-[1 1 0]-[1 1 1], table B.1. These can be transformed to 63 orientations in the unit triangle [0 0 1]-[1 0 0]-[1 1 0] of the tetragonal structure of which 51 orientations are unique. If improper rotations are not allowed the larger unit triangle [0 0 1]-[1 0 0]-[0 1 0] has to be used, resulting in 126 orientation of which 91 are unique, figure B.1.

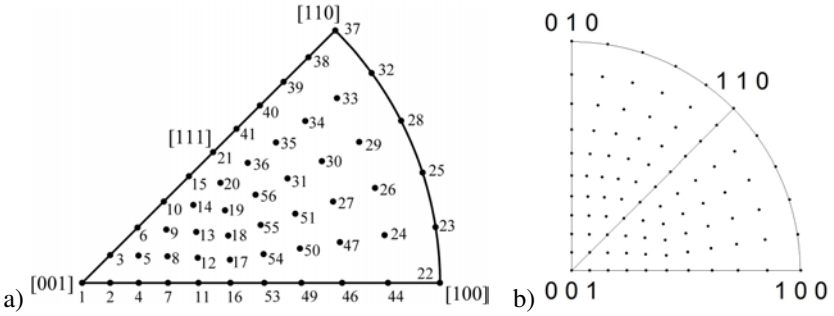

Fig. B.1: a) The 51 near-equidistant orientations as numbered in table B.1; b) [0 0 1] IPF (stereographic projection) of the 91 near-equidistant directions as displayed by the software OIM-DA

If needed, a coarser ($\Delta = 15°$) or finer ($\Delta = 5°$) discretization of the orientation space can be chosen. A resolution of 9° was found to give a good trade-off between accurate description of the orientation dependence of the indentation process and the computational effort to calculate the discrete orientations. An accurate description is fulfilled if a smooth transition of the pile-up patterns simulated for neighboring discrete orientations can be observed.

B.3 Orientation representation of the hexagonal phase

The 4-digit *Miller-Bravais classification* is used widely for orientation characterization of hexagonal crystals in materials science. It has the advantage of a clear and simple representation of equivalent directions and planes (Hosford, 1993, Appendix 1). For a computational processing of hexagonal orientation data it is, however, much simpler to calculate back to the cartesian description of directions and plane normals. In this work this was done following the convention in Hosford (1993) which is as follows:

Direction $\boldsymbol{a_1} = \langle \bar{2}110 \rangle$ is parallel to the cartesian vector $\boldsymbol{e_1} = [1, 0, 0]$; Vector $\boldsymbol{e_2} = [0, 1, 0]$ is 30° away from $\boldsymbol{a_2} = \langle 1\bar{2}10 \rangle$; The hexagonal c-axis is then aligned with the cartesian base vector $\boldsymbol{e_3}$.

For this convention, figure B.2, a direction $[u\,v\,t\,w]$ can be expressed as a vector in an orthogonal coordinates by

$$\boldsymbol{d} = \frac{3}{2}ua\boldsymbol{e_1} + \frac{\sqrt{3}}{2}(2v + u)a\boldsymbol{e_2} + w\gamma a\boldsymbol{e_3}$$

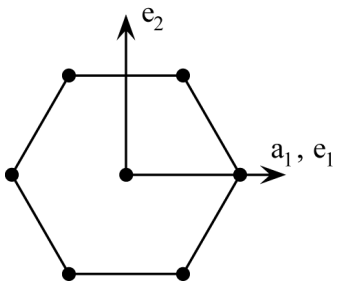

Fig. B.2: Convention for the choice of an orthogonal coordinate frame in hexagonal materials;

where $\gamma = {}^{c}/_{a}$. The plane normal to $(h\,k\,i\,l)$ is

$$\boldsymbol{n} = (h/a)\boldsymbol{e_1} + \frac{2k+h}{\sqrt{3}a}\boldsymbol{e_2} + (l/c)\boldsymbol{e_3}.$$

In another convention the second base vector, $\boldsymbol{e_2}$, is aligned with one of the Miller-Bravais axes, usually with $\boldsymbol{a}_2$. One has to take care about correct ±30° rotation between the respective methods.

The orientation of the hexagonal phase can be expressed in a rotation from the γ-M1 matrix variant as follows (with the assumption of a cubic γ-structure): $x_{hex} = [1\,0\,\overline{1}]\frac{1}{\sqrt{2}}$, $y_{hex} = [\overline{1}\,2\,\overline{1}]\frac{1}{\sqrt{6}}$, $z_{hex} = [1\,1\,1]\frac{1}{\sqrt{3}}$

Appendix C

Periodic boundary conditions

Since the boundary conditions might influence the simulation results significantly at least for the polycrystal calculations (Cailletaud et al., 2003), the employed periodic boundary conditions are presented in the following. The motivation for choosing periodic boundary conditions on the model surface is the minimization of 'surface effects' or artefacts.

In general, homogeneous boundary conditions, where every node on the surface has a prescribed displacement based on the macroscopic deformation gradient by $\boldsymbol{x} = \boldsymbol{F}_{macro}\boldsymbol{X}$, lead to a too stiff response, i. e. too high average stresses. In contrast, free surface (zero traction) boundary conditions are too soft. Close to the surface of the volume element, they neglect the confining effect of the surrounding grains and will therefore underestimate the average stress level. This softening could be minimized by simulating large aggregates, however, the computational cost would very soon become prohibitive.

Periodic boundary conditions are expected to lie in-between those extreme cases and to approximate the real situation best. 'Real situation' here means the case of a polycrystalline sample where the grain size is generally much smaller than the sample size and most of the grains are located far away from the unconstrained surfaces.

Periodic boundary conditions were defined on opposing nodes. One corner node of the model is kept fixed at all times in the three directions. Three control nodes were chosen on the corners of the hexahedral models. In figure C.1 the control nodes are number 2, 4, and 5. Periodic boundary conditions are implemented in the form of displacement constraints as follows: For all pairwise opposite nodes (n_i, n_j) on the opposing faces (superscript '+', '−') with face normal parallel to the first cartesian unit direction, $\boldsymbol{e_1}$ (superscript 'x'), of the hexahedral model, the displacements, u, have to observe the constraint

$$u_i^{x^+} - u_j^{x^-} = u_2^x - u_1^x$$

and since $u_1^x = 0$ at all times, the constraint for node n_i is

$$u_i^{x^+} = u_j^{x^-} + u_2^x$$

The corresponding constraints are formulated for the other two directions $\boldsymbol{e_2}$ and $\boldsymbol{e_3}$ (superscripts y and z).

$$u_i^{y^+} = u_j^{y^-} + u_4^y \quad \text{and} \quad u_i^{z^+} = u_j^{z^-} + u_5^z$$

A simple crystal plasticity simulation with periodic boundary conditions, for compression of an aggregate of eight hexahedral crystals of different orientations, is shown in figure C.1.

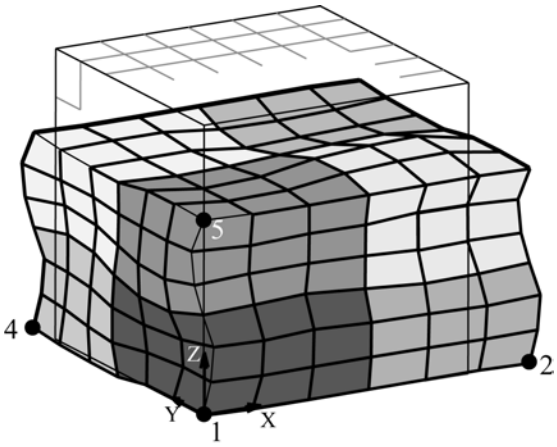

Fig. C.1: Periodic boundary conditions acting on a cubic model during compression. Each of the eight differently oriented crystals is split into 27 hexahedral elements.

The number of constraints used for the implementation of periodic boundary conditions was $N = (3(3n^2 + 3n - 2))$, where n is the number of elements along one direction of an equally subdivided hexahedral model.

Abstract

Titanium aluminide alloys based on the phase γ-TiAl are a promising class of materials for high temperature structural applications. In this thesis, their micromechanical behavior was investigated through the combination of experimental and computational techniques. First, an advanced characterization technique for γ-TiAl based microstructures is presented. Through the use of high accuracy measurement parameters and an enhanced indexing algorithm, the electron backscatter diffraction (EBSD) method was improved to reliably resolve the γ-TiAl order domains. This makes available for the first time the automatic acquisition of large and detailed microstructural maps of the domain-resolved crystal orientation and phase distribution in this material.

The improved orientation mapping technique was used to study the orientation dependent nanoindentation of the γ-TiAl phase. Single crystals of γ-TiAl cannot be grown in the near-stoichiometric compositions that are present inside two-phase γ/α_2-microstructures with attractive mechanical properties. Because of this limitation, an approach was developed to study the single crystal constitutive behavior of γ-TiAl by nanoindentation experiments in single phase regions of these γ/α_2-microstructures. The indented crystallographic orientations were characterized by the order domain resolved orientation mapping technique. Atomic force microscopy was employed to measure the evolving material pile-up around the impressions.

A 3D elasto-viscoplastic crystal plasticity formulation was extended to incorporate the deformation behavior of γ-TiAl. Deformation systems were implemented for dislocation glide on four ordinary dislocation systems and eight superdislocation systems. Additionally, four true twinning systems were implemented as uni-directional deformation systems.

The crystal plasticity model is coupled with the finite element method. Thereby, it was possible to perform simulations of single crystal indentation. Experiments and simulations were combined to study the orientation dependent indentation pile-up. A convention was defined to unambiguously relate any indentation axis to a crystallographic orientation.

The characteristic pile-up topographies around indents were simulated throughout the unit triangle of γ-TiAl and represented graphically in the newly introduced inverse pole figure of pile-up patterns. The spatially resolved simulation of the activation of competing deformation mechanisms during indentation, enabled an assessment of their relative strengths. Through this approach, easy activation of ordinary dislocation glide in stoichiometric γ-TiAl was confirmed independently from dislocation observation by transmission electron microscopy.

On the length-scale of multi-grain aggregates, two kinds of microstructures were investigated. The lamellar microstructure was analyzed in terms of kinematic constraints perpendicular to densely spaced lamellar boundaries which lead to pronounced plastic anisotropy. A homogenized crystal plasticity model is presented that quantitatively captures the micromechanics of the lamellar two-phase microstructure. Furthermore, the mechanical behavior of refined microstructures was modeled. The assumption of a lower degree of kinematic constraints for these microstructures resulted in less plastic anisotropy on the single grain scale. Also lower compatibility stresses evolved during the simulated deformation of a 64-grain aggregate with refined microstructure in comparison to a fully lamellar aggregate. On the macroscopic length scale, the simulations could explain the pre-yielding of lamellar microstructures.

Zusammenfassung

Titanaluminid-Legierungen basierend auf der Phase γ-TiAl sind eine attraktive Klasse von Strukturmaterialien für Hochtemperaturanwendungen. In der vorliegenden Arbeit wurde ihre Mikromechanik durch die Kombination von experimentellen und computergestützten Methoden untersucht. Zunächst wird eine optimierte Technik zur Charakterisierung γ-TiAl basierter Mikrostrukturen vorgestellt. Durch hochgenaue Messparameter und einen weiterentwickelten Indizierungs-Algorithmus wurde die Technik der Orientierungsmikroskopie (engl. EBSD) derart verbessert, dass die Ordnungvarianten von γ-TiAl verlässlich unterschieden werden können. Damit ist erstmalig die automatisierte Aufnahme von großen und detaillierten Mikrostrukturkarten der Ordnungsdomänen sowie der Phasenverteilung in diesem Material möglich.

Die verbesserte Orientierungsmikroskopie wurde eingesetzt, um die die orientierungsabhängigen Eigenschaften der γ-TiAl Phase bei Nanoindentierung zu untersuchen. Einkristalle der γ-TiAl Phase können für die nahezu stöchiometrische Zusammensetzung, wie sie auch in den zweiphasigen γ/α_2-Mikrostrukturen mit guten mechanischen Eigenschaften vorliegt, nicht hergestellt werden. Um diese Einschränkung zu überwinden wurde ein Ansatz erarbeitet, mit dem die Einkristallmechanik von γ-TiAl durch Nanoindentierung einphasiger Bereiche dieser Mikrostrukturen untersucht werden konnte. Die indentierten kristallographischen Orientierungen wurden mit der die Ordungsdomänen auflösenden Orientierungmikroskopie bestimmt. Mittels Rasterkraftmikroskopie wurde der um die Härteindrücke entstehende Materialaufwurf vermessen.

Eine 3D elastisch-viskoplastische Kristallplastizitäts-Formulierung wurde zur Beschreibung des Verformungsverhaltens von γ-TiAl erweitert. Verformungssysteme für Versetzungsgleitung auf vier Systemen von Einfach-Versetzungen und acht Systemen von Superversetzungen wurden implementiert. Zusätzlich wurden vier Zwillingssysteme als einsinnige Schersysteme realisiert.

Das Kristallplastizitätsmodell ist mit der Finite-Elemente-Methode gekoppelt. Dadurch war es möglich Simulationen zur Einkristallindentierung durchzuführen. Experimente und Simulationen wurden kombiniert, um den orientierungsabhängigen Materialaufwurf bei Indentierung zu untersuchen. Eine Konvention wurde definiert, die eine beliebige Indentierungsachse eindeutig einer kristallographischen Orientierung zuordnet.

Die charakteristischen Topographien der Härteeindrücke wurden im Standard-Orientierungsdreieck von γ-TiAl simuliert. Sie wurden grafisch dargestellt in der neu eingeführten inversen Polfigur von Härteeindruck-Topografien. Die ortsaufgelöste Simulation der Aktivierung konkurrierender Verformungssysteme bei der Indentierung, ermöglichte die Abschätzung deren relativer Scherfestigkeiten. Dadurch konnte die leichte Aktivierung von Einfachversetzungsgleitung in stöchiometrischem γ-TiAl, unabhängig von der Versetzungsbeobachtung im Transmissionselektronenmikroskop, nachgewiesen werden.

Auf der Größenskala mehrkörniger Aggregate, wurden zwei Typen von Mikrostrukturen untersucht. Die lamellare Mikrostruktur wurde hinsichtlich der kinematischen Zwangsbedingungen senkrecht zu den eng aufeinander folgenden Lamellengrenzen untersucht, aus welchen eine ausgeprägte Anisotropie der plastischen Verformung folgt. Ein homogenisiertes Kristallplastizitätsmodell wird vorgestellt, das

die Mikromechanik von zweiphasig lamellaren Mikrostrukturen quantitativ erfasst. Darüber hinaus wurde das mechanische Verhalten von gefeinten Mikrostrukturen abgebildet. Die Annahme einer geringeren Wirksamkeit der kinematischen Zwangsbedingungen in gefeinten Mikrostrukturen resultierte in einer verringerten plastischen Verformungsanisotropie auf der Längenskala der Mikrostrukturbestandteile. Auch entwickelten sich bei der simulierten Verformung eines 64-Korn-Aggregates mit dem Modell der gefeinten Mikrostruktur, im Vergleich zur vollständig lamellaren Mikrostruktur, geringere Spannungen durch Verformungsinkompatibilitäten. In Hinsicht auf das Fließverhalten erklärten die Simulationen die bei geringen Spannungen eintretende, ausgeprägte Mikroplastizität von lamellaren Mikrostrukturen.

Symbols and abbreviations

Symbols

α	Half opening angle of a conical indenter
a, c	Crystal lattice parameters of γ-TiAl
$\boldsymbol{b}$	Burgers vector
$A, A_\perp$	Area, projected contact area during indentation
$\mathbb{C}$	Fourth-rank elastic operator
Δ	Resolution constant for near-equidistant directions
$\mathbb{D}$	Jacobian matrix, consistent tangent
ε	Mechanical strain
η	Inclination angle of the polar coordinates (η, ζ)
$\boldsymbol{e}_1, \boldsymbol{e}_2, \boldsymbol{e}_3$	Unit basis vectors in a cartesian coordinate system
$\boldsymbol{E}$	Green-Lagrange strain
$\boldsymbol{F}$	Deformation gradient
$\gamma, \dot{\gamma}$	Crystallographic shear and shear rate
$\boldsymbol{g}$	Orientation matrix
G	Shear modulus
H	Hardness
h	Indentation depth, penetration
$\boldsymbol{I}$	Second-rank identity
k	Hall-Petch constant
λ	Lamellar spacing
$\boldsymbol{L}$	Plastic velocity gradient
m	Size of convolution mask (Hough transformation)
$\boldsymbol{n}$	Normal vector
$\varphi_1, \Phi, \varphi_2$	Bunge Euler angles
Φ_L	Angle between the lamellar interfaces and the loading axis
P	Indenter normal load
q	Hardening coefficient, components of the hardening matrix
ρ	Distance of a line from the center (Hough transformation)
R	Radius of an indenter tip
σ	Mechanical stress
σ_y	Yield stress
$\boldsymbol{T}$	Cauchy stress
τ	Shear stress
τ_c	Critical resolved shear stress (CRSS)
ζ	Azimuth angle of the polar coordinates (η, ζ)

Abbreviations

3D	Three-dimensional
AFM	Atomic force microscopy
BSE	Backscatter electron
CPFEM	Crystal plasticity finite element method
CRSS	Critical resolved shear stress
DDD	Discrete dislocation dynamics
EBSD	Electron backscatter diffraction
ECCI	Electron channeling contrast imaging
FEG-SEM	Field emission gun SEM
FIB	Focused ion beam
FL	Fully lamellar (microstructure)
HRTEM	High resolution TEM
IPF	Inverse pole figure
MD	Molecular dynamics
OIM-DA	Orientation Imaging Microscopy Data Analysis, TSL/EDAX
OIM-DC	Orientation Imaging Microscopy Data Collection, TSL/EDAX
PST	Polysynthetically-twinned microstructure
PX	Polycrystal, polycrystalline
RD, TD, ND	Rolling, transverse, and normal direction
RF	Refined (microstructure)
RT	Room temperature
SEM	Scanning electron microscope
SX	Single crystal, single-crystalline
TEM	Transmission electron microscopy
TOCA	Crystallographic software written by S. Zaefferer

Bibliography

Abou-Ras, D., Gibmeier, J., Nolze, G., Gholinia, A., and Konijnenberg, P. On the capability of revealing the pseudosymmetry of the chalcopyrite-type crystal structure. *Crystal Research and Technology*, 43(3), 234–239 (2008). doi: 10.1002/crat.200711082. Cited on page 79.

Aindow, M., Chaudhuri, K., Das, S., and Fraser, H.L. On the Influence of Stoichiometry and Purity on the Deformation Mechanisms in the Intermetallic Compound TiAl. *Scripta Metallurgica et Materialia*, 24(6), 1105–1108 (1990). Cited on page 42.

Alcalá, J., Barone, A.C., and Anglada, M. The influence of plastic hardening on surface deformation modes around Vickers and spherical indents. *Acta Materialia*, 48(13), 3451–3464 (2000). doi: 10.1016/S1359-6454(00)00140-3. Cited on page 67.

Alcala, J., Casals, O., and Ocenasek, J. Micromechanics of pyramidal indentation in fcc metals: Single crystal plasticity finite element analysis. *Journal of the Mechanics and Physics of Solids*, 56(11), 3277–3303 (2008). doi: 10.1016/j.jmps.2008.07.004. Cited on page 70.

Altmann, S.L. *Rotations, Quaternions, and Double Groups*. Dover, 2nd edition (2005). Cited on page 165.

Anderson, O.L. A Simplified Method for Calculating Debye Temperature From Elastic Constants. *Journal of Physics and Chemistry of Solids*, 24(7), 909–& (1963). Cited on page 38.

Antunes, J., Fernandes, J., Menezes, L., and Chaparro, B. A new approach for reverse analyses in depth-sensing indentation using numerical simulation. *Acta Materialia*, 55(1), 69–81 (2007). doi: 10.1016/j.actamat.2006.08.019. Cited on page 69.

Appel, F. An electron microscope study of mechanical twinning and fracture in TiAl alloys. *Philosophical Magazine*, 85(2), 205–231 (2005). Cited on pages 43, 44, and 140.

Appel, F., Beaven, P.A., and Wagner, R. Deformation processes related to interfacial boundaries in 2-phase gamma-Titanium Aluminides. *Acta Metallurgica et Materialia*, 41(6), 1721–1732 (1993). Cited on pages 44 and 140.

Appel, F. and Christoph, U. Coherency stresses and interface-related deformation phenomena in two-phase titanium aluminides. *Intermetallics*, 7, 1173–1182 (1999). Cited on page 29.

Appel, F., Christoph, U.B.U., Eggert, S., Janschek, P., Lorenz, U., Müllauer, J., Oehring, M., and Paul, J. Recent progress in the Development of Gamma Titanium Aluminide Alloys. *Advanced Engineering Materials*, 2(11), 699–720 (2000). Cited on pages 44 and 139.

Appel, F. and Oehring, M. Gamma-Titanium Aluminide Alloys: Alloy Design and Properties. In Leyens and Peters (2003), chapter 4, pages 89–152. Cited on pages 20, 24, and 44.

Appel, F., Paul, J.D.H., Oehring, M., Clemens, H., and Fischer, F.D. Physical metallurgy of high Nb-containing TiAl alloys. *Zeitschrift fur Metallkunde*, 95(7), 585–591 (2004). Cited on page 26.

Appel, F. and Wagner, R. Slip-twin Interactions in Gamma-titanium Aluminides. In M.H. Yoo and M. Wuttig, editors, *Twinning in Advanced Materials*, pages 317–330. TMS, TMS (1994). Cited on page 44.

Appel, F. and Wagner, R. Microstructure and deformation of two-phase gamma-titanium aluminides. *Materials Science and Engineering*, R22, 187–268 (1998). doi: 10.1016/S0927-796X(97)00018-1. Cited on pages 20, 26, 41, 47, and 50.

Asaro, R.J. and Needleman, A. Overview 42. Texture Development and Strain-Hardening in Rate Dependent Polycrystals. *Acta Metallurgica*, 33(6), 923–953 (1985). Cited on pages 53, 54, and 100.

Baba-Kishi, K.Z. Review - Electron backscatter Kikuchi diffraction in the scanning electron microscope for crystallographic analysis. *Journal of Materials Science*, 37(9), 1715–1746 (2002). Cited on page 79.

Bartels, A., Bystrzanowski, S., Chladil, H., Leitner, H., Clemens, H., Gerling, R., and Schimansky, F.P. Massive Transformation in High Niobium Containing TiAl-Alloys. In *Mater. Res. Soc. Symp. Proc. Vol. 842*, pages S5.48.1–6 (2005). Cited on pages 35, 79, and 86.

Bassani, J.L. and Wu, T.Y. Latent Hardening in Single-crystals .2. Analytical Characterization and Predictions. *Proceedings of the Royal Society of London Series A-mathematical Physical and Engineering Sciences*, 435(1893), 21–41 (1991). Cited on page 111.

Bathe, K.J. *Finite element procedures*. Prentice Hall (1996). Cited on page 104.

Bažant, Z. and Oh, B. Efficient Numerical Integration of the Surface of a Sphere. *Z. angew. Math. u. Mech.*, 66(1), 37–49 (1986). Cited on page 131.

Beom, J. and Zikry, M.A. Nanoindentation and microstructural evolution of poly-crystalline gold. *J. Mater. Res.*, 24, 1093–1104 (2009). doi: 10.1557/JMR.2009.0133. Cited on page 70.

Berkovich, E.S. Three-faceted diamond pyramid for micro-hardness testing. *Ind. Diamond Rev.*, 11, 129–133 (1951). Cited on page 63.

Bertram, A. *Elasticity and plasticity of Large Deformations*. Springer (2005). Cited on page 97.

Bhattacharya, A.K. and Nix, W.D. Finite-element Simulation of Indentation Experiments. *International Journal of Solids and Structures*, 24(9), 881–891 (1988). Cited on pages 69 and 124.

Bieler, T., Eisenlohr, P., Roters, F., Kumar, D., Mason, D., Crimp, M., and Raabe, D. The role of heterogeneous deformation on damage nucleation at grain boundaries in single phase metals. *International Journal of Plasticity*, 25, 1655–1683 (2009). doi: 10.1016/j.ijplas.2008.09.002. Cited on pages 56, 98, and 153.

Biener, M., Biener, J., Hodge, A., and Hamza, A. Dislocation nucleation in bcc Ta single crystals studied by nanoindentation. *Physical Review B*, 76(16), 165422–1–6 (2007). doi: 10.1103/PhysRevB.76.165422. Cited on pages 66 and 67.

Bird, N., Jiao, S., and Taylor, G. The formation of ordered domains during crystal growth of [gamma]-TiAl. *Intermetallics*, 8(2), 133–141 (2000). doi: 10.1016/S0966-9795(99)00077-1. Cited on pages 29, 30, and 42.

Biwa, S. and Storåkers, B. An analysis of fully plastic Brinell indentation. *Journal of the Mechanics and Physics of Solids*, 43(8), 1303–1333 (1995). doi: 10.1016/0022-5096(95)00031-D. Cited on page 69.

Blackburn, M. Some aspects of phase transformations in titanium alloys. In R. Jaffee and N. Promisel, editors, *The science, technology and applications of titanium; proceedings of a conference held 1968 in London*, page 633. Pergamon Press (1970). Cited on page 28.

Blackburn, M. and Smith, M. AFWAL-TR-82-4086. *US Air Force Report* (1982). Cited on page 20.

Bocciarelli, M., Bolzon, G., and Maier, G. Parameter identification in anisotropic elastoplasticity by indentation and imprint mapping. *Mechanics of Materials*, 37(8), 855–868 (2005). doi: 10.1016/j.mechmat.2004.09.001. Cited on page 138.

Bolshakov, A. and Pharr, G.M. Influences of pileup on the measurement of mechanical properties by load and depth sensing indentation techniques. *Journal of Materials Research*, 13(4), 1049–1058 (1998). doi: 10.1557/JMR.1998.0146. Cited on page 69.

Botten, R., Wu, X., Hu, D., and Loretto, M.H. The significance of acoustic emission during stressing of TiAl-based alloys. Part 1: Detection of cracking during loading up in tension. *Acta Materialia*, 49(10), 1687–1691 (2001). Cited on page 52.

Bouvier, S. and Needleman, A. Effect of the number and orientation of active slip systems on

plane strain single crystal indentation. *Modelling and Simulation in Materials Science and Engineering*, 14(7), 1105–1125 (2006). doi: 10.1088/0965-0393/14/7/001. Cited on page 70.

Braun, J., Ellner, M., and Predel, B. Experimental investigations of the structure and stability of the TiAl phase. *Zeitschrift fur Metallkunde*, 86(12), 870–876 (1995). Cited on pages 23 and 24.

Britton, T.B., Liang, H., Dunne, F.P.E., and Wilkinson, A.J. The effect of crystal orientation on the indentation response of commercially pure titanium: experiments and simulations. *Proceedings of the Royal Society A*, 466, 695–719 (2010). doi: 10.1098/rspa.2009.0455. Cited on page 70.

Brockman, R.A. Analysis of elastic-plastic deformation in TiAl polycrystals. *International journal of plasticity*, 19(10), 1749– (2003). doi: 10.1016/S0749-6419(02)00102-X. Cited on pages 56 and 144.

Brocks, W., Cornec, A., and Steglich, D. Two-Scale Finite Element Modelling of Microstructures. *1st International Conference on New Materials for Extreme Environments Book Series: Advanced Materials Research*, 59, 3–17 (2009). Cited on page 55.

Brookes, C., O'Neill, J., and Redfern, B. Anisotropy in Hardness of Single Crystals. *Proceedings of the Royal Society of London Series A*, 322(1548), 73–88 (1971). Cited on page 65.

Bulychev, S.I., Alekhin, V.P., Shorshorov, M.K., Ternovskii, A.P., and Shnyrev, G.D. Determination of Youngs Modulus According to Indentation Diagram. *Zavodskaya Laboratoriya*, 41(9), 1137–1140 (1975). Cited on page 60.

Bumps, E.S., Kessler, H.D., and Hansen, M. Titanium-Aluminum System. *Transactions of the American Institute of Mining and Metallurgical Engineers*, 194(6), 609–614 (1952). Cited on page 23.

Bunge, H. *Texture Analysis in Materials Science*. Butterworths Publishers, London (1982). Cited on page 165.

Caillard, D. and Couret, A. The Hall-Petch Law Investigated by Means of In Situ Straining Experiments in Lamellar TiAl and Deformed Al. *Microscopy Research and Technique*, 72(3), 261–269 (2009). doi: 10.1002/jemt.20679. Cited on page 51.

Cailletaud, G., Forest, S., Jeulin, D., Feyel, F., Galliet, I., Mounoury, V., and Quilici, S. Some elements of microstructural mechanics. *Computational Materials Science*, 27, 351–374 (2003). Cited on page 169.

Cao, G.X., Fu, L.F., Lin, J.G., Zhang, Y.G., and Chen, C.Q. The relationships of microstructure and properties of a fully lamellar TiAl alloy. *Intermetallics*, 8(5–6), 647–653 (2000). Cited on page 50.

Carrasco, E., de la, O.R., Gonzalez, M.A., and Rojo, J.M. Dislocation cross slip and formation of terraces around nanoindentations in Au(001). *Physical Review B*, 68(18), 180102–1–4 (2003). doi: 10.1103/PhysRevB.68.180102. Cited on pages 66, 67, and 68.

Carrasco, E., Fuente, O.R.D.L., and Rojo, J. Dislocation emission at the onset of plasticity during nanoindentation in gold. *Philosophical Magazine*, 88(3), 281–296 (2008). doi: 10.1080/14786430701798951. Cited on pages 63, 66, and 68.

Casals, O. and Forest, S. Finite element crystal plasticity analysis of spherical indentation in bulk single crystals and coatings. *Computational Materials Science*, 45(3), 774–782 (2009). doi: 10.1016/j.commatsci.2008.09.030. Cited on page 70.

Casals, O., Ocenasek, J., and Alcala, J. Crystal plasticity finite element simulations of pyramidal indentation in copper single crystals. *Acta Materialia*, 55(1), 55–68 (2007). doi: 10.1016/j.actamat.2006.07.018. Cited on page 70.

Chang, S., Chiang, F.P., and Rosenberger, A. A Micromechanics Study of Lamellar TiAl. *Experimental Mechanics*, 46, 173–178 (2006). Cited on page 153.

Chang, S.C. and Chen, H.C. The determination of F.C.C. crystal orientation by indentation. *Acta Metallurgica et Materialia*, 43(6), 2501–2505 (1995). doi: 10.1016/0956-7151(94)00420-X. Cited on page 138.

Charpentier, A., Hazotte, A., and Daoz, D. Lamellar transformation in near-gamma TiAl alloys - Quantitative analysis of kinetics and microstructure. *Materials Science and Engineering A*, 491(1–2), 321–330 (2008). doi: 10.1016/j.msea.2008.02.009. Cited on page 31.

Chaudhri, M. A note on a common mistake in the analysis of nanoindentation data. *Journal of Materials Research*, 16(2), 336–339 (2001). doi: 10.1557/JMR.2001.0052. Cited on page 60.

Chaudhri, M.M. Strain hardening around spherical indentations. *Phys. Stat. Sol.*, 182, 641–652 (2000). Cited on page 64.

Chaudhri, M.M. Dislocations and Indentations. In F. Nabarro and J.P. Hirth, editors, *Dislocations in Solids, Vol. 12*, volume 12, chapter 70. Elsevier (2004). Cited on page 65.

Chen, C. and Hendrickson, A. Indentation creep of silver single crystals at low temperatures. *Matellurgical Transactions*, 2, 328–329 (1971). Cited on page 66.

Chen, G.L. and Zhang, L.C. Deformation mechanism at large strains in a high-Nb-containing TiAl at room temperature. *Materials Science and Engineering A*, 329, 163–170 (2002). Cited on page 140.

Chen, G.L., Zhang, W.J., Liu, Z.C., Li, S.J., and Kim, Y.W. Microstructure and properties of high-Nb containing TiAl-base alloys. In Kim et al. (1999b), pages 371–380. Cited on page 24.

Cheng, Y.T. and Cheng, C.M. Scaling, dimensional analysis, and indentation measurements. *Materials Science & Engineering R-reports*, 44(4–5), 91–149 (2004). doi: 10.1016/j.mser.2004.05.001. Cited on page 69.

Chladil, H., Clemens, H., Leitner, H., Bartels, A., Gerling, R., Schimansky, F.P., and Kremmer, S. Phase transformations in high Nb and C containing g-TiAl based alloys. *Intermetallics*, 14(12), 1194–1198 (2006). doi: 10.1016/j.intermet.2005.11.016. Cited on page 28.

Chraponski, J. The effect of lamellar separation on the properties of a Ti-46Al-2Nb-2Cr intermetallic alloy. *Materials Characterization*, 56(4-5), 414–420 (2006). doi: 10.1016/j.matchar.2006.01.011. 9th ECSIA and 7th STERMAT: Stereology and Image Analysis in Materials Science. Cited on page 34.

Christian, J.W. and Mahajan, S. Deformation Twinning. *Progress in Materials Science*, 39(1–2), 1–157 (1995). Cited on page 43.

Chudoba, T. and Jennett, N. Higher accuracy analysis of instrumented indentation data obtained with pointed indenters. *Journal of Physics D-applied Physics*, 41(21) (2008). doi: 10.1088/0022-3727/41/21/215407. Cited on page 69.

Clemens, H., Bartels, A., Bystrzanowski, S., Chladil, H., Leitner, H., Dehm, G., Gerling, R., and Schimansky, F. Grain refinement in [gamma]-TiAl-based alloys by solid state phase transformations. *Intermetallics*, 14(12), 1380–1385 (2006). doi: 10.1016/j.intermet.2005.11.015. Cited on page 34.

Clemens, H. and Kestler, H. Processing and applications of intermetallic gamma-TiAl-based alloys. *Advanced Engineering Materials*, 2(9), 551–570 (2000). Cited on page 19.

Cornec, A., Werwer, M., and V.Heitmann. Micromechanical modelling of deformation and fracture in lamellar gamma-TiAl-alloys. In Y.W. Kim, H. Clemens, and A. Rosenberger, editors, *Gamma Titanium Aluminides 2003*, pages 493–501. The Minerals, Metals and Materials Society (TMS), Warrendale (2003). Cited on page 55.

Coulet, A.L., Minari, F., and Capella, L. Geometry of Sliding Products by Indentation on Copper Monocrystall Face (111). *Comptes Rendus Hebdomadaires Des Seances De L Academie Des Sciences Serie C*, 269(6), 408–& (1969). Cited on page 66.

Coulet, A.L., Minari, F., and Capella, L. Dislocation Configuration Obtained After Indentation on a (iii) Face of a Copper Monocrystal. *Scripta Metallurgica*, 4(8), 593–& (1970). Cited on page 66.

Couret, A., Molénat, G., Galy, J., and Thomas, M. Microstructures and mechanical properties of TiAl alloys consolidated by spark plasma sintering. *Intermetallics*, 16(9), 1134–1141 (2008). doi: 10.1016/j.intermet.2008.06.015. Cited on pages 153 and 154.

Court, S.A., Vasudevan, V.K., and Fraser, H.L. Deformation Mechanisms in the Intermetallic Compound TiAl. *Philosophical Magazine A*, 61(1), 141–158 (1990). Cited on page 42.

Cuitino, A.M. and Ortiz, M. Computational Modeling of Single-crystals. *Modelling and Simulation in Materials Science and Engineering*, 1(3), 225–263 (1992). Cited on page 111.

Cupid, D., Fabrichnaya, O., Rios, O., Ebrahimi, F., and Seifert, H. Thermodynamic reassessment of the Ti-Al-Nb system. *International Journal of Materials Research*, 100(2), 218–233 (2009). doi: 10.3139/146.110015. Cited on page 24.

Dao, M., Chollacoop, N., Vliet, K.J.V., Venkatesh, T.A., and Suresh, S. Computational modeling of the forward and reverse problems in instrumented sharp indentation. *Acta Materialia*, 49(19), 3899–3918 (2001). doi: 10.1016/S1359-6454(01)00295-6. Cited on pages 62 and 69.

Dao, M., Kad, B.K., and Asaro, R.J. Deformation and fracture under compressive loading in lamellar TiAl microstructures. *Philosophical Magazine A*, 74(3), 569–591 (1996). Cited on page 53.

de la Fuente, O.R., Zimmerman, J.A., Gonzalez, M.A., de la, J., Hamilton, J.C., Pai, W.W., and Rojo, J.M. Dislocation emission around nanoindentations on a (001) fcc metal surface studied by scanning tunneling microscopy and atomistic simulations. *Physical Review Letters*, 88(3) (2002). doi: 10.1103/PhysRevB.88.036101. Cited on page 66.

de Neto, E.S., Peric, D., and Owen, D. *Computational Methods for Plasticity: Theory and Applications*. Wiley (2008). ISBN 0470694521. Cited on page 97.

Dehm, G. Miniaturized single-crystalline fcc metals deformed in tension: New insights in size-dependent plasticity. *Progress in Materials Science*, 54(6), 664–688 (2009). doi: 10.1016/j.pmatsci.2009.03.005. A collection of invited lectures at the MRS Spring Meeting 2008. Cited on pages 113 and 161.

Delannay, L., Jacques, P.J., and Kalidindi, S.R. Finite element modeling of crystal plasticity with grains shaped as truncated octahedrons. *International Journal of Plasticity*, 22(10), 1879–1898 (2006). doi: 10.1016/j.ijplas.2006.01.008. Cited on page 98.

Demir, E., Raabe, D., Zaafarani, N., and Zaefferer, S. Investigation of the indentation size effect through the measurement of the geometrically necessary dislocations beneath small indents of different depths using EBSD tomography. *Acta Materialia*, 57(2), 559–569 (2009). doi: 10.1016/j.actamat.2008.09.039. Cited on page 62.

Deng, X., Chawla, N., Chawla, K.K., and Koopman, M. Deformation behavior of (Cu, Ag)-Sn intermetallics by nanoindentation. *Acta Materialia*, 52(14), 4291–4303 (2004). doi: 10.1016/j.actamat.2004.05.046. Cited on page 69.

Denquin, A. and Naka, S. On the Existence of Transformation-induced Antiphase Boundaries in the Gamma-phase of 2-phase TiAl-based Alloys. *Philosophical Magazine Letters*, 68(1), 13–20 (1993). Cited on page 34.

Denquin, A. and Naka, S. Phase-transformation mechanisms in two-phse TiAl-based alloys. In Kim et al. (1995), page 141. Cited on page 34.

Denquin, A. and Naka, S. Phase-transformation mechanisms involved in two-phase TiAl-based alloys –I. Lamellar structure formation. *Acta Materialia*, 44, 343–352 (1996). Cited on pages 27, 28, and 31.

Desch, C.H. *Intermetallic Compounds*. Longmans, Green and Co. (1914). Cited on pages 60 and 61.

Dey, S.R., Hazotte, A., and Bouzy, E. Multiscale gamma variant selection in a quarternary near-gamma Ti-Al alloy. *Philosophical Magazine*, 86(20), 3089–3112 (2006a). Cited on pages 30, 78, and 79.

Dey, S.R., Morawiec, A., Bouzy, E., Hazotte, A., and Fundenberger, J.J. A technique for determination of gamma/gamma interface relationships in a (alpha(2)+gamma) TiAl base alloy using TEM Kikuchi patterns. *Materials Letters*, 60(5), 646–650 (2006b). doi: 10.1016/j.matlet.2005.09.052. Cited on page 78.

Dey, S., Hazotte, A., and Bouzy, E. Crystallography and phase transformation mechanisms in TiAl-based alloys - A synthesis. *Intermetallics*, 17(12), 1052–1064 (2009). doi: 10.1016/j.intermet.2009.05.013. Cited on page 28.

Dimiduk, D. Gamma titanium aluminides – An emerging materials technology. In Kim et al. (1995). Cited on page 20.

Dimiduk, D.M., Hazzledine, P., Parthasarathy, T., Seshagiri, S., and Mendiratta, M. The role of grain size and selected microstructural parameters in strengthening fully lamellar TiAl alloys. *Metallurgical and Materials Transactions A*, 29(1), 37–47 (1998). Cited on pages 50, 77, and 153.

Dimiduk, D.M., Parthasarathy, T.A., and Hazzledine, P.M. Design-tool representations of strain compatibility and stress-strain relationships for lamellar gamma titanium aluminides. *Intermetallics*, 9(10-11), 875– (2001). doi: 10.1016/S0966-9795(01)00085-1. Cited on pages 47, 51, and 143.

Doerner, M. and Nix, W. A method for interpreting the data from depth-sensing indentation instruments. *Journal of Materials Research*, 1(4), 601–609 (1986). doi: 10.1557/JMR.1986.0601. Cited on page 60.

Doghri, I. *Mechanics of Deformable Solids - Linear and Nonlinear, Analytical and Computational Aspects*. Springer (2000). Cited on page 37.

Dorner, D., Roller, K., Skrotzki, B., Stockhert, B., and Eggeler, G. Creep of a TiAl alloy: a comparison of indentation and tensile testing. *Materials Science and Engineering A*, 357(1–2), 346–354 (2003). doi: 10.1016/S0921-5093(03)00205-3. Cited on page 161.

Durst, K., Göken, M., and Pharr, G.M. Finite element simulation of spherical indentation in the elastic-plastic transition. *Zeitschrift für Metallkunde*, 93(9), 857–861 (2002). Cited on page 69.

Dyer, L.D. Actual Dislocation Distribution Around a Ball Indentation on Cube Face of Copper. *ASM Transactions Quarterly*, 58(4), 620–644 (1965). Cited on page 66.

Ehret, A., Itskov, M., and Schmid, H. Numerical integration of the unit sphere and its effect on the material symmetry of constitutive equations – A comparative study. *Int. J. Numer. Meth. Engng.*, 81(2), 189–206 (2009). doi: 10.1002/nme.2688. Cited on page 131.

Eidel, B. and Stukowski, A. A variational formulation of the quasicontinuum method based on energy sampling in clusters. *Journal of the Mechanics and Physics of Solids*, 57(1), 87–108 (2009). doi: 10.1016/j.jmps.2008.09.017. Cited on page 69.

Erschbaumer, H., Podloucky, R., Rogl, P., et al. Atomic Modeling of Nb, V, Cr, and Mn Substitutions in Gamma-TiAl. 1. c/a-ratio and Site Preference. *Intermetallics*, 1, 99–106 (1993). Cited on page 27.

Farenc, S., Coujou, A., and Couret, A. An Insitu Study of Twin Propagation in TiAl. *Philosophical Magazine A*, 67(1), 127–142 (1993). Cited on page 43.

Fischer, F.D., Schaden, T., Appel, F., and Clemens, H. Mechanical twins, their development and growth. *European Journal of Mechanics A – Solids*, 22(5), 709–726 (2003). doi: 10.1016/S0997-7538(03)00081-0. Cited on page 44.

Fischer-Cripps. *Introduction to Contact Mechanics*. Springer (2000). Cited on page 139.

Fischer-Cripps, A. *Nanoindentation*. Springer, 2nd edition (2004). Cited on pages 60, 63, 64, and 67.

Fischer-Cripps, A. Critical review of analysis and interpretation of nanoindentation test data. *Surface and Coatings Technology*, 200(14-15), 4153–4165 (2006). doi: 10.1016/j.surfcoat.2005.03.018. Cited on page 67.

Fleischer, R.L., Dimiduk, D.M., and Lipsitt, H.A. Intermetallic Compounds for Strong High-temperature Materials - Status and Potential. *Annual Review of Materials Science*, 19, 231–263 (1989). Cited on page 20.

Flom, D.G. and Komanduri, R. Some indentation and sliding experiments on single crystal and polycrystalline materials. *Wear*, 252, 401–429 (2002). Cited on page 66.

Franciosi, P. and Zaoui, A. Multislip in F.C.C. Crystals a Theoretical Approach Compared with Experimental Data. *Acta Metallurgica*, 30(8), 1627–1637 (1982). Cited on page 111.

Frank, G.J., Olson, S.E., and Brockman, R.A. Numerical models of orthotropic and lamellar grain structures. *Intermetallics*, 11(4), 331–340 (2003). doi: 10.1016/S0966-9795(03)00004-9. Cited on page 56.

Fröhlich, F., Grau, P., and Grellmann, W. Performance and analysis of recording microhardness tests. *Physica Status Solidi A*, 42(1), 79–89 (1977). doi: 10.1002/pssa.2210420106. Cited on pages 60 and 66.

Friedel, J. *Dislocations*. Pergamon (1964). Cited on page 52.

Froes, F.H., Suryanarayana, C., and Eliezer, D. Synthesis, Properties and Applications of Titanium Aluminides. *Journal of Materials Science*, 27(19), 5113–5140 (1992). Cited on page 20.

Fu, C.L. and Yoo, M.H. Elastic-constants, Fault Energies, and Dislocation Reactions in TiAl - a 1st-principles Total-energy Investigation. *Philosophical Magazine Letters*, 62(3), 159–165 (1990). Cited on page 39.

Fujiwara, T., Nakamura, A., Hosomi, M., Nishitani, S.R., Shirai, Y., and Yamaguchi, M. Deformation of Polysynthetically Twinned Crystals of TiAl With a Nearly Stoichiometric Composition. *Philosophical Magazine A*, 61(4), 591–606 (1990). Cited on page 55.

Gane, N. and Cox, J.M. Micro-hardness of Metals at Very Low Loads. *Philosophical Magazine*, 22(179), 881–891 (1970). doi: 10.1080/14786437008221059. Cited on page 66.

Gebhard, S., Pyczak, F., and Göken, M. Microstructural and micromechanical characterisation of TiAl alloys using atomic force microscopy and nanoindentation. *Mater. Sci Engr. A*, in press (2009). doi: 10.1016/j.msea.2009.05.068. Cited on page 70.

George, E., Mills, M., and Yamaguchi, M., editors. *High-temperature ordered intermetallic alloys IX*, volume 552 of *Mater. Res. Soc. Proc.* MRS, MRS (1999). Cited on page 163.

George, E.P., Yamaguchi, M., Kumar, K.S., and Liu, C.T. Ordered Intermetallics. *Annual Review of Materials Science*, 24, 409–451 (1994). Cited on page 20.

Gerday, A., Bettaieb, M.B., Duchêne, L., Clément, N., Diarra, H., and Habraken, A. Interests and limitations of nanoindentation for bulk multiphase material identification: Application to the [beta] phase of Ti-5553. *Acta Materialia*, 57, 5186–5196 (2009). doi: 10.1016/j.actamat.2009.07.020. Cited on page 70.

Gerk, A.P. Effect of Work-hardening Upon Hardness of Solids - Minimum Hardness. *Journal of Materials Science*, 12(4), 735–738 (1977). Cited on pages 59 and 67.

Giannakopoulos, A.E., Larsson, P.L., and Vestergaard, R. Analysis of Vickers Indentation. *International Journal of Solids and Structures*, 31(19), 2679–2708 (1994). Cited on page 69.

Göken, M., Kempf, M., and Nix, W. Hardness and modulus of the lamellar microstructure in PST-TiAl studied by nanoindentations and AFM. *Acta Materialia*, 49(5), 903–911 (2001). doi: 10.1016/S1359-6454(00)00375-X. Cited on pages 70 and 123.

Goo, E. Application of von Mises criterion to single and dual phase TiAl. *Scripta Materialia*, 38(11), 1711–1716 (1998). Cited on page 44.

Gottstein, G. *Physical Foundations of Material Science*. Springer (2003). Cited on page 44.

Grossin, D., Henrist, C., Mathieu, J.P., Meslin, S., Harnois, C., Noudem, J.G., Cloots, R., and Chateigner, D. EBSD study on YBCO textured bulk samples: correlation between crystal growth and 'microtexture'. *Superconductor Science & Technology*, 19(2), 190–199 (2006). doi: 10.1088/0953-2048/19/2/007. Cited on page 79.

Grujicic, M. and Batchu, S. A crystal plasticity materials constitutive model for polysynthetically-twinned gamma-TiAl+alpha(2)-Ti3Al single crystals. *Journal of Materials Science*, 36(12), 2851–2863 (2001). Cited on pages 55 and 144.

Grujicic, M. and Cao, G. Crack growth in lamellar titanium aluminides containing beta phase precipitates. *Journal of Materials Science*, 37(14), 2949–2963 (2002). Cited on page 55.

Grujicic, M., Cao, G., and Batchu, S. Crystal plasticity-based finite element analysis of deforma-

tion and fracture of polycrystalline lamellar γ-TiAl + α_2-Ti_3Al alloys. *Journal of Materials Science*, 38, 307–322 (2003). Cited on page 55.

Grujicic, M. and Zhang, Y. Crystal plasticity analysis of the effect of dispersed [beta]-phase on deformation and fracture of lamellar [gamma]+[alpha]2 titanium aluminide. *Materials Science and Engineering A*, 265(1-2), 285–300 (1999). doi: 10.1016/S0921-5093(98)00858-2. Cited on page 55.

Gwyddion. Free SPM (AFM, SNOM/NSOM, STM, MFM, ...) data analysis software (2004–2009). Cited on page 114.

Hall, E.O. The deformation and ageing of mild steel: 3. Discussion of results. *Proc. Phys. Soc. B*, 64, 747–753 (1951). Cited on page 49.

Hao, Y.L., Xu, D.S., Cui, Y.Y., Yang, R., and Li, D. The site occupancies of alloying elements in TiAl and Ti3Al alloys. *Acta Materialia*, 47(4), 1129–1139 (1999). Cited on page 27.

Hazzledine, P. Coherency and loss of coherency in TiAl. *Intermetallics*, 6, 673–677 (1998). Cited on pages 28 and 51.

Hazzledine, P. and Kad, B. Yield and fracture of lamellar γ/α_2 TiAl alloys. *Mater. Sci. Engr. A*, 192/193, 340–346 (1995). Cited on pages 31 and 48.

He, Y., Schwarz, R.B., Darling, T., Hundley, M., Whang, S.H., and Wang, Z.M. Elastic constants and thermal expansion of single crystal gamma-TiAl from 300 to 750 K. *Materials Science and Engineering A*, 240, 157–163 (1997). Cited on pages 38, 39, and 40.

Hecht, U., Daloz, D., Lapin, J., Drevermann, A., Witusiewicz, V., and Zollinger, J. Solidification of TiAl-based alloys. In *Advanced Intermetallic-Based Alloys for Extreme Environment and Energy Applications, edited by M. Palm, B.P. Bewlay, M. Takeyama, J.M.K. Wiezorek, Y-H. He (Mater. Res. Soc. Symp. Proc. Volume 1128, Warrendale, PA* (2009). Cited on pages 24, 26, and 86.

Heinz, A. and Neumann, P. Representation of Orientation and Disorientation Data for Cubic, Hexagonal, Tetragonal and Orthorhombic Crystals. *Acta Crystallographica, Section A*, 47, 780–789 (1991). Cited on page 165.

Helming, K., Tamm, R., and Fels, B. An Automated Component Method. *Mater. Sci. Forum*, 273-275, 119–124 (1998). Cited on pages 131 and 165.

Hemker, K.J. and Sharpe, W.N. Microscale characterization of mechanical properties. *Annual Review of Materials Research*, 37, 93–126 (2007). doi: 10.1146/annurev.matsci.36.062705.134551. Cited on pages 113 and 161.

Heripre, E. *Methode de couplage multi-echelles entre simulations numeriques polycristallines et mesures de champs pour l'identification des parametres de lois de comportement et de fissuration des materiaux metalliques.* Onera, DGA, Ecole Polytechnique (2006). Cited on page 56.

Hériprе, E., Dexet, M., Crepin, J., Geléebart, L., and A. Roos M. Bornert, D.C. Coupling between experimental measurements and polycrystal finite element calculations for micromechanical study of metallic materials. *International Journal of Plasticity*, 23, 1512–1539 (2007). Cited on page 56.

Herzig, C., Przeorski, T., Friesel, M., Hisker, F., and Divinski, S. Tracer solute diffusion of Nb, Zr, Cr, Fe, and Ni in [gamma]-TiAl: effect of preferential site occupation. *Intermetallics*, 9(6), 461–472 (2001). doi: 10.1016/S0966-9795(01)00025-5. Cited on page 26.

Hill, R. Generalized Constitutive Relations for Incremental Deformation of Metal Crystals by Multislip. *Journal of the Mechanics and Physics of Solids*, 14(2), 95–102 (1966). doi: 10.1016/0022-5096(66)90040-8. Cited on page 100.

Hill, R., Storakers, F., and Zdunek, A. A theroretical study of the Brinnell hardness test. *Proc. R. Soc. Lond. A*, 423, 301–330 (1989). Cited on pages 64 and 69.

Hirsch, P.B., Pirouz, P., Roberts, S.G., and Warren, P.D. Indentation Plasticity and Polarity

of Hardness on (111) Faces of GaAs. *Philosophical Magazine B*, 52(3), 759–784 (1985). Cited on page 66.

Hirth, J. and Lothe, J. *Theory of Dislocations*. Krieger Publishing, 2nd edition (1992). Originally published Wiley 1982. Cited on pages 38 and 40.

Hollatz, M., Bobeth, M., Pompe, W., and Marx, V. Orientation dependent crack patterns in alumina films on NiAl single crystals due to spherical indentation. *Acta Materialia*, 44(10), 4149–4159 (1996). Cited on page 68.

Hono, K., Abe, E., Kumagai, T., and Harada, H. Chemical compositions of ultrafine lamellae in the water-quenched Ti-48Al alloy. *Scripta Materialia*, 35(4), 495–499 (1996). doi: 10.1016/1359-6462(96)00123-6. Cited on page 34.

Hosford, W.F. *The mechanics of crystals and texured polycrystals*. Oxford University Press (1993). Cited on page 167.

Howe, J., Pond, R., and Hirth, J. The role of disconnections in phase transformations. *Progress in Materials Science*, 54(6), 792–838 (2009). doi: 10.1016/j.pmatsci.2009.04.001. A collection of invited lectures at the MRS Spring Meeting 2008. Cited on page 33.

Howell, J., Hellmann, J., and Muhlstein, C. Correlations between free volume and pile-up behavior in nanoindentation reference glasses. *Materials Letters*, 62(14), 2144–2146 (2008). doi: 10.1016/j.matlet.2007.11.067. Cited on page 67.

Hsiung, L.M., Schwartz, A.J., and Nieh, T.G. In situ TEM observations of interface sliding and migration in a refined lamellar TiAl alloy. *Intermetallics*, 12(7-9), 727–732 (2004). doi: 10.1016/j.intermet.2004.02.012. Intermetallic and Advanced Metallic Materials - A Symposium Dedicated to Dr. C.T. Liu, 3-6 March 2003, San Diego, CA, USA. Cited on page 49.

Hsiung, L., Nieh, T.G., Choi, B.W., and Wadsworth, J. Interfacial dislocations and deformation twinning in fully lamellar TiAl. *Mater. Sci. Engr. A*, 329–331, 637–643 (2002). Cited on pages 44, 49, and 140.

Hu, D. and Botten, R.R. Phase transformations in some TiAl-based alloys. *Intermetallics*, 10(7), 701–715 (2002). Cited on pages 27 and 34.

Hu, D., Huang, A., Jiang, H., Mota-Solis, N., and Wu, X.H. Pre-yielding and pre-yield cracking in TiAl-based alloys. *Intermetallics*, 14(1), 82–90 (2006a). doi: 10.1016/j.intermet.2005.04.016. Cited on pages 52 and 153.

Hu, D., Huang, A.J., Novovic, D., and Wu, X. The effect of boron and alpha grain size on the massive transformation in Ti-46Al-8Nb-xB alloys. *Intermetallics*, 14(7), 818–825 (2006b). doi: 10.1016/j.intermet.2005.12.003. Cited on page 34.

Hu, D., Huang, A.J., and Wu, X. On the massive phase transformation regime in TiAl alloys: The alloying effect on massive/lamellar competition. *Intermetallics*, 15(3), 327–332 (2007). Cited on pages 34 and 35.

Hu, D., Huang, A., Gregoire, A., Li, X., Wu, X., and Loretto, M. Determining continuous cooling phase transformation behaviour in Ti-46Al-8Nb using Jominy end quenching. *Materials Forum*, 29, 172–175 (2005). Cited on pages 27 and 28.

Huang, A., Hu, D., Wu, X., and Loretto, M. The influence of interrupted cooling on the massive transformation in Ti46Al8Nb. *Intermetallics*, 15, 1147–1155 (2007a). Cited on pages 26, 34, and 79.

Huang, A.J., Hu, D., Loretto, M.H., Mei, J., and Wu, X.H. The influence of pressure on solid-state transformations in Ti-46Al-8Nb. *Scripta Materialia*, 56(4), 253–256 (2007b). Cited on page 35.

Huang, A., Hu, D., Loretto, M., and Wu, X. The formation of grain boundary gamma during cooling of Ti46Al8Nb. *Intermetallics*, 17(5), 285–290 (2009). doi: 10.1016/j.intermet.2008.09.012. Cited on page 34.

Huang, S. and Chestnutt, J. Gamma TiAl and its Alloys. In Westbrook and Fleischer (2000c), chapter 4, pages 75–92. Cited on page 20.

Huber, N. and Tsakmakis, C. Determination of constitutive properties fromspherical indentation data using neural networks. Part i:the case of pure kinematic hardening in plasticity laws. *Journal of the Mechanics and Physics of Solids*, 47(7), 1569–1588 (1999). doi: 10.1016/S0022-5096(98)00109-4. Cited on page 62.

Hug, G., Loiseau, A., and Veyssiere, P. Weak-beam Observation of a Dissociation Transition in TiAl. *Philosophical Magazine A*, 57(3), 499–523 (1988). Cited on page 40.

Häussler, D., Bartsch, M., Aindow, M., Jones, I.P., and Messerschmidt, U. Dislocation processes during the plastic deformation of gamma-TiAl. *Philosophical Magazine A*, 79(5), 1045–1071 (1999). Cited on page 42.

Hysitron Inc. TriboIndenter User's Manual (2003). Cited on page 140.

Imayev, V., Khismatullin, T., Oleneva, T., Imayev, R., Valiev, R., Wunderlich, R., Minkow, A., Hecht, U., and Fecht, H.J. Grain Refinement in Cast Ti-46Al-8Nb AND Ti-46Al-8Ta Alloys via Massive Transformation. *Advanced Engineering Materials*, 10(12), 1095–1100 (2008). doi: 10.1002/adem.200800159. Cited on page 34.

Inui, H., Matsumuro, M., Wu, D.H., and Yamaguchi, M. Temperature dependence of yield stress, deformation mode and deformation structure in single crystals of TiAl (Ti-56 at% Al). *Philosophical Magazine A*, 75(2), 395–423 (1997). Cited on pages 42 and 45.

Inui, H., Nakamura, A., Oh, M.H., and Yamaguchi, M. Deformation Structures in Ti-rich TiAl Polysynthetically Twinned Crystals. *Philosophical Magazine A*, 66(4), 557–573 (1992a). Cited on page 40.

Inui, H., Oh, M., and Nakamura, A. Room-temperature tensile deformation of polysynthetically twinned (PST) crystals of TiAl. *Acta Metallurgica et Materialia*, 40(11), 3095–3104 (1992b). Cited on pages 28, 29, 31, 34, 42, 49, and 78.

Inui, H., Oh, M., Nakamura, A., and Yamaguchi, M. Ordered domains in TiAl coexisting with Ti3Al in the lamellar structure of Ti-rich TiAl compounds. *Philosophical Magazine A*, 66(4), 539–555 (1992c). Cited on pages 29 and 30.

Inui, H., Toda, Y., Kishida, K., Shirai, Y., and Yamaguchi, M. Variation of CRSS for Various Slip Systems with Al Concentration in Ti3Al Single Crystals. *Journal of the Japan Institute of Metals*, 59(5), 586–587 (1995). In Japanese. Cited on page 47.

ISO. *Metallic materials - Instrumented indentation test for hardness and materials parameters - Part 1: Test method (ISO 14577-1:2002); German version EN ISO 14577-1:2002*. Beuth (2003a). Cited on page 60.

ISO. *Metallic materials - Instrumented indentation test for hardness and materials parameters - Part 2: Verification and calibration of testing machines (ISO 14577-2:2002); German version EN ISO 14577-2:2002*. Beuth (2003b). Cited on page 60.

ISO. *Metallic materials - Instrumented indentation test for hardness and materials parameters - Part 3: Calibration of reference blocks (ISO 14577-3:2002); German version EN ISO 14557-3:2002*. Beuth (2003c). Cited on page 60.

Jarvis, D.J. and Voss, D. IMPRESS integrated project - An overview paper. *Materials Science and Engineering A*, 413, 583–591 (2005). doi: 10.1016/j.msea.2005.09.066. Cited on page 19.

Jiang, C. First-principles study of site occupancy of dilute 3d, 4d and 5d transition metal solutes in L1(0) TiAl. *Acta Materialia*, 56(20), 6224–6231 (2008). doi: 10.1016/j.actamat.2008.08.047. Cited on page 27.

Jiang, H., Garcia-Pastor, F., Hu, D., Wu, X., Loretto, M., Preuss, M., and Withers, P. Characterization of microplasticity in TiAl-based alloys. *Acta Materialia*, 57(5), 1357–1366 (2009). doi: 10.1016/j.actamat.2008.11.029. Cited on page 153.

Jin, Z. and Bieler, T.R. A Numerical Force and Stress-analysis on a Thin Twin Layer in TiAl. *Philosophical Magazine A*, 72(5), 1201–1219 (1995). Cited on page 44.

Jirásek, M. and Bažant, Z.P. *Inelastic Analysis of Structures*. Wiley (2001). Cited on page 97.

John, R., Porter, W., and Olson, S. Measurement and modeling of orthotropic elastic behav-

ior of grainsin a gamma titanium aluminide alloy. *Intermetallics*, 12(1), 1–9 (2004). doi: 10.1016/j.intermet.2003.07.006. Cited on page 56.

Jones, S. and Kaufman, M. Phase equilibria and transformations in intermediate titanium-aluminum alloys. *Acta Metallurgica et Materialia*, 41(2), 387–398 (1993). doi: 10.1016/0956-7151(93)90069-5. Cited on pages 27 and 34.

Kad, B.K. and Asaro, R.J. Apparent Hall-Petch effects in polycrystalline lamellar TiAl. *Philosophical Magazine A*, 75(1), 87–104 (1997). Cited on pages 49, 50, 51, 53, and 155.

Kad, B.K., Dao, M., and Asaro, R.J. Numerical Simulations of Plastic-deformation and Fracture Effects in 2 Phase Gamma-TiAl+alpha-2-Ti3Al Lamellar Microstructures. *Philosophical Magazine A*, 71(3), 567–604 (1995). Cited on pages 53 and 144.

Kad, B.K. and Fraser, H.L. Effects of Oxygen on the Deformation-Behavior in Single-Phase Gamma-TiAl Alloys. *Philosophical Magazine Letters*, 70(4), 211–220 (1994). doi: 10.1080/09500839408240977. Cited on pages 26 and 42.

Kalidindi, S.R., Bronkhorst, C.A., and Anand, L. Crystallographic Texture Evolution in Bulk Deformation Processing of FCC Metals. *Journal of the Mechanics and Physics of Solids*, 40(3), 537–569 (1992). doi: 10.1016/0022-5096(92)80003-9. Cited on pages 98, 102, and 103.

Kalidindi, S.R. and Schoenfeld, S.E. On the prediction of yield surfaces by the crystal plasticity models for fcc polycrystals. *Materials Science and Engineering A*, 293(1–2), 120–129 (2000). Cited on page 101.

Kalidindi, S. Incorporation of deformation twinning in crystal plasticity models. *Journal of the Mechanics and Physics of Solids*, 46(2), 267–290 (1998). Cited on page 104.

Kalidindi, S. Micro-Mechanical Finite Element Models for Crystal Plasticity. In Raabe et al. (2004a), pages 529–542. doi: 10.1002/3527603786. Cited on page 102.

Katzarov, I., Malinov, S., and Sha, W. A phase-field model for computer simulation of lamellar structure formation in gamma-TiAl. *Acta Materialia*, 54(2), 453–463 (2006). doi: 10.1016/j.actamat.2005.09.016. Cited on page 32.

Katzarov, I.H., Cawkwell, M.J., Paxton, A.T., and Finnis, M.W. Atomistic study of ordinary 1/2 <110] screw dislocations in single-phase and lamellar gamma-TiAl. *Philosophical Magazine*, 87(12), 1795–1809 (2007). doi: 10.1080/14786430601080252. Cited on page 140.

Katzarov, I. and Paxton, A. Atomistic studies of interactions between the dominant lattice dislocations and [gamma]/[gamma]-lamellar boundaries in lamellar [gamma]-TiAl. *Acta Materialia*, 57(11), 3349–3366 (2009). doi: 10.1016/j.actamat.2009.03.042. Cited on page 140.

Kawabata, T., Fukai, H., and Izumi, O. Effect of ternary additions on mechanical properties of TiAl. *Acta Materialia*, 46(6), 2185–2194 (1998). Cited on page 86.

Kearney, C., Zhao, Z., Bruet, B.J.F., Radovitzky, R., Boyce, M.C., and Ortiz, C. Nanoscale anisotropic plastic deformation in single crystal aragonite. *Physical Review Letters*, 96(25) (2006). doi: 10.1103/PhysRevLett.96.255505. Cited on page 70.

Kempf, M., Göken, M., and Vehoff, H. The mechanical properties of different lamellae and domains in PST-TiAl investigated with nanoindentations and atomic force microscopy. *Material Science and Engineering A*, 329(Sp. Iss. SI), 184–189 (2002). doi: 10.1016/S0921-5093(01)01561-1. Cited on page 70.

Kestler, H. and Clemens, H. Production, Processing and Application of γ(TiAl)-Based Alloys. In Leyens and Peters (2003), chapter 14, pages 351–392. Cited on pages 20, 23, and 26.

Khan, A. and Huang, S. *Continuum Theory of Plasticity*. Wiley-Interscience (1995). Cited on page 97.

Kibey, S., Liu, J., Johnson, D., and Sehitoglu, H. Predicting twinning stress in fcc metals: Linking twin-energy pathways to twin nucleation. *Acta Materialia*, 55(20), 6843–6851 (2007). doi: 10.1016/j.actamat.2007.08.042. Cited on page 43.

Kiely, J.D. and Houston, J.E. Nanomechanical properties of Au (111), (001), and (110) surfaces. *Physical Review B*, 57(19), 12588–12594 (1998). Cited on page 66.

Kiener, D., Motz, C., Dehm, G., and Pippan, R. Overview on established and novel FIB based miniaturized mechanical testing using in-situ SEM. *International Journal of Materials Research*, 100(8), 1074–1087 (2009). doi: 10.3139/146.110149. Cited on page 113.

Kim, M., Nomura, M., Vitek, V., and Pope, D. Deformation of PST TiAl Single Crystals with near-hard orientations. In E. George, M. Yamaguchi, and M. Mills, editors, *Mat. Res. Soc. Symp. Proc.*, volume 552, page KK3.1.1 (1999a). Cited on page 147.

Kim, Y.W. Intermetallic Alloys Based on Gamma Titanium Aluminide. *JOM - Journal of the Minerals Metals & Materials Society*, 41(7), 24–30 (1989). Cited on page 20.

Kim, Y.W. Ordered Intermetallic Alloys. 3. Gamma-Titanium Aluminides. *JOM-Journal of the Minerals Metals & Materials Society*, 46(7), 30–39 (1994). Cited on pages 20 and 23.

Kim, Y.W. Strength and ductility in TiAl alloys. *Intermetallics*, 6(7), 623–628 (1998). Cited on page 153.

Kim, Y.W. and Dimiduk, D.M. Progress in the Understanding of Gamma Titanium Aluminides. *JOM*, 43(8), 40–47 (1991). Cited on page 20.

Kim, Y.W., Dimiduk, D., Loretto, M.H., Wagner, R., and Yamaguchi, M., editors. *Gamma Titanium Aluminides I, held during TMS annual meeting in Las Vegas, Nevada*. TMS The Minerals, Metals and Materials Society (1995). Cited on pages 163, 181, 182, and 188.

Kim, Y.W., Dimiduk, D., and Loretto, M., editors. *Gamma Titanium Aluminides, Proceedings of a symposium held during the 1999 TMS annual meeting*. TMS, TMS The Minerals, Metals and Materials Society (1999b). Cited on pages 163 and 180.

Kim, Y.W. and Boyer, R.R., editors. *Microstructure/Property Relationships in Titanium Aluminides and Alloys*. TMS, TMS The Minerals, Metals and Materials Society (1991). Cited on page 163.

Kim, Y.W., Clemens, H., and Rosenberger, A.H., editors. *Gamma Titanium Aluminides III*. TMS, TMS The Minerals, Metals, & Materials Society (2003). ISBN 0873395433. International Symposium on Gamma Titanium Aluminides, 2003: San Diego, Calif., USA. Cited on page 163.

Kim, Y.W., Morris, D.G., Yang, R., and Leyens, C., editors. *Structural Aluminides for Elevated Temperature Applications*. TMS The Minerals, Metals and Materials Society (2008). ISBN 978-0-87339-720-9. Cited on page 163.

Kishida, K., Inui, H., and Yamaguchi, M. Deformation of lamellar structure in TiAl-Ti_3Al two phase alloys. *Philosophical Magazine A*, 78, 1–28 (1998). Cited on pages 40, 44, and 147.

Kishida, K., Takahama, Y., and Inui, H. Deformation twinning in single crystals of a $D0_{19}$ compound with an off-stochiometric composition (Ti-36.5at.%Al). *Acta Materialia*, 52, 4941–4952 (2004). Cited on page 47.

Knapp, J.A., Follstaedt, D.M., Myers, S.M., Barbour, J.C., and Friedmann, T.A. Finite-element modeling of nanoindentation. *Journal of Applied Physics*, 85(3), 1460–1474 (1999). doi: 10.1063/1.369178. Cited on page 69.

Kobayashi, E., Kobayashi, E., Shinmoto, K., Miura, S., Suzuki, T., and Mishima, Y. Effect of deviation from the stoichiometry on the lattice constants and strength of the $L1_0$ TiAl-X (X=Cr, V or Nb) alloys at ambient temperature. In Kim et al. (1995), pages 347–352. Cited on page 86.

Kocks, U.F. Relation Between Polycrystal Deformation and Single-crystal Deformation. *Metallurgical Transactions*, 1(5), 1121–& (1970). Cited on page 50.

Kocks, U.F. and Mecking, H. Physics and phenomenology of strain hardening: the FCC case. *Progress in Materials Science*, 48(3), 171–273 (2003). Cited on page 111.

Krieger-Lassen, N.C., Juul-Jensen, D., and Conradsen, K. Image-processing Procedures for Analysis of Electron Back Scattering Patterns. *Scanning Microscopy*, 6(1), 115–121 (1992). Cited on page 83.

Krieger-Lassen, N. Automatic high-precision measurements of the location and width of

Kikuchi bands in electron backscatter diffraction patterns. *J. Microscopy*, 190, 375–391 (1998). Cited on page 95.

Kröner, E. Allgemeine Kontinuumstheorie der Versetzungen und Eigenspannungen. *Archive for Rational Mechanics and Analysis*, 4, 273–334 (1960). Cited on page 98.

Lamirand, M. Relative effects of Cr and niobium on microstructure and mechanical properties as a function of oxygen content in TiAl alloys. *Scripta Materialia*, 56, 325–328 (2007). Cited on page 27.

Larsson, P.L. Modelling of sharp indentation experiments: some fundamental issues. *Philosophical Magazine*, 86(33–35), 5155–5177 (2006). doi: 10.1080/14786430600589089. Cited on page 69.

Larsson, P.L., Giannakopoulos, A.E., Soderlund, E., Rowcliffe, D.J., and Vestergaard, R. Analysis of Berkovich indentation. *International Journal of Solids and Structures*, 33(2), 221–& (1996). Cited on page 69.

Laursen, T.A. and Simo, J.C. A Study of the Mechanics of Microindentation Using Finite-Elements. *Journal of Materials Research*, 7(3), 618–626 (1992). doi: 10.1557/JMR.1992.0618. Cited on page 69.

Lay, S., Loubradou, M., and Bonnet, R. Atomic structures of linear singularities at close-packed $\{111\}_\gamma \parallel (0001)_{\alpha_2}$ interfaces in a 60Ti-40Al (at%) alloy. *Physica Status Solidi A*, 178(2), 681–700 (2000). Cited on page 28.

Lebensohn, R. Modelling the role of local correlations in polycrystal plasticity using viscoplastic self-consistent schemes. *Modelling and Simulation in Materials Science and Engineering*, 7(5), 739–746 (1999). Cited on pages 53 and 55.

Lebensohn, R., Uhlenhut, H., Hartig, C., and Mecking, H. Plastic flow of gamma-TiAl-based polysynthetically twinned crystals: Micromechanical modeling and experimental validation. *Acta Materialia*, 46(13), 4701–4709 (1998). Cited on pages 47, 53, and 55.

Lebensohn, R.A., Turner, P.A., and Canova, G.R. Recent advances in modelling polycrystals with complex microstructures. *Computational Materials Science*, 9(1-2), 229–236 (1997). doi: 10.1016/S0927-0256(97)00078-5. Cited on page 55.

Lee, B.J., Ahzi, S., Kad, B.K., and Asaro, R.J. On the Deformation Mechanisms in Lamellar Ti-Al Alloys. *Scripta Metallurgica et Materialia*, 29(6), 823–828 (1993). Cited on page 53.

Lee, E.H. Elastic-plastic Deformation at Finite Strains. *Journal of Applied Mechanics*, 36(1), 1–6 (1969). Cited on page 98.

Lee, Y.H., Hahn, J.H., Nahm, S.H., Jang, J.I., and Kwon, D. Investigations on indentation size effects using a pile-up corrected hardness. *Journal of Physics D: Applied Physics*, 41(7), 074027 (5pp) (2008). doi: 10.1088/0022-3727/41/7/074027. Cited on pages 66 and 68.

Lefebvre, W., Loiseau, A., Thomas, M., and Menand, A. Influence of oxygen on the alpha → gamma massive transformation in a Ti-48 at.% Al alloy. *Philosophical Magazine A*, 82(11), 2341–2355 (2002). doi: 10.1080/01418610210144403. Cited on pages 26 and 35.

Leyens, C. and Peters, M., editors. *Titanium and Titanium Alloys: Fundamentals and Applications*. Wiley-VCH (2003). ISBN 3527305343. Cited on pages 20, 177, and 187.

Lipsitt, H.A., Shechtman, D., and Schafrik, R.E. Deformation and Fracture of TiAl at Elevated-temperatures. *Metallurgical Transactions A*, 6(11), 1991–1996 (1975). Cited on page 40.

Liu, C.T. and Maziasz, P.J. Microstructural control and mechanical properties of dual-phase TiAl alloys. *Intermetallics*, 6(7–8), 653–661 (1998). Cited on page 50.

Liu, C.T., Schneibel, J.H., Maziasz, P.J., Wright, J.L., and Easton, D.S. Tensile properties and fracture toughness of TiAl alloys with controlled microstructures. *Intermetallics*, 4(6), 429–440 (1996). Cited on page 33.

Liu, L., Ogasawara, N., Chiba, N., and Chen, X. Can indentation technique measure unique elastoplastic properties? *J. Mater. Res.*, 24(3), 784–800 (2009a). Cited on page 62.

Liu, Y., Lin, D.L., Liu, Z.G., and Wang, Z.G. Superlattice dislocations in Ti-rich polysyntheti-

cally twinned crystals of TiAl. *Philosophical Magazine A*, 79(12), 2965–2978 (1999). Cited on page 41.

Liu, Y., Ma, S.V.J., Lu, M.Y.H., and Komanduri, R. Orientation effects in nanoindentation of single crystal copper. *International Journal of Plasticity*, 24(11), 1990–2015 (2008). doi: 10.1016/j.ijplas.2008.02.009. Cited on pages 68, 69, and 70.

Liu, Y., Wang, B., Yoshino, M., Roy, S., Lu, H., and Komanduri, R. Combined numerical simulation and nanoindentation for determining mechanical properties of single crystal copper at mesoscale. *J. Mech. Phys. Solids*, 53, 2718–2741 (2005). Cited on page 70.

Liu, Y., Li, H., Wang, S., and Ye, H. Nb effects on the structural and mechanical properties of TiAl alloy: Density-functional theory study. *Journal of Materials Research*, 24, 3165–3173 (2009b). doi: 10.1557/JMR.2009.0394. Cited on page 27.

Liu, Z.C., Lin, J.P., Li, S.J., and Chen, G.L. Effects of Nb and Al on the microstructures and mechanical properties of high Nb containing TiAl base alloys. *Intermetallics*, 10(7), 653–659 (2002). Cited on page 26.

Lütjering, G. and Williams, J.C. *Titanium (Engineering Materials and Processes)*. Springer (2007). ISBN 3540713972. doi: 10.1007/978-3-540-73036-1. Cited on page 20.

Lu, L., Siegl, R., Girshick, A., Pope, D.P., and Vitek, V. Energy and structure of interfaces in polysynthetically twinned TiAl. *Scripta Materialia*, 34(6), 971–976 (1996). Cited on page 31.

Ma, A., Roters, F., and Raabe, D. On the consideration of interactions between dislocations and grain boundaries in crystal plasticity finite element modeling - Theory, experiments, and simulations. *Acta Materialia*, 54(8), 2181–2194 (2006a). doi: 10.1016/j.actamat.2006.01.004. Cited on page 143.

Ma, A., Roters, F., and Raabe, D. Studying the effect of grain boundaries in dislocation density based crystal-plasticity finite element simulations. *International Journal of Solids and Structures*, 43(24), 7287–7303 (2006b). doi: 10.1016/j.ijsolstr.2006.07.006. Size-dependent Mechanics of Materials. Cited on page 143.

Ma, Q. and Clarke, D.R. Size-dependent Hardness of Silver Single-crystals. *Journal of Materials Research*, 10(4), 853–863 (1995). doi: 10.1557/JMR.1995.0853. Cited on page 66.

Mahapatra, R., Girshick, A., Pope, D.P., and Vitek, V. Deformation mechanisms of near-stoichiometric single-phase TiAl single-crystals – a combined experimental and atomistic modeling study. *Scripta Metallurgica Et Materialia*, 33(12), 1921–1927 (1995). Cited on pages 42, 56, and 139.

Mahon, G.J. and Howe, J.M. Transmission Electron-Microscopy Investigation of Interfaces in a 2-phase TiAl Alloy. *Metallurgical Transactions A*, 21(6), 1655–1662 (1990). doi: 10.1007/BF02672580. Cited on page 28.

Marketz, W., Fischer, F., and Clemens, H. Deformation mechanisms in TiAl intermetallics – experiments and modeling. *Intl. J. of Plasticity*, 19, 281–321 (2003). Cited on page 54.

Maruyama, K., Suzuki, G., Kim, H.Y., Suzuki, M., and Sato, H. Saturation of yield stress and embrittlement in fine lamellar TiAl alloy. *Materials Science and Engineering A*, 329, 190–195 (2002). Cited on pages 31, 51, and 77.

Maruyama, K., Yamada, N., and Sato, H. Effects of lamellar spacing on mechanical properties of fully lamellar Ti-39.4mol%Al alloy. *Materials Science and Engineering A*, 319, 360–363 (2001). Cited on page 51.

Maruyama, K., Yamaguchi, M., Suzuki, G., Zhu, H., Kim, H.Y., and Yoo, M. Effects of lamellar boundary structural change on lamellar size hardening in TiAl alloy. *Acta Materialia*, 52, 5185–5194 (2004). Cited on pages 28, 33, 51, and 134.

Mason, J.K., Lund, A.C., and Schuh, C.A. Determining the activation energy and volume for the onset of plasticity during nanoindentation. *Physical Review B*, 73(5), 054102–1–14 (2006). doi: 10.1103/PhysRevB.73.054102. Cited on page 68.

Maziasz, P.J. and Liu, C.T. Development of ultrafine lamellar structures in two-phase gamma-

TiAl alloys. *Metallurgical and Materials Transactions A*, 29(1), 105–117 (1998). Cited on page 50.

McDowell, D.L. Viscoplasticity of heterogeneous metallic materials. *Materials Science & Engineering R-reports*, 62(3), 67–123 (2008). doi: 10.1016/j.mser.2008.04.003. Cited on page 97.

McElhaney, K.W., Vlassak, J.J., and Nix, W.D. Determination of indenter tip geometry and indentation contact area for depth-sensing indentation experiments. *Journal of Materials Research*, 13(5), 1300–1306 (1998). doi: 10.1557/JMR.1998.0146. Cited on pg 82 in FischerCripps;: Nanoindentation. Cited on pages 67 and 68.

Mecking, H., Hartig, C., and Kocks, U.F. Deformation modes in gamma-TiAl as derived from the single crystal yield surface. *Acta Materialia*, 44(4), 1309–1321 (1996). Cited on page 44.

Menand, A., Huguet, A., and Nerac-Partaix, A. Interstitial solubility in gamma and alpha(2) phases of TiAl-based alloys. *Acta Materialia*, 44(12), 4729–4737 (1996). Cited on page 26.

Mesarovic, S.D. and Fleck, N.A. Spherical indentation of elastic-plastic solids. *Proceedings of the Royal Society of London Series A-mathematical Physical and Engineering Sciences*, 455(1987), 2707–2728 (1999). Cited on page 69.

Meyer, E. Investigations on hardness testing and hardness. *Zeitschrift des Vereines Deutscher Ingenieure*, 52, 645 (1908). Untersuchungen über Härteprüfung und Härte. Cited on page 59.

Mills, M.J., Inui, H., Clemens, H., and Fu, C.L., editors. *Integrative and Interdisciplinary Aspects of Intermetallics (Symposium S of MRS fall meeting 2004)*, volume 842 of *Mater. Res. Soc. Symp. Proc.* MRS, MRS, Warrendale, PA (2005). Cited on page 163.

Minari, F., Y, M., Pichaud, B., and Bellandi, P. Determination of Most Stressed Slipping System in Each Point of a cfc Monocrystal With Primary Stages of Indentation by a Sphere. *Scripta Metallurgica*, 4(10), 843–& (1970). Cited on page 66.

Mishin, Y. and Herzig, C. Diffusion in the Ti-Al system. *Acta Materialia*, 48(3), 589–623 (2000). Cited on page 26.

Morawiec, A. *Orientations and Rotations - Computations in Crystallographic Textures*. Springer (2004). ISBN 3-540-40734-0. Cited on pages 119 and 165.

Moses, A.J. *The characters of crystals*. D. Van Nostrand (1899). Cited on page 66.

MSC Software. *Marc2007r1, Volume A – Theory and User Information*. MSC.Software Corp. (2007a). Cited on page 105.

MSC Software. *Marc2007r1, Volume C – Program Input*. MSC.Software Corp. (2007b). Cited on page 105.

MSC Software. *Marc2007r1, Volume D – User Subroutines and Special Routines*. MSC.Software Corp. (2007c). Cited on page 105.

Mukhopadhyay, N.K. and Paufler, P. Micro- and nanoindentation techniques for mechanical characterisation of materials. *International Materials Reviews*, 51(4), 209–245 (2006). doi: 10.1179/174328006X102475. Cited on page 59.

Musienko, A., Tatschl, A., Schmidegg, K., Kolednik, O., Pippan, R., and Cailletaud, G. Three-dimensional finite element simulation of a polycrystalline copper specimen. *Acta Materialia*, 55(12), 4121–4136 (2007). doi: 10.1016/j.actamat.2007.01.053. Cited on page 98.

Nabarro, F., Shrivastava, S., and Luyckx, S. The size effect in microindentation. *Philosophical Magazine*, 86, 4173–4180 (2006). Cited on page 62.

Nakamura, M. Elastic Properties. In Westbrook and Fleischer (2000b), chapter 1, pages 1–24. Cited on page 38.

Nakano, T., Biermann, H., Riemer, M., Mughrabi, H., Nakai, Y., and Umakoshi, Y. Classification of gamma-gamma and gamma-alpha(2) lamellar boundaries on the basis of continuity of strains and slip-twinning planes in fatigued TiAl polysynthetically twinned crystals. *Philosophical Magazine A*, 81(6), 1447–1471 (2001). Cited on page 52.

Nakano, T., Yokoyama, A., and Umakoshi, Y. Effect of Nb Addition on the Plastic Behavior

of Ti_3Al Crystals Containing Oriented Lamellae. *Scripta Metallurgica et Materialia*, 27(10), 1253–1258 (1992). Cited on page 48.

Nakano, T., Hayashi, K., Umakoshi, Y., Chiu, Y.L., and Veyssière, P. Effects of long-period superstructures on plastic properties in Al-rich TiAl single crystals. *Mater. Res. Soc. Proc.*, 842, S7.4.1–1–S7.4.1–6 (2005). Cited on page 30.

Nave, M. and Inoue, H. Reliable Titanium Aluminide Texture Measurement Using EBSD. *Materials Science Forum*, 561–565, 431–434 (2007). Cited on page 79.

Newnham, R.E. *Properties of Meaterials*. Oxford University Press (2005). Cited on page 38.

Nibur, K.A., Akasheh, F., and Bahr, D.F. Analysis of dislocation mechanisms around indentations through slip step observations. *Journal of Materials Science*, 42(3), 889–900 (2007). doi: 10.1007/s10853-006-0007-x. Cited on pages 66 and 68.

Nibur, K.A. and Bahr, D.F. Identifying slip systems around indentations in FCC metals. *Scripta Materialia*, 49(11), 1055–1060 (2003). doi: 10.1016/j.scriptamat.2003.08.021. Cited on pages 66 and 68.

Nie, J. and Muddle, B. Orientation and structure of planar facets on the massive phase gamma(m) in a near-TiAl alloy. *Metallurgical and Materials Transactions A*, 33(8), 2381–2389 (2002). Cited on page 34.

Nie, J.F., Howe, J.M., Vasudevan, V.K., and Aaronson, H.I. Discussion of "Surface relief and the displacive transformation to the lamellar microstructure in TiAl" and "nanometer-scale, fully lamellar microstructure in an ages TiAl-based alloy". *Metallurgical and Materials Transactions A*, 31(9), 2377–2379 (2000). doi: 10.1007/s11661-000-0153-8. Cited on page 33.

Nix, W.D. and Gao, H.J. Indentation size effects in crystalline materials: A law for strain gradient plasticity. *Journal of the Mechanics and Physics of Solids*, 46(3), 411–425 (1998). Cited on pages 62 and 71.

Novoselova, T., Malinov, S., and Sha, W. Experimental study of the effects of heat treatment on microstructure and grain size of a gamma TiAl alloy. *Intermetallics*, 11(5), 491–499 (2003). Cited on page 33.

Nowak, R., Manninen, T., Heiskanen, K., Sekino, T., Hikasa, A., Niihara, K., and Takagi, T. Peculiar surface deformation of sapphire: Numerical simulation of nanoindentation. *Applied Physics Letters*, 83(25), 5214–5216 (2003). doi: 10.1063/1.1635983. Cited on page 69.

Nowell, M.M. and Wright, S.I. Phase differentiation via combined EBSD and XEDS. *Journal of Microscopy*, 213, 296–305 (2004). Cited on page 82.

Nye, J.F. *Physical Properties of Crystals*. Oxford University Press (1957). Cited on pages 38 and 40.

Ogden, H.R., Maykuth, D.J., Finlay, W.L., and Jaffee, R.I. Constitution of Titanium-aluminum Alloys. *Transactions of the American Institute of Mining and Metallurgical Engineers*, 191(12), 1150–1155 (1951). Cited on page 23.

Oliver, W.C. and Pharr, G.M. Measurement of hardness and elastic modulus by instrumented indentation: Advances in understanding and refinements to methodology. *Journal of Materials Research*, 19(1), 3–20 (2004). doi: 10.1557/JMR.2004.0002. Cited on page 60.

Oliver, W. and Pharr, G. An improved technique for determining hardness and elastic modulus using load and displacement sensing indentation experiments. *Journal of Materials Research*, 7, 1564 (1992). Cited on page 66.

O'Neill, H. Hardness tests on crystals of aluminium. *Journal of the Institute of Metals*, 30(1), 299–308 (1923). Cited in Dyer (1965). Cited on page 66.

Orowan, E. Plasticity of crystals. *Z. Physik*, 89, 605–659 (1934). Cited on page 99.

Osmond, F. and Cartaud, G. Figures of pressure or percussion on crystallised plastic metals. *Comptes Rendus Hebdomadaires Des Seances De L Academie Des Sciences*, 141, 122–124 (1905). Cited in Tammann1926. Cited on page 67.

Osmond, F. and Cartaud, G. Die Kristallographie des Eisens. *Metallurgie - Zeitschrift für die gesamte Hüttenkunde*, 15, 522–545 (1906). Cited on pages 66, 67, and 136.

Paidar, V. and Yamaguchi, M. Constrained deformation of a lamellar structure. *Materials Science and Engineering: A*, 462(1-2), 460–464 (2007). doi: 10.1016/j.msea.2006.01.180. International Symposium on Physics of Materials, 2005. Cited on page 147.

Paidar, V., Zghal, S., and Couret, A. Intrinsic Misfit Dislocations on 120° Interface in TiAl. *Mater. Res. Soc. Proc.*, 552, KK 3.2 (1999). Cited on page 29.

Palm, M., Bewlay, B., Takeyama, M., Wiezorek, J., and He, Y.H., editors. *Advanced Intermetallic-Based Alloys for Extreme Environment and Energy Applications (Symposium U of MRS Fall metting 2008)*, volume 1128 of *Mater. Res. Soc. Symp. Proc.* MRS, Warrendale, PA (2009). Cited on page 163.

Pan, L. and Luzzi, D.E. A study on diffusion couples of Ti and polysynthetically twinned (PST) Ti-Al: I. Microstructure characterization. *Intermetallics*, 14(1), 61–67 (2006). doi: 10.1016/j.intermet.2005.04.009. Cited on page 31.

Parteder, E., Siegmund, T., Fischer, F.D., and Schlögl, S. Numerical-Simulation of the Plastic Behavior of Polysynthetically Twinned Ti-Al Crystals. *Materials Science and Engineering A*, 193, 149–154 (1995). Cited on pages 53 and 54.

Parthasarathy, T., Mendiratta, M., and Dimiduk, D. Flow behavior of PST and fully lamellar polycrystals of Ti-48Al in the microstrain regime. *Acta Materialia*, 46(11), 4005–4016 (1998). Cited on pages 31 and 134.

Peirce, D., Asaro, R.J., and Needleman, A. An Analysis of Nonuniform and Localized Deformation in Ductile Single-crystals. *Acta Metallurgica*, 30(6), 1087–1119 (1982). doi: 10.1016/0001-6160(82)90005-0. Cited on pages 100 and 111.

Peirce, D., Asaro, R.J., and Needleman, A. Material Rate Dependence and Localized Deformation in Crystalline Solids. *Acta Metallurgica*, 31(12), 1951–1976 (1983). doi: 10.1016/0001-6160(83)90014-7. Cited on pages 53 and 100.

Peralta, P., Ledoux, R., Dickerson, R., Hakik, M., and Dickerson, P. Characterization of surface deformation around vickers indents in monocrystalline materials. *Metallurgical and Materials Transactions A*, 35(8), 2247–2255 (2004). Cited on page 66.

Perdrix, F., Trichet, M.F., Bonnentien, J.L., Cornet, M., and Bigot, J. Influence of cooling rate on microstructure and mechanical properties of a Ti-48Al alloy. *Intermetallics*, 7(12), 1323–1328 (1999). Cited on pages 31 and 50.

Petch, N.J. The Cleavage Strength of Polycrystals. *Journal of the Iron and Steel Institute*, 174(1), 25–28 (1953). Cited on page 49.

Pethica, J.B., Hutchings, R., and Oliver, W.C. Hardness Measurement at Penetration Depths as Small as 20 nm. *Philosophical Magazine A*, 48(4), 593–606 (1983). Cited on pages 60 and 62.

Pfeil, L. The effect of cold-work on the structure and hardness of single iron crystals and the changes produced by subsequent annealing. *J. Iron Steel Inst.*, 16, 153–210 (1927). Cited on page 66.

Pfetzing, J., Wagner, M.F.X., Zarnetta, R., Tak, K.G., and Eggeler, G. On the Influence of Grain Orientation on Nanoindentation Testing of Pure Iron. *Praktische Metallographie-Practical Metallography*, 46(2), 63–76 (2009). Cited on page 66.

Pharr, G.M. and Oliver, W.C. Measurement of Thin-film Mechanical-properties Using Nanoindentation. *MRS Bulletin*, 17(7), 28–33 (1992). Cited on page 60.

Polmear, I. *Light alloys: From traditional alloys to nanocrystals*. Butterworth-Heinemann (Elsevier), 4th edition (2006). Cited on page 20.

Pope, D.P. Mechanical Properties of Intermetallic Compounds. In R.W. Cahn and P. Haasen, editors, *Physical Metallurgy (Vols. 1–3)*, chapter 24, pages 2075–2104. North Holland, 4th edition (1996). Cited on pages 20 and 42.

Porter, D.A. and Easterling, K.E. *Phase Transformations in Metals and Alloys*. Chapman and Hall, 2nd edition (1992). Cited on page 34.

Porter, W., Uchic, M., John, R., and Barnas, N. Compression property determination of a gamma titanium aluminide alloy using micro-specimens. *Scripta Materialia*, 61(7), 678–681 (2009). doi: 10.1016/j.scriptamat.2009.05.038. Cited on page 49.

Pouchou, J.L., Denquin, A., and Ferrini, A. Contribution of EBSD to the understanding of massive transformation in TiAl. *Microchimica Acta*, 145, 177–182 (2004). doi: 10.1007/s00604-003-0149-3. Cited on pages 34 and 79.

Python. Programming language (version 2.6). Cited on page 105.

Raabe, D., Ma, D., and Roters, F. Effects of initial orientation, sample geometry and friction on anisotropy and crystallographic orientation changes in single crystal microcompression deformation: A crystal plasticity finite element study. *Acta Materialia*, 55(13), 4567–4583 (2007). doi: 10.1016/j.actamat.2007.04.023. Cited on pages 98 and 111.

Raabe, D., Roters, F., Barlat, F., and Chen, L.Q., editors. *Continuum Scale Simulation of Engineering Materials*. Wiley-VCH (2004a). doi: 10.1002/3527603786. Cited on pages 97 and 187.

Raabe, D., Sachtleber, M., Zhao, Z., Roters, F., and Zaefferer, S. Micromechanical and macromechanical effects in grain scale polycrystal plasticity experimentation and simulation. *Acta Materialia*, 49(17), 3433–3441 (2001). doi: 10.1016/S1359-6454(01)00242-7. Cited on page 98.

Raabe, D., Zhao, Z., and Roters, F. Study on the orientational stability of cube-oriented FCC crystals under plane strain by use of a texture component crystal plasticity finite element method. *Scripta Materialia*, 50(7), 1085–1090 (2004b). doi: 10.1016/j.scriptamat.2003.11.061. Cited on page 98.

Raghavan, V. Al-Nb-Ti (aluminum-niobium-titanlum). *Journal of Phase Equilibria and Diffusion*, 26(4), 360–368 (2005). doi: 10.1361/154770305X56827. Cited on page 24.

Rao, S., Dimiduk, D., Parthasarathy, T., Uchic, M., Tang, M., and Woodward, C. Athermal mechanisms of size-dependent crystal flow gleaned from three-dimensional discrete dislocation simulations. *Acta Materialia*, 56(13), 3245–3259 (2008). doi: 10.1016/j.actamat.2008.03.011. Cited on page 62.

Rickerby, D.G. and Macmillan, N.H. Hardness of Cubic Single-crystals by Spherical Indentation. *Materials Science and Engineering*, 40(2), 251–259 (1979). Cited on page 66.

Roos, A., Chaboche, J.L., Gelebart, L., and Crepin, J. Multiscale modelling of titanium aluminides. *International Journal of Plasticity*, 20(4), 811–830 (2004). Cited on page 56.

Rostamian, A. and Jacot, A. A numerical model for the description of the lamellar and massive phase transformations in TiAl alloys. *Intermetallics*, 16(10), 1227–1236 (2008). doi: 10.1016/j.intermet.2008.07.008. Cited on page 27.

Roters, F. Application of crystal plasticity FEM from single crystal to bulk polycrystal. *Computational Materials Science*, 32(3-4), 509–517 (2005). doi: 10.1016/j.commatsci.2004.09.014. Cited on page 97.

Roters, F., Eisenlohr, P., Hantcherli, L., Tjahjanto, D.D., Bieler, T.R., and Raabe, D. Overview of constitutive laws, kinematics, homogenization, and multiscale methods in crystal plasticity finite element modeling: theory, experiments, applications. *Acta Materialia*, 58(4), 1152–1211 (2010). doi: 10.1016/j.actamat.2009.10.058. Cited on page 97.

Rösler, J., Haders, H., and Bäker, M. *Mechnisches Verhalten der Werkstoffe*. Teubner (2006). Cited on page 100.

Saage, H., Huang, A., Hu, D., Loretto, M., and Wu, X. Microstructure and tensile properties of massively transformed and aged Ti46Al8Nb and Ti46Al8Ta alloys. *Intermetallics*, 17, 32–38 (2009). Cited on pages 27, 34, 35, 149, 153, and 154.

Sakai. Principles and Applications of Indentation. In F. Yang and J.C. Li, editors, *Micro- and*

Nanomechanical Testing of Materials and Devices, chapter 1, pages 1–48. Springer (2008). Cited on page 63.

Sauthoff, G. *Intermetallics*. Wiley-VCH (1999). Cited on page 20.

Schaden, T., Fischer, F., Clemens, H., Appel, F., and Bartels, A. A study of the Deformation Behaviour of Lamellar γ-TiAl by Numeric Modeling. In *Mater. Res. Soc. Symp. Proc. Vol. 842* (2005). Cited on page 54.

Scheu, C., Cha, L., Sturm, S., Chladil, H., Mayrhofer, P., Clemens, H., Wole, W., and Podloucky, R. Structure models of massively transformed high niobium containing TiAl alloys. In *Mater. Res. Soc Proc. Vol 980, Advanced Intermetallic-Based Alloys*, volume 980, pages 401–406 (2007). Cited on pages 26 and 35.

Schlögl, S.M. and Fischer, F.D. The role of slip and twinning in the deformation behaviour of polysynthetically twinned crystals of TiAl: A micromechanical model. *Philosophical Magazine A*, 75(3), 621–636 (1997a). doi: 10.1080/01418619708207193. Cited on pages 53, 54, and 143.

Schlögl, S.M. *Micromechanical Modelling of the Deformation Behaviour of Gamma Titanium Aluminides*. Ph.D. thesis, Montanuniversität Leoben (1997). Cited on page 54.

Schlögl, S. and Fischer, F. Numerical simulation of yield loci for PST crystals of TiAl. *Materials science & engineering A*, 239–240, 790–803 (1997b). doi: 10.1016/S0921-5093(97)00668-0. Cited on pages 54 and 143.

Schmid, E. and Boas, W. *Plasticity of Crystals*. Hughes & Co. (1950). Translated from the German edition from 1935. Cited on page 66.

Schneibel, J.H., Hanada, S., Hemker, K.J., Noebe, R.D., and Sauthoff, G., editors. *High-temperature ordered intermetallic alloys IX*, volume 646 of *Mater. Res. Soc. Proc.* MRS, MRS (2001). Cited on page 163.

Schuster, J.C. and Palm, M. Reassessment of the binary Aluminum-Titanium phase diagram. *Journal of Phase Equilibria and Diffusion*, 27, 255–277 (2006). doi: 10.1361/154770306X109809. Cited on pages 24 and 28.

Schwartz, A.J., Kumar, M., Field, D.P., and Adams, B.L., editors. *Electron Backscatter Diffraction in Materials Science*. Springer, 2nd edition (2009). Cited on page 21.

Shechtman, D., Blackburn, M.J., and Lipsitt, H. The plastic deformation of TiAl. *Metallurgical Transactions*, 5, 1373–1381 (1974). Cited on pages 40 and 43.

Shim, S., Oliver, W.C., and Pharr, G.M. A critical examination of the Berkovich vs. conical indentation based on 3D finite element calculation. In *Fundamentals of Nanoindentation and Nanotribology III*, volume 841 of *Materials Research Society Symposium Proceedings*, pages 39–44. Materials Research Society (2005). ISSN 0272-9172. Cited on page 69.

Simkin, B.A., Ng, B.C., Bieler, T.R., Crimp, M.A., and Mason, D.E. Orientation determination and defect analysis in the near-cubic intermetallic gamma-TiAl using SACP, ECCI, and EBSD. *Intermetallics*, 11(3), 215–223 (2003). Cited on page 79.

Simo, J. and Hughes, T. *Computational Inelastictiy*. Springer (1998). Cited on page 97.

Singer, H., Singer, I., and Jacot, A. Phase-field simulations of alpha $\rightarrow$ gamma precipitations and transition to massive transformation in the Ti-Al alloy. *Acta Materialia*, 57(1), 116–124 (2009). doi: 10.1016/j.actamat.2008.08.055. Cited on page 34.

Singh, S.R. and Howe, J.M. High-resolution Electron-microscopy of Gamma-alpha-2 Interfaces in Titanium Aluminide. *Philosophical Magazine A*, 66(5), 739–771 (1992). Cited on page 28.

Skrotzki, B. Crystallographic aspects of deformation twinning and consequences for plastic deformation processes in γ-TiAl. *Acta Materialia*, 48, 851–862 (2000). doi: 10.1016/S1359-6454(99)00385-7. Cited on pages 43 and 44.

Smith, R., Christopher, D., Kenny, S.D., Richter, A., and Wolf, B. Defect generation and pileup of atoms during nanoindentation of Fe single crystals. *Physical Review B*, 67(24), 245405–1–10 (2003). doi: 10.1103/PhysRevB.67.245405. Cited on pages 66 and 67.

Sneddon, I. The Relationship between Load and Penetration in the Axisymmetric Boussinesq Problem for a Punch of Arbitrary Profile. *Int. J. Engng. Sci.*, 3, 47–57 (1965). Cited on page 60.

Souptel, D., Löser, W., and Behr, G. Vertical optical floating zone furnace: Principles of irradiation profile formation. *Journal of Crystal Growth*, 300(2), 538–550 (2007). doi: 10.1016/j.jcrysgro.2006.12.042. Cited on pages 86 and 113.

Stelmashenko, N.A., Walls, M.G., Brown, L.M., and Milman, Y.V. Microindentations on W and Mo Oriented Single-crystals - an Stm Study. *Acta Metallurgica et Materialia*, 41(10), 2855–2865 (1993). Cited on pages 66 and 68.

Stilwell, N.A. and Tabor, D. Elastic Recovery of Conical Indentations. *Proceedings of the Physical Society of London*, 78(500), 169–& (1961). Cited on page 60.

Sun, Y. Nanometer-scale, fully lamellar microstructure in an aged TiAl-based alloy. *Metallurgical and Materials Transactions A*, 29(11), 2679–2685 (1998a). doi: 10.1007/s11661-998-0308-6. Cited on page 33.

Sun, Y. Discussion of Studies, 'Surface relief and the displacive transformation to the lamellar microstructure in TiAl' and 'Nanometer-scale, fully lamellar microstructure in an aged TiAl-based alloy' - author's reply. *Metallurgical and Materials Transactions A*, 31(9), 2379–2383 (2000). doi: 10.1007/s11661-000-0154-7. Cited on page 33.

Sun, Y.Q. Strengthening of fully-lamellar TiAl: a dislocation pileup analysis. *Materials Science and Engineering A*, 239-240, 131–136 (1997). doi: 10.1016/S0921-5093(97)00571-6. Cited on page 49.

Sun, Y.Q. Surface relief and the displacive transformation to the lamellar microstructure in TiAl. *Philosophical Magazine Letters*, 78(4), 297–305 (1998b). Cited on page 33.

Sun, Y.Q. An example supporting the importance of dislocation core structure: an explanation of the relative yield stresses of <110] and <011] slips in gamma-TiAl. *Philosophical Magazine Letters*, 79(12), 897–900 (1999). Cited on page 42.

Swadener, J.G., George, E.P., and Pharr, G.M. The correlation of the indentation size effect measured with indenters of various shapes. *Journal of the Mechanics and Physics of Solids*, 50(4), 681–694 (2002a). Cited on page 62.

Swadener, J.G., Misra, A., Hoagland, R.G., and Nastasi, A. A mechanistic description of combined hardening and size effects. *Scripta Materialia*, 47(5), 343–348 (2002b). Cited on page 62.

Tabor, D. A Simple Theory of Static and Dynamic Hardness. *Proceedings of the Royal Society of London Series A-mathematical and Physical Sciences*, 192(1029), 247–274 (1948). Cited on page 59.

Tabor, D. *The hardness of metals*. Clarendon Press, Oxford University Press, Oxford, London, UK (1951). Cited on pages 59 and 67.

Tabor, D. The hardness of solids. *Review of Physics in Technology*, 1(3), 145–179 (1970). Cited on page 67.

Tadmor, E. and Bernstein, N. A first-principles measure for the twinnability of FCC metals. *J. Mech. Phys. Solids*, 52, 2507–2519 (2004). Cited on page 43.

Takeyama, M., Ohmura, Y., Kikuchi, M., and Matsuo, T. Phase equilibria and microstructural control of gamma TiAl based alloys. *Intermetallics*, 6(7–8), 643–646 (1998). Cited on page 23.

Takeyama, M., Yamamoto, Y., Morishima, H., Koike, K., Chang, S.Y., and Matsuo, T. Lamellar orientation control of Ti-48Al PST crystal by unidirectional solidification. *Materials Science and Engineering A*, 329-331, 7–12 (2002). doi: 10.1016/S0921-5093(01)01493-9. Cited on page 34.

Tammann, G. and Müller, A. Über Verfahren zur Bestimmung der Orientierung der Kristallite. *Zeitschrift für Metallkunde*, 18, 69–79 (1926). Cited on pages 63, 66, and 67.

Tanaka, K., Ichitsubo, T., Inui, H., Yamaguchi, M., and Koiwa, M. Single-crystal elastic constants of gamma-TiAl. *Philosophical Magazine Letters*, 73(2), 71–78 (1996a). Cited on page 39.

Tanaka, K., Okamoto, K., Inui, H., Minonishi, Y., Yamaguchi, M., and Koiwa, M. Elastic constants and their temperature dependence for the intermetallic compound Ti3Al. *Philosophical Magazine A*, 73(5), 1475–1488 (1996b). Cited on page 40.

Tymiak, N.I., Kramer, D.E., Bahr, D.F., Wyrobek, T.J., and Gerberich, W.W. Plastic strain and strain gradients at very small indentation depths. *Acta Materialia*, 49(6), 1021–1034 (2001). Cited on page 62.

Uchic, M., Shade, P., and D.M.Dimiduk. Plasticity of micrometer-scale single-crystals in compression. *Annu.Rev. Mater.Res*, 39, 361–86 (2009). Cited on page 113.

Uhlenhut, H. *Ursachen plastischer Anisotropie von γ-TiAl Basislegierungen*. Shaker Verlag (1999). Cited on pages 47, 55, and 148.

Umakoshi, Y. Deformation of Intermetallic Compounds. In H. Mughrabi, editor, *Materials Science and Technology, Vol. 6: Plastic deformation and fracture of materials*, chapter 6, pages 253–310. VCH (1993). Cited on page 37.

Umakoshi, Y. and Nakano, T. The Role of Ordered Domains and Slip Mode of Alpha-2 Phase in the Plastic Behavior of TiAl Crystals Containing Oriented Lamellae. *Acta Metallurgica et Materialia*, 41(4), 1155–1161 (1993). Cited on pages 49 and 54.

Van Vliet, K.J., Li, J., Zhu, T., Yip, S., and Suresh, S. Quantifying the early stages of plasticity through nanoscale experiments and simulations. *Phys. Rev. B*, 67(10), 104105 (2003). doi: 10.1103/PhysRevB.67.104105. Cited on page 69.

Vasudevan, V.K., Court, S.A., Kurath, P., and Fraser, H.L. Effect of Grain-size and Temperature on the Yield Stress of the Intermetallic Compound TiAl. *Scripta Metallurgica*, 23(4), 467–469 (1989a). Cited on page 49.

Vasudevan, V.K., Court, S.A., Kurath, P., and Fraser, H.L. Effect of Purity on the Deformation Mechanisms in the Intermetallic Compound TiAl. *Scripta Metallurgica*, 23(6), 907–912 (1989b). Cited on page 42.

Veeraraghavan, D., Wang, P., and Vasudevan, V.K. Kinetics and thermodynamics of the [alpha] → [gamma] m assive transformation in a Ti-47.5 at. *Acta Materialia*, 47(11), 3313–3330 (1999). doi: 10.1016/S1359-6454(99)00195-0. Cited on page 27.

Villars, P. and Calvert, L., editors. *Pearson's Handbook of Crystallographic Data for Intermetallic Phases*. ASM International (1991). Cited on page 25.

Vitek, V., Ito, K., Siegl, R., and Znam, S. Structure of interfaces in the lamellar TiAl: effects of directional bonding and segregation. *Materials Science and Engineering A*, 239-240, 752–760 (1997). doi: 10.1016/S0921-5093(97)00663-1. Cited on page 30.

Vitek, V. and Paidar, V. Non-planar Dislocation Cores: A Ubiquitous Phenomenon Affecting Mechanical Properties of Crystalline Materials. In J.P. Hirth, editor, *Dislocations in Solids*, volume 14, chapter 87. Elsevier (2008). Cited on page 47.

Vlassak, J.J. and Nix, W.D. Indentation Modulus of Elastically Anisotropic Half-spaces. *Philosophical Magazine A*, 67(5), 1045–1056 (1993). Cited on page 60.

Vlassak, J.J. and Nix, W.D. Measuring the Elastic Properties of Anisotropic Materials by Means of Indentation Experiments. *Journal of the Mechanics and Physics of Solids*, 42(8), 1223–1245 (1994). doi: 10.1016/0022-5096(94)90033-7. Cited on pages 59 and 114.

Wang, P. and Vasudevan, V.K. Composition dependence of the massive transformation from alpha to gamma in quenched TiAl alloys. *Scripta Metallurgica et Materialia*, 27(1), 89–94 (1992). Cited on page 34.

Wang, Y., Raabe, D., Klüber, C., and Roters, F. Orientation dependence of nanoindentation pile-up patterns and of nanoindentation microtextures in copper single crystals. *Acta Materialia*, 52(8), 2229–2238 (2004). doi: 10.1016/j.actamat.2004.01.016. Cited on pages 66, 68, 69, 70, 98, 123, and 136.

Weber, F., Schestakow, I., Roters, F., and Raabe, D. Texture Evolution During Bending of a Single Crystal Copper Nanowire Studied by EBSD and Crystal Plasticity Finite Element Simula-

tions. *Advanced Engineering Materials*, 10, 737–741 (2008). doi: 10.1002/adem.200800102. Cited on page 113.

Weber, G. and Anand, L. Finite Deformation Constitutive-Equations and a Time Integration Procedure for Isotropic, Hyperelastic Viscoplastic Solids. *Computer Methods in Applied Mechanics and Engineering*, 79(2), 173–202 (1990). Cited on page 102.

Weimer, M. and Kelly, T. Gamma-TiAl applications at GE aviation. *Structural Aluminides for Elevated Temperatures: Gamma Titanium and Other: Metallic Aluminides*, pages 5–6 (2008). Cited on page 19.

Wen, C.E. and Chen, C.Q. New microstructure-property approach: Quenching/tempering treatment in gamma TiAl alloy. *Scripta Metallurgica et Materialia*, 33(8), 1283–1288 (1995). doi: 10.1016/0956-716X(95)00348-Y. Cited on page 34.

Wen, Y., Chen, L., Hazzledine, P., and Wang, Y. A three-dimensional phase-field model for computer simuation of lamellar structure formation in gammaTiAl intermetallic alloys. *Acta Materialia*, 49, 2341–2353 (2001). Cited on pages 32 and 33.

Werwer, M. and Cornec, A. Numerical simulation of plastic deformation and fracture in polysynthetically twinned (PST) crystals of TiAl. *Computational Materials Science*, 19(1), 97–107 (2000). Cited on pages 55 and 143.

Werwer, M. and Cornec, A. The role of superdislocations for modeling plastic deformation of lamellar TiAl. *International Journal of Plasticity*, 22(9), 1683–1698 (2006). doi: 10.1016/j.ijplas.2006.02.005. Cited on pages 55 and 143.

Westbrook, J.H. and Conrad, H., editors. *The science of hardness testing and its research applications*. American Society for Metals, Metals Park, Ohio (1973). Based on papers presented at a symposium of the American Society for Metals, October 18 to 20, 1971. Cited on page 60.

Westbrook, J.H. and Fleischer, R., editors. *Intermetallic Compounds – Principles and Practice, Volume 3: Progress*. Wiley (2002). ISBN 0 471 49315 5. Cited on pages 20 and 199.

Westbrook, J. and Fleischer, R., editors. *Intermetallic Compounds, I. Crystal Structures*. Wiley (2000a). Cited on page 20.

Westbrook, J. and Fleischer, R., editors. *Intermetallic Compounds, II. Basic Mechanical Properties and Lattice Defects of Intermetallic Compounds*. Wiley (2000b). Cited on pages 20 and 191.

Westbrook, J. and Fleischer, R., editors. *Intermetallic Compounds, III. Structural Applications of Intermetallic Compounds*. Wiley (2000c). Cited on pages 20 and 185.

Westbrook, J. and Fleischer, R., editors. *Intermetallic Compounds, IV. Magnetic, Electrical and Optical Properties and Applications of Intermetallic Compounds*. Wiley (2000d). Cited on page 20.

Wiezorek, J., Fu, C.L., Takeyama, M., Morris, D., and Clemens, H., editors. *Advanced Intermetallic-Based Alloys (Symposium II from the 2006 MRS Fall Meeting)*, volume 980 of *Mater. Res. Soc. Proc.* MRS, Warrendale, PA (2007). Cited on page 163.

Woodward, C. and Rao, S.I. Ab-initio simulation of (a/2)< 110] screw dislocations in gamma-TiAl. *Philosophical Magazine*, 84(3–5), 401–413 (2004). doi: 10.1080/14786430310001611626. Cited on pages 39, 47, and 55.

Wriggers, P. *Nichtlineare Finite-Element-Methoden*. Springer (2001). Cited on page 97.

Wriggers, P. *Nonlinear finite element methods*. Springer (2008). Cited on pages 103 and 104.

Wright, S.I. and Adams, B.L. Automatic-analysis of Electron Backscatter Diffraction Patterns. *Metallurgical Transactions A*, 23(3), 759–767 (1992). Cited on page 86.

Wu, X., Hu, D., and Loretto, M. The influence of microstructure and surface residual stresses on pre-yield cracking in TiAl alloys. In *Gamma Titanium Aluminides 2003*, pages 517–20 (2003). Cited on page 153.

Wu, X.H., Hu, D., and Loretto, M.H. Alloy and process development of TiAl. *Journal of Materials Science*, 39(12), 3935–3940 (2004). Cited on pages 23 and 36.

Wu, X.H., Jiang, H., Huang, A., Hu, D., Mota-Solis, N., and Loretto, M.H. Microstructural study of pre-yielding and pre-yield cracking in TiAl-based alloys. *Intermetallics*, 14(1), 91–101 (2006). doi: 10.1016/j.intermet.2005.04.014. Cited on page 52.

Wu, X. and Hu, D. Microstructural refinement in cast TiAl alloys by solid state transformations. *Scripta Materialia*, 52(8), 731–734 (2005). doi: 10.1016/j.scriptamat.2004.12.021. Cited on pages 148 and 149.

Yamaguchi, M., Inui, H., and Ito, K. High-temperature structural intermetallics. *Acta Materialia*, 48(1), 307–322 (2000). Cited on page 50.

Yamaguchi, M. and Umakoshi, Y. The Deformation-Behavior of Intermetallic Superlattice Compounds. *Progress in Materials Science*, 34(1), 1–148 (1990). doi: 10.1016/0079-6425(90)90002-Q. Cited on page 37.

Yamaguchi, M., Zhu, H., Suzuki, M., Maruyama, K., and Appel, F. Importance of microstructural stability in creep resistance of lamellar TiAl alloys. *Materials Science and Engineering A*, 483–484, 517–520 (2007). doi: 10.1016/j.msea.2006.09.147. 14th International Conference on the Strength of Materials. Cited on page 26.

Yamamoto, Y. and Takeyama, M. Physical metallurgy of single crystal gamma titanium aluminide alloys: orientation control and thermal stability of lamellar microstructure. *Intermetallics*, 13(9), 965–970 (2005). doi: 10.1016/j.intermet.2004.12.011. Cited on page 77.

Yamamoto, Y., Takeyama, M., and Matsuo, T. Stability of lamellar microstructure consisting of gamma/gamma interfaces in Ti-48Al-8Nb single crystal at elevated temperatures. *Materials Science and Engineering A*, 329, 631–636 (2002). Cited on pages 26, 30, and 34.

Yang, B. and Vehoff, H. Dependence of nanohardness upon indentation size and grain size – A local examination of the interaction between dislocations and grain boundaries. *Acta Materialia*, 55(3), 849–856 (2007). Cited on pages 117 and 123.

Yoo, M.H. Dislocation mechanisms for deformation twinning in the $L1_0$ structure. *Scripta Materialia*, 39(4–5), 569–575 (1998). Cited on page 43.

Yoo, M.H. Twinning and Mechanical Behavior. In Westbrook and Fleischer (2002), chapter 21, pages 403–436. Cited on page 43.

Yoo, M., Zou, J., and Fu, C. Mechanistic modeling of deformation and fracture behavior in TiAl and Ti_3Al. *Mater. Sci. Engr. A*, 192–193, 14–23 (1995). Cited on pages 39 and 40.

Zaafarani, N., Raabe, D., Roters, F., and Zaefferer, S. On the origin of deformation-induced rotation patterns below nanoindents. *Acta Materialia*, 56(1), 31–42 (2008). doi: 10.1016/j.actamat.2007.09.001. Cited on pages 66, 68, 70, 98, and 123.

Zaafarani, N., Raabe, D., Singh, R.N., Roters, F., and Zaefferer, S. Three-dimensional investigation of the texture and microstructure below a nanoindent in a Cu single crystal using 3D EBSD and crystal plasticity finite element simulations. *Acta Materialia*, 54(7), 1863–1876 (2006). doi: 10.1016/j.actamat.2005.12.014. Cited on pages 66, 70, 98, and 123.

Zaefferer, S. New developments of computer-aided crystallographic analysis in transmission electron microscopy. *Journal of Applied Crystallography*, 33, 10–25 (2000). Cited on pages 78 and 80.

Zaefferer, S. Computer-aided crystallographic analysis in the TEM. *Advances in Imaging and Electron Physics, Vol 125 Book Series: Advances in Imaging and Electron Physics*, 125, 355–415 (2002). Cited on pages 78 and 82.

Zaefferer, S. *Habilitation thesis*. RWTH Aachen (2009). Cited on page 82.

Zambaldi, C., Roters, F., Raabe, D., and Glatzel, U. Modeling and experiments on the indentation deformation and recrystallization of a single-crystal nickel-base superalloy. *Materials Science and Engineering A*, 454, 433–440 (2007). doi: 10.1016/j.msea.2006.11.068. Cited on pages 68, 70, 98, and 123.

Zghal, S., Thomas, M., Naka, S., Finel, A., and Couret, A. Phase transformations in TiAl

based alloys. *Acta Materialia*, 53(9), 2653–2664 (2005). doi: 10.1016/j.actamat.2005.02.025. Cited on page 31.

Zhang, X.D., Li, Y.G., Kaufman, M.J., and Loretto, M.H. The structure and origin of boundaries between antiphase regions in $L1_0$ intermetallics. *Acta Materialia*, 44(9), 3735–3747 (1996). doi: 10.1016/1359-6454(95)00454-8. Cited on page 28.

Zhao, M.H., Slaughter, W.S., Li, M., and Mao, S.X. Material-length-scale-controlled nanoindentation size effects due to strain-gradient plasticity. *Acta Materialia*, 51(15), 4461–4469 (2003). doi: 10.1016/S1359-6465(03)00281-7. Cited on pages 70 and 126.

Zhao, Z., Ramesh, M., Raabe, D., Cuitiño, A., and Radovitzky, R. Investigation of three-dimensional aspects of grain-scale plastic surface deformation of an aluminum oligocrystal. *International Journal of Plasticity*, 24(12), 2278–2297 (2008). doi: 10.1016/j.ijplas.2008.01.002. Cited on page 98.

Zienkiewicz, O. and Taylor, R. *The finite element method for solid and structural mechanics*. Elsevier, 6th edition (2005). Cited on page 104.

Znam, S., Nguyen-Manh, D., Pettifor, D.G., and Vitek, V. Atomistic modelling of TiAl - I. Bond-order potentials with environmental dependence. *Philosophical Magazine*, 83(4), 415–438 (2003). doi: 10.1080/0141861021000054601. Cited on pages 30 and 31.

Zong, Z., Lou, J., Adewoye, O.O., Elmustafa, A.A., Hammad, F., and Soboyejo, W.O. Indentation size effects in the nano- and micro-hardness of fcc single crystal metals. *Materials Science and Engineering A*, 434(1–2), 178–187 (2006). doi: 10.1016/j.msea.2006.06.137. Cited on page 66.

Zupan, M. and Hemker, K. Yielding behaviour of aluminum-rich single crystalline gamma-TiAl. *Acta Materialia*, 51, 6277–6290 (2003). doi: 10.1016/S1359-6454(03)00451-8. Cited on pages 42, 47, 107, and 109.

Lebenslauf (CV)

Persönliche Daten

Name:	Claudio Zambaldi
Geburtsdatum:	8. April 1978
Geburtsort:	München

Schulbildung (Education)

1984–1988	Grundschule, Bruckberg
1988–1997	Karl-Ritter-von-Frisch-Gymnasium, Moosburg

Zivildienst (Civilian service)

1997–1998	Juliane-Maier-Haus, Moosburg

Studium (Academic studies)

1998–1999	Architektur (abgebrochen), TU München
1999–2005	Materialwissenschaft, Universität Bayreuth
8/04–4/05	Diplomarbeit “Modellierung und experimentelle Untersuchung des Rekristallisationsverhaltens der Nickelbasis-Superlegierung CMSX-4”, durchgeführt am Max-Planck-Institut für Eisenforschung, Düsseldorf

Berufliche Tätigkeit (Professional experience)

2003–2004	Werkstudent, BMW Group am Standort Landshut, “Modellierung und Verifikation der Prozessierung von kohlefaserverstärkten Kunststoffen”
seit 2005	Wissenschaftlicher Mitarbeiter am Max-Planck-Institut für Eisenforschung, Düsseldorf
10/07–12/07	Postgraduierten-Stipendium der Japanischen Gesellschaft zur Förderung der Wissenschaft

Ausgewählte Veröffentlichungen (Selected publications)

Zambaldi, C., Zaefferer, S., and Wright, S. Characterization of order domains in γ-TiAl by orientation microscopy based on electron backscatter diffraction. *Journal of Applied Crystallography*, 42(6), 1092–1101 (2009). doi: 10.1107/S0021889809036498.

Zambaldi, C. and Raabe, D. Crystal plasticity modelling and experiments for deriving microstructure-property relationships in γ-TiAl based alloys. *Journal of Physics – Conference Series (ICSMA-15)*, 240(1), 012140 (2010a). doi: 10.1088/1742-6596/240/1/012140.

Zambaldi, C. and Raabe, D. Plastic anisotropy of γ-TiAl revealed by axisymmetric indentation. *Acta Materialia*, 58(9), 3516–3530 (2010b). doi: 10.1016/j.actamat.2010.02.025.